Role of Brain Angiotensin II in Cardiovascular Regulation and Erythropoiesis

Inaugural-Dissertation

to obtain the academic degree

Doctor rerum naturalium (Dr. rer. nat.)

submitted to the Department of Biology, Chemistry, Pharmacy

of the Freie Universität Berlin

by

André Felipe Rodrigues

from Brusque, Brazil

2021

The following work was carried out under the supervision of Prof. Dr. Michael Bader between December 2016 and December 2021 at the Max Delbrück Center for Molecular Medicine in the Helmholtz Association (MDC, Berlin).

1st Reviewer: Prof. Dr. Michael Bader

2nd Reviewer: Prof. Dr. Volker Haucke

Date of defense: 07.04.2022

Declaration of independence

I declare that my doctoral thesis entitled "Role of Brain Angiotensin II in Cardiovascular Regulation and Erythropoiesis" has been written independently and with no other sources and aids than quoted.

Berlin, December 2021 André Felipe Rodrigues

Dedicated to the two Ivos in my life

I. Acknowledgments

I would like to express my gratitude towards my supervisor Prof. Dr. Michael Bader, who gave me an opportunity but also helped me realizing the dream of doing a PhD abroad. I am particularly glad you gave me freedom and time to apply my ideas. Also, it was very motivating having such an enthusiastic researcher/mentor and a great listener during the whole process.

I specially thank members of the Bader lab that had major contributions to this work. Prof. Dr. Mihail Todiras who introduced me to the field of cardiovascular phenotyping as well as helped a lot with the *in vivo* procedures. Thanks for being extremely professional and having such an intense way of working that led us to make an unstoppable team. I am also glad for having Dr. Natalia Alenina along the years giving suggestions and helping me to deal with the bureaucracies of the animal work. I am thankful that Dr. Fatimunnisa Qadri helped with the imaging techniques and explained many things. Thanks to Dr. Elena Popova who implemented various protocols to generate a *knockin* model for the project. I am also thankful to all other members of the Bader lab and others that I met along my PhD at the campus. I won't list all of you because I would certainly forget some. I got the chance to meet, work and/or exchange with many amazing people which was very helpful to learn, grow, and keep curious.

I am glad that some external collaborators contributed to this work with advice or experiments. Dr. Veniamin Fishman help with the nanopore sequencing and Dr. Zouhair Aherrahrou with the genomic wide association study, thanks for helping and discussing the findings. I must thank Prof. Dr. Roland Veelken that let me and Michael to visit his lab to discuss my project and the renal denervation procedure. Another fruitful exchange was with Dr. Marko Poglitsch and Dr. Oliver Domenig from Attoquant diagnostics that performed Angiotensin measurements and were keen to discuss our findings. It also was great to count on the services offered by the animal phenotyping facility of the MDC, thanks to Patrick Langner for helping with the measurement of biochemical and hematological parameters.

I appreciate that Prof. Dr. Dominik Müller and PD. Dr. Enno Klußmann accepted to monitor the progress of my PhD project serving as committee members. Also, I am very pleased that Prof. Dr. Volker Haucke promptly agreed on taking some extra work evaluating my thesis.

I wish to thank the Max Delbrück Center as an organization for providing great conditions and opportunities during my PhD training. I am particularly thankful to the employees of the PhD office and PhD reps which I had an honor to compose for a year. Both were always very kind and helpful, and care about the students.

It was great to count on travel fundings from the German center for cardiovascular research (DZHK) that I used to go to high-hank conferences to show my work and network with different kind of scientists in the field. Another valuable opportunity was provided by the PROBRAL program of the DAAD. With the PROBRAL, I could go to Brazil to visit the laboratories of the professors Marco A.P. Fontes, Robson Santos and Maria J. C. Santos where I could learn more *in vivo* techniques as well as discuss my project.

I want to thank my families in Brazil and here. My Brazilian family always motivated me to work hard on my dreams since the beginning but also supported me in my decisions. Special thanks to my parents, grandparents, and my brother. I must recognize my partner´s role, she always stood beside me from writing applications for PhD positions until now with the thesis. She has been the perfect balance from my work-life especially when the experiments wouldn´t work. I am very happy that our baby boy came into the world recently bringing so much joy in our lives but also boosting my motivation to write this thesis. Finally, I am very happy that I had the family of my partner who welcomed me with open arms and made their best to help and make me feel at home.

II. Table of Contents

III. Summary

Hypertension prevalence is still growing worldwide as well as the number of drug-therapy non-responsive patients. Therefore, improving the current and developing new therapies to control blood pressure (BP) is warranted. Growing literature points to the sympathetic nerve system as the major system controlling long-term BP homeostasis, and human hypertension is often accompanied by increased sympathetic nerve activity (SNA). The renin angiotensin system (RAS) is involved in cardiovascular control and beyond due to the broad actions of the powerful hormone angiotensin II (Ang II) produced in the circulation or within organs. The project aimed to further characterize the modulatory effects of the RAS on SNA and its impact on cardiovascular control and erythropoiesis, particularly focusing on the role of brain-borne Ang II. These questions were experimentally addressed with RAS gain and loss of function mouse models in the FVB/N background strain, and complementary experiments were performed with rats and mixed background mice.

A transgenic line with brain-specific angiotensinogen (Agt) expression was validated (Agt-Tg) and used to demonstrate *in vivo* local brain Ang II formation. FVB/N mice cardiovascular regulation revealed predicted and surprising phenotypes. As expected FVB/N mice lacking the major Ang II receptor (AT1a-KO) presented reduced BP, and Agt-Tg displayed increased BP accompanied by increased SNA. Surprisingly, adult FVB/N mice lacking Agt (Agt-KO) were normotensive contrasting previous findings in other strains. Paradoxically, the genetic brain-rescue of Agt in Agt-KO (Agt-KO-Tg) strongly reduced BP. Using integrative physiology, we identified that the normotension in Agt-KO is driven by increased vascular tone due to exaggerated sympathetic outflow and impaired nitric oxide production which is reversed by brain Ang II in Agt-KO-Tg contrasting Agt-Tg. Agt-KO-Tg also presented better renal function compared to Agt-KO despite similar renal morphological damage. In addition, brain Ang II strongly activated renal SNA in Agt-KO-Tg, and renal denervation had minimal effect on Agt-KO and Agt-KO-Tg baseline BP.

A genome-wide-association-study was employed to uncover the genetic alteration causing FVB/N Agt-KO to fail in reducing BP. For this, a mixed background (FVB/N x C57BL/6N) F2

Agt-KO line was generated. Strikingly, the phenotyping data of the F2 Agt-KO strongly indicates a single recessive allele responsible for the BP phenotype in FVB/N Agt-KO once the BP in the F2 presented a clear bimodal distribution with most mice being hypotensive. However, the association analyses demonstrated that several loci likely contribute to the phenotype in FVB/N Agt-KO.

Finally, we identified one central and one peripheral mechanism of erythropoiesis regulation modulated by the RAS. In the brain, Ang II favors erythropoiesis via SNA. Agt-Tg with elevated brain Ang II displayed increased erythropoiesis that was reverted by peripheral sympathectomy, and rats with depleted brain Agt presented decreased baseline erythropoiesis. In the periphery, the experiments revealed that the RAS influences the iron homeostasis because Agt-KO mice presented microcytic anemia accompanied by reduced levels of circulating and tissue-stored iron.

Altogether, the data set generated within the frame of my doctoral thesis supports local formation and function of brain Ang II. Furthermore, we provided evidence that brain Ang II is involved in differential SNA regulation to different organs impacting BP homeostasis. Finally, two unprecedented mechanisms of erythropoiesis control modulated by the RAS via SNA and iron homeostasis were revealed.

Keywords: Sympathetic nerve activity, hypertension, brain RAS, rodent models, red blood cell, iron metabolism

IV. Zusammenfassung

Die Prävalenz von Bluthochdruck nimmt weltweit weiter zu, ebenso wie die Zahl der Patienten, die nicht auf eine medikamentöse Therapie ansprechen. Daher ist die Verbesserung der derzeitigen und die Entwicklung neuer Therapien zur Kontrolle des Blutdrucks gerechtfertigt. Zunehmend weist Literatur darauf hin, dass das sympathische Nervensystem das wichtigste System für die Steuerung langfristiger Blutdruckhomöostase ist, außerdem wird Bluthochdruck oft von einer erhöhten sympathischen Nervenaktivität (SNA) begleitet. Das Renin-Angiotensin-System (RAS) ist an der Kontrolle des Herz-Kreislauf-Systems beteiligt. Das potente Hormon Angiotensin-II (Ang-II) des RAS wird im Blutkreislauf oder in den Organen gebildet und besitzt vielfältige physiologische Effekte. Das Projekt zielte darauf ab, die modulatorischen Wirkungen des RAS auf die SNA und entsprechenden Folgen auf die kardiovaskuläre Kontrolle und die Erythropoese weiter zu charakterisieren, wobei der Schwerpunkt auf der Rolle des im Gehirn gebildeten Ang II lag. Dieses Ausgangsinteresse wurde experimentell mit RAS Gain und Loss-of-Function-Mausmodellen im FVB/N Hintergrundstamm untersucht. Ergänzend wurden Versuche mit Ratten und Mäusen mit gemischtem genetischen Hintergrund durchgeführt.

Eine transgene Linie mit gehirnspezifischer Angiotensinogen-Expression (Agt) wurde validiert (Agt-Tg) und verwendet, um die lokale Ang-II-Bildung im Gehirn in vivo zu demonstrieren. Die Ergebnisse zur kardiovaskulären Regulation von FVB/N-Mäusen ergaben die vermuteten und überraschende Phänotypen. Wie erwartet hatten FVB/N-Mäuse, denen der wichtigste Ang-II-Rezeptor (AT1a-KO) fehlte, einen verminderten Blutdruck. Außerdem zeigte Agt-Tg einen erhöhten Blutdruck im Zusammenhang mit erhöhter SNA. Im Gegensatz zu früheren Befunden bei anderen Stämmen, waren erwachsene FVB/N-Mäuse ohne Agt (Agt-KO), überraschenderweise normotensiv. Paradoxerweise senkte die spezifische Wiederherstellung der Agt Genexpression im Gehirn von Agt-KO (Agt-KO-Tg) den Blutdruck dramatisch. Mithilfe von integrativer Physiologie konnten wir feststellen, dass die Normotonie bei Agt-KO durch einen erhöhten Gefäßtonus aufgrund eines übermäßigen Sympathikotonus und einer beeinträchtigten Stickoxidproduktion verursacht wird. Diese werden bei Agt-KO-Tg im Gegensatz zu Agt-Tg durch Ang II im Gehirn umgekehrt. Agt-KO-Tg wies im Vergleich zu Agt-KO trotz ähnlicher morphologischer Nierenschäden eine bessere Nierenfunktion auf. Des Weiteren aktivierte Ang II

im Gehirn die renale SNA in Agt-KO-Tg stark, wohingegen eine renale Denervierung nur minimale Auswirkungen auf den Basisblutdruck von Agt-KO und Agt-KO-Tg hatte.

Eine genomweite Assoziationsstudie wurde implementiert um die genetische Veränderung, die zu der Normotonie bei FVB/N Agt-KO führt, aufzudecken. Für diesen Zweck wurde eine F2 Agt-KO-Linie mit gemischtem Hintergrund (FVB/N x C57BL/6N) erzeugt. Bemerkenswerterweise wiesen die Phänotypisierungsdaten durch eine klare bimodale Verteilung des Basisblutdrucks in der F2 Agt-KO stark auf ein einzelnes rezessives Allel hin, das für den Blutdruck-Phänotyp in FVB/N Agt-KO verantwortlich ist, wobei die meisten Mäuse hypoton waren. Die Assoziationsanalysen zeigten jedoch, dass wahrscheinlich mehrere Loci zum Phänotyp bei FVB/N Agt-KO beitragen.

Im letzten Teil der Arbeit identifizierten wir zwei Regulationsmechanismen der Erythropoese- (zentraler und peripherer), die durch das RAS moduliert werden. Im Gehirn begünstigt Ang II die Erythropoese über SNA, da Agt-Tg mit gesteigertem Ang-II im Gehirn eine erhöhte Erythropoese zeigte, die durch periphere Sympathektomie rückgängig gemacht wurde. Außerdem zeigten Ratten mit verminderter Agt-Expression im Gehirn eine verringerte Erythropoese. In der Peripherie zeigten die Experimente, dass das RAS die Eisenhomöostase beeinflusst, da Agt-KO-Mäuse eine mikrozytäre Anämie aufwiesen, die mit reduzierten Konzentrationen von zirkulierendem und im Gewebe gespeichertem Eisen einherging.

Zusammenfassend zeigen die im Rahmen meiner Doktorarbeit erhobenen Daten die lokale Bildung und Funktion von Ang II im Gehirn. Darüber hinaus konnten wir nachweisen, dass Ang II im Gehirn an der differenzierten SNA-Regulierung in verschiedenen Organen beteiligt ist, was sich auf die Homöostase des Blutdrucks auswirkt. Schließlich wurden zwei neue Mechanismen der Erythropoese Kontrolle aufgedeckt, die durch das RAS über SNA und Eisenhomöostase moduliert werden.

Schlüsselwörter: Sympathische Nervenaktivität, Bluthochdruck, Gehirn-RAS, Nagetiermodelle, rote Blutkörperchen, Eisenstoffwechsel

1 Introduction

1.1 Blood pressure and hypertension

Classically blood pressure (BP) is defined as the product of the cardiac output and total peripheral resistance. The cardiac output depends on the heart rate (HR) and stroke volume (essentially the blood volume pumped *per* heartbeat in a given time frame). While the peripheral resistance is the resistance encountered by the blood pumped into the circulatory system that is governed by the blood volume in the system itself and neurohumoral modulators of the arterial tone[1] (1). Baseline BP levels vary considerably throughout a day in response and adaptation to alternating environmental conditions including but not restricted to stress, physical activity, sleep and emotions (2). However, the long-term average levels of BP vary minimally because several organs and hormonal systems that operate in an interdependent manner to keep long-term BP levels constant (3) (Figure 1).

The appreciation that BP control is complex already emerged in the 1940s by the observations of Irvine Page who proposed the "Mosaic Theory of Hypertension" in which hypertension was for the first time described as a complex disorder (4). Different organs have specific and relative contributions for short-term and long-term BP control. Hence, the malfunctioning of one of these components potentially triggers a systemic chain of reactions that may result in hypertension (Figure 1). One example is the classical hypertension model of chronic angiotensin II (Ang II) overload in experimental animals which mimics conditions as renal artery stenosis[2]. Chronically increased Ang II levels lead to major alterations impacting BP control including renal salt and water reabsorption, vasoconstriction, vascular remodeling and dysfunction, immune cell activation, baroreflex impairment and increased sympathetic nerve activity (SNA). In this model, the alterations mentioned induce changes in the cardiac output and vascular resistance that ultimately raise basal BP levels chronically establishing hypertension (5).

[1] Arterial tone refers to the degree of constriction of the arteries. For details see section 1.5.
[2] Narrowing of the renal artery leading to renal hypoxia and consequently increased renin release and Ang II production in the circulation.

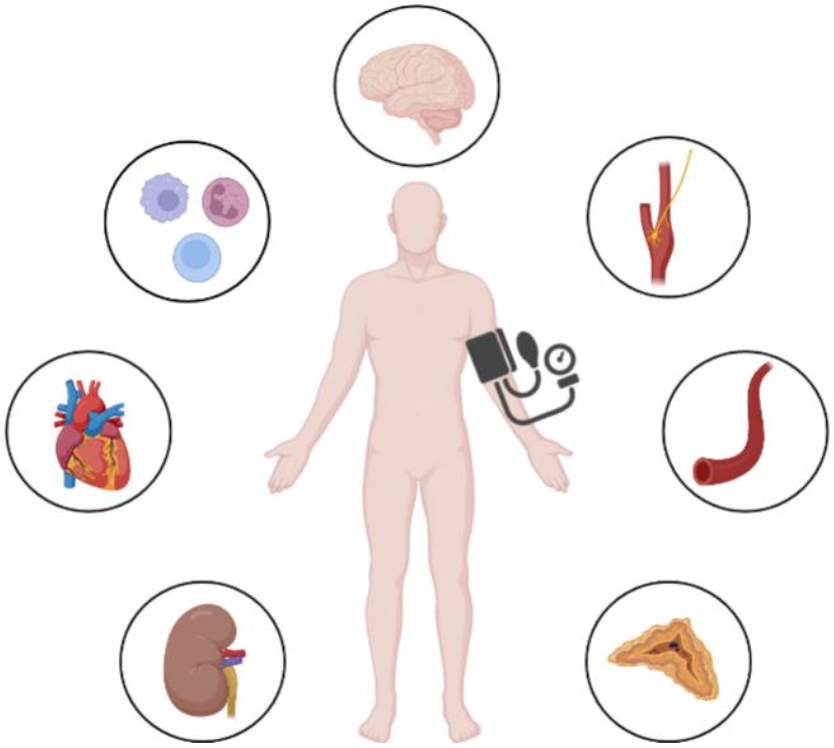

Figure 1 - Major tissues controlling short-term and long-term BP levels.
Major organs and organ systems shown modulate BP via multiple interactions involving different neuroendocrine systems as the sympathetic nervous system (SNS) and the renin–angiotensin system (RAS). From left to right kidneys, heart, immune system, brain, baroreceptors, vasculature and adrenal glands are represented. This illustration was created in BioRender.com.

Hypertension is characterized by chronically elevated baseline BP levels. Essential hypertension, also known as primary hypertension, is the most common form of hypertension diagnosed, affecting around 85-90% of the hypertensive population. The main feature of essential hypertension is the fact that there is no evident cause. The remaining cases of hypertension are classified as secondary hypertension in which a known factor causes hypertension as renal artery stenosis, adrenal adenoma, Cushing's syndrome, and single gene mutations (6, 7). The socio-medical relevance of hypertension is of great interest, taking recent clinical data and recent guidelines for hypertension identification and management into account, between 1/3 to 1/2 of the adult world population is estimated to be hypertensive (8–10). In addition, hypertension prevalence grew in the last decades especially in low income countries (11, 12). Associated to environmental and genetic predisposition, primary hypertension is a major risk factor for the development of cardiovascular diseases such as heart failure and arteriosclerosis as well as stroke, dementia and renal diseases (8, 11, 13). Currently a major problem in hypertension management worldwide is that half of the treated patients present uncontrolled hypertension also known as resistant hypertension despite the large number of drugs available to lower BP.

Therefore, innovative therapies are needed to manage BP levels in hypertensive patients with uncontrolled BP (10, 14).

Given that hypertension is a chronic condition, the most obvious treatment would be targeting the major long-term BP regulator. There have been many debates in the scientific literature surrounding this topic in the last decades. The classic model developed by Guyton and Coleman that places the kidney in a central position regulating BP via blood volume was widely accepted until recently. In this model, a pressure natriuresis curve was described, BP essentially increases renal perfusion pressure, and sodium and water excretion driving blood volume depletion to prevent that BP increases. In view of that, all manifestations of hypertension would be caused by increased blood volume, however, essential hypertension is usually accompanied by reduced blood volume (15). In the last two decades, the Guyton and Coleman model has been challenged, and the sympathetic nervous system (SNS) with its ability to connect virtually all visceral organs emerged as a major organ system integrating the short-term and long-term BP control (3, 16–19). Moreover, essential hypertension patients usually present increased muscle SNA, which is the largest vascular bed in the body therefore significantly contributing to baseline BP. Interestingly, exaggerated SNA is found before hypertension development in humans with high likelihood to become hypertensive (20–23). Sympathetically driven hypertension is supported by several recent studies in humans and preclinical models, and it is often referred as neurogenic hypertension. Note, the SNS modulates renal excretory mechanisms directly via renal innervation and indirectly via BP levels (pressure natriuresis). Thus, the cause of blood volume depletion in primary hypertension might be attributed to the high BP levels triggered by increased SNA supporting that volume depletion during hypertension might be the consequence of increased renal excretion due to high BP (17, 24).

1.2 The autonomic nervous system

The autonomic nervous system is a self-governing system involved in homeostasis adjustment and adaptation to changes in the environment. Among physiological functions under autonomic influence are BP, digestion, body temperature, mineral balance and respiration. Two distinct arms compose the autonomic system, the SNS and the parasympathetic nervous system. Classically the SNS is associated with fight-or-flight response while the parasympathetic system with rest and

digest, and both are known to override each other during different behavioral states. The reciprocal activity among both arms is achieved due to distinct interconnected brain nuclei which are responsible for sympathetic and parasympathetic efferent outflow. The neuronal populations within autonomic centers are subjected to direct modulation by factors as Ang II and sodium but also fine-tuned by peripheral sensors (afferent neurons) (3, 25, 26).

1.2.1 The sympathetic nervous system (SNS)

Innervating virtually all organs in the animal's body, the SNS releases neurotransmitters that control cellular responses at targeted tissues. The most abundant and effector sympathetic neurotransmitter released is norepinephrine (NE), additionally neuropeptide Y and ATP are co-released at sympathetic terminals. NE is synthesized within neurons from the amino acid tyrosine in three enzymatic steps: first tyrosine is converted in L-3,4-Dihydroxyphenylalanine (L-DOPA) by tyrosine hydroxylase that is also the rate limiting enzyme, second DOPA decarboxylase converts L-DOPA in dopamine, and finally dopamine is transported into synaptic vesicles where dopamine β-hydroxylase synthetizes NE from dopamine (27). After NE release by prejunctional neurons, around 90% of the NE is reuptaken into the presynaptic neuron, around 5% binds to receptors on cells of a target organ and is internalized and degraded, the remaining NE is readily degraded at the extracellular space. At targeted tissues, NE binds to two major classes of receptors, α and β, containing 9 different subtypes ($\alpha1_A$, $\alpha1_B$, $\alpha1_D$; $\alpha2_A$, $\alpha2_B$, $\alpha2_C$; β1, β2, β3), and these are all G protein coupled receptors (GPCRs). Importantly, the α2 receptors are also expressed at presynaptic neurons serving as autoreceptors inhibiting the release of NE (28–30).

At an organizational level, the SNS is composed of presympathetic neurons mainly originating from two brain areas, the paraventricular nucleus of the hypothalamus (PVN) and the rostro ventrolateral medulla (RVLM), located in the hypothalamus and brainstem, respectively. Importantly, there are several brain nuclei projecting and modulating the activity of the two areas mentioned including the nucleus tractus solitarii (NTS), the subfornical organ (SFO) and the organum vasculosum of the lamina terminalis (OVLT) (Figure 4). The PVN and RVLM neurons project to spinal sympathetic preganglionic neurons at the intermediolateral cell column (IML) which synapses in peripheral sympathetic ganglia releasing mostly acetylcholine. Acetylcholine stimulates nicotinic receptors on postganglionic neurons that are the neurons effectively innervating peripheral organs (3, 31, 32) (Figure 2). Peripheral reflexes are sensed by afferent

neuronal projections of neurons located in the spinal cord at the dorsal root ganglia. Ultimately the signal reaches the NTS the main nucleus of the brainstem integrating visceral inputs that in the end lead to downstream efferent responses by modulating RVLM neuronal activity (Figure 2). The NTS projects directly to the RVLM or via the CVLM which contains mostly inhibitory neurons. Ang II modulates SNA binding to angiotensin type 1 and type 2 receptors (AT1 and AT2) receptors that are expressed by neurons in all mentioned nuclei (Figure 4) (33, 34).

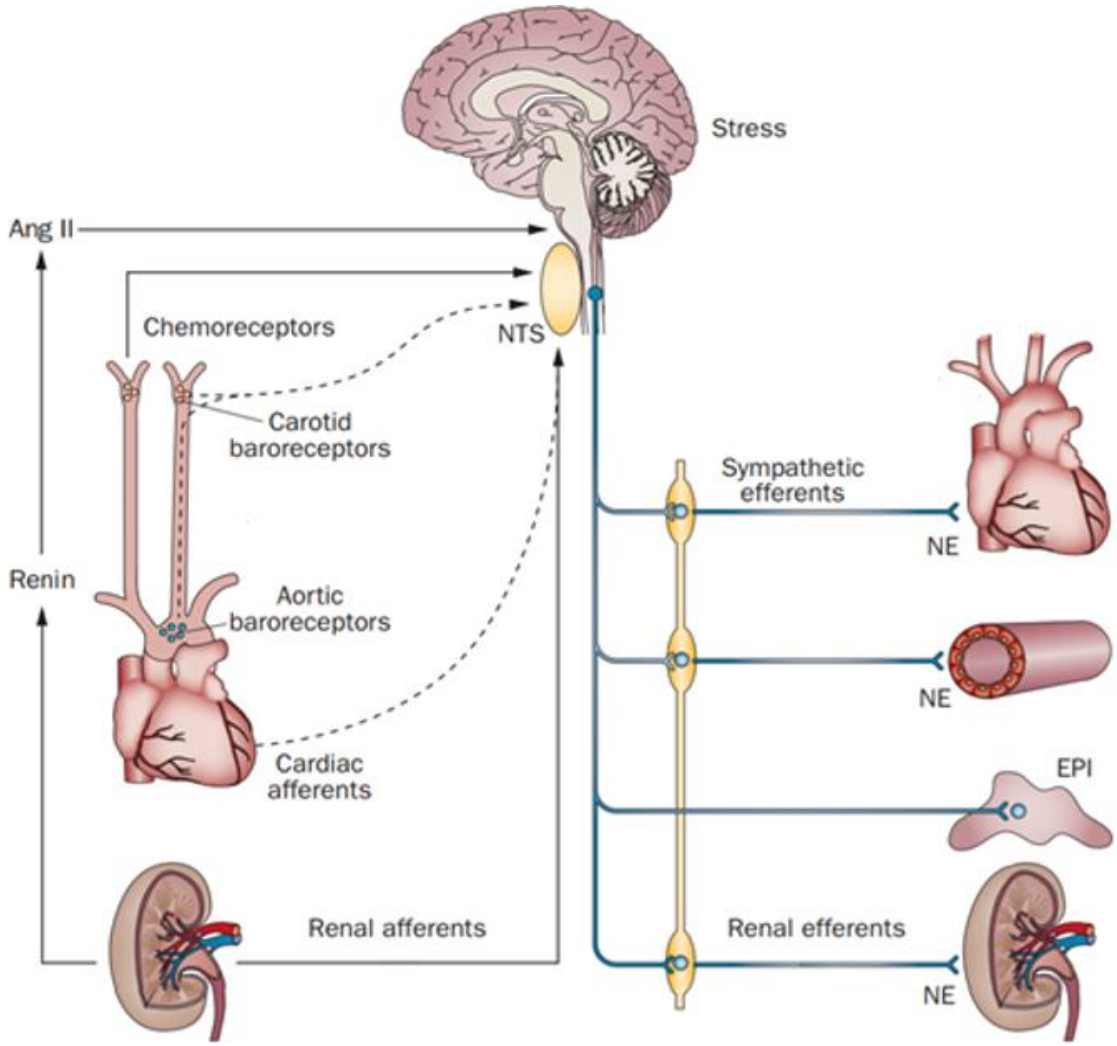

Figure 2 - Schematic representation of the SNS innervating cardiovascular organs.
The SNS (blue) leaves the brain through the spinal cord projecting to sympathetic ganglia, and postganglionic neurons innervate peripheral organs as the ones controlling cardiovascular homeostasis. SNS activity is modulated by interconnected brain areas subjected to modulatory effects of factors as Ang II, sodium, and stress. Peripheral sensors including baroreceptors, chemoreceptors, and renal afferents fine tune SNA to maintain BP homeostasis. NE = norepinephrine, EPI = epinephrine. Modified from Victor, 2015 (35).

1.2.2 SNS, BP control and a target for hypertension treatment

The cardiovascular homeostasis is well known to be modulated by the SNS as it is seen as the most relevant system integrating BP control. SNA directly and indirectly affects the cardiac output and total peripheral resistance. The sympathetic control over the baseline BP levels is achieved at different organs including the heart, kidneys, adrenal medulla and vasculature (Figure 2). NE binding to β1 adrenergic receptors increases HR and cardiomyocyte constriction. In the kidney, renal nerves innervate generally three distinct structures (vasculature, renal tubules and juxtaglomerular apparatus) with well described functions. The renal vasculature is constricted by sympathetic stimulation increasing renal vascular resistance provoking a reduction in glomerular filtration rate; tubule cells stimulated by the SNS absorb more water and sodium, and juxtaglomerular cells stimulation control expression and secretion of Renin (Ren) (16, 36). The adrenal cortex is a component of the SNS that releases epinephrine (80%) and NE (20%) in the circulation (37). The body vasculature including smooth muscle cells of veins and arteries as well as pericytes from capillaries are innervated by the SNS and constrict upon NE release. Importantly, different peripheral target organs and vascular beds are innervated by distinct branches of the SNS making a branch specific activation or deactivation possible depending on local demand. A classic example is the role of differential SNA during exercise to improve muscle blood flow and oxygenation (3, 38).

Peripheral sensors detect BP, blood volume and blood gas composition to adjust SNA outflow accordingly, aiming to regulate perfusion and BP. Located at the carotid sinuses, the baroreceptors sense pressure and are mostly responsible for buffering short-term changes in BP by altering SNA and HR accordingly. Volume sensitive mechanoreceptors in the heart and lung respond to changes in blood volume and adjust vascular SNA. Carotid body chemoreceptors sense hypoxia and are key for blood gas homeostasis triggering respiratory changes but also modulating vascular SNA (10, 26, 30). Other key sensors are the renal afferents with mechano-and-chemo sensitive receptors that modulate renal SNA. Normally activation of the renal afferents suppresses renal SNA in process known as the reno-renal-reflex. Importantly, during renal pathologies the reno-renal-reflex might operate inversely and additionally overstimulate vascular SNA (Figure 2). At each cardiac cycle BP is sensed by the baroreceptors strongly rebounding pressor and depressor variations therefore keeping short-term BP levels constant.

However, the baroreceptors are unable to control the long-term BP levels because their neuronal firing activity resets to a new BP set-point *e.g* during hypertension when long-term baseline BP changes to a new level. On the other side resting SNA has been attributed as the major factor controlling the long-term BP levels. Several locally produced substances or circulating substances modulate the activity of neuronal populations critical for resting SNA control including sodium, leptin and Ang II (30, 39, 40).

The first successful therapies to lower BP in hypertensive patients were developed in the 1940s and targeted the SNS. Either chemically or surgically, these interventions lowered the overall SNA across the body leading to BP reduction but also several side effects (12). Nowadays, the understanding of the mechanisms behind SNA control in physiology and pathophysiology grew. Different manifestations of hypertension as those associated to high salt intake or obesity display distinctly altered patterns of SNA branch distribution often referred as sympathetic signatures (17, 39, 41). Therefore, specific sympathetic branch ablation or inhibition have been developed and are being implemented in patient care. The most advanced therapy is renal denervation which has shown success in lowering BP of patients with drug-resistant hypertension. The benefits are not yet fully described but the above-mentioned renal mechanisms modulated by SNA are potentially involved as those triggered by pathological afferent nerve activation. Other therapies include chronic baroreceptor stimulation, and carotid body ablation which ultimately will reduce SNA especially to the vasculature leading to baseline BP levels reduction (42, 43).

1.3 The renin-angiotensin system (RAS)

Research on the RAS started in 1898 when Tigerstedt and Bergman observed the presence of a pressor compound in rabbit renal extracts when injecting in recipient animals (44). Because of the renal origin this component was named renin (Ren). Decades later in the 1930s, Harry Goldblatt proved that BP increases due to Ren secretion upon renal arterial blood flow restriction in dogs based on observations from autopsied patients who died from fulminant hypertension (45). The notion that Ren forms a vasoactive substance by interacting with some blood-derived protein was discovered in parallel by two different groups of Irvine Page and Braun Menendez in 1939 and 1940, respectively. The formed unknown substance was named hypertensin and angiotonin by

the different groups that later agreed on a fused name “angiotensin” (46). Shortly after, it was discovered that two angiotensin peptides exist in the circulation (Ang I and Ang II, Figure 3), and that Ang I is inactive, but it is converted in circulation to the active peptide Ang II (47).

In the last three decades, it became clear that the RAS is comprised of various peptides with specific receptors acting on the cardiovascular system (Figure 3). These newly discovered peptides are in most of the cases classified as protective peptides of the RAS, essentially having antagonistic effects on those elicited by Ang II, except Ang III which has a similar affinity for the AT1 and AT2 receptor as Ang II (48, 49). Perhaps the most expressive example is Ang 1-7 which is a degradation product of Ang II produced by at least three distinct enzymes including angiotensin converting enzyme 2 (ACE2). Later, ACE2 was characterized to have other physiological roles beyond Ang II metabolism including gut tryptophan uptake as well as being the viral entry receptor for SARS-CoV and SARS-CoV-2 (50). A current overview of all RAS peptides, receptors, pathways, and physiological relevance is displayed in Figure 3.

1.3.1 Classical RAS

Over 100 years after the initial postulation of the RAS existence, the classical RAS peptide production has been understood in terms of enzymes and tissue expression. The two enzymatic steps required to form Ang II in the circulatory system involves Ren and angiotensin converting enzyme (ACE) (Figure 3). However, some aspects are not yet fully described, perhaps the most intriguing aspect surrounds the Ren production and activation. In adult animals, Ren is produced as a proenzyme by renal juxtaglomerular cells, part of Ren is constitutively secreted ~90%, and part stored in secretory vesicles ~10% where it is activated. Part of constitutively secreted Ren is most likely activated in the circulation, but the mechanisms are not fully defined. Stored Ren is released on demand by the influence of several factors including SNA, BP and nitric oxide (NO), occurring for example during acute bleeding (51). During renal development, Ren positive cells are abundant and give origin to smooth muscle cells of afferent arteriole, arterioles and arteries. If homeostasis is threat, in adult life, *e.g* dehydration and hypotension smooth muscle cells of the renal vascular tree retransform into Ren expressing cells to increase blood Ang II levels. This mechanism is driving by different stimuli including NE and

prostaglandins that recruit the cAMP pathway triggering the nuclear translocation of the transcription factor CREB[3] (36). Angiotensinogen (Agt), the precursor protein of all RAS peptides, is secreted by the liver hepatocytes into the circulation after losing its signal peptide (52, 53). The only known substrate for Ren is Agt, the reaction results in the production of Ang I that comprises the 10 initial amino acids of the N-terminal sequence of Agt. Ang I is an inactive peptide that is cleaved at its C-terminal portion by ACE to form the potent octapeptide Ang II. Ang II formation mostly takes place in the pulmonary circulation because the transmembrane enzyme ACE is abundantly expressed by lung endothelial cells (33) (Figure 3).

The octapeptide Ang II directly or indirectly regulates cardiovascular function and hydromineral balance via its receptors that are expressed at all cardiovascular relevant organs. Ang II binds to AT1 and AT2 receptors that are coupled primarily to $G_{q/11,}$ and $G_{i,}$ respectively. Most of the physiological effects of Ang II are mediated via the Ang II/AT1 axis. The AT2 receptor generally has antagonistic effects, and it is included in the protective arm of the RAS (33) (Figure 3). In addition to the G-protein signal, the Ang II/AT1 axis is recognized to activate several G-protein independent pathways including mitogen-activated protein kinase and β-arrestin dependent signaling (48). Ang II signaling seems to be important during embryonic development, a well-documented example is the role of the Ang II/AT1 receptor during renal development (54). Importantly, rodents have two isoforms of the AT1 receptor AT1a and AT1b encoded by the genes *Agtr1a* and *Agtr1b*, respectively. However, the AT1a is the most abundantly expressed and relevant receptor for cardiovascular control (52).

[3] CREB = cAMP response element-binding protein

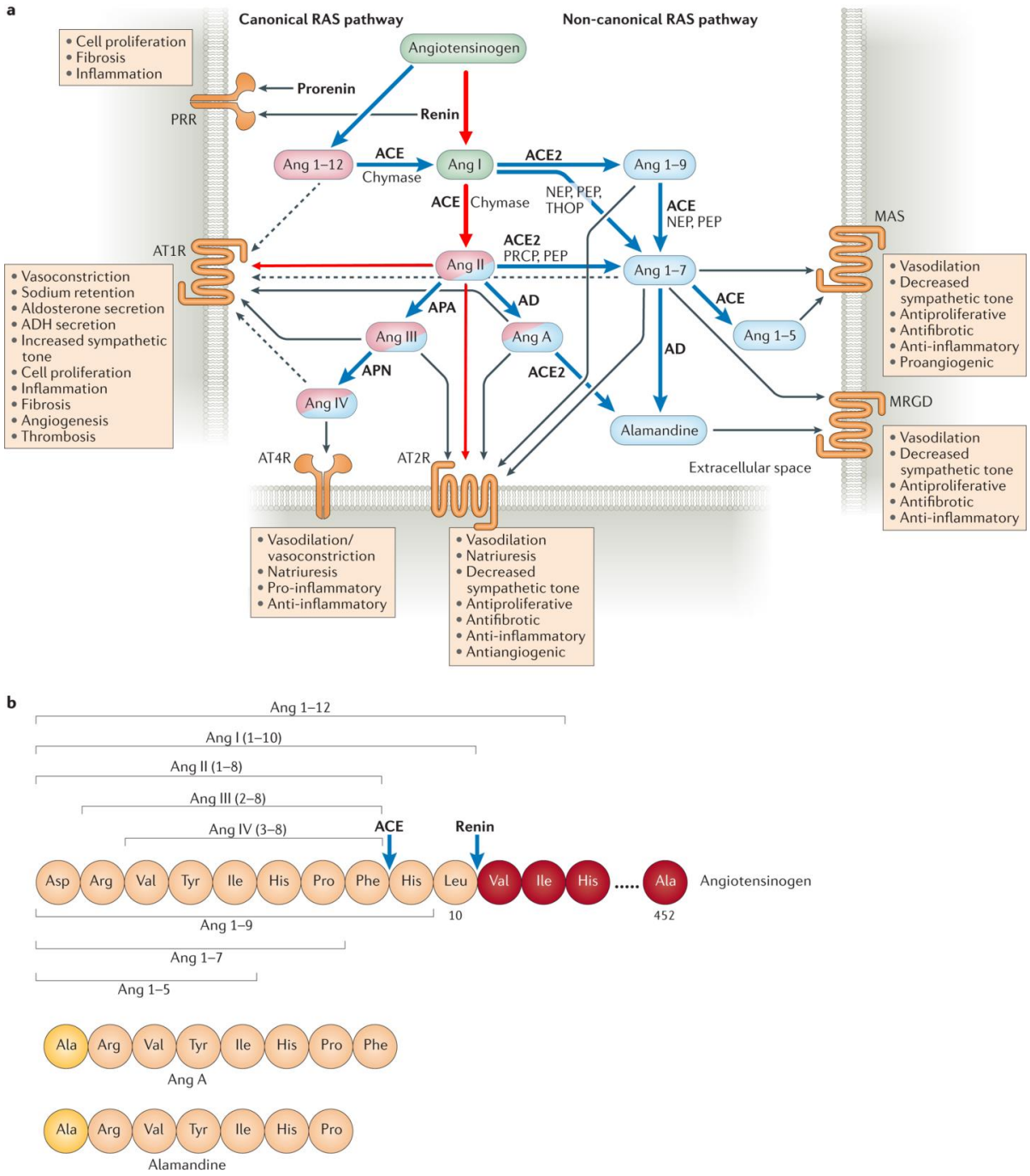

Figure 3 - Current overview of the RAS peptides and its physiological roles.
(**a**) RAS peptides, RAS enzymes, and RAS receptors. Downstream receptor signaling effects including cellular and physiological responses are included in the boxes next to the receptors. Red arrows indicate the classical RAS, highlighting the production of Ang II and the binding of the octapeptide to its two receptors (AT1 and AT2). Effector peptides showed in pink boxes indicate canonical RAS (associated to deleterious effects), and effectors in blue the non-canonical (protective arm, counteracts the effects of Ang II). Mixed color indicates peptides with both effects. (**b**) Amino acid sequence of the Agt and RAS peptides. Angiotensin converting enzyme = ACE and Ren cleaving site are showed by the blue arrows. Ang = angiotensin, AD = aspartate decarboxylase, ADH = antidiuretic hormone =AVP, APA = aminopeptidase A, APN = aminopeptidase N, NEP = neprilysin, PEP = prolylendopeptidase, PRCP = prolylcarboxypeptidase, THOP = thimet oligopeptidase. Modified from Bekassy et al. 2021 (55).

1.3.2 Tissue RAS

Besides the classical RAS forming Ang II in the circulation, the presence of local RAS systems has been described in diverse cardiovascular tissues. This concept started with the studies from Detlev Ganten that demonstrated Ren-like activity and angiotensin peptides formation in tissues including the brain (56–58). RAS components are either expressed in tissues or imported from the circulation to locally form angiotensin peptides (33, 59, 60). Ren, Agt and ACE infiltrate tissues. Endothelial ACE might be shedded from the cell membrane and retain reduced enzymatic activity to metabolize Ang I to Ang II. The functional production of angiotensin peptides in different organs of the cardiovascular system is supported by elegant studies on animal models that demonstrated cardiovascular responses to local tissues specific-RAS ablation or overexpression (61–65). In addition, the benefits of RAS blockers as a treatment for hypertension is suggested to be due to local tissue RAS suppression (66). This idea was strengthened in a study that demonstrated BP reduction in spontaneously hypertensive rats treated with a specific siRNA against liver Agt. The treatment reduced tissue Agt and Ang II while circulating Agt levels were reduced but not Ang II levels (by Ren compensatory mechanisms), showing a key role of tissue Ang II and circulating Agt to infiltrate tissues and locally form Ang II which is relevant for BP homeostasis (67).

1.3.3 Brain RAS

Different from all peripheral organs, the brain is isolated from most of the circulating substances by the blood-brain-barrier (BBB). RAS components do not cross the BBB including Ang II, except in pathological conditions such as hypertension where Ang II penetrates the BBB. Brain Ang II is recognized to modulate SNA, arginine-vasopressin (AVP) release, thirst and salt appetite. These responses are complex considering that Ang II receptors are expressed in most of the cardiovascular nuclei mediating the physiological responses whilst neuronal nuclei modulate each other by sending projections (Figure 4). Some of these nuclei are subjected to actions of circulating Ang II because these neuronal populations are positioned in brain areas where the BBB lacks the typical tight junction formation (68). These areas are important peripheral sensors of the brain. Thirst, salt appetite and AVP as well as SNA are triggered by blood-borne Ang II

binding to AT1 receptors at the SFO and OVLT (Figure 4). In addition, other brain nuclei protected by the BBB, including the PVN and RVLM, express AT1 and AT2 receptors and are known to control AVP release and SNA (Figure 4). Another well characterized cardiovascular center within the BBB is the NTS where Ang II modulates the baroreflex function. Thus, local actions of Ang II on these areas not accessible to blood-borne Ang II are presumably from locally formed Ang II when the BBB is intact (33, 69, 70) (Figure 4).

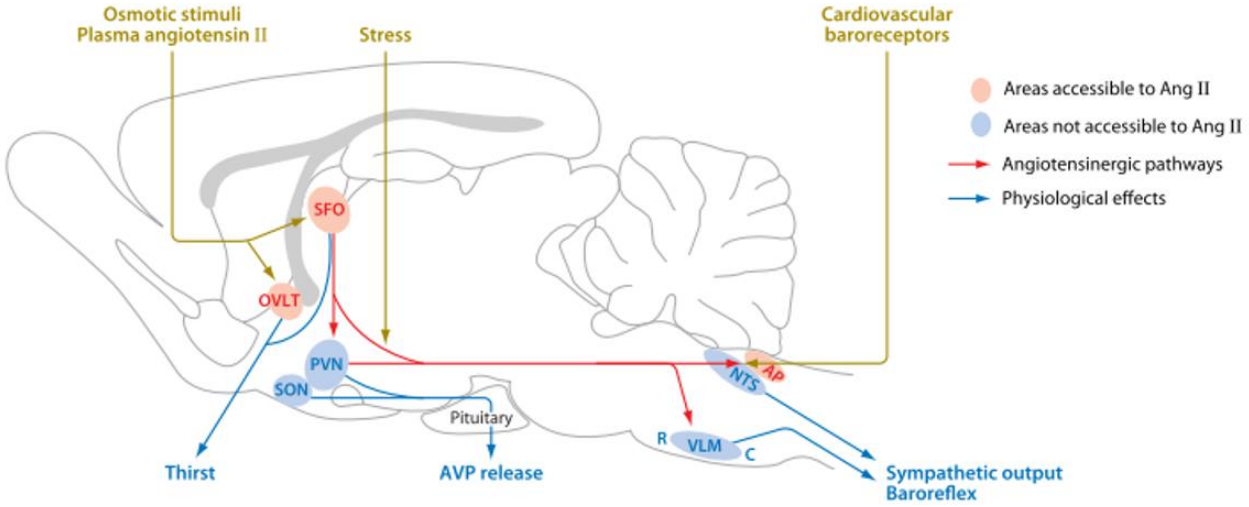

Figure 4 - Schematic representation of cardiovascular brain nuclei responsive to Ang II.
There brain nuclei marked in red are accessible to circulating Ang II. Other brain areas marked in blue are within the BBB therefore brain-borne Ang II acts on these neuronal populations. SFO = subfornical organ, PVN = paraventricular nucleus, RVLM = rostral ventrolateral medulla, CVLM = caudal ventrolateral medulla, NTS = nucleus tractus solitarii, SON = supraoptic nucleus, OVLT = organum vasculosum of the lamina terminalis, AVP = arginine vasopressin. Modified from: Bader, 2010 (33).

The RAS precursor protein Agt is an abundant protein produced and secreted mostly by astrocytes (~90%) in the brain (71, 72). Ren is the limiting factor for brain Ang II production because its expression levels and activity in the brain are very low. Brain ACE expression is mostly abundant on brain endothelial cells and choroid plexus, neurons have a lower ACE production including neurons at cardiovascular nuclei like SFO and PVN (73). *In vivo* experiments support ACE functional formation of Ang II in the brain extracellular space because injections of Ren in the brain of rodents triggers the same effects of Ang II which are an increase in BP and thirst, and these responses are blocked by ACE or AT1 blockers. Ang II receptors are expressed predominantly by neurons, some studies using techniques as immunofluorescence demonstrated Ang II receptors on glial cells. However, *in situ* hybridization and reporter mouse lines showed neuronal exclusive expression of AT1a and AT2 receptors, and normally the expression of the different receptor subtypes does not overlap (74, 75).

In rats, brain Ren activity represents only 2.5% of the plasma activity. However, if the rats are prior perfused, a 60% reduction in brain Ren activity is observed meaning that most of the "brain Ren activity" measured is actual blood-derived Ren. Another level of complexity is that brain Ren is expressed by neurons. In these neurons a splice variant encodes a truncated version of Ren that is enzymatically active because the signal peptide sequence and part of the pro sequence are not encoded. Thus, this truncated form remains restricted in the cytoplasm (76–78). The remaining extreme low amount of secreted Ren represents only ~2% and must be activated by yet unknown mechanisms. One candidate that was proposed to solve this puzzle is the prorenin receptor. This single transmembrane receptor protein is ubiquitously expressed by neuronal cells. Ren and prorenin bind to the prorenin receptor, the binding of the prorenin promotes a non-enzymatic activation of Ren, rearranging the 43 amino acid prosegment thereby exposing the catalytic site (Figure 3). However, the binding affinity seems to be too low to even activate the high levels of Ren in the circulation (79). Thus, researchers are starting to abandon this concept while the brain Ang II formation remains controversial.

1.3.4 RAS, BP control and a target for hypertension treatment

The RAS with its powerful peptide hormone Ang II is a major system controlling BP and water balance. Ang II stimulates blood volume increase directly by thirst and salt appetite, or indirectly stimulating the release of the hormones AVP and aldosterone, from the brain and from the adrenal cortex, respectively. AVP modulates renal water reabsorption and has vasoconstrictor properties while aldosterone stimulates sodium reabsorption by the kidneys. In addition, Ang II itself controls renal sodium and water reabsorption. BP control exerted by the Ang II formation besides volume expansion includes the vascular constrictor action of Ang II, and SNA modulation. Ang II/AT1 axis has been associated to end-organ damage with the potential to contribute to hypertension. These damages caused by Ang II include several organs controlling BP, cardiac hypertrophy, vascular dysfunction, baroreceptor signal dumping and immune cell activation. Reactive oxygen species formation, inflammation, and fibrosis are among the cellular mechanism of the pathology triggered (6, 33).

Currently RAS blockers and diuretics are the most prescribed drugs to pharmacologically treat hypertension. RAS blockers are designed to reduce Ang II reactivity. Thus Ren, ACE and AT1 receptor blockers are given to patients with hypertension to manage their BP. The first RAS inhibitors developed were ACE inhibitors introduced in the 1980s, later AT1 blockers and Ren inhibitors were introduced sequentially (8, 80). AT1 and ACE blockers are the most prescribed RAS blockers and some of these drugs as candesartan and lisinopril penetrate the BBB potentially blocking brain AT1 receptors and brain ACE activity, respectively. RAS blockers are largely prescribed due to its efficacy in view that Ang II modulates BP at different organs. In comparison to SNS blockers as α1 blockers, blocking the RAS reactivity has reportedly less side effects (81, 82).

1.4 Interaction between RAS and SNS

RAS and SNS modulate each other's activity. There is evidence that Ang II does not only modulate SNA at the brain level, but also in the spinal cord, sympathetic ganglia, and postganglionic neurons. Prejunctional neurons express AT1 receptors and Ang II facilitates NE containing vesicles release via membrane depolarization (30, 35, 83, 84). Also, Ang II contributes to the release of epinephrine and NE from the adrenal medulla. Another well-known interaction node is the renal sympathetic modulation of the RAS rate-limiting enzyme Ren expression and release in the kidney. Ren is controlled by NE via β-adrenergic receptor binding which is coupled to Gs that triggers the production of cAMP and thereby Ren expression and release (36).

1.5 Vascular tone and BP control

Arteries are essentially constituted of three layers from the inside out: endothelial cells, smooth muscle, and adventitia. Blood vessels are composed of several layers of smooth muscle cells. Smooth muscle cells are capable to constrict and relax in response to neurohumoral factors modulating the vascular caliber that influences peripheral resistance and ultimately BP. The vascular tone of a blood vessel is the relative constriction level of the maximal dilated capacity of this vessel. Several substances such as Ang II, NE, AVP, endothelin-1 serotonin, bradykinin, neuropeptide Y, ATP and many others act locally on vascular smooth muscle cells and modulate the vascular tone. Vasoactive substances might be produced in the circulation (modulating the

systemic vascular tone) or locally (modulating the local vascular tone) like during muscle exercise. Sympathetic terminals innervate the smooth muscle cell layer and locally release its vesicular content. Because the SNS has a branch-specific activity the vascular adrenergic tone is a very important system to control local blood flow and redistribute blood throughout the body (27, 38).

Vasoconstrictors and vasorelaxants usually act on vascular smooth muscle receptors recruiting different intracellular pathways. These intracellular pathways modulate the levels of cytoplasmatic calcium by extracellular calcium entry or release from the endoplasmic reticulum reservoir. Calcium is essential to trigger vasoconstriction by forming the calcium-calmodulin complex which leads to myosin light-chain kinase activation. Active myosin light-chain kinase fosters the interaction between myosin and actin by phosphorylation of myosin resulting in vasoconstriction. In addition, vasoactive substances may trigger vasoconstriction via calcium independent mechanism involving RhoA/ROCK kinase pathway which directly or indirectly inhibits myosin light chain phosphatase activity (85, 86).

The monolayer of endothelial cells play an important role modulating the vascular tone. The smooth muscle contractile machinery is modulated by endothelium-derived relaxing factors, including NO, prostaglandins, and endothelium-derived hyperpolarizing factor. The vasorelaxant properties of NO are the most studied. NO is produced from the amino acid L-arginine by three distinct NO synthases, endothelial cells have a specific isoform termed endothelial NO synthase. NO production is stimulated by several substances binding to endothelial receptors including Ang II, NE, endothelin-1, acetylcholine as well as shear stress that activates NO synthase without a ligand. Calcium-calmodulin dependent mechanisms activate also endothelial NO synthase (87). NO easily diffuses across cell membranes and causes vasodilation acting within smooth muscle cells. NO binds and activates soluble guanylyl cyclase triggering cyclic guanosine monophosphate (cGMP) production that leads to vasorelaxation by different mechanisms including reduction of extracellular calcium uptake and reticular release, hyperpolarization by cytoplasmic potassium extrusion and myosin light chain phosphatase activation (88).

1.6 The blood and hematopoieses

The blood is an essential media that connects all organs in the body by transporting hormones, nutrients, metabolic waste and gases, such as O_2 and CO_2. Additional functions of the blood for homeostasis regulation includes the pH control in cooperation with the kidneys, temperature control via vascular responses, immune response by transporting immune cells, and injury repair by platelet activation. The blood is essentially composed by a liquid matrix (plasma) and cellular components including red blood cells (RBC), white blood cells (WBC) and platelets. The plasma fraction of the blood is usually the most abundant ~55%, the remaining are cellular components. The major plasma component is water ~90% and the other ~10% are organic and inorganic substances, such as proteins and ions (89, 90).

Among the cellular elements of the blood, RBC also called erythrocytes comprise around 99% of all circulating cellular mass. Their main function is to make the gas exchange between the lungs and other tissues. Hematopoiesis defines the process of formation of all blood cell types including erythrocytes. Hematopoietic stem cells (HSC) give origin to all blood cells and have the capacity to self-renew. Therefore, the blood has a highly regenerative capability because HSC constantly renew the blood´s cellular component across the entire life-span (91, 92). The bone marrow has specific microenvironments named niches where HSC amplify and differentiate. To assure homeostatic self-renewal and production of all blood cells, HSC activity is regulated by gene expression, metabolism, as well as local (produced by niche cells including macrophages and endothelial cells) or external neurohumoral modulators (92).

1.7 Erythropoiesis

Erythrocytes have a life cycle of ~120 days in humans and ~40 days in mice therefore these cells are constantly renewed in a process known as erythropoiesis (93). There are two kinds of erythropoiesis during life, primitive and definitive, during fetal development and adult life, respectively. Fetal erythropoiesis involves RBC production by the liver and spleen. As the animal grows erythropoiesis is transferred to the bone marrow during adult life. Erythropoiesis might be transferred back to spleen and liver in adulthood during certain pathological conditions or insults, such as anemia (94). In the adult bone marrow, erythropoiesis starts with hematopoietic cell lineage-commitment of pluripotent myeloid progenitor cells, these differentiate into erythroid

progenitors, precursors, and finally into RBC (Figure 5). Each process of cellular differentiation is controlled by changes in gene expression patterns that are tightly controlled by the action of several cytokines including erythropoietin, iron, and oxygen levels among others (95, 96). Progenitor cells (BFU-E, burst-forming unit erythroid and CFU-E, colony-forming unit erythroid) are classified based on the properties of these cell types in producing erythroid cells in culture. Erythroid precursors form and develop in an erythroblast island which is surrounded by a central macrophage. It plays a key role during the differentiation steps, and at the end it phagocytes the extruded nucleus during enucleated RBC formation (Figure 5) (96).

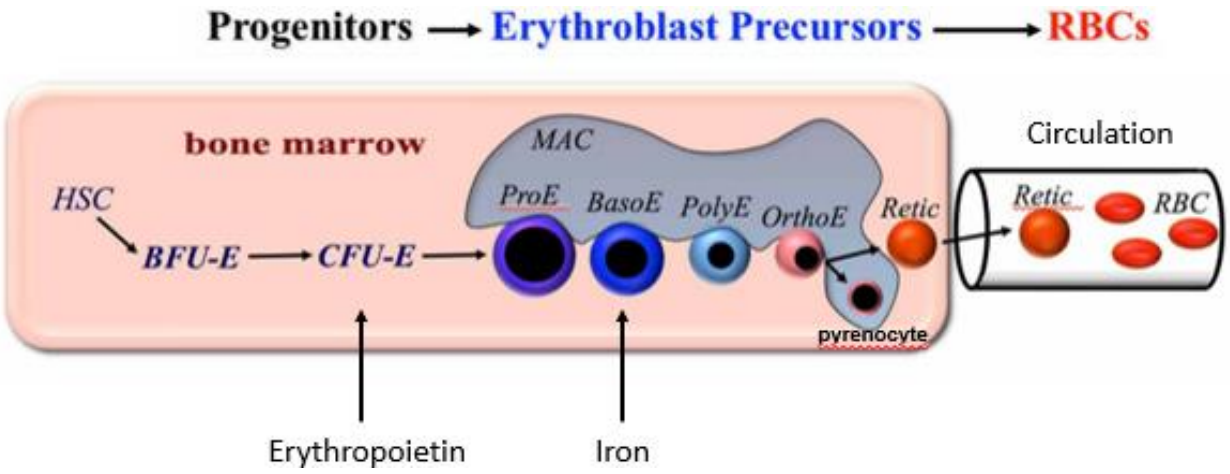

Figure 5 - Overview of the bone marrow erythropoiesis.
Dynamic process of differentiation of hematopoietic stem cell (HSC) to red blood cell (RBC) starting in the bone marrow and finishing in the circulation. HSC gives origin to erythroid progenitors (BFU-E = burst forming unit and CFU-E = colony forming unit). Erythropoietin promotes survival and proliferation of CFU-E. Erythroid precursor development based on distinct morphological features as progressive size decrease and nuclear condensation. Basophilic erythroblasts (BasoE) express the transferrin receptor. Orthochromatic erythroblasts (OrthoE) divides into two cells, one with a condensed nucleus pyrenocyte and another enucleated reticulocyte (Retic) that will maturate in RBC in the circulation. MAC = macrophage, ProE = proerythroblasts, PolyE = polychromatophilic erythroblasts. Modified from Palis, 2015 (96).

Erythropoietin and iron are major factors required for physiological baseline erythropoiesis. The production of erythropoietin takes place primarily in renal cortical fibroblasts, and the major stimulus controlling erythropoietin expression is the reduction of renal oxygen levels. During hypoxia, HIF-2α increases erythropoietin expression to increase erythropoiesis. Erythropoietin acts as an antiapoptotic factor binding to its receptor expressed by progenitor cells. Erythroid progenitor proliferation and differentiation are stimulated by erythropoietin, thus, favoring erythropoiesis (Figure 5). Moreover, the knockout of erythropoietin and erythropoietin

receptor are incompatible with life leading to death during gestational development in mice, highlighting the essential role of this element for RBC production (97, 98).

The iron cation contained in the heme group of hemoglobin is the core component because it binds to oxygen molecules to be transported by RBC in the circulation. The circulating iron concentration during erythropoiesis is a critical direct determinant for the synthesis of hemoglobin. The ferritin receptor is expressed by basophilic erythroblasts and internalizes iron making it available for the synthesis of the heme group during this erythropoietic step (96, 98) (Figure 5).

1.7.1 Iron homeostasis

Iron is an essential metal for cellular functions; however, the body iron homeostasis needs to be tightly controlled because iron in excess is very toxic. Circulating or intracellularly stored iron is majorly (~98%) bound to proteins because free iron has redox properties producing free radicals by Fenton reaction. Insufficient iron is related to anemia development while iron excess is associated with iron accumulation in tissues and organ damage. The body balance of iron levels involves different cell types including gut enterocytes, erythrocytes, macrophages, and hepatocytes, most of these cells import, store and export iron. Iron uptake takes place mostly in the duodenum and proximal jejunum by enterocytes expressing the divalent metal transporter 1 (DMT1) and ferroportin that uptakes iron from the intestinal lumen and exports it into the circulation, respectively. In the gut lumen Fe^{3+} is enzymatically reduced to Fe^{2+} that enters enterocytes and binds to ferritin or goes into the blood stream via ferroportin. In the circulation, iron is oxidized to Fe^{3+} and carried by transferrin, and specific transferrin receptors are indispensable to deliver iron to different cell types by receptor mediated endocytosis. Within endosomes iron is released from transferrin, reduced to Fe^{2+} and enters the cytoplasm via DMT1. Cytoplasmic iron either binds to ferritin for storage or is exported to the blood stream by ferroportin closing the cycle (99–101).

During physiological conditions most of the iron content in the organism is recycled from senescent RBC that are phagocytosed by spleen and liver resident macrophages. These resident macrophages express heme oxygenase which degrades the heme group and releases free iron that moves into the circulation for reuse. Only around 5-10% of the iron is absorbed by enterocytes to

compensate daily body iron loss. The iron absorption process is controlled mostly by a peptide hormone expressed by the liver named hepcidin. Hepcidin modulates iron uptake binding to ferroportin forcing the internalization of the iron exporter. Hepcidin, additionally, inhibits organ stored iron release leading to tissue iron accumulation in conditions of iron overload. The transcriptional regulation of hepcidin is dictated by circulating and tissue iron concentrations that are sensed by liver sinusoidal endothelial cells. High levels of iron induce these endothelial cells to release ligands that activate hepatocyte hepcidin expression. In addition, inflammatory cytokines as interleukin-6 directly control hepcidin expression by binding to hepatocytes (100, 102).

1.7.2 SNS and erythropoiesis

The bone and bone marrow are innervated by the autonomous system. Sympathetic nerves enter the bone via the nutrient foramen and sympathetic terminals are found in close proximity with the bone marrow niche (103). A well characterized role of the SNS is the modulation of the HSC niche, where SNA is recognized to mobilize HSC from the bone marrow into the circulation in a circadian fashion that relies on the circadian pattern of SNA. The mobilization of HSC is key to replace tissues resident immune cells, and during immune modulatory responses to injury (91). Not only HSC but also progenitors and other cells in the bone marrow express adrenergic receptors. Therefore, the modulatory role of the SNS on erythropoiesis is rather complex involving direct modulatory actions on progenitor cells or indirect via modulating the release of factors as cytokines by other cells of the niche. Because of the highly complex interaction between the SNS with other factors regulating erythropoiesis in physiological and pathological conditions, the role of NE is not precisely defined and most likely differs depending on homeostatic conditions. Clinical evidence points to a certain role of the SNS in baseline erythropoiesis because patients with autonomic failure (impaired SNA) develop anemia. This effect can be reproduced in rodents subjected to peripheral ablation of the SNS (104, 105).

1.7.3 RAS and erythropoiesis

Erythropoietin is connected to the RAS because renal cortical fibroblast producing erythropoietin precursor cells are Ren-expressing cells during embryonic development. Extreme examples

involving gene manipulation in rodents leading to HIF-2α accumulation led to erythropoietin production in Ren cells. The opposite has also been observed during anemia, fibroblast normally producing erythropoietin may start to produce Ren (36). Interestingly, precursor cells expressing Ren are not exclusive to the kidney, but they were found across the body. There are tissues where the Ren expression is restricted to embryonic development and there are tissues in which precursors are expressed in adulthood these include bone marrow and spleen. Bone marrow Ren positive cells are precursors of B-lymphocytes. In the bone marrow, not only Ren but all genes encoding proteins of the classical RAS were identified in different stromal cell types, thus, angiotensin peptides might be locally formed or imported from the circulation. The AT1 receptor expression has been identified in HSC progenitors expressing CD34 as well as erythroid progenitors (106, 107).

There have been associations between the RAS and erythropoiesis. Most of the knowledge originated in clinical observations from patients treated with RAS blockers. Some of these patients develop anemia during a long-term RAS blockade. These findings have been further studied in knockout mouse models and it turned out that the Ang II/AT1 axis influences erythropoiesis (108). In addition, either hypertensive patients with increased circulating RAS often estimated by plasma Ren activity or preclinical models of hypertension chronically infused with Ang II present an increased hematocrit. The mechanism whereby Ang II increases erythropoiesis is not yet precisely dissected. Mechanisms suggested operating via the Ang II/AT1 axis include erythropoietin expression and secretion by activation of the transcription factor Egr-1 at erythropoietin positive renal fibroblasts. Another proposed mechanism is that Ang II acts on bone marrow erythroid precursor cells as a growth factor similarly to erythropoietin stimulating growth and differentiation (109, 110).

2 Aims of the study

Primary hypertension characterized by chronic elevation of BP with an unknown origin is the most prevalent form of hypertension. Cumulated research data rendered the SNA the major long-term BP regulator, thus, a potential target for therapies to treat hypertension. However, global SNA inhibition leads to unwanted side effects and the regulation of its branch-specific activation is very complex and incompletely understood. Therefore, the major aim of this work goes towards further understanding the modulatory effects of the RAS on SNA relevant for BP control, especially focusing on the role of brain-borne Ang II using gain and loss of function rodent models.

2.1 Specific aims

- Confirm and understand the brain pathway(s) of Ang II production using a novel transgenic mouse model with brain specific increased Agt synthesis.
- Study the impact of increased brain Ang II on cardiovascular modulation, focusing on the SNA control to cardiovascular organs.
- Implement a genome-wide-association-study (GWAS) to understand the molecular basis of the unexpected BP phenotype in FVB/N mice lacking Agt globally (Agt-KO).
- Evaluate the impact of gain and loss of function in the RAS on erythropoiesis, with a special focus on the role of brain-borne Ang II.
- Use CRISPR/Cas9 to generate novel channelrhodopsin 2 knockin rats to study the sympathetic control of BP exerted by neurons expressing the Ang II type 1a receptor (AT1a).

3 Material and methods

3.1 Materials

3.1.1 Chemicals, reagents, buffers and solutions

A list of chemicals and reagents used in this study is provided below as purchased buffers and solutions (Table 1). Buffers and solutions that were prepared are included in their respective methodology sections. If not indicated buffers and solution were prepared and/or diluted with ultrapure water (Milli-Q). The desired pH was adjusted using a pH meter and NaOH or HCl solutions.

Table 1 - Chemical and reagents.

Chemical or reagent	Manufacturer (location, country)
2-methylbutane (isopentane)	Carl Roth (Karlsruhe, Germany)
Acetic acid glacial	Carl Roth (Karlsruhe, Germany)
Acrylamide and bisacrylamide stock solution Rotiphorese® Gel 30 (37,5:1)	Carl Roth (Karlsruhe, Germany)
Agarose	Biozym (Oldendorf, Germany)
Alt-R® S.p. Cas9 Nuclease	IDT (Newark, USA)
Ammonium Persulfate (APS)	Sigma-Aldrich (St. Louis, USA)
Ampicillin	Serva (Heidelberg, Germany) or
Ampicillin	Life Technologies (Carlsbad, USA)
Ascorbic acid	Sigma-Aldrich (St. Louis, USA)
Bicinchoninic acid solution	Sigma-Aldrich (St. Louis, USA)
Bovine Serum Albumin (BSA)	Sigma-Aldrich (St. Louis, USA)
Bromophenol blue	Sigma-Aldrich (St. Louis, USA)
Chloroform	Merck (Darmstadt, Germany)
Complete, protease inhibitor cocktail tablets	Roche (Basel, Schweiz)
Copper (II) sulfate solution	Sigma-Aldrich (St. Louis, USA)
D(+)-Saccharose	Carl Roth (Karlsruhe, Germany)
Deoxyribonucleotide (dNTP)	Bioline (London, UK)
Diethylpyrocarbonate (DEPC)	Serva (Heidelberg, Germany)
Dimethyl sulfoxide (DMSO)	Sigma-Aldrich (St. Louis, USA)
Disodium phosphate (Na_2HPO_4)	Sigma-Aldrich (St. Louis, USA)
Eosin Y solution	Sigma-Aldrich (St. Louis, USA)

Chemical or reagent	Manufacturer (location, country)
Ethanol	Berkel AHK (Berlin, Germany)
Ethidium Bromide	Carl Roth (Karlsruhe, Germany)
Ethylenediaminetetraacetic acid (EDTA)	Carl Roth (Karlsruhe, Germany)
Eukitt® Quick-hardening mounting medium	Sigma-Aldrich (St. Louis, USA)
Gel loading dye Purple (6x)	New England Biolabs (Ipswich, USA)
Glycerol	Carl Roth (Karlsruhe, Germany)
Glycine	Carl Roth (Karlsruhe, Germany)
Hematoxylin Solution	Sigma-Aldrich (St. Louis, USA)
Heparin Sodium, 5.000 U/mL	B. Braun (Melsungen, Germany)
Hydrochloric acid 37% (HCl)	Carl Roth (Karlsruhe, Germany)
Isopropanol	Carl Roth (Karlsruhe, Germany)
LB-Agar (Luria/Miller)	Carl Roth (Karlsruhe, Germany))
LB-Medium (Luria/Miller)	Carl Roth (Karlsruhe, Germany)
Methanol	Chemsolute/ Th.Geyer (Renningen, Germany)
MicroAmp Optical Adhesive Film	Applied Biosystems (Foster City, USA)
Normal donkey serum	dianova Jackson ImmunoResearch (West Grove, USA)
Nuclease-free water	Promega (Fitchburg, USA)
Odyssey® Blocking Buffer	LI-COR Bioscience (Lincoln, USA)
Odyssey® two-color protein molecular weight marker	LI-COR Bioscience (Lincoln, USA)
Paraffin	Carl Roth (Karlsruhe, Germany)
Paraformaldehyde Solution (PFA), 4% buffered	Otto Fischar (Saarbrücken, Germany)
Phenol	Sigma-Aldrich (St. Louis, USA)
Phosphatase inhibitor cocktail tablets, PhosStop	Roche (Basel, Schweiz)
Phosphate buffered saline (PBS)	Sigma-Aldrich (St. Louis, USA)
Picric acid solution, 1.3%	Applichem (Darmstadt, Germany)
Ponceau S	Sigma-Aldrich (St. Louis, USA)
Potassium Acetate	Merck (Darmstadt, Germany)
Potassium chloride (KCl)	Sigma-Aldrich (St. Louis, USA)
Potassium dihydrogenphosphate (KH2PO4)	Merck (Darmstadt, Germany)
Procaine hydrochloride solution, 1 %	Steigerwald Arzneimittelwerk (Darmstadt, Germany)
Random primers	Promega (Fitchburg, USA)
Revert Total Protein Stain	LI-COR Bioscience (Lincoln, USA)
RIPA Buffer (10X)	Cell Signaling Technology (Danvers, USA)
RNA*later*®	Sigma-Aldrich (St. Louis, USA)
RNAsin® Ribonuclease Inhibitor (Rnasin)	Promega (Fitchburg, USA)

Chemical or reagent	Manufacturer (location, country)
Roti-load 1 protein loading buffer	Carl Roth (Karlsruhe, Germany)
Rotiphorese TAE Buffer, 50x	Carl Roth (Karlsruhe, Germany)
Sirius red F3B (Direct Red 80)	Sigma-Aldrich (St. Louis, USA)
Sodium acetate	Sigma-Aldrich (St. Louis, USA)
Sodium carbonate (Na2CO3)	Sigma-Aldrich (St. Louis, USA)
Sodium chloride (NaCl)	Sigma-Aldrich (St. Louis, USA)
Sodium citrate	Merck (Darmstadt, Germany)
Sodium disulfite	Sigma-Aldrich (St. Louis, USA)
Sodium dodecyl sulfate (SDS)	Serva (Heidelberg, Germany)
Sodium hydroxide (NaOH)	Carl Roth (Karlsruhe, Germany)
Tetramethylethylenediamine (TEMED)	Carl Roth (Karlsruhe, Germany)
Tissue-Tek® OCT™ Compound	Sakura (Staufen, Germany)
Tris(hydroxymethyl)aminomethane	Carl Roth (Karlsruhe, Germany)
Triton X-100	Sigma-Aldrich (St. Louis, USA)
Trizol® (Invitrogen)	Thermo Fisher Scientific (Waltham, USA)
Tween-20	Sigma-Aldrich (St. Louis, USA)
Vectashield® Mounting Medium with DAPI	Vector Laboratories (Burlingame, USA)
Xylene	Carl Roth (Karlsruhe, Germany)
β-Mercaptoethanol	Sigma-Aldrich (St. Louis, USA)

3.1.2 Drugs administered *in vivo*

Table 2 - Drugs used for *in vivo* administration in this study.

Substance (injected intravenously)	Manufacturer (location, country)	Company reference
Angiotensin II acetate salt (Ang II)	Bachem (Bubendorf, Switzerland)	05-23-0101
CV 11974 (Candesartan)	Tocris (Bristol, UK)	4791/10
Dexmedetomidine hydrochloride	Tocris (Bristol, UK)	2749
Endothelin-1	Tocris (Bristol, UK)	1160
Hexamethonium bromide	Sigma-Aldrich (St. Louis, USA)	H0879
Nifedipine	Tocris (Bristol, UK)	1075
Nω-Nitro-L-arginine methyl ester hydrochloride (L-NAME)	Sigma-Aldrich (St. Louis, USA)	N5751
Phenylephrine	Sigma-Aldrich (St. Louis, USA)	P1250000
Prazosin hydrochloride	Tocris (Bristol, UK)	0623
Sodium nitroprusside dihydrate (SNP)	Sigma-Aldrich (St. Louis, USA)	71778
Tyramine	Sigma-Aldrich (St. Louis, USA)	T90344
Y-27632 dihydrochloride	Tocris (Bristol, UK)	1254
Yohimbine hydrochloride	Sigma-Aldrich (St. Louis, USA)	Y3125
Substance (injected intraperitoneally)	**Manufacturer (location, country)**	**Company reference**
6-Hydroxydopamine hydrochloride (6-OHDA)	Sigma-Aldrich (St. Louis, USA)	4006473
Sterile Saline (NaCl, 0.9 %)	B. Braun (Melsungen, Germany)	06063042

3.1.3 Elisa, kits, molecular weight markers and enzymes

Table 3 - Elisa, kits, molecular weight markers and enzymes used in this study.

Elisa	**Manufacturer (location, country)**
Human/Mouse/Rat Copeptin EIA Kit	RayBiotech (Peachtree Corners, USA)
Norepinephrine ELISA kit (Noradrenaline)	LDN (Nordhorn, Germany)
Kits	**Manufacturer (location, country)**
Bicinchoninic Acid (BCA) Protein Assay Kit	Sigma-Aldrich (St. Louis, USA)
GeneJET RNA Purification Kit	Thermo Fisher Scientific (Waltham, USA)
GenElute™ Mammalian Genomic DNA Miniprep Kits	Sigma-Aldrich (St. Louis, USA)
Guide-it Long ssDNA Production System	Takara (Kyoto, Japan)
Nitrate/Nitrite Colorimetric Assay Kit	Cayman (Michigan, USA)
PureYield™ Plasmid Maxiprep System	Promega (Fitchburg, USA)
RNAscope 2.5 HD Reagent Kit-RED assay	ACD (Newark, USA)
Wizard ® SV Gel and PCR Clean-Up System	Promega (Fitchburg, USA)
Wizard® HMW DNA Extraction Kit	Promega (Fitchburg, USA)
Molecular weight markers	**Manufacturer (location, country)**
Precision plus protein™ standards all blue	Bio-Rad Laboratories (Hercules, USA)
Quick-Load© 1 kb DNA ladder	New England Biolabs (Ipswich, USA)
Quick-Load© 100 bp DNA ladder	New England Biolabs (Ipswich, USA)
Enzymes	**Manufacturer (location, country)**
Alkaline Phosphatase, Calf Intestinal (CIP)	New England Biolabs (Ipswich, USA)
DNase I recombinant	Roche (Basel, Schweiz)
GoTaq® qPCR Master Mix	Promega (Fitchburg, USA)
Moloney Murine Leukemia Virus Reverse Transcriptase (M-MLV)	Promega (Fitchburg, USA)
Phusion® High-Fidelity DNA Polymerase	New England Biolabs (Ipswich, USA)
Proteinase K	Carl Roth (Karlsruhe, Germany)
Restriction enzymes	New England Biolabs (Ipswich, USA)
RNAse A	Promega (Fitchburg, USA)
RNasin® Plus RNase Inhibitor:	Promega (Fitchburg, USA)
T4-DNA-Ligase	Promega (Fitchburg, USA)
T4 Polynucleotide Kinase (T4 PNK)	Promega (Fitchburg, USA)
T7 RNA Polymerase Plus	Thermo Fisher Scientific (Waltham, USA)
Taq DNA Polymerase with ThermoPol Buffer	New England Biolabs (Ipswich, USA)

3.1.4 Oligonucleotides

All oligonucleotides used for polymerase chain reaction (PCR), reverse transcriptase PCR (RT-PCR), reverse transcriptase quantitative PCR (RT-qPCR), vectorette PCR, and single-guide RNA (sgRNA) production were purchased from Biotez GmbH (Berlin, Germany). Following manufacturer instructions, the lyophilized oligonucleotides were resuspended in nuclease-free water to final concentrations of 100 or 50 pmol/µL and stored at -20 °C. For most applications, an aliquot containing the working concentration was prepared from the stock solution in nuclease-

free water and kept at -20 °C. The specific primer sequences used in the different applications are enclosed within the specific sections.

3.1.5 Antibodies

Table 4 - Primary antibodies used in this study.

Antigen	Host	Manufacturer (Reference)	Usage	Diluent (dilution)
Agt	Rabbit	IBL (28101)	WB	PBS-T/blocking solution (1:100)
α-SMA	Rabbit	Novus Biologicals (NBP2-67436)	WB	PBS-T/blocking solution (1:2000)
AVP	Rabbit	Sigma-Aldrich (AB1565)	IF	PBS (1:1000)
GAPDH	Rabbit	Cell Signaling (2118)	WB	PBS-T/blocking solution (1:2000)
GFAP	Guinea pig	SySy (173004)	IF	PBS (1:500)
IBA-1	Rabbit	Waco (016-20001)	WB	PBS-T/blocking solution (1:1000)

WB = Western blot, IF = immunofluorescence.

Table 5 - Secondary antibodies used in this study.
WB = Western blot, IF = immunofluorescence.

Immunogen	Conjugate	Host	Manufacturer (Reference)	Usage	Diluent (dilution)
Rabbit IgG	IRDye®680RD	Donkey	LI-COR (926-68073)	WB	PBS-T (1:10000)
Rabbit IgG	IRDye®800CW	Donkey	LI-COR (926-32213)	WB	PBS-T (1:10000)
Guinea pig IgG	Alexa Fluor® 488	Donkey	Jackson (706-545-148)	IF	PBS (1:500)
Rabbit IgG	Cy™3 550	Donkey	Jackson (711-165-152)	IF	PBS (1:500)

WB = Western blot, IF = immunofluorescence.

3.1.6 Laboratory equipment

Table 6 - Laboratory equipment and expendables.

Instruments, devices and consumables	Manufacturer (location, country)
Instruments and devices	
Ambient Pressure Reference Monitor APR2	Data Science International (St. Paul, USA)
Agarose gel electrophoresis chamber	Biometra (Göttingen, Germany)
Analytical Balance	Sartorius (Göttingen, Germany)
Bacteria shaker Certomat®H	B.Braun (Melsungen, Germany)
Centrifuge Biofuge 13	Heraeus (Hanau, Germany)
Centrifuge Sorvall RC 5C	Heraeus (Hanau, Germany)
Cooling centrifuge 5804 R	Eppendorf (Hamburg, Germany)
Cryostat	Thermo Fisher Scientific (Waltham, USA)
Electronic multichannel pipettes Xplorer	Eppendorf (Hamburg, Germany)
Electronic multistep pipettes Xplorer	Eppendorf (Hamburg, Germany)
Electroporator 2510	Eppendorf (Hamburg, Germany)
FastPrep™-24 instrument	MP Biomedicals (Illkirch, France)
Fluorescence microscope BZ-9000	Keyence (Neu-Isenburg, Germany)

Instruments, devices and consumables	Manufacturer (location, country)
Gel Imager C200	Azure Biosystems (Dublin, USA)
Gel Imager Transilluminator MultiImage™Light Cabinet	Alpha Innotech (San Leandro, USA)
Hematocrit centrifuge	Hettich (Kirchlengern, Germany)
Magnetic stirrer	Thermo Fisher Scientific (Waltham, USA)
Micro balance	Sartorius (Göttingen, Germany)
Microm modular tissue embedding center EC350-2	Thermo Fisher Scientific (Waltham, USA)
Microm STP 120 spin tissue processor	Thermo Fisher Scientific (Waltham, USA)
Microplate Reader Infinite® M200	Tecan (Männedorf, Schweiz)
Microwave 8020	Privileg (Fürth, Germany)
Mini-PROTEAN® gel casting system	Bio-Rad Laboratories (Hercules, USA)
NanoDrop™ 1000 spectrophotometer	Peqlab (Erlangen, Germany)
Odyssey® infrared imaging system	LI-COR Bioscience (Lincoln, USA)
pH Meter pH Level 1	WTW (Weilheim, Germany)
Pipetboy	Integra Biosciences (Zizers, Switzerland)
Pipettes	Discovery Abimed (Langenfeld, Germany)
Pipettes	Sartorius (Göttingen, Germany)
Power supply PowerPac™ HC	Bio-Rad Laboratories (Hercules, USA)
Real-Time PCR System QuantStudio 5	Applied Biosystems (Foster City, USA)
Roller mixer SRT1	Snijders (Tilburg, Netherlands)
Roller mixer SU1400	sunlab (Mannheim, Germany)
Rotable platform Polymax 1040	Heidolph Instruments (Schwabach, Germany)
Rotary microtome HM 355 S	Microm (Walldorf, Germany)
Scil Vet abc	Scil (Viernheim, Germany)
SDS-PAGE gel electrophoresis chamber	Bio-Rad Laboratories (Hercules, USA)
Serological Pipette, disposable	Gilson (Middleton, WI, USA)
Single channel Transferpette® micropipettes	Brand (Wertheim, Germany)
Stereo microscope MZFLIII	Leica (Wetzlar, Germany)
Thermocycler C1000	Bio-Rad Laboratories (Hercules, USA)
Thermocycler Master cycler nexus GX2	Eppendorf (Hamburg, Germany)
Thermocycler peqSTAR	Peqlab (Erlangen, Germany)
Thermomixer 5437	Eppendorf (Hamburg, Germany)
Trans-blot turbo transfer system	Bio-Rad Laboratories (Hercules, USA)
Vacuum pump BVC 21	Brand (Wertheim, Germany)
Consumables	
384-well optical plate MicroAmp	Applied Biosystems (Foster City, USA)
96-well clear microplates	R&D Systems (Wiesbaden-Nordenstadt, Germany)

Instruments, devices and consumables	Manufacturer (location, country)
DAKO Pen	Dako Deutschland GmbH (Hamburg, Germany)
Falcon tubes (15 and 50 ml)	Greiner AG (Kremsmünster, Austria)
FastPrep™ lysing matrix, tubes and caps	MP Biomedicals (Eschwege, Germany)
Felt marker, alcohol-resistant	Sarstedt (Nümbrecht, Germany)
Felt marker, waterproof	Sarstedt (Nümbrecht, Germany)
Filter tips (10, 20, 200 and 1000 ml) Surphob	Biozym (Oldendorf, Germany)
GenePulse® Cuvettes	GenePulse® Cuvettes BioRad Laboratories Richmond
GenePulse® electroporation cuvettes	Bio-Rad Laboratories (Hercules, USA)
Haematocrit sealing compound	Brand (Wertheim, Germany)
Latex gloves	Sänger (Schrozberg, Germany)
Magnetic stirrer bars	Thermo Fisher Scientific (Waltham, USA)
Micro-hematocrit capillaries	Hirschmann (Eberstadt, Germany)
MiniCollect® K3EDTA-coated tubes	Greiner (Kremsmünster, Austria)
MiniCollect® Lithium Heparin	Greiner (Kremsmünster, Austria)
Nitrile gloves	Cardinal Health (The Hague, The Netherlands)
Nitrocellulose Membrane	Thermo Fisher Scientific (Waltham, USA)
Pasteur pipettes	Carl Roth (Karlsruhe, Germany)
PCR strip tubes with cap Axygen®	Corning (Corning, USA)
Petri dish	Sarstedt (Nümbrecht, Germany)
Pipette tips	Sarstedt (Nümbrecht, Germany)
Plastipak™ Plastic Concentric Luer-Lock 50 mL Syringe	BD (Franklin Lakes, USA)
Save-Lock Tubes	Eppendorf (Hamburg, Germany)
Serological pipettes Cellstar®	Greiner AG (Kremsmünster, Austria)
SuperFrost® Plus slides	Menzel Gläser (Braunschweig, Germany)
Whatman paper (3 mm)	Whatman (Madison, USA)

3.1.7 Equipments and expendables used for *in vivo* experiments

Table 7 - Equipment and expendables used for *in vivo* experiments.

Instruments and devices	Manufacturer (location, country)
Ambient Pressure Reference Monitor, APR2	Data Science International (St. Paul, USA)
Analytical balance	Sartorius (Göttingen, Germany)
Angled graefe forceps	Fine Science Tools (North Vancouver, Canada)
Bridge amplifier, ML110	Data Science International (St. Paul, USA)
Cotton carrier	Dimeda (Tuttlingen, Germany)
Digital caliper	Wabeco (Remscheid, Germany)
Dumont #3c forceps	Fine Science Tools (North Vancouver, Canada)
Dumont #5 - fine forceps	Fine Science Tools (North Vancouver, Canada)
Fine Scissors - large loops	Fine Science Tools (North Vancouver, Canada)
Goldstein retractor	Fine Science Tools (North Vancouver, Canada)
Halsey needle holders	Fine Science Tools (North Vancouver, Canada)

Instruments and devices	Manufacturer (location, country)
Heating plate	FMI (Seeheim, Germany)
Mercury sphygmomanometer, Mercuro 300	Speidel & Keller (Juningen, Germany)
MX2 Matrix 2.0 with dataquest A.R.T. software	Data Science International (St. Paul, USA)
Optic light source	Schott (Wiesbaden, Germany)
PowerLab/4sp with LabChart Software v5	AD Instruments (Castle Hill, Australia)
Pressure transducers, MLT0699	Data Science International (St. Paul, USA)
RPC-1 single receiver	Data Science International (St. Paul, USA)
S&T vessel cannulation forceps	Fine Science Tools (North Vancouver, Canada)
Scantainer	Scanbur (Karlslunde, Denmark)
Stereo microscope, Leica S6 E	Leica microsystems (Wetzlar, Germany)
Stereo microscope, Zeiss Stemi SV6	Carl Zeiss (Gottingen, Germany)
Strabismus scissors	Fine Science Tools (North Vancouver, Canada)
Student halsted mosquito hemostat	Fine Science Tools (North Vancouver, Canada)
Tabletop anesthesia unit, Univentor 400	AgnTho (Lidingö, Sweden)
Temperature-controlled surgical table	FMI GmbH (Seeheim, Germany)
Trimming machine, exacta	Aesculap (Tuttlingen, Germany)
Ultra-fine hemostats	Fine Science Tools (North Vancouver, Canada)
Expendables	**Company (location, country)**
22 - 27G Needle	B. Braun (Melsungen, Germany)
Absorbable suture 4/0 with needle	Johnson & Johnson (New Brunswick, USA)
Biocompatible gel, Re-gel	Data Science International (St. Paul, USA)
Glass pasteur pipettes	Brand (Wertheim, Germany)
Hamilton microsyringe, 100 µL	Hamilton (Bonaduz, Switzerland)
Histoacryl tissue adhesive	B. Braun (Melsungen, Germany)
Kalt suture needle	Fine Science Tools (North Vancouver, Canada)
Micro-Renathane® tubing, MRE-025	Braintree Scientific Inc (Braintree, MA, USA)
Paint brush, 0.5 mm	da Vinci (Nürnberg, Germany)
Paperclip	Durable (Dorset, England)
Parafilm	Bemis (Neenah, USA)
Polyethylene tubing, PE-50	Braintree Scientific Inc (Braintree, MA, USA)
RenaSil silicone rubber tubing, SIL-080	Braintree Scientific Inc (Braintree, MA, USA)
Reusable feeding needles	Fine Science Tools (North Vancouver, Canada)
Silk black 4/0, cassette pack 100 m	SMI AG (St. Vith, Belgium)
Silk black 6/0, cassette pack 100 m	RESORBA Medical GmbH (Nuremberg, Germany)
Silk suture 3/0 with needle SH-1	Johnson & Johnson (New Brunswick, USA)
Spinocan anesthesia needle 29 G × 3½ with red-coded stylet	B. Braun (Melsungen, Germany)
Sterile cotton balls	Johnson & Johnson (New Brunswick, USA)
Surgical disposible scalpel	B. Braun (Melsungen, Germany)
Syringe (1 mL) with integrated needle (26G)	BD (Heidelberg, Germany)
Syringes Omnifix® Solo, 1mL	B. Braun (Melsungen, Germany)
Telemetrical Pressure Transmitters, PA-C10	Data Science International (St. Paul, USA)

3.1.8 Drugs and substances used for animal anesthesia, analgesia and asepsia

Table 8 - Drugs and substances used for animal anesthesia, and asepsis in this study.

Anesthesia	**Manufacturer (location, country)**
Isoflurane	Abbott (Wiesbaden, Germany)
Ketamidor (Ketamine), 100 mg/mL	Pfizer (New York, USA)
Rompun (Xylazine), 2%	Bayer (Leverkusen, Germany)
Analgesia	**Manufacturer (location, country)**
Novaminsulfon (Metamizol), 500 mg/mL	Ratiopharm (Ulm, Germany)
Asepsis	**Manufacturer (location, country)**
Betaisodona solution, 0,1 g/mL	Mundipharma (Frankfurt, Germany)

3.1.9 Plasmid vectors

Table 9 - Plasmid vectors used in this study.

Plasmid	**Manufacturer (location, country)**	**Company ref.**
pAAV-EF1a-double floxed-hChR2(H134R)-EYFP-WPRE-HGHpA	Addgene (Watertown, USA)	20298
pGEM®-T Easy Vector	Promega (Fitchburg, USA)	A1360
pX330-U6-Chimeric_BB-CBh-hSpCas9	Addgene (Watertown, USA)	42230

3.1.10 Bacterial strains

All plasmid vectors were cloned using the electrocompetent *Escherichia coli* strain One Shot™ TOP10 Chemically Competent (Invitrogen, Germany).

3.2 Animals

3.2.1 Mouse husbandry

All mouse lines were maintained in pathogen-free conditions at the animal facility of the Max Delbrück Center, Berlin. A maximum of 6 mice were maintained in individually ventilated cages at controlled room temperature of 22±1°C, under a standard light/dark cycle of 12 hours each. All mice received commercial standard mouse chow and water *ad libitum*. Line maintenance and experimental breeding were performed with either 1 male x 2 females or 1 male x 1 female. The weaning was performed between 21 and 23 days after birth. Genotyping biopsies collected from 7-14 days-old mice were toenail, while from mice older than 14 days were ear punches. Genotyping biopsies were systematically collected to imprint the mouse´s ID either on the fingertips or the ears for further distinction. For the *in vivo* experiments, animals were kept in the experimental room in conventional open cages covered with a polyester filter sheet. Food, water,

room temperature and light schedule were kept as described above. To acclimatize mice that were submitted to any *in vivo* protocol, mice were transferred to the experimental rooms at least 5 days prior of the beginning of the experiment. All *in vivo* procedures were performed according to the national and institutional guidelines and were previously reviewed and approved by institutional animal welfare officers and the local official animal ethic committee (LaGeSo, Berlin, Germany).

3.2.2 Mouse lines

Most of the experiments of this thesis were performed using the transgenic and knockout mouse lines showed in Figure 6. These lines were either generated or backcrossed in the FVB/N background strain over ten generations, and at least twice a year therefore FVB/N wildtypes were used as controls. Further mouse strains described below were used in complementary experiments, those were in some cases mixed background strains and in these particular experiments wildtype littermates were used as controls.

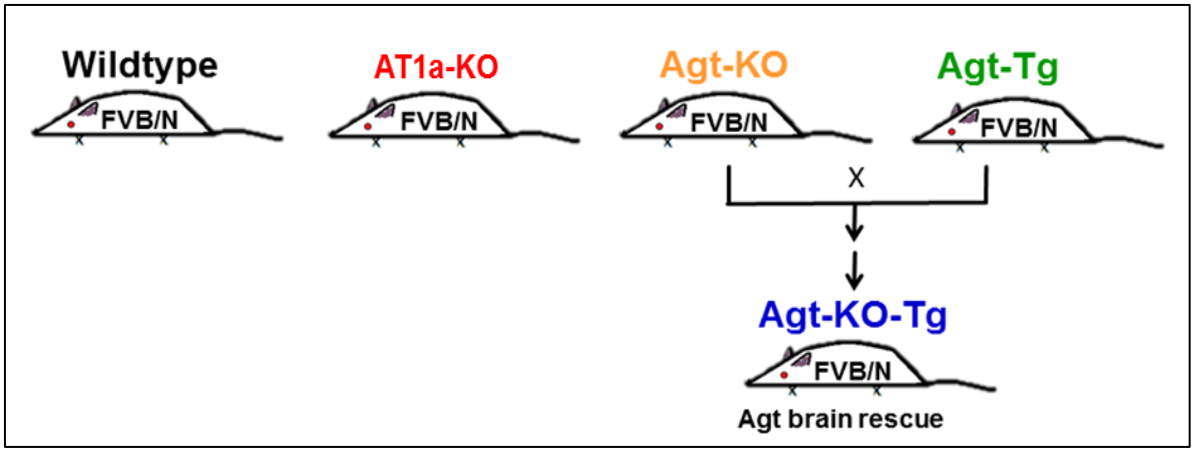

Figure 6 - Mouse lines used in this study.
Agt-KO-Tg (brain rescue of Agt expression of the Agt-KO line) was generated by crossing Agt-Tg with Agt-KO and the F1 heterozygous littermates among themselves.

3.2.2.1 Global Ang II Type Ia receptor knockout AT1a knockout = AT1a-KO

The AT1a-KO mouse (*Agtr1a*$^{tm1.1Cof}$) was generated by Ito *et al.* (111), using the classical gene knockout technique. For this, 0.5-kb of the mouse *Agtr1a* coding exon 3 was replaced by the neomycin resistance cassette. This line was obtained from Prof. Dr. Thomas M. Coffman in the

mixed background strain and was backcrossed for more than 10 generations with the FVB/N strain at the animal facility of the Max Delbrück Center, Berlin.

3.2.2.2 Global Agt knockout = Agt-KO

The Agt-KO mouse (*Agt*^{tm1Afu}) was generated by Tanimoto *et al.* (112), using the classical gene knockout technique. For this, ~0.9-kb of the second exon (containing the Ang II coding sequence) of the mouse *Agt* gene was substituted with the ~1.1-kb neomycin resistance cassette. This mouse line was obtained in the mixed background from Prof. Dr. Akiyoshi Fukamizu and was backcrossed for more than 10 generations with the FVB/N strain at the animal facility of the Max Delbrück Center, Berlin.

3.2.2.3 Brain Agt transgene = Agt-Tg

Before the start of this PhD project, the Bader group had generated a new transgenic mouse line expected to overexpress the rat Agt specifically in the brain by astrocytes FVB/N-Tg(hGFAP-r*Agt*)24*Bdr* (Agt-Tg). In this newly generated transgenic line, the rat Agt is expressed under the control of the human glial fibrillary acidic protein (hGFAP) promoter as previously successfully used in rodents (61, 113, 114). The rat Agt full-length cDNA (XM_008772597) was amplified by PCR with the following specific primers (5′-GGACACACAGAAGCAAGTCC-3′ and 5′-CATGGCTACACAGGAGGCAT-3′). To generate Agt-Tg, a DNA linear construct (Figure 7) was prepared by molecular cloning and used for pronuclear injection into pronuclei of FVB/N zygotes.

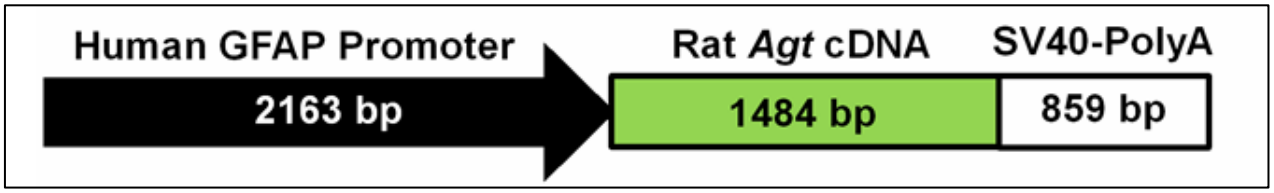

Figure 7 - Schematic representation of the DNA construct used to generate Agt-Tg.
The linear DNA construct was microinjected into FVB/N zygotes, and positive founders identified by genotyping.

3.2.2.4 Brain Agt rescue of Agt-KO = Agt-KO-Tg

The brain Agt expression was specifically rescued in Agt-KO. For this, Agt-KO was crossed with the newly generated transgenic line Agt-Tg which expresses Agt specifically in the brain (see transgene expression validation in section 4.1.3). Males Agt-KO were mated with females Agt-

Tg and heterozygous mice for mAgt harboring the transgene "rAgt*"* were intercrossed to obtain Agt-KO-Tg (Figure 6).

3.2.2.5 Global Agt knockout F2 = F2 Agt-KO

To generate a mixed F2 generation of Agt-KO mice containing 50% of the FVB/N and 50% of the C57BL/6N genome, FVB/N Agt-KO males were crossed with wildtype C57BL/6N. Thereafter, the resulting heterozygous F1 littermates were intercrossed and the ~25% born F2 Agt-KO were used for the GWAS (see Figure 45A, a schematic representation of the breeding scheme).

3.2.2.6 Global Renin 1c knockout = Ren-KO

The Ren-KO mouse (Ren1c^{tm1Unc}) was generated by Takahashi *et al.* (115), using the classical gene knockout technique. For this, a large portion ~14.5-kb of the mouse *Ren1c* gene containing partial promoter region up to exon 6 (including the catalytic sequence) was deleted and substituted with the ~1.1-kb neomycin resistance cassette. This mouse line was obtained in the C57BL/6 background from the late Prof. Dr. Oliver Smithies. For experiments this line was backcrossed to the FVB/N background for 2 generations and littermates were used as controls. Note: wildtype controls expressed *Ren1d* as FVB/N.

3.2.3 Rat husbandry

All rats were kept on pathogen-free conditions according to the German Animal Protection Law at the animal facility Max Delbrück Center, Berlin. Rats were kept in individually ventilated cages with unrestricted access to water and standard chow. The animals were kept 2 - 5 per cage, depending on the cage size, in a room with a constant temperature of 21±1˚C, and light and dark entertainment of 12h light/12h dark. The weaning was performed 21 days after birth. Ear punch biopsies were collected from rats older than 14 days for genotyping. All *in vivo* procedures were performed according to the national and institutional guidelines and were previously reviewed and approved by institutional animal welfare officers and the local official animal ethic committee (LaGeSo, Berlin, Germany).

3.2.4 Rat lines

All rats used in experiments were bred to the outbred Sprague-Dawley (SD) strain.

3.2.4.1 TGR(ASrAOGEN)680 = TGR-680

This transgenic rat line was generated in the laboratory of Prof. Dr. Michael Bader. TGR-680 carries an antisense RNA against rAgt in astrocytes, astrocyte-specific antisense RNA expression was achieved using the hGFAP promoter as described by Schinke *et al.* (61). As consequence TGR-680 presents 90% reduced brain Agt protein but normal peripheral Agt production (61).

3.2.4.2 Rat AT1a knockout and knockin generation

Rats are the rodent model of choice in cardiovascular research, because rats are ten times bigger than mice not only surgical procedures are easier but more stability and minimal interference from probe implantation is observed during cardiovascular data acquisition (116). However, the generation of knockout and knockin rat models lacked a reliable methodology until recently. The ability of CRISPR/Cas9 to cause DNA double-strand break at predefined genome sites made generating knockout rats possible by inducing mutations during non-homologous end joining (NHEJ) events and knockin rats using enhanced homology-directed repair (HDR) (Figure 8). For detailed information about sgRNA and HDR generation refer to sections 3.4.7.1 and 3.4.7.2, respectively. Channelrhodopsins are light-gated ion channel that may be used as a tool to spatiotemporally control neuronal circuits (117). If channelrhodopsin expression is controlled by a neuron population specific promoter, this unique tool offers a distinct method to explore the role of this neuronal population on cardiovascular homeostasis in freely moving rats. To our knowledge, there is no record of successful cloning of the AT1a receptor promoter, leading us to attempt to insert channelrhodopsin 2 (ChR2) into the coding exon of the rat AT1a receptor (*Agtr1a*). The function of “angiotensinergic” brain circuits was not deeply explored in rodent models yet. Therefore, we aimed to generate a unique model to manipulate AT1a positive neurons in cardiovascular centers and study the impact on cardiovascular control including BP and extracellular SNA recordings. The selected approach drives ChR2 expression in all cells expressing AT1a including neurons, using heterozygous animals AT1a and ChR2 expression is expected.

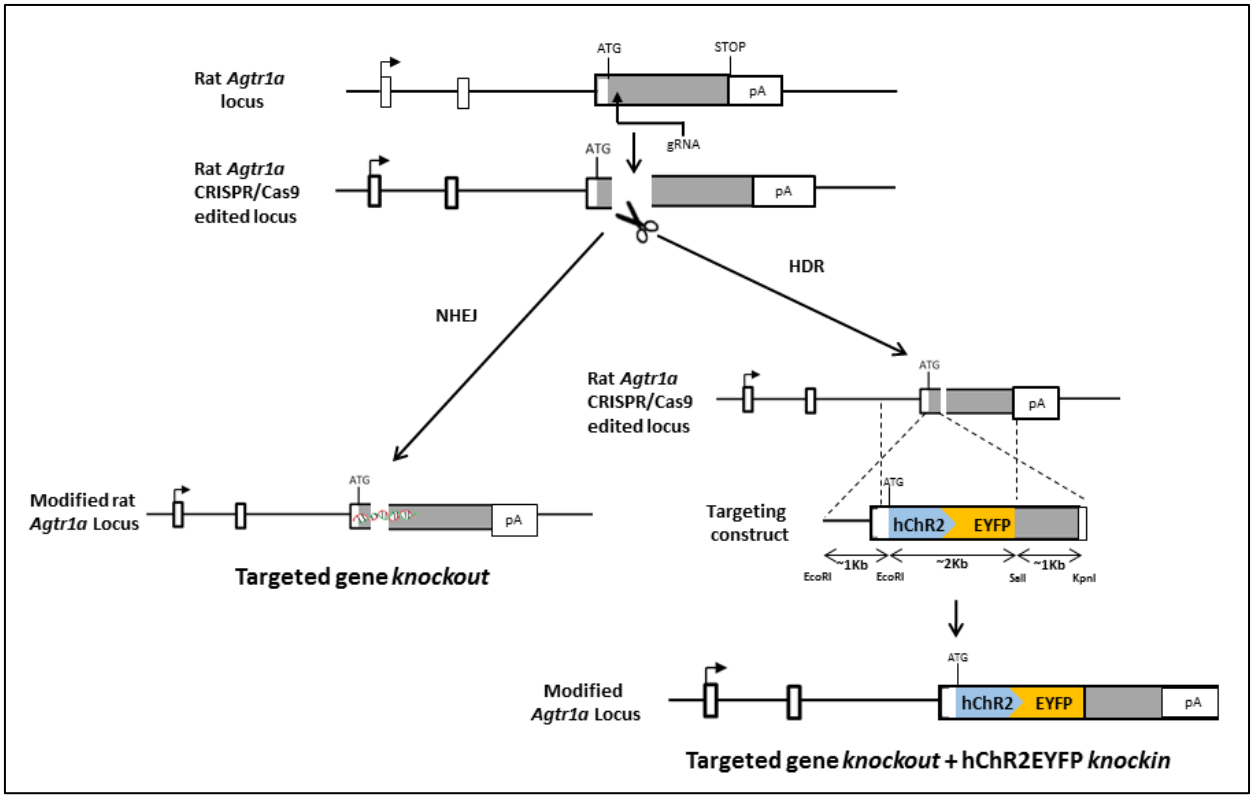

Figure 8 - Schematic representation of the planned knockout and knockin of the rat AT1a receptor (*Agtr1a* locus). CRISPR/Cas9 mediated non-homologous end joining (NHEJ) and homology-directed repair (HDR) using a DNA template donor. Rat zygote pronuclei microinjection or electroporation of a specific gRNA for the rat *Agtr1a* with Cas9 protein, disrupts (double-strand break) the locus few base pairs downstream of its starting codon at exon 3. Upon CRISPR/Cas9 mediated double-strand break rat lines are obtained in two different ways. First, targeted gene knockout is achieved by NHEJ endogenous repair machinery. During this process few nucleotides are lost or inserted and these mutations likely result in frameshift therefore gene knockout (**left panel**). Second, channelrhodopsin 2-EYFP fusion protein is inserted by co-injecting a donor DNA template that is obtained by cloning homologous recombination arms into a commercial vector (**right panel**). Note, the donor DNA was constructed in a way that it excludes the *Agtr1a* starting codon and part of the sgRNA binding sequence, allowing ribosomal protein translation to be started from the channelrhodopsin2-EYFP fusion protein and avoiding CRISPR/Cas9 to cut the construct, respectively.

3.3 *In vivo* methods

3.3.1 *In vivo* animal experiments

All *in vivo* experiments were performed with adult male mice aged between 12-20 weeks unless otherwise stated. To avoid experimental bias, all mouse lines were simultaneously bred and randomly included at the same time in each experiment. To prevent circadian bias during acute recordings, all data was acquired between ZT3 and ZT7 (3-7 hours after the onset of the light). All surgeries were performed on a thermo-controlled plate under the constant monitor of the animal's rectal temperature. As anesthetic either ketamine and xylazine mixture (100 and 10

mg/kg *ip*, respectively) and/or 1-2% isoflurane air mixture supplied with a small animal anesthesia unit were used (Table 10). After each surgical procedure, the animal returned to its home cage placed on a 37 °C pre-warmed heating pad until full anesthesia recovery. Pain was alleviated providing 3 days before and 2 or 3 days after surgery 200 mg/Kg/day metamizole in drinking water (Table 10). All surgical instruments and the surgery bench were previously sterilized. The instruments were made aseptic placing for at least 2 hours in 6% hydrogen peroxide with posterior ddH_20 washing, while the working benches were cleaned with 70% ethanol (Table 10). If noted that an animal did not recover well from the surgery (*e.g.* reduced locomotor activity, considerable weight or hair loss) it was immediately sacrificed and the data excluded.

Table 10 - Anesthesia and analgesic solutions, and surface and tool sterilization solutions.

Anesthesia and analgesia solutions	**Composition**	**Diluent**
Anesthesia (ketamine/xylazine)*	(1:10, v/v) Ketamine, 100 mg/mL (1:20, v/v) Xylazine, 20 mg/mL	Sterile saline, 0.9%
Metamizole§	(1:375, v/v) Metamizole, 500 mg/mL	Tap water
Surface and tools sterilization solutions	**Composition**	**Diluent**
Ethanol	(15:35, v/v) Ethanol, 99%	ddH_20
Hydrogen peroxide	(1:5, v/v) Hydrogen peroxide, 30% (15:35, v/v)	ddH_20

*Injected *ip* in the volume of 10µL/g body weight.
§Calculated on a daily drinking volume of 150 µL/g/day, polyuric lines received the drug diluted accordingly.

3.3.2 Long-term cardiovascular phenotyping by radio-telemetry

Cardiovascular parameters (BP and HR) as well as locomotor activity were chronically acquired implanting telemetric probes. This methodology is the current gold standard to determine basal cardiovascular parameters in rodents, because the animal remains the entire time at his home cage with free access to food and water while the parameters are constantly recorded over 24 hours (118, 119). Also, the data acquisition may be initiated weeks after the probe implantation, when anesthesia effects and inflammation are resolved. Another advantage is the large battery autonomy allowing intermittent recording over a month.

3.3.2.1 Surgery (probe implantation)

Sterile PhysioTel PA-C10 pressure transmitters (DSI) were implanted, this transmitter allows recording BP (systolic, diastolic and mean arterial), HR, and locomotor activity. For transmitter implanting, the mouse was deeply anesthetized and placed on supine position. Two ~1.0 cm skin

incisions over the femoral triangle and the intrascapular space were performed, with previous local shaving and sterilization of the areas. First, the catheter of the pressure transducer was tunneled from the neck incision to the femoral triangle using an oral gavage needle as a conduit. The gavage needle was removed from the femoral incision and the body of the transmitter pushed subcutaneously into a pouch in the back region of the mouse. To introduce the tip of the catheter in the femoral artery, angled Graefe forceps were used to carefully visualize and isolate the femoral vessels (artery and vein) from the surrounding fat and nerves. After isolating the vessels, they were occluded distal (permanently) and proximal (temporary) ~0.5 cm apart allowing a window for catheter insertion. To prevent backflow, the distal ligation portion was knotted with a suture cable (4/0 silk), and the inflow was prevented proximally using a third-hand approach where the vessels were a suspended with a suture cable (6/0 silk) and a Halsey needle holder. Two additional suture lines were placed underneath the vessels for posterior catheter fixation. Briefly before implantation, to prevent blood clotting, the catheter tip was rubbed with biocompatible gel (DSI). Using an iris scissor, a small incision on the artery was made. The catheter was then inserted into the vessel lumen using a vessel cannulation forceps and a bent 27-G hypodermic needle as an introducer. Around 1.5 cm of the catheter was inserted towards the proximal part of the vessel, therefore, reaching the abdominal aorta before the renal artery bifurcation. At the end, all three-suture cables were ligated with double knots to secure the catheter into the artery. The fat originally covering the vessels was placed back onto the vessels and secured with a suture stitch (4/0 silk). Finally, the skin incisions were closed with discontinuous sutures (4/0 silk) and the animal allowed to recover for 2 days or 12-14 days depending on the protocol. Note: the whole procedure was performed under a Leica stereomicroscope.

3.3.2.2 Data acquisition and processing

Upon surgery recovery, mice were transferred to the recording room equipped with PhysioTel RPC-1 receivers where the cages were placed on and kept during the complete habituation and recording periods. The RPC-1 receivers were connected to a DSI data exchange matrix that transmits the signal to a computer with the software Dataquest ART. The cardiovascular parameters were recorded during 10 sec every 5 min. The hour averaged data was exported to an

excel file for further processing. Pulse pressure was calculated as: pulse pressure = systolic - diastolic pressure. Note: the recording was shortly stopped in case cages had to be chanced or drug had to be administered.

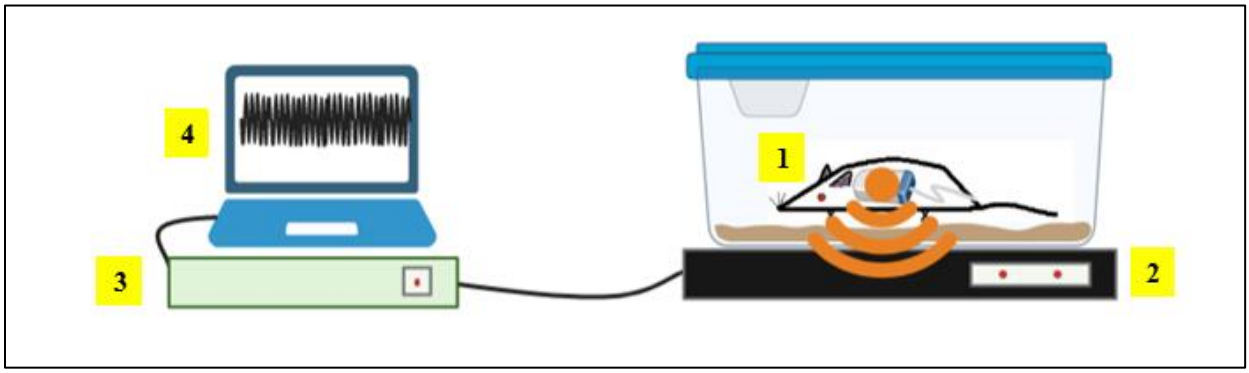

Figure 9 - Schematic representation of the long-term cardiovascular sampling using radiotelemetry.
(**1**) A mouse with an implantable telemetry probe at its home cage. (**2**) RPC-1 receivers receive radio signals from the cardiovascular parameters 24 hours every 5 min for 10 seconds. (**3**) The data exchange matrix forwards the signal to a (**4**) computer with the software Dataquest A.R.T.. This illustration was partially created in BioRender.com.

3.3.3 Short-term cardiovascular phenotyping and intravenous drug administration

The Bader lab has mastered its own technique for mouse femoral catheters handcrafting and implantation as described by Todiras *et al*. (120). By implanting two femoral catheters in the artery and vein, exterior extensions of the arterial and venous systems are created, respectively. The method allows to record cardiovascular parameters (BP and HR) for short-term from a conscious and freely moving mouse at its home cage in a cost-effective manner. Additionally, the method is optimal to monitor short-term (second to minutes, beat-by-beat) cardiovascular effects of any drug that is administered by intravenous route, without previous contact with the mouse, in periods where the cardiovascular parameters are stable such as during minimal movement. Note: Acute BP recording and drug infusion in rats were performed as described for mice using appropriated catheters.

3.3.3.1 Catheter construction

The femoral artery and vein catheters were constructed using 2 distinct tubing: a Micro-Renathane silicone tubing (MRE-025) ~3.5 cm connected to a second polyethylene tubing (PE-50) ~ 5.0 cm. The tip of the silicone tube was tapered heating the silicon tube containing a red-coded stylet from an anesthesia needle 29 G × 3½ (Spinocan) in the internal lumen. The end of

the tube was extended in proximity of a heating plate at 300 °C with a Student Hemostat tool until a tip dimension of ~ 0.3 mm (inner diameter) × 0.4 mm (outer diameter) was reached. The length of the produced tip was typically ~1.0 - 1.5 cm, which is about the size required to reach the abdominal aorta starting from the femoral artery. After heat stretching, the tip was cut straight with a scalpel in order to have a smooth end. Before connecting the silicon catheter to the polyethylene, one extremity of second was enlarged ~2.0 mm by heating and introducing a blunted 22-G hypodermic needle. Finally, the silicone tube was pushed into the dilated part of the polyethylene tube. The procedure was performed with the two tubes on the red-coded stylet 29 G × 3½ to avoiding glue accumulation in the internal lumen during the last step, which consists in filing the dead space between the walls with histoacryl tissue adhesive. Before use, the catheters were allowed to dry in an upstanding position for several days, and its patency and connection leakage were verified by flushing the catheter with tap water. Before implantation, the catheters were sterilized with 6% hydrogen peroxide for at least 12 hours and washed with ddH_2O.

3.3.3.2 Surgery (catheter implantation)

The animals were anesthetized, the femoral triangle region shaved and sterilized. A ~1.0 cm incision over the femoral triangle was made to visualize the femoral vein and artery. These vessels were carefully isolated from the surrounding fat and nerves. After vessel isolation with Graefe forceps, they had to be occluded distal (permanently) and proximal (temporary) ~0.5 cm apart allowing a window to introduce the catheters. To prevent backflow, the distal ligation portion was knotted with a suture cable (4/0 silk), and the inflow was prevented proximally using a third-hand approach where the vessels were a suspended with a suture cable (6/0 silk) with a Halsey needle holder. Two additional suture lines were placed underneath the vessels, and the vessels were dilated applying a drop of 1% procaine solution. To prevent blood clotting, the catheters were filled with heparinized saline (100 U/ml) before implanting, and the tip rubbed with biocompatible gel. Both catheters were closed at the other extremity, the arterial inserting a red-coded stylet from an anesthesia needle 29 G × 3½ (Spinocan), while the vein catheter with a 23-G stainless steel plug. Using an iris scissor, one at a time, one small incision in each vessel was made. The catheters were then inserted into the respective lumen using a vessel cannulation forceps and a bent 27-G hypodermic needle as an introducer. Around 1.5 cm of each catheter was

inserted towards the proximal part of the vessel, therefore, reaching the abdominal aorta and vena cava inferior. At the end, all three suture cables were ligated with double knots to secure the catheters into the vessels. The arterial catheter was clamped with a Hemostat tool, the stylet was taken out from it, and like the venous catheter the arterial catheter was closed with a 23-G stainless steel plug. Both catheters were then routed subcutaneously up to the extrascapular space and exteriorized. For this, a silicone tube bridged the catheters to a 15 cm round-shape smooth edges metal bar. The fat and connective tissues retracted during the vascular cleaning were placed back over the vessels, and the fat and the skin wounds were separated sutured with a (4/0 silk). In the last step, with both catheter extremities out, both catheter extremities were inserted into a 5 mm of silicone tubing (type SIL-080) and then altogether secured under the skin with a suture cable (3/0 silk) (see Figure 10). The animal recovered from surgery on a heated pad until consciousness was regained. The animal was allowed to further recover for 2 days at its home cage with free access to water and food. The catheters were daily flushed (~100 µL) once a day with the heparinized saline (100 U/ml) during the recovery period. At the day of the experiment, the catheters were flushed just before connecting the animal to the BP recording unit. The arterial catheter was connected to the pressure transducer, and after the recording, the animal rests until the next day, with maximal number of 3 days (3 experimental days). Immediately, after finishing the *in vivo* protocol the animals were killed by cervical dislocation.

Table 11 - Heparinized saline solutions preparation.

Solution	Component	Diluent
Heparinized saline, 20 U/mL	(1:250, v/v) Sodium heparine, 5000 I.U/mL	Sterile saline, 0.9%
Heparinized saline, 100 U/mL	(1:50, v/v) Sodium heparine, 5000 I.U/mL	Sterile saline, 0.9%

3.3.3.3 Drug infusion (*i.v*)

A 100 µL Hamilton syringe connected to a ~50 cm long polyethylene tubing (PE-50) was connected to the venous catheter for drug infusion. Before connecting the tubes, the syringe and the tube were filled with heparinized saline (20 U/ml), and the substance in solution loaded at the tip of the tube leaving small air bubble of ~0.3 µL (to avoid drug dilution) (see Figure 10). After connecting the tube and before injecting the substance, the animal was allowed to an acclimation period of ~60 min. When the animal displayed minimal locomotor activity, the substance was injected in *bolus*. Drugs were diluted that the volume of 0.5 µL/g body weight was injected, and a total volume of 100 µL was injected. *e.g* for a typical 30 g FVB/N mouse this consists of 15 µL

of the drug + 85 µL of heparinized saline (20 U/mL). The extra volume injected is important to wash out the implanted catheter which contains a volume of ~15 µL. Injecting 100 µL of vehicle (saline) in *bolus* causes only very slight MAP elevation ~4 mmHg. During the experiments 4 - 7 animals from distinct lines were recorded in parallel, each animal was used to test the effect of maximal 3 different drugs. To avoid possible synergic effects, different drugs were administered with a 24 hour interval and drug administration sequence was alternated within the groups. All substances injected intravenously were diluted in purchased sterile 0.9% saline. Candesartan and nifedipine were diluted in saline containing Na_2CO_3 and DMSO, respectively (Table 12). To avoid drug concentration bias, each substance used was only once diluted in sterile physiological saline and stored in several aliquots at -20 °C, for each experiment a new vial was thawed.

Table 12 - Vasoactive drugs administered intravenously for cardiovascular effect quantification.

Drug	Concentration in solution	Injected concentration	Diluent
Angiotensin II acetate salt (Ang II)	200 ng/mL	100 ng/Kg	Sterile saline
Candesartan (CV 11974)	0.2-2 mg/mL	0.1-1 mg/Kg	Sterile saline with Na_2CO_3, 0,01% (w/v)
Dexmedetomidine Hydrochloride	10 µg/mL	5 µg/Kg	Sterile saline
Endothelin-1	2 µg/mL	1 µg/Kg	Sterile saline
Hexamethonium bromide	40 mg/mL	20 mg/Kg	Sterile saline
Nifedipine	1.6 mg/mL	0.8 mg/Kg	Sterile saline with DMSO 5 % (v/v)
Nω-Nitro-L-arginine methyl ester hydrochloride (L-NAME)	60 mg/mL	30 mg/Kg	Sterile saline
Phenylephrine	2-20 µg/mL	1-10 µg/Kg	Sterile saline
Prazosin hydrochloride	200 µg/mL	100 µg/Kg	Sterile saline
Sodium nitroprusside dihydrate	10 µg/mL	10 µg/Kg	Sterile saline
Tyramine	2 mg/mL	1 mg/Kg	Sterile saline
Y-27632 dihydrochloride	1.2 mg/mL	0.6 mg/Kg	Sterile saline
Yohimbine hydrochloride	2 mg/mL	1 mg/Kg	Sterile saline

3.3.3.4 Data acquisition

Data was acquired using pressure transducers model MLT0699 connected to a PowerLab/4sp via bridge amplifiers ML110 (AD Instruments). Importantly, the recording unit was calibrated before and after each individual recording (mouse) with a two-point calibration (0 and 120 mmHg) using a precision mercury manometer. To record cardiovascular parameters, the arterial catheter was connected to a heparin/saline filled tube connected to the pressure transducer. BP was recorded constantly (beat-by-beat) at 200 Hz before during and after *i.v* drug injection. MAP was automatically calculated with the formula MAP = ((systolic + (2 x diatolic)) / 3), and the cardiac

frequency (HR) was deduced from the oscillatory pressure waveform. Data was acquired and analyzed using a computer equipped with a LabChart v5 software (AD Instruments).

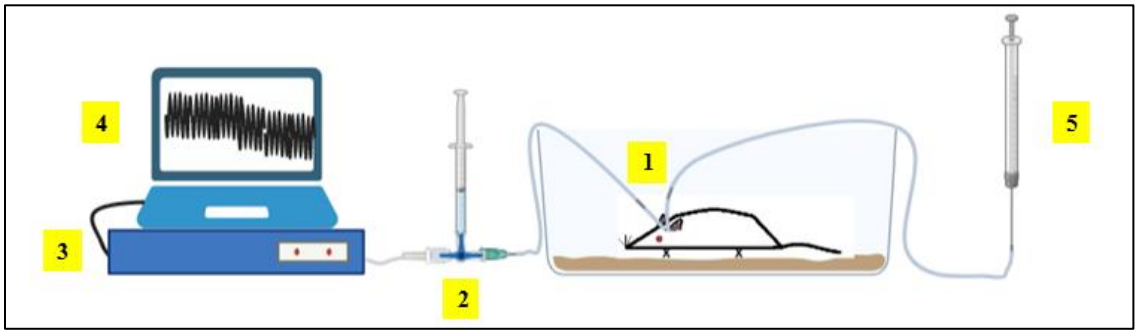

Figure 10 - Schematic representation of the short-term cardiovascular sampling using the catheter setup.
A freely moving mouse at its home cage instrumented with arterial and venous catheters that were exteriorized at the intrascapular space (**1**). The arterial catheter is connected to a pressure transducer (converts mechanical to electrical energy) that is coupled to a 3-way stopcock, allowing intraarterial fluid injection for signal improvement (**2**). The voltage signal is amplified and converted to pressure signal using bridge amplifiers and a Powerlab 5, respectively (**3**). Cardiovascular data are recorded and analyzed using a computer with the software labChart 5 (**4**). A Hamilton syringe coupled to a polyethylene tubing loaded with drug in solution is connected to the venous catheter to deliver chosen concentrations of vasoactive drugs (**5**). Intravenous drug infusion takes place when the animal displays minimal locomotor activity, therefore, stable cardiovascular parameters. This illustration was partially created in BioRender.com.

Drug infusion (ΔMAP and ΔHR) responses were calculated by the differences between the maximal MAP or HR (peak or trough) response and the averaged immediate (~1 minute before drug infusion) see the example below (Figure 11). Baseline cardiovascular parameters were quantified before any drug administration for at least 60 min.

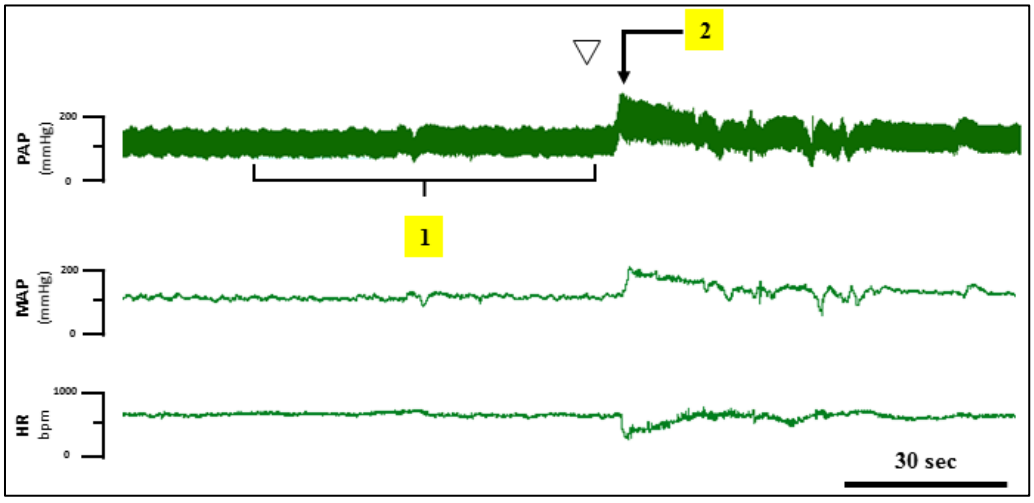

Figure 11 - Example of a ΔMAP and ΔHR calculation.
A wildtype FVB/N mouse received a 10 µg/kg phenylephrine injection, showed by symbol "▽" , triggering an immediate increase in MAP and decrease in HR (baroreflex of the HR), middle and bottom diagrams, respectively. To calculate ΔMAP and ΔHR, baseline MAP and HR are averaged immediately before injection for ~1 min (**1**) as the peak or tough maximal response for ~5 heart beats (**2**). Cardiovascular responses are calculated with the following formulas ΔMAP = (maximal MAP response - baseline MAP) and ΔHR = (maximal HR response - baseline HR). Note: MAP and HR, middle and lower diagrams, are automatically calculated from pulsatile arterial pressure recording (top diagram). PAP = pulsatile arterial pressure, MAP = mean arterial pressure, HR = heart rate.

3.3.4 Baroreflex control of the heart rate

The baroreflex control of the HR was calculated monitoring changes in HR induced by transient increase and decrease in BP induced by intravenous bolus injection of vasoconstrictor and vasorelaxant substances in freely moving mice. Bradycardia response was induced by administering equipressor "~20 mmHg" doses of the vasoconstrictor phenylephrine (1-10 μg/kg), while tachycardia response was induced by intravenous injection of the vasorelaxant sodium nitroprusside (10 μg/kg). To calculate the baroreceptor sensitivity index, the MAP and HR peak responses to phenylephrine and sodium nitroprusside were recorded beat-by-beat using the catheter method. First, the basal and the peak response changes in the HR were converted to changes in pulse interval (PI,ms) by the formula 60,000/HR. The PI was calculated using the formula (PI = peak response PI - basal PI). Finally, the baroreflex sensitivity index was calculated with the formula (BRS = PI/MAP, ms/mmHg) (121).

3.3.5 Renal denervation

Mice instrumented with radio-telemetry receivers, in which the baseline BP had been acquired for 48 hours were deeply anesthetized with isoflurane vapor (3-4% induction, 1-2% maintenance) for bilateral renal denervation. A flank incision (skin and muscle layers) was opened to gain access to the kidney and renal vessels. The renal vessels were identified, and the kidney gently retracted using a self-customized hook made with a paperclip. A gauze soaked in physiological saline was placed between the hook and the kidney to avoid tissue damage. Carefully, the renal vein and artery were isolated from surrounding tissue using sterile cotton wrapped on a cotton carrier as well as fine forceps. After connective tissue clearing, the renal vessels were isolated using fine surgical instruments and/or a glass pipette, which the tip was previously tapered by gentle stretching on a flame. This procedure melts the glass pipette tip and a smooth tip develops. Using a stereomicroscope (Leica), all renal nerves identified were mechanically destroyed with fine instruments. To assure the complete clearing of the nerves, using a 0.5 mm paint brush and/or a cotton carrier, the vessels were painted with renal denervation solution containing 10% phenol for ~5 min (Table 13). To avoid phenol spreading into the abdominal cavity, a small piece of parafilm was placed underneath the vessels before phenol application. Additionally, the

vessels were cleared with physiological saline and dried at the end with sterile cotton. Upon phenol clearing, the parafilm was removed, and muscle and skin layers were separately closed with discontinues sutures (silk 4/0). The same procedure was repeated on the contralateral side. Renal denervation success was verified at the end of the acquisition of cardiovascular parameters (one week after surgery) by quantification of renal norepinephrine levels as described in section 3.7.2.

Table 13 - Phenol solution used for renal denervation.

Solution	Component	Solvent
Denervation solution	10% (w/v) Phenol	Ethanol, 95%

3.3.6 Chemical Sympathectomy

Total peripheral SNS ablation was performed administering 6-hydroxydopamine hydrobromide (6-OHDA), a drug that does not penetrate the blood-brain-barrier in adult rodents (122). 6-OHDA was injected once a day 100 mg/kg *i.p* for 5 days. The drug was prepared daily in a dark room diluting 6-OHDA in sterile physiological saline containing 0.01% ascorbic acid to prevent oxidation (Table 14). 6-OHDA solution final concentration was 10 mg/mL and the volume of 10 µL/g body weight was injected. This dosage was chosen because it ablates most of the peripheral sympathetic terminals in mouse between 3 to 5 days (122–124).

Table 14 - Solutions used for *in vivo* chemical sympathectomy.

Solution	Component	Diluent or Solvent
0.01% Ascorbic acid	0.01% (w/v) Ascorbic acid	Sterile saline, 0.9%
6-OHDA solution	10 mg/mL 6-Hydroxydopamine hydrobromide	0.01% ascorbic acid

3.3.7 Sample (organs, blood and urine) collection for *ex vivo* experiments

Ex vivo experiments were in most of the cases performed in an attempt to elucidate the molecular basis of the *in vivo* cardiovascular phenotypes found. Therefore, similar to the acute cardiovascular phenotyping, organs from 12-20 weeks old male mice were harvested between ZT4 and ZT6 (4-6 hours after the onset of the light) unless otherwise stated. Mice were sacrificed either by cervical dislocation, decapitation or isoflurane overdose followed by exsanguination. Rats were only sacrificed using isoflurane overdose.

For most of the downstream applications, organs were immediately harvested, shortly rinsed in ice cold PBS or 0.9% saline to remove blood excess (Table 15), snap frozen in dry ice

or liquid nitrogen, and stored at -80 °C until usage. Organs used for histology were placed in 4% paraformaldehyde solution after rinsing in PBS. Aorta and mesenteric artery used for mRNA analyses were directly placed in a tube containing RNAlater and stored at 4 °C for a maximum of 7 days. Fat and connective tissue were removed from aorta and second/third branch mesenteric arteries under a stereomicroscope using a petri dish containing RNAlater with fine surgical instruments. Once cleared, aorta and mesenteric arteries were placed in tubes containing Trizol and stored at -80 °C until mRNA extraction. Blood was collected from a cardiac puncture performed upon a thoracotomy using a 23 G needle coupled to a 1 mL syringe. Blood for hematological analyses was collected into MiniCollect® EDTA-K3 coated tubes and was stored at room temperature. Plasma samples were separated centrifuging at 2000 *g* for 10 min at 4 °C blood collected into lithium-heparin or MiniCollect® EDTA-K3 coated tubes. Plasma was transferred to new tube, snap frozen in dry ice, and stored at -80 °C until processing. Timed spontaneous urine was collected by holding the mouse over an empty tube. In case a small urine volume was collected or the mouse´s bladder was found empty, the procedure was repeated on the following day. The collected urine was snap frozen in dry ice and stored at -80 °C until usage.

Table 15 - Buffers used for blood excess removal.

Buffer	Components
10x Phosphate-buffered saline (PBS), pH 7.4*	1.37 M NaCl 27 mM KCl 100 mM Na2HPO4 18 mM KH2PO4
0.9% Saline	0.9% (w/v) NaCl

*PBS was prepared 10x concentrated, and before use it was diluted to 1x (working concentration).

3.3.7.1 Organ collection for Agt-Tg validation

To validate the brain-specificity of the transgene expression, pieces of the following tissues were collected and polled from 2 wildtype and 2 Agt-KO-Tg mice: White fat, brown fat, brain, kidney, liver, salivary gland, lung, bladder, heart, duodenum, spleen, stomach, adrenal glands, testes, muscle, gut, skin and aorta. The tissues were briefly rinsed in ice-cold saline to remove blood excess, snap-frozen in dry ice, and stored at -80 °C until mRNA extraction.

3.3.8 Biometrical measurements

Mouse body weight was taken by placing the mouse into a 1-liter plastic beaker on an analytical scale. Organs (heart, spleen, kidney, adrenal glands, and lungs) were harvested immediately after the mouse death and washed in PBS to remove blood excess. Using forceps, the PBS excess was removed from the heart cavities squeezing the organ against a dry paper towel, other organs were only rolled on a dry paper towel. Finally, wet organ weight was taken using a digital analytical balance. The tibia length was measured using a digital caliper, after bone dissection and surrounding tissue clearing.

3.3.9 Embryo manipulation

These experiments were performed by Dr. Elena Popova which optimized the technique for transgenic rat generation in the Prof. Dr. M. Bader group. Briefly, AT1a knockout rats were generated by delivering SD rat zygotes or 2-cell stage embryos recombinant Cas9 protein (1280 ng/ µL, IDT) and *in vitro* transcribed sgRNA (258 ng/µL; see section 3.4.7.1) or a commercial sgRNA 258 ng/µL each (CRISPR RNA, crRNA; trans-activating CRISPR RNA, tracRNA) by electroporation (50-70V, 2.6ms, 1 pulse). For AT1a knockin generation additional to purchased sgRNA Cas9 protein, HDR templates (circular vector, ssDNA or dsDNA, see sections 3.4.7.2 and 3.4.7.1) were delivered by electroporation, microinjection, or a combination of both methods into SD rat zygotes and 2-cell embryos. For microinjection concentrations were: Cas9 protein (30 ng/µL), sgRNA (crRNA/tracRNA, 12.5 ng/µL each), and HDR template 5 ng/µL. Zygotes were isolated by hormonally induced superovulation of SD rats and differentiated in culture to 2-cell embryos. In both cases, after embryo manipulation, zygote or 2-cell stages were implanted into pseudo-pregnant foster mothers as described by Popova *et al.* (125).

3.4 Molecular biology methods

3.4.1 Polymerase chain reaction (PCR)

Using a DNA template with known sequence, PCRs might be used to amplify segments of any given sequence of DNA in an exponential manner using a specific complementary primer pair, nucleotides and the thermostable DNA polymerase, Taq polymerase. Conventional PCRs were performed to amplify DNA fragments. For most of the applications including genotyping, RT-

PCR and vectorette PCR a Taq DNA polymerase with ThermoPol buffer (NEB) was used. PCR mixes were assembled into PCR stripe tubes (Table 16). The reaction tubes were capped, shortly spun down, placed into a thermocycler, and the PCR run using specific cycling conditions which were optimized concerning annealing and elongation temperatures as well as the elongation length. To assure proper template preparation and no reaction contamination, a positive control (when possible) and a water control sample, respectively, were included in each PCR round. The sequence specificity of each primer pair sequence was verified using the online BLAST tool[4] and the appearance of the expected amplicon size by agarose electrophoresis (see section 3.4.2). In case of a dubious result, part of the PCR reaction was purified (see section 3.4.5), and forwarded for sequencing (see section 3.4.12) and the resulting sequence finally analyzed *in silico* with the online BLAST tool[1].

Table 16 - Conventional PCR mix composition using Taq polymerase.

Stock concentration	Component	Volume (µL)
10x	ThermoPol® Buffer (NEB)	2.5
5 mM	dNTPs	1.0
10 µM	Primer 1	0.5
10 µM	Primer 2	0.5
10 µM	Primer 3*	0.5
-	Nuclease-free water	18.875
5 U/µL	Taq DNA polymerase	0.125
Variable	Template DNA	1
Final volume		25

The annealing temperature is primer-specific and elongation time depends on the amplified fragment. *In case the PCR only required two primers the volume 0.5 µl of ultrapure water was pipetted instead.

To amplify DNA fragments for downstream applications where proof-reading was ideal such as subcloning, the Phusion® high-fidelity DNA polymerase was used. PCR mixes using Phusion polymerase were prepared as described in Table 17.

[4] https://blast.ncbi.nlm.nih.gov/Blast.cgi

Table 17 - Conventional PCR mix composition using phusion polymerase.

Stock concentration	Component	Volume (µL)
5x	Phusion Buffer (NEB)	10.0
5 mM	dNTPs	2.0
10 µM	Primer 1	2.5
10 µM	Primer 2	2.5
-	Nuclease-free water	31.5
2 U/µL	Phusion DNA polymerase	0.5
Variable	Template DNA	1
Final volume		50

3.4.2 Agarose gel electrophoresis

The agarose electrophoresis was performed to size-separate and visualize vector insert integration, PCR amplicons which many times were used as tool determine mouse genotypes or to verify primer specificity by a unique and size predicted amplicon. The gels were prepared briefly heating 1-3% (w/v) agarose in Tris-acetate-EDTA (TAE) buffer (40 mM Tris; 20 mM acetic acid; 1 mM EDTA) (Table 18) using a microwave oven until complete dilution. 5 µL of 0.2% ethidium bromide was mixed to 40 mL of agarose solution that was allowed to polymerize at room temperature in a horizontal gel casting. In the following step, 0.1 volume units of 10x DNA loading buffer (Table 18) was added to the samples (PCR mixes) and 10 µL of the samples and a reference 1 Kb or 100 bp DNA ladder were loaded into the gel slots placed into a horizontal TAE buffer-filled gel chamber. Each electrophoresis (100-120 V) had a duration between 10-30 min. Finally, fluorescent bands were visualized and documented with 302 nm UV light using a Gel Imager C200 (Azure Biosystems). When the DNA fragment was visualized with the purpose of purification, the gel was visualized with 365 nm UV light to minimize DNA damage.

Table 18 - Buffers and solutions used for agarose electrophoresis.

Solution or buffer	Component	Solvent
Ethidium bromide	2% (w/v) Ethidium bromide	Ultrapure water
TE buffer, pH 8.0	10 mM Tris 1 mM EDTA	Ultrapure water
10x DNA loading buffer	40% (w/v) Sucrose 0.02% (w/v) Bromophenol blue	TE Buffer
50x Tris-acetate-EDTA (TAE), pH 8.5	2 M Tris 1 M Acetic acid 50 mM EDTA	Ultrapure water

TAE was prepared 50x concentrated, before use it was diluted to 1x (working concentration).

3.4.3 Animal Genotyping

All mouse and rat lines were genotyped between birth and weaning, for experimental and colony maintenance purposes. In addition, each animal used in experimental procedures was re-genotyped to assure the correct genotype.

3.4.3.1 Genomic DNA extraction for genotyping

Genomic DNA was extracted and used for mouse genotyping; mainly three types of biopsies were collected: ear, toe-nail, or tail. Probes were incubated (30 µL, toe-nail; 50 µL, ear; 100 µL, tail) in sample digestion buffer (Table 19) overnight at 55 °C in an orbital shaker. This buffer contains the fungal proteinase K, that, with its broad proteinase activity releases mammalian DNA that may be used for downstream molecular biology applications including PCR. After overnight incubation, samples were briefly heated for 10 min at 95 °C in other to inactivate the proteinase K. The RNA contained in the sample was digested adding RNase A diluted in TE buffer pH 8.0 (Table 19). The volume added to the digested toe-nail, ear and tail biopsies were 250 µL, 500 µL and 750 µL, respectively. Probes were stored at 4 °C for short-term usage or -20 °C for long-term usage. This procedure usually yields a final concentration of genomic DNA in solution ranging between 30 - 200 ng/µL.

Table 19 - Buffers used for genomic DNA extraction from toe-nail, ear and tail biopsies.

Buffer	Component
Sample digestion buffer, pH 7.0 with proteinase K	200 mM NaCl 100 mM Tris 0.1 mM EDTA 1% (w/v) SDS 1 mg/mL Proteinase K
TE buffer, pH 8.0 with RNAse	10 mM Tris 1 mM EDTA 20 µg/mL RNase A

3.4.3.2 Mouse genotyping protocols

Each mouse line was genotyped using PCR mix with specific primers designed to produce short DNA amplicons used to distinguish wildtype, knockout and heterozygous mice or transgenic (Table 20). The method allows the genotyping of transgenic and targeted-mutation (knockout)

containing mice, however, heterozygous and homozygous transgenic animals are not distinguishable with the method unless the integration site is fully mapped. Genotyping PCRs were assembled as described in section 3.4.1, using specific primers and 1 µL of genomic DNA as template. Detailed primer sequence, PCR cycling information and expected amplicon sizes are listed in Table 20,21. Each PCR round contained a reaction with water instead of genomic DNA, and another with a positive control to monitor contamination and sample DNA extraction quality, respectively. Note: A PCR reaction was used to distinguish the wildtype Ren genes in mixed background mice; Ren1c from Ren1d expressed by the C57BL/6N and FVB/N, respectively. The PCR with the target "Tg of Agt-Tg" in Table 20 was designed to differentiate heterozygous from homozygous Agt-Tg mice, the design of this PCR was only possible after mapping the transgene integration site as described in 4.1.2.

Table 20 - Genotyping primers (sequence, annealing temperature, elongation time and expected band size).

Mouse line or Target	**Sequence (5' to 3')**	**Sense**	**Annealing temperature (°C)**	**Elongation time (s)**	**Genotype - band length (bp)**
AT1a-KO	GAAGCCCAGGATGTTCTTGG GTGTCTGAGACCAACTCAACC GGCAGCGCGGCTATCGTGG	Reverse Forward	58	45	wildtype - 645 knockout - 800
Agt-KO	CCATTCAGGCCAAGACCTCC CTTGTGTCCATCTAGTCGGG GGCAGCGCGGCTATCGTGG	Forward Reverse Reverse	60	40	wildtype - 320 knockout - 600
Agt-Tg	TGACACCAACCCCCGAGTGG TCTGCCCAGAAAGTGCAGCG	Forward Reverse	55	45	wildtype - 809 transgenic -190
Ren1c-KO	CAGCAAGACTGACTCCTGGC GTAGCACGTAGTCCGTACTGC CGTTGGCTACCCGTGATATT	Forward Reverse Forward	60	50	wildtype - 943 knockout - 707
C57BL/6N - Ren1c; FVB/N - Ren1d	CTTTACACAAGTTACCTGAACC CCAGTATGTGTCAGGGACTC	Forward Reverse	60	30	Ren1c - 276 Ren1d - 326
Tg of Agt-Tg	GGCACCTTGGTGTTCCTATC GAACATTGTGTCTGTGCCAA TCACCCACTTTCCCAGCTTC	Forward Reverse Reverse	60	60	wt/wt - 318 Tg/Tg - 700 wt/ Tg - both

wt = wildtype, Tg = transgenic = Agt-Tg.

Table 21 - PCR cycling program for genotyping PCRs.

PCR step	**Time (s)**	**Temperature (°C)**	**Cycles**
Initial denaturation	180	95	1
Denaturation	30	95	40
Annealing	30	55-60	
Elongation	30-50	68	
Final elongation	600	68	1
Hold	∞	4	-

All PCRs were performed with cycler lid at 105 °C.

3.4.3.3 Rat genotyping protocols

Putative founders of AT1a knockout and knockin rat lines were genotyped using conventional PCRs (Table 16) with specific primers (Table 22).

Knockout: To verify CRISPR/Cas9-induced mutations by NHEJ, a PCR mix of 25 µL was prepared. This PCR amplifies the region flanking the expected double strand break by Cas9 (Table 22). After running the PCR program, 5 µL of the reaction mix was mixed with DNA loading buffer and run through a 2% agarose gel to verify the success of amplification (see section 3.4.2). The remaining PCR mix (~20 µL) was purified (see section 3.4.4.5), and forwarded for sequencing as described in section 3.4.12. The resulting sequencing files were analyzed with the software SnapGene Viewer.

Knockin: To determine if the construct containing ChR2 integrated in the genome a conventional PCR with specific primers (Table 22) was performed (see section 3.4.1), and positive founders were identified running the PCR product through a 2% agarose gel (see section 3.4.2). In case a positive founder was identified, another conventional PCR was performed with a primer pair upstream of the 5' homology recombination arm and another in reverse orientation in the ChR2 sequence. Success of the knockin was verified running the PCR product through a 1% agarose gel (see section 3.4.2).

Table 22 - Primers used for genotyping founders of AT1a knockout and knockin lines.

Target	Sequence (5' to 3')	Sense	Annealing temperature (°C)	Elongation time (s)	Genotype - band length (bp)
ds-break at the CRISPR/Cas9 binding site **	GAACCACTAGATTTGTGGTGG	Forward	58	45	wildtype - 271
	CAAAGATGATGCTGTAGAGGG	Reverse			gene edited - ~271
ChR2 positive animals	GAGGATCCACACTCAAATCC	Forward	60	30	Positive - ~350
	AGCTTGCTGATGTCTGATTG	Reverse			negative - none
ChR2 integration by HDR	GAGGATCCACACTCAAATCC	Forward	60	90	Integration - ~1200
	CATCCGGCACAGTAACATTG	Reverse			Non-integration - none

** To find mutations induced by CRISPR/Cas9 mediated NHEJ, the PCR product was purified and sequenced using the forward primer. ChR2 = channelrhodopsin 2, HDR = homology directed repair.

3.4.4 Qualitative and quantitative gene expression analyses

3.4.4.1 Tissue RNA isolation

Total RNA was extracted with the Trizol-chloroform method. 1 mL of Trizol® was pipetted on 100 mg of tissue in a FastPrep™ tube containing 4-5 ceramic matrix beads (diameter 2.8 mm) (MP Biomedical). Samples were homogenized 2-4 times (depending on the organ) for 40 s at speed level 4 using a Benchtop homogenizer, FastPrep-24 (MP Biomedical). To assure the complete nucleoprotein complex dissociation, the samples were incubated 10 min at room temperature. Then, 200 µL of chloroform was added to the homogenate, samples were shaken for 15 s and incubated for 3 min at room temperature. Subsequently samples were centrifuged at 12.000 *g* for 15 min at 4 °C, and the aqueous upper phase containing the RNA was transferred to a new 1.5 mL tube. To precipitate the RNA of the aqueous phase, 500 µL of isopropanol was added and the tube mixed by inversion then incubated at room temperature for 10 min. The tubes were centrifuged at 12.000 *g* for 15 min at 4 °C, and the pellets containing RNA were washed by resuspension in 1 mL of 70% ethanol and centrifuging at 12.000 *g* for 15 min at 4 °C. The ethanol was then discarded with a pipette and the excess removed air-drying the pellets at room temperature for 15-30 min. Finally, the RNA pellets were resuspended in DEPC-water (10-50 µL) (Table 23), and to facilitate dilution tubes were shortly vortexed and incubated 10 min at 55 °C. The RNA concentration and purity was verified using a spectrophotometer NanoDrop™ 1000 (Peqlab), and by running 0.5-1 µg of RNA on a 1% agarose gel. Samples were stored at -80 °C until further use.

Table 23 - Preparation of DEPC water.

Water	Component
DEPC-water	0.1% (v/v) Diethylpyrocarbonate (DEPC)

The solution was stirred overnight at 37°C and autoclaved to degrade DEPC.

3.4.4.2 DNA digestion and complementary DNA synthesis (cDNA)

DNase I treatment: To avoid amplification of remaining genomic DNA, the RNA samples were submitted to a DNase treatment. 1-5 µg of total RNA were mixed with DNase I (Roche) (Table 24) and incubated in a thermocycler following manufacturer instructions (Table 24). The last step (75 °C, 10 min) is required to denature DNase I. At the end, RNA concentration and purity were verified with a NanoDrop™ 1000 (Peqlab).

Table 24 - DNAse I protocol, mix and cycling conditions, for digestion of genomic DNA in RNA samples.

Component	Volume (µL)
10x DNAse I buffer	2.0
RNasin (50 U/µL)	0.5
DNase I (10 U/µl)	0.5
RNA (1-5 µg)	Variable
Nuclease-free water	to 20

DNA digestion steps	Time (min)	Temperature (°C)
DNA digestion	30	25
DNase I inactivation	5	75
Hold	∞	4

cDNA library preparation: The reverse transcription (RT) of the RNA was used to synthetize cDNA templates. For this, 0.5-2.0 µg of DNase I treated RNA was converted to cDNA using the moloney murine leukemia virus reverse transcriptase (M-MLV). The cDNA was produced in two steps. First, RNA secondary structures were melted incubating the volume containing 0.5-2.0 µg of RNA plus nuclease-free water to complete 11.2 µL with 1 µL of random hexamer primers (RH) at 70 °C for 5 min, and the reaction was chilled at 4 °C for 5 min (Table 25). Second, working on ice 7.8 µL of a mix containing M-MLV (Promega) was added to the sample, the RT reaction was incubated in a thermocycler following manufacturer instructions (Table 25). The cDNA produced was stored at -20 °C until usage.

Table 25 - Reverse transcription protocol, mix and cycling conditions, of RNA samples.

First step

Component	Volume (µL)
Random primers (500 µg/mL)	1
RNA (0.5-2.0 µg)	Variable
Nuclease-free water	to 12.2

RT Steps	Time (min)	Temperature (°C)
Secondary structure melting	5	70
Chilling	5	4

Second step

Component	Volume (µL)
5x M-MLV Buffer	4
dNTPs (5 mM)	2.5
RNasin (50 U/µL)	0.5
M-MLV (200 U/µL)	0.8

RT Steps	Time (min)	Temperature (°C)
Priming	15	25
Transcription	60	37
Enzyme inactivation	15	70
Hold	0.5	4

3.4.4.3 Quantitative mRNA expression

mRNA gene expression level was determined using reverse transcription and quantitative PCR (RT-qPCR). RT-qPCR was performed using a GoTaq® qPCR reaction mix (Promega) that

contains 2 fluorescent dyes: a DNA-binding SYBR Green® and the reference CXR. The cDNA samples were diluted to final concentrations ranging between 1-5 ng/µL. 20 µL RT-qPCR mixes were assembled into a MicroAmp® optical 384-Well plate (Applied Biosystems). 9 µL of the diluted cDNA was pipetted together with the GoTaq® master mix, CXR and specific primers (Table 26). All primers were designed to a have a similar melting point, thus all reactions were performed at the same annealing temperature of 60 °C. Only primers displaying a single meting curve peak and expected amplicon band sized were included, a list of primers used is displayed in Table 27. All RT-qPCR samples were run in duplicates using a QuantStudio 5 Real-Time-PCR-System (Applied Biosystems), and the PCR program is displayed in Table 26. The data was acquired and analyzed using the software QuantStudio™ Design & Analysis Software v1.3.1 (Applied Biosystems). The Ct values obtained in the exponential phase of amplification from the gene of interest and an appropriate housekeeping gene (*Gapdh, Actb* or *18s*) were used to calculate the relative gene expression to the control group using the method of Livak and Schmittgen (126) ($2^{-\Delta\Delta CT}$).

Table 26 - RT-qPCR, mix and cycling conditions.

Components	Volume (µL)
cDNA (1-5 ng/µL)	9
2x GoTaq® master mix	10
Primer forward (10 µM)	0.4
Primer reverse (10 µM)	0.4
100x CXR reference dye	0.2

RT-qPCR	Time (s)	Temperature (°C)	Cycles
Priming	120	95	1
Initial denaturation	600	95	1
Denaturation	15	95	40
Annealing/ elongation	60	60	
Melt curve 1	15	95	1
Melt curve 2	60	60	1
Melt curve 3	15	95	1

Table 27 - List of primer pairs used for RT-qPCR.

Target, *Gene*	Sequence (5' to 3')	Sense	Amplicon (bp)
18s, *Rn18s*	TTGATTAAGTCCCTGCCCTTTGT CGATCCGAGGGCCTCACTA	Forward Reverse	75
Agt (mouse, mAgt), *Agt*	CTGAATGAGGCAGGAAGTGGG GCAGTCTCCCTCCTTCACAG	Forward Reverse	150
Agt (rat, rAgt), *Agt*	CTGAGTGAGGCAAGAGGTGTA GCAGTCTCCCTCCTTCACAG	Forward Reverse	150
Agt (mouse and rat, tAgt), *Agt*	CCATTCAGGCCAAGACCTCC GCAGTCTCCCTCCTTCACAG	Forward Reverse	299
Aquaporin-2, *Aqp2*	ATGTGGGAACTCCGGTCCATA ACGGCAATCTGGAGCACAG	Forward Reverse	137
AT1a, *Agtr1a*	AAAGCCTGCGTCTTGTTCTG TCGTGAGCCATTTAGTCCGA	Forward Reverse	103

Target, *Gene*	**Sequence (5' to 3')**	**Sense**	**Amplicon (bp)**
AT1b, *Agtr1b*	TGTGGGCAGTTTATACCGCT ACACTGGCGTAGAGGTTGAA	Forward Reverse	100
AT2, *Agtr2*	ATGATTGGCTTTTTGGACCTGT AAGGGTAGATGACCGATTGGT	Forward Reverse	126
Akr1b7, *Akr1b7*	CTGGACCTGTATCTGGTCCAC GTCCACCAGTTCCTCCATGG	Forward Reverse	138
CD3, *CD3e*	ATGCGGTGGAACACTTTCTGG GCACGTCAACTCTACACTGGT	Forward Reverse	126
CD68, *Cd68*	TGTCTGATCTTGCTAGGACCG GAGAGTAACGGCCTTTTTGTGA	Forward Reverse	75
CD86, *Cd86*	TCTCCACGGAAACAGCATCT CTTACGGAAGCACCCACGA	Forward Reverse	101
C-Fos, *Fos*	CGGGTTTCAACGCCGACTA TGGCACTAGAGACGGACAGAT	Forward Reverse	165
Collagen I, *Col1a1*	CTTCACCTACAGCACCCTTGTG GATGACTGTCTTGCCCCAAGTT	Forward Reverse	67
Collagen III, *Col3a1*	GCTGGCATTCCTCAGACTTCT ACTGTTTTTGCAGTGGTATGTAATG	Forward Reverse	67
Collagen IV, *Col4a1*	TCCGGGAGAGATTGGTTTCC CTGGCCTATAAGCCCTGGT	Forward Reverse	118
ENaCα, *Scnn1a*	CCAAGGGTGTAGAGTTCTGTGA AGAAGGCAGCCTGCAGTTTA	Forward Reverse	78
Endothelin A receptor, *Ednra*	TGCTGGTTCCCTCTTCACTT ACAGCAACAGAGGCAGGACT	Forward Reverse	210
eNOS, *Nos3*	CCTTCCGCTACCAGCCAGA CAGAGATCTTCACTGCATTGGCTA	Forward Reverse	105
Erythropoietin, *Epo*	ACTCTCCTTGCTACTGATTCCT ATCGTGACATTTTCTGCCTCC	Forward Reverse	123
Fibronectin, *Fn1*	ACCATTACTGGTCTGGAGCC GGGTAACCAGTTGGGGAAGC	Forward Reverse	124
Gapdh, *Gapdh*	TCACCACCATGGAGAAGGC GCTAAGCAGTTGGTGGTGC	Forward Reverse	168
GFAP, *Gfap*	CGGAGACGCATCACCTCTG AGGGAGTGGAGGAGTCATTCG	Forward Reverse	126
Hepcidin, *Hamp1*	AGGGCAGACATTGCGATACC GCAACAGATACCACACTGGGA	Forward Reverse	101
Hepcidin, *Hamp2*	CTGAGCAGCACCACCTATCTC TCTTCACAACAGATACCACAGGAG	Forward Reverse	191
Icam, *Icam1*	TTCACACTGAATGCCAGCTC GTCTGCTGAGACCCCTCTTG	Forward Reverse	182
Interleukin-6, *Il6*	CTGCAAGAGACTTCCATCCAGTT GAAGTAGGGAAGGCCGTGG	Forward Reverse	70
NCC, *Slc12a3*	ACACGGCAGCACCTTATACAT GAGGAATGAATGCAGGTCAGC	Forward Reverse	142
NHE3, *Slc9a3*	CAAGGTCACCAGTATCGTCCC GCATGAAGTATCCAGCATCCAAC	Forward Reverse	167
NKCC2, *Slc12a1*	GATGGGTGAAAGGTGTGCTG CAATTCCCGCTTCTCCTACAAT	Forward Reverse	96
nNOS, *Nos1*	TTCAAACGCAAAGTGGGAGGT AATGCCCCTGAGAACTTCCA	Forward Reverse	201
PAX8, *Pax8*	ATGCCTCACAACTCGATCAGA	Forward	101

Target, *Gene*	Sequence (5' to 3')	Sense	Amplicon (bp)
	ATGCGTTGACGTACAACTTCT	Reverse	
Rantes, *Ccl5*	GCTGCTTTGCCTACCTCTCC TCGAGTGACAAACACGACTGC	Forward Reverse	104
Renin, *Ren1* and *Ren2*	CAAAGTCATCTTTGACACGGG AGTCAGAGGACTCATAGAGGC	Forward Reverse	107
TGF-β, *Tgfb1*	CTTTGTACAACAGCACCCGC TAGATGGCGTTGTTGCGGTC	Forward Reverse	127
TNFα, *Tnf*	ACCCTCACACTCAGATCATCTTC TGGTGGTTTGCTACGACGT	Forward Reverse	71
Vcam, *Vcam1*	TGAACCCAAACAGAGGCAGAGT GGTATCCCATCACTTGAGCAGG	Forward Reverse	138
$\alpha 1_{A}$ - *Adra1a*	CCAGCACAGGTGAACATTTC GATGCCGATGACAGGCCAC	Forward Reverse	118
$\alpha 1_{B}$ - *Adra1b*	ACATTGGGGTGCGATACTCTC TTGGGCGCAGGTTCTTTCC	Forward Reverse	139
$\alpha 1_{d}$ - *Adra1d*	CGGACCTTCTGCGACGTATG TGGCTGGATACTTGAGCGAGT	Forward Reverse	124
$\alpha 2_{A}$ - *Adra2a*	GGTGACACTGACGCTGGTTT ACTGGTGAACACCGCGATAATA	Forward Reverse	91
$\alpha 2_{B}$ - *Adra2b*	GAGTCCAAGAAGCCCCATCC GGTGTCCATTAGCCTCTCCG	Forward Reverse	103
$\alpha 2_{c}$ - *Adra2c*	TCTGGATCGGCTACTGCAAC GCTTGAAAGAGCGCCTGAAG	Forward Reverse	81
β-actin, *Actb*	CTGGCCTCACTGTCCACCTT CGGACTCATCGTACTCCTGCTT	Forward Reverse	61
β1 - *Adrb1*	CTCATCGTGGTGGGTAACGTG ACACACAGCACATCTACCGAA	Forward Reverse	215
β2 - *Adrb2*	GGGAACGACAGCGACTTCTT GCCAGGACGATAACCGACAT	Forward Reverse	125

3.4.4.4 Qualitative mRNA expression

Tissue transgene (rAgt) mRNA expression was verified using reverse transcription PCR (RT-PCR). Several organs were collected (see section 3.3.7.1) and RNA extraction, DNAse I treatment and cDNA synthesis was performed as described in sections 3.4.4.1 and 3.4.4.2, respectively. The mouse and rat cDNA sequences were *in silico* aligned to design a primer pair amplifying both rat and mouse *Agt* cDNA (299 bp) (Table 28). To perform RT-PCR organ cDNA was diluted to a final concentration of 10 ng/µL and PCR mixes were assembled as described in section 3.4.1. The presence of mAgt or rAgt was identified running the PCR product through a 2% agarose gel (see section 3.4.2). To finally confirm transgene brain expression, PCRs from wildtype and Agt-KO-Tg containing amplified brain mRNA were purified (see section 3.4.4.5), and forwarded for sequencing (see section 3.4.12). The resulting DNA sequences were blasted to verify the presence of mAgt and rAgt in wildtypes and Agt-KO-Tg, respectively. Note: the primer pair in Table 28 was designed within the deleted region of the endogenous mAgt in Agt-

KO, meaning that the primer pair does not amplify endogenous mAgt mRNA from Agt-KO as Agt-KO-Tg tissues.

Table 28 - Primer pair use to amplify tAgt, endogenous (mouse) and transgene (rat) *Agt*.

Target	Sequence (5' to 3')	Sense	Annealing temperature (°C)	Elongation time (s)	Amplicon (bp)
Mouse and rat *Agt* exon 2	CCATTCAGGCCAAGACCTCC GCAGTCTCCCTCCTTCACAG	Forward Reverse	60	30	wildtype - 299 transgenic -299

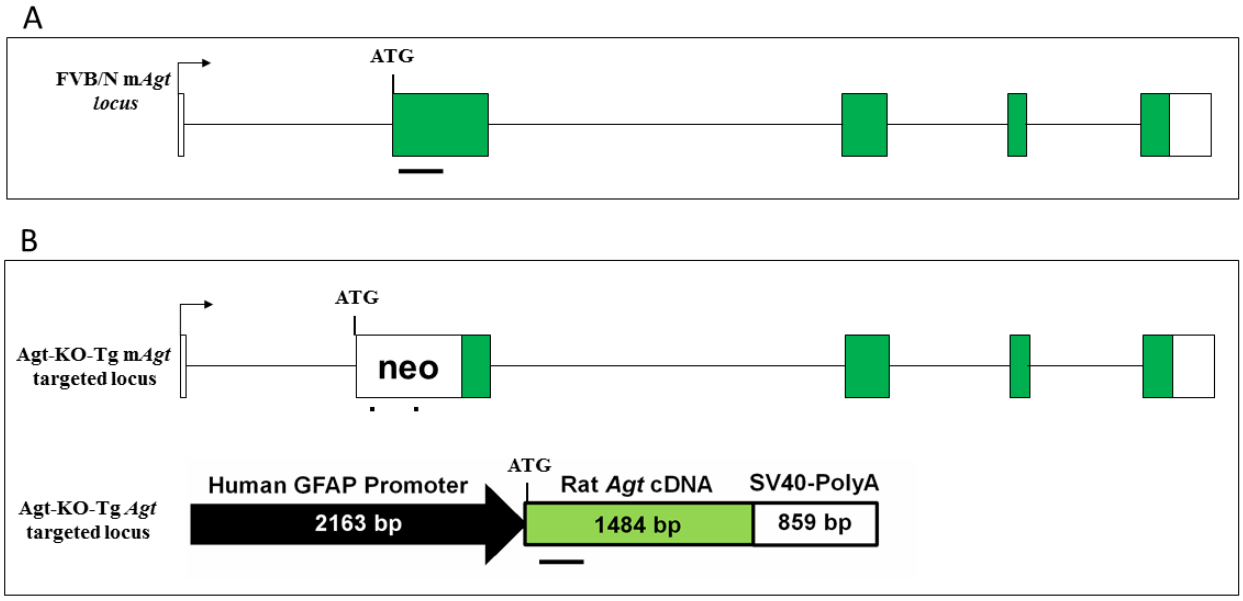

Figure 12 - RT-PCR strategy to amplify mAgt and rAgt.
Schematic representations of mouse wildtype locus encoding the mAgt (**A**), and targeted mAgt locus in Agt-KO (**B**, top panel) and the construct used to generate Agt-Tg with the rAgt cDNA (**B**, bottom panel). The thick line represents the amplification of DNA fragments from mAgt in wildtype (**A**) and exclusive rAgt in Agt-KO-Tg (**B**) when using the primer pair displayed in Table 28, because the primers represented as ". ." (**B**) is designed in the deleted region of the mAgt. Neo = neomycin resistance cassette.

3.4.4.5 qPCR for transgene copy number quantification

To quantify the transgene copy number in Agt-Tg, a qPCR was performed with genomic DNA. Sample genomic DNA concentration was measured (see section 3.4.6), and an aliquot containing 1 ng/µL prepared. qPCR was performed using the primers showed in Table 25 which do not bind to Agt-KO and following the protocol described in 3.4.4.3. However, for this experiment the CT values were used to estimate the transgene copy number instead of the $2^{-\Delta\Delta CT}$. Another qPCR with a primer pair targeting the *Adra2a* (Table 27) was performed to control genomic DNA

dilution. The transgene copy number was estimated comparing *Agt* CT values among mice with one or two copies of the endogenous mAgt and mice heterozygous for the transgene with one or two copies of the endogenous mAgt.

3.4.5 DNA fragment purification

To purify DNA fragments from PCR reactions directly or selectively by band excision from agarose gels, the Wizard® SV Gel and PCR Clean-up System (Promega) was used according to the manufacturer's instructions. For gel fragment purification, the band of interest was visualized with UV light (365 nm) using the gel imager C200 (Azure Biosystems) and excised with a scalpel.

3.4.6 Measurement of nucleic acid concentration

DNA and RNA concentration and purity were measured using a NanoDrop 1000 (Peqlab) spectrophotometer. For this 1 µL of nucleic acid was pipetted onto the lower measurement pedestal. Before each measurement a zero-reference standard (water or TE buffer) was included depending on each aqueous solution the nucleic acids were diluted.

Nucleic acid concentrations were calculated using a modified the Beer-Lambert equation $c = (A * e)/b$, where: Where **c** is the nucleic acid concentration in ng/µL, **A** is the absorbance in AU, **e** is the wavelength-dependent extinction coefficient in **ng-cm/µL r** and **b** is the path length in cm.

Below are the commonly accepted extinction coefficients for nucleic acids at 260 nm:

- Double-stranded DNA: 50 ng-cm/µL
- Single-stranded DNA: 33 ng-cm/µL
- RNA: 40 ng-cm/µL

The ratio between the absorbances 260/280 of 1.8 for DNA and 2.0 for RNA indicates purity.

3.4.7 Molecular cloning

Molecular cloning was used to generate sgRNA, targeted constructs used for zygote electroporation and pronuclear microinjections as well as PCR amplicon sequencing. The commercial vectors used in this study are displayed in section 3.1.9. Cloning strategies were delineated by identifying restriction sites at the plasmid´s provider webpage and for the insert with an online tool[5]. To introduce subcloning sticky ends on amplified DNA fragments, restriction enzyme binding sites were included at the 5' of the primers with additional 4-5 nucleotides to assure restriction.

3.4.7.1 Cloning of single guide RNA (sgRNA)

A sgRNA specifically targeting the Rat AT1a receptor (*Agtr1a*) was designed using the online tool[6]. To produce sgRNA, complementary DNA oligonucleotides containing the sgRNA corresponding sequence (20bp) plus overhanging sequences for vector insertion were synthetized (Table 29). The lyophilized oligonucleotides were diluted in nuclease-free water to a final concentration of 100 µM, and phosphorylated and annealed in a single step using T4 Polynucleotide Kinase (Table 30). The vector pX330 (pX330-U6-Chimeric_BB-CBh-hSpCas9, Addgene) was used to subclone the phosphorylated and annealed oligos, this vector contains a double *BbsI* restriction site that if opened matches with the annealed oligos (Table 29). 1 µg of pX330 was digested with *BbsI*. Annealed oligos were diluted 1:200 in nuclease-free water and ligated to the open vector (50 ng, 1 µL of the previous reaction). After ligation, circular vectors were transformed into electrocompetent bacteria, and the plasmid purified as described in section 3.4.11. From all purified vectors the correct sequence was checked by vector sequencing using the primer shown in Table 29. Because the cloned fragment is under the control of the U6 promoter this plasmid produces the CRISPR RNA (crRNA) already fused to the trans-activating CRISPR RNA (tracRNA; Cas9 scaffold) in mammalian cells. In addition, Cas9 with a nuclear signal is also expressed by the vector under the CBh promoter. In other words, pX330 with the sgRNA subcloned can be readily used for genome editing in mammalian cells including zygotes.

[5] https://sites.ualberta.ca/~stothard/javascript/index.html.
[6] http://Crispr.mit.edu/

However, studies as well as our laboratory experience indicated that zygote gene edition using CRISPR/cas9 electroporation or microinjection of the sgRNA plus Cas9 recombinant protein yield higher efficiency in comparison to vector delivery. Therefore, *in vitro* transcription was used to produce the sgRNA (crRNA + tracRNA). For this, a T7 promoter sequence was introduced by PCR using Phusion polymerase (NEB) (see section 3.4.1) and purified pX330 vector (2 ng) as template. The primers used for amplification are shown in Table 29. The purified PCR product was used for sgRNA synthesis by *in vitro* transcription using T7 RNA Polymerase (Thermo Fisher) following manufacturer's instructions. Finally, the RNA molecules were purified using the GeneJET RNA Purification Kit.

Table 29 - Oligonucleotides used for subcloning and generation of sgRNA targeting the rat *Agtr1a* locus.

Target	Sequence (5' to 3')	Sense
sgRNA subcloning	caccATCTTCAGCAGAAGAGTTAA	Reverse
	aaacTTAACTCTTCTGCTGAAGAT	Forward
pX330 sequencing primer	GGCCTATTTCCCATGATTCC	Forward
T7 promoter introduction	**TAATACGACTCACTATAG**ATCTTCAGCAGAAGAGTTAA	Forward
	AAAAGCACCGACTCGGTGCC	Reverse

Lower case letters indicate overhangs used for creating sticky ends to the annealed oligonucleotides used for subcloning into the vector pX330. Bold letters indicate an overhang that produces a T7 RNA Polymerase promoter when amplified by PCR.

Table 30 - Mixes for sgRNA annealing (left table) and subcloning (right table).

Component	Volume (µL)
10x T4 Ligation buffer	1.0
Oligo 1 (100 µM)	1.0
Oligo 2 (100 µM)	1.0
T4 PNK (Promega)	0.5
Nuclease-free water	6.5

Annealing conditions were 37°C for 30 min, 95°C for 5 min, and cool down to room temperature on the bench.

Component	Volume (µL)
pX330, open with Bbs I	1
Annealed oligos, diluted 1:250 (v/v)	2
T4 Ligase (Promega)	1
10x T4 Ligation buffer	1
Nuclease-free water	5

Ligation was performed overnight incubating the mix at 16°C.

3.4.7.2 Cloning and preparation of homologous recombination templates

Double-stranded DNA (dsDNA) HDR template preparation: Due to CRISPR/Cas9 precise genome double-strand break at predetermined sites, a construct containing ~1Kb of the up and downstream sequence flanking the expected CRISPR/Cas9 cutting position was assembled in order to flank the fusion protein ChR2-EGFP (Figure 8). To generate the construct suitable for HDR, two homology arms (arm 1 and 2) were sub cloned into the vector (pAAV-EF1a-double

floxed-hChR2(H134R)-EYFP-WPRE-HGHpA, Addgene plasmid #20298). Homology arms 1 and 2 were produced using PCR reactions performed with conventional Taq polymerase (NEB) using the primers shown in Table 31. PCR reaction mixes assemble and cycling conditions are described in section 3.4.1. For homology recombination arm preparation, rat genomic DNA was used as template (see section 3.4.3.1). After amplification verification by agarose gel (see section 3.4.2), each PCR mix was purified with the Wizard® SV Gel and PCR Clean-up System (Promega) (see section 3.4.4.5) and subcloned into the pGEM®-T Easy Vector (Promega). Subsequently, small-scale bacteria cultivation were performed, the plasmid was isolated (see sections 3.4.10 and 3.4.11) and sequenced with the primers showed in Table 31. Both homology arms were extracted from the vector using restriction enzyme digestion, homology arm 1 was extracted using EcoR I and homology arm 2 by Sal I and Kpn I, for details see section 3.2.4.2. After restriction digests, the reaction mixes were run through a 1% agarose gel, and the released fragment was observed, and the corresponding band excised and purified with the Wizard® SV Gel and PCR Clean-up System (Promega) (see section 3.4.4.5). Digested and purified homology arms 1 and 2 were subcloned into the backbone of predigested vector containing ChR2 one at a time with EcoRI and Sal I/Kpn I, respectively. Each round of subcloning was considered successful after analyzing the insert orientation using restriction enzyme digestions followed by gel visualization and *in silico* sequence analyses. After successful subcloning steps, one bacterial small-scale preparation was expanded to a large scale and the plasmid isolated as described in section 3.4.11. For use as HDR template either the circular vector or the ~4 kb linearized construct were used. The linear fragment was extracted from the vector using the restriction enzymes Spe I and Kpn I (Figure 8). Note, the sequence recognized by the sgRNA was excluded from the template, so the sgRNA does not bind to it and it remains intact during and after possible homologous recombination event.

Table 31 - Primers used to generate homologous recombination arms to match with rat *Agtr1a* locus.

Target	Sequence (5' to 3')	Sense	Annealing temperature (°C)	Elongation time (s)	Expected Amplicon (kb)
Homology arm 1	ccaagaattcactAgtTCAGACCCCATTCAGACTAAC	Forward	60	90	~1.1
	ttttggaattcTGGGTTGAGTTGGTCTCAG	Reverse			
Homology arm 2	ggccgtcgacTCTTCTGCTGAAGATGGTATC	Forward	60	90	~1.2
	ttggtggtaccTTCAAAGTCTTCTCTCAGAG	Reverse			
T- vector sequencing	TAATACGACTCACTATAGGG	Forward	-	-	-
	CTATTTAGGTGACACTATAG	Reverse			

Capital letters indicate sequences overlapping with the template sequence. Lower case letters indicate overhang and restriction enzyme sequences which are underlined. Restriction enzyme sequences are: gaattc = EcoR I, actAgt = Spe I, gtcgac = Sal I, ggtacc = Kpn I. HDR = homology directed repair.

Single-stranded DNA (ssDNA) HDR template preparation: Several studies observed increased HDR success using ssDNA template comparing against templates consisting of double-stranded DNA (127–129). Therefore, the size of the HDR arms 1 and 2 were decreased from ~1.0 kb to ~0.5 Kb. To generate the ssDNA template, Guide-it™ Long ssDNA Strandase Kit (Takara) was used following manufacturer's instructions. Briefly, a double-stranded DNA template was generated by PCR using a high-fidelity polymerase included in the kit and a customized primer pair where the sense primer is phosphorylated at the 5´ end (Table 29). The phosphate group serves as a recognition site for the strandase that digests the phosphorylated strand thereby producing ssDNA that is cleaned and concentrated to (0.5 - 1 µg/µL) with a column purification system included in the kit.

Table 32 - Primers used to generate a ssDNA template for HDR to match with rat *Agtr1a* locus.

Target	Sequence (5' to 3')	Sense	Annealing temperature (°C)	Elongation time (s)	Expected Amplicon (kb)
ssDNA template	**P**-GTGACACCAGTTCGTGGAAC ATCAGCCAGATGATGATGCAG	Forward Reverse	60	30	~3.0

The elongation time of the Phusion polymerase used is 1 Kb/5 sec. ssDNA = single-stranded DNA. **P** = phosphate group to phosphorylate the primer at the 5´ for strandase digestion of the amplicon.

3.4.8 DNA restriction

Vector and inserts as genomic DNA were digested by restriction enzymes. To integrate DNA fragments into circular vectors, the insert generation as well as the vector opening were performed with the same restriction enzyme(s). Restriction enzymes and their corresponding buffers (New England Biolabs) were used following the instructions of the supplier. The reactions were typically performed at 37°C and 1 U of enzyme used to completely digest 1 µg of

DNA between 15-60 min. To prevent vector recircularization in case the vector was opened with a single restriction enzyme, after restriction digestion the reaction was incubated with calf intestinal alkaline phosphatase (2 U/µg DNA; CIP) for 5 min at 37 °C. CIP keeps the vector open by dephosphorylation of the 5' ends.

3.4.9 DNA ligation

The ligation of a double-stranded DNA insert into a linearized vector was performed adding ~50-100 ng of vector DNA, 2-5 times molar excess of DNA insert[7], 1 µL 10x ligation buffer, 1 µL (1-3 U) T4 DNA ligase (Promega) and nuclease-free water to a final volume of 10 µL. The reaction mix was incubated over night at 16 °C and stored at -20 °C if not immediately used.

3.4.10 Transformation and cultivation of bacteria

One aliquot of electrocompetent bacteria (30 µL) was thawed on ice, 2-5 µL of ligation reaction or 50 ng of purified plasmid DNA were mixed with the bacteria. The mixture was transferred to an ice-prechilled GenePulse® cuvette, which was rapidly placed into the sample chamber of the electroporator 2510 (Eppendorf). Electroporation of bacteria was performed at 1350 V for 5 ms. Immediately, 1 mL of LB media without antibiotics was added and the electroporated bacteria transferred to new tube that was incubated at 37 °C for 1 hour to allow vector expression. To select successfully transformed bacteria, a glass cell spreader was used to spread 50 µL of the LB medium contain bacteria on ampicillin -containing LB-Agar plates that were cultivated over night at 37 °C. For initial bacterial grow, positive colonies were picked with 200 µL sterile tips and expanded in a 15 mL falcon tube containing 5 mL of LB medium (mini-prep) with ampicillin over night at 37 °C on a shaker at 180 rpm. After mini-prep, plasmids were extracted as described below section 3.4.11, and the correct DNA fragment integration was verified either by sequencing (see section 3.4.12) and/or by plasmid restriction (see section 3.4.8) followed by observation of expected fragment size by running the digested plasmid on an agarose gel (see section 3.4.2). After finding the correct fragment insertion, 100 µL of the bacteria from the

[7] https://nebiocalculator.neb.com/#!/ligation

previous step was further grown in a plastic Erlenmeyer flask filled with 250 mL of LB medium (maxi-prep) containing antibiotic over night at 37 °C on a shaker at 180 rpm.

Table 33 - Buffer solution and media used for bacteria cultivation.

Buffer, solution or media	Component
Ampicillin	100 mg/mL Ampicillin
LB Medium, pH 7.0	0.5% (w/v) Bacto™ Yeast extract 1.0% (w/v) Bacto™ Tryptone 1.0% (w/v) NaCl
LB plates	LB medium 1.5% (w/v) Bacto™ Agar 100 µg/mL Ampicillin

LB Medium with ampicillin was prepared mixing ampicillin with LB media to a final concentration of 100 µg/mL Ampicillin.

3.4.11 Bacteria plasmid extraction and purification

To extract plasmids from the initial bacterial culture (Mini-prep), 4 mL of the bacterial overnight culture was centrifuged for 5 min at 6.000 *g* and the supernatant removed. The pellet containing the bacterial cells was resuspended in 250 µL of Solution A (Table 34) by vortexing. 250 µL of Solution B (Table 34) was added, mixed gently by inversion and incubated 5 min at room temperature to lyse the bacterial cells. Next, 250 µL of Solution C (Table 34) was pipetted for sample neutralization. After solution C addition a white clot containing DNA, protein and SDS was observed, the samples were then incubated on ice for 20-30 min and centrifuged for 10 min at 13.000 *g*. The supernatant was transferred to a new 1.5 mL tube, and 500 µL isopropanol was added, mixed by inversion, and incubated for 10 min at room temperature to precipitate the plasmid DNA. Samples were centrifuged for 15 min at 13.000 *g*, the supernatant discarded, and the pellet washed by adding 500 µL of 70% ethanol that centrifuged for 15 min at 13.000 *g*. After removing the ethanol, the pellet was air-dried and resuspended in nuclease-free water.

To isolate plasmid DNA from large scale bacterial growth (maxi-prep), the PureYield™ plasmid maxiprep system (Promega) was used following manufacturer's instructions. In principle, an alkaline and SDS containing buffer lyses the bacteria and centrifugation removes genomic DNA, proteins and cell debris, while the plasmid DNA in the supernatant can be bound to a silica column. After column washing to remove endotoxin and remaining cellular contaminants, plasmid DNA was eluted in nuclease-free water and stored at -20 °C until use.

Table 34 - Solutions used for plasmid extraction of initial bacterial growth.

Solution	Components
Solution A	50 mM Glucose 10 mM EDTA, pH 8.0 25 mM Tris, pH 8 1% (v/v) RNase (4 mg/mL)
Solution B	200 mM NaOH 1% (w/v) SDS
Solution C	3.1 M Potassium acetate pH 5.5

3.4.12 Sequencing of DNA

DNA sequencing was controlled with specific primers binding the sequence flanking the region of interest, using the chain termination method of Sanger and Coulson (130). All sequencing was performed by LGC Genomics GmbH (Berlin, Germany). Sequencing results were analyzed with the free software SnapGene Viewer.

3.4.13 Single nucleotide polymorphism (SNP) genotyping

F2 Agt-KO mice were genotyped using the mouse universal genotyping array (MUGA) by submitting the samples to Neogen (Scotland, UK). The Giga-MUGA genotyping array contains 143,259 genetic markers covering most of the inbred mouse strains including FVB/N and C57BL/6. At the end of the cardiovascular phenotyping, livers were collected from all F2 Agt-KO mice for DNA extraction. Liver genomic DNA was extracted using a commercial kit based on a column purification system, GenElute™ (Sigma-Aldrich). Briefly, ~25 mg of liver was collected and digested with proteinase K following manufacturer's instruction. After column purification, 20 µL of DNA (~100 ng/µL) was air-dried overnight, placing open tubes containing the samples on a thermo-block at 50°C, and shipped at room temperature to Neogen.

3.4.13.1 SNP validation by restriction digest

After performing the GWAS, a restriction digest of all F2 Agt-KO mice phenotyped was used to validate the most significant locus at chromosome 1. SNP rs31768697 produces a HincII restriction site only in FVB/N. The restriction digest of the PCR product flanking this SNP allows to identify the carriers of the mono and/or biallelic strain-specific (FVB/N and/or C57BL/6)

locus. The primer sequences and the restrict digestion of the PCR product are shown in Table 35, PCR mix and restriction digestion are described in sections a 3.4.1 and 3.4.8, respectively.

Table 35 - Primers used to amplify the SNP rs31768697.

Target	Sequence (5' to 3')	Sense	Annealing temperature (°C)	Elongation time (s)	Amplicon (bp)	HincII digestion (bp)
rs31768697	GTGGGTCACCATATTTGTACCG ACTTTACACCTTCAGTTCTGG	Forward Reverse	60	30	250	C57BL/6 - 250 FVB/N - 110/140

3.4.14 Agt-Tg transgene integration mapping by vectorette PCR

To determine the precise integration site of the transgene in the mouse genome, a vectorette PCR approach was used. First, the construct sequence was mapped *in silico*[8] to find restriction sites close to the construct´s (used to generate Agt-Tg) 5´ and 3´ extremities (Figure 13B). We have designed different strategies, for different restriction enzymes but only Bfa I rendered positive results, therefore, this approach is described below (Figure 13). Genomic DNA was extracted as described in section 3.4.3.1 from an Agt-Tg mouse. Non-digested tissue and cellular debris were removed by a tube spin-down at 13.000 *g* for 1 min, and the supernatant was transferred to a clean tube. The DNA concentration was estimated as described in section 3.4.6. Then 1 µg of genomic DNA was digested with Bfa I restriction enzyme as described in section 3.4.8 in a final volume of 30 µL, and the enzyme was inactivated by heat at 80°C for 20 min. A vectorette adapter with a 3´ AT overhang (to stick to the digested genomic DNA form Agt-Tg) was created annealing the primers depicted in Table 36 without phosphorylation with T4 Polynucleotide Kinase to avoid adaptor self-ligation during the ligation step (Figure 13A and Table 37). The adapter was ligated to the genomic DNA using T4 DNA Ligase (Promega) (Figure 13C and Table 38). The construct containing an unknown genome piece was amplified using nested PCR with primer pairs designed to bind the construct and the adapter (Figure 13D). First, amplification was performed as described (Table 39) using a conventional Taq polymerase (NEB). Second, a nested PCR was assembled with 1 µL from the previous reaction. The amplicon was visualized in a 2% agarose gel as described in section 3.4.2. The amplicon was subcloned into the backbone of the T-vector (promega) and amplified as described in 3.4.7 and 3.4.10, respectively. Finally, the

[8] https://www.bioinformatics.org/sms2/

plasmid was purified and submitted to Sanger sequencing for posterior *in silico* analyses to determine the transgene integration site.

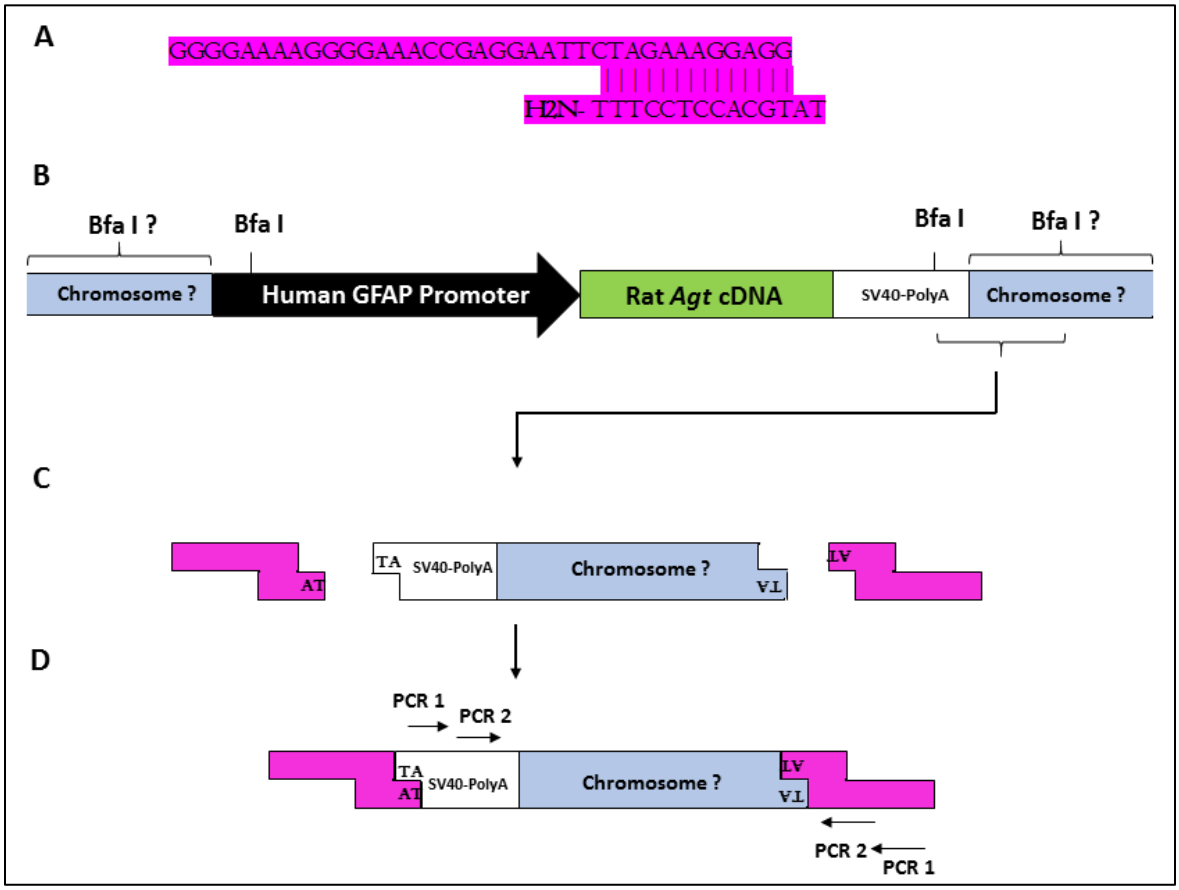

Figure 13 - Schematic representation of the vectorette PCR strategy used for transgene integration mapping.
Representation of the annealed adapter containing an amine group preventing the extension by Taq polymerase of the lower strand 3´ end to prevent circularization "suppression PCR" (**A**). Representation of the construct used to generate Agt-Tg integrated in the genomic DNA with mapped restriction sites for Bfa I at the 5´and 3´ ends as well as putative region on the flanking unknown chromosomal sequence (**B**). Closer look at the SV40-polyA region digested with Bfa I containing a downstream unknown DNA fragment. In pink are representative adaptor molecules containing AT overhangs matching with the genomic DNA fragments digested with Bfa I (**C**). Adaptor molecules ligated to the fragment of interest. The adjacent DNA sequence is amplified by nested PCR and sequenced to uncover the transgene integration site (**D**). The arrow lines indicate the forward and reverse primers.

Table 36 - Primers used for adapter generation and unknown flanking sequence by nested PCR.

Primer pair	Sequence (5' to 3')	Sense
Adapter	GGGGAAAAGGGGAAACCGAGGAATTCTAGAAAGGAGG	Forward
	TATGCACCTCCTTT-H2N	Reverse
PCR 1	GGGGAAAAGGGGAAACCGAGG	Forward/Reverse
	GTGGTTTGTCCAAACTCATCAATG	Reverse/Forward
PCR 2	CCGAGGAATTCTAGAAAGGAGG	Forward/Reverse
	CTCATCAATGTATCTTATCATGTCTGGATC	Reverse/Forward

Underlined primer pair sequences are designed to bind to the vectorette and non-underlined to the SV40-PolyA. The primers from PCR 1 and 2 sense depends if the transgene is integrated in sense or reverse orientation.

Table 37 - Mix components and conditions for annealing the adapter for vectorette PCR.

Component	Volume (µL)
Oligo 1 (100 µM)	1.0
Oligo 2 (100 µM)	0.5
10x T4 Ligation Buffer (Promega)	1.0
Nuclease-free water	To 10.0

Annealing conditions were 37°C for 30 min, 95°C for 5 min, and cool down to room temperature on the bench.

Table 38 - Ligation mix to ligate the adaptor to digested genomic DNA.

Component	Volume (µL)
Annealed oligos from Table 37	2.0
10x T4 Ligation buffer (Promega)	1.0
T4 DNA Ligase (Promega)	1.0
Digested genomic DNA (200 ng)	6.0

Ligation was performed overnight incubating the mix at 16°C.

Table 39 - PCR reaction mix and cycling program for nested PCR, PCR 1.

Stock concentration	Component	Volume (µL)
10x	ThermoPol® Buffer (NEB)	2.5
5 mM	dNTPs	1.0
10 µM	Primer 1	0.5
10 µM	Primer 2	0.5
-	Nuclease-free water	18.750
5 U/µL	Taq DNA Polymerase	0.250
-	Ligation reaction (Table 38)	1
	Final volume	25

PCR step	Time (s)	Temperature (°C)	Cycles
Initial denaturation	180	95	1
Denaturation	30	95	7
Annealing	30	60	
Elongation	300	68	
Initial denaturation	180	95	1
Denaturation	30	95	40
Annealing	30	60	
Elongation	120	68	
Final elongation	600	68	1
Hold	∞	4	-

All PCRs were performed with cycler lid at 105 °C.

Table 40 - PCR reaction mix and cycling program for nested PCR, PCR 2.

Stock concentration	Component	Volume (µL)
10x	ThermoPol® Buffer (NEB)	2.5
5 mM	dNTPs	1.0
10 µM	Primer 1	0.5
10 µM	Primer 2	0.5
-	Nuclease-free water	18.750
5 U/µL	Taq DNA Polymerase	0.250
-	Ligation reaction (Table 38)	1
	Final volume	25

PCR step	Time (s)	Temperature (°C)	Cycles
Initial denaturation	180	95	1
Denaturation	30	95	40
Annealing	30	60	
Elongation	120	68	
Final elongation	600	68	1
Hold	∞	4	-

All PCRs were performed with cycler lid at 105 °C.

After finding the integration site of the transgene, few conventional PCRs were performed to validate the sequence of the integration site. The primer sequences are shown in Table 41, and

the PCR mixes were assembled with a conventional Taq polymerase (NEB) for detailed information see section 3.4.1.

Table 41 - Primer pair sequences used to validate the transgene integration site in Agt-Tg.

Name as in Figure 14	Target	Sequence (5' to 3')	Sense	Annealing Temp (°C)	Elongation time (s)	Band length (bp)
PCR 1	3´ Tg junction (Chr 5/Sv-40)	GGCACCTTGGTGTTCCTATC	Forward	60	30	wildtype - none
		GTGGTTTGTCCAAACTCATCAATG	Reverse			Agt-Tg - ~350
PCR 1.1	3´ Tg junction (Chr 5/rAgt)	GGCACCTTGGTGTTCCTATC	Forward	60	45	wildtype - none
		TGCACTTTCTGGGCAGAGTG	Reverse			Agt-Tg - ~700
PCR 2	hGFAP 5´end region in Agt-Tg	CACATGTCCAAATGCAGAGC	Forward	58	30	wildtype - none
		TGTAGAGATAGGGTCTTGCC	Reverse			Agt-Tg - 148
PCR 3	5´ Tg junction (Chr 5/hGFAP)	GGCACCTTGGTGTTCCTATC	Forward	60	30	wildtype - none
		GAACATTGTGTCTGTGCCAA	Reverse			Agt-Tg ~ 700
PCR 4	3´ Tg junction (Sv-40/Chr 5)	GTGGTTTGTCCAAACTCATCAATG	Forward	60	30	wildtype - none
		TCACCCACTTTCCCAGCTTC	Reverse			Agt-Tg - ~100
PCR 4.1	3´ Tg junction (Sv-40/Chr 5)	GTGGTTTGTCCAAACTCATCAATG	Forward	60	60	wildtype - none
		GTGGTTTGTCCAAACTCATCAATG	Reverse			Agt-Tg - up to ~1Kb
PCR 4.2	3´ Tg junction (Sv-40/Chr 5)	GTGGTTTGTCCAAACTCATCAATG	Forward	60	90	wildtype - none
		CAAACTGTCGCCCAGCTTATTG	Reverse			Agt-Tg - up to ~2.5Kb

Tg = Transgene. For better overview refer to Figure 14 at section 4.1.2.

3.4.15 Agt-Tg transgene integration mapping by nanopore sequencing

In addition to the vectorette PCR, the transgene integration site was determined by nanopore sequencing. This experiment was performed in collaboration with Dr. Veniamin Fishman at the Institute of Cytology and Genetics of the Novosibirsk State University. High molecular weight genomic DNA was extracted from freshly collected EDTA-whole blood (see section 3.3.7) from an Agt-Tg mouse with the kit Wizard® HMW DNA extraction kit (Promega). This kit allows to extract DNA fragments up to 500 kb which is ideal for long-reading sequencing such as the nanopore sequencing. Following manufacturer's instructions, the last two steps are: 1) wash the

DNA pellet with 70% ethanol; 2) resuspend the DNA pellet in solution. The last step (DNA resuspension) was omitted, and instead the DNA pellet was air-dried for 1 hour and shipped.

3.5 Hematology methods

3.5.1 Capillary hematocrit

Freshly collected blood into a lithium-heparin tube (see section 3.3.7) was transferred to a hematocrit glass capillary (Hirschmann). One of the tube's extremities was closed with a dedicated sealing clay (Brand). The tubes were centrifuged at 13.000 rpm for 10 min in a hematocrit centrifuge (Hettich), and the percentage of red blood cells (RBC) was deduced from total volume measured with a digital caliper (Wabeco).

3.5.2 Mouse clinical hematology

Whole blood collected into EDTA-coated tubes (see section 3.3.7) was kept at room temperature to preserve cell morphology, and blood cell analyses were carried out with an automated hematology analyzer (IDEXX #ProCyte DX) within 4 hours after sampling at the animal phenotyping facility of the Max Delbrück Center for Molecular Medicine (Berlin).

3.5.3 Rat clinical hematology

10 week old rats were sacrificed by isoflurane overdose, and blood was collected from a cardiac puncture into EDTA-coated tubes immediately after death. Blood cell composition was quantified shortly after sampling using an automated veterinary hematology analyzer (scil Vet abc, SCIL Animal Care).

3.6 Histology methods

3.6.1 Paraffin sections preparation

Brains and kidneys were fixed in 4% PFA for at least 1 week. The organs were dehydrated using a spin tissue processor Microm STP 120 (Thermo Fisher). Accordingly, brains and kidneys were rinsed twice in PBS and subjected to an ascending ethanol dehydration (twice in 70%, twice in 80%, twice in 96%), additionally incubated twice in isopropanol and twice in xylol, each

incubation lasted 1 hour. Brains and kidneys were embedded in paraffin, a pre-infiltration step with paraffin for 1 hour at 67˚C and final infiltration step repeating the previous in fresh paraffin. 5 µm brain and kidney sections were cut using an automatic microtome HM 355S (Thermo Fisher), and collected on microscopy adhesion slides. The slides were air-dried overnight and before usage in the staining protocols were deparaffinized and rehydrated in xylol and descending ethanol concentrations following sequence: thrice in xylol, thrice in 100% ethanol, once in 90% ethanol, once in 80% ethanol, once in 70% ethanol, once in 60% ethanol, once in 50% ethanol, once in 40% ethanol, once in 30% ethanol and twice in ddH_2O, each for 5 min.

3.6.2 *In situ* hybridization using RNAScope technology

To visualize the transgene (rAgt), *in situ* hybridization (ISH) using RNAScope technology was used with a specific probe designed by Advanced Cell Diagnostics (Rn-Agt-O1 #553841, Lot #20205A). The designed target-specific ISH double-Z probes (ZZ-ISH) with its specific signal amplification technology, binding exclusively to paired Z probes, allows visualization of single RNA molecules. This assay consists of mainly 4 steps: first, tissue sections are permeabilized; second, 20 ZZ-ISH probes bind to RNA molecules; third: preamplifier oligonucleotide molecules linked to several amplifiers containing multiple color molecules bind to ZZ-ISH probes; fourth, single molecules of RNA are visualized with light or fluorescence microscopy. After rehydrated as described in section 3.6.1, brain sections were mounted on super frost glass slides, and air dried for 10 min. Section were incubated with 3% H_2O_2 for 10 min at RT to block endogenous peroxidase, and H_2O_2 was removed washing the sections with ultrapure water. Sections were then heated at 100–104 °C in antigen retrieval buffer (RNAscope Target Retrieval, Ref. #322001, Advanced Cell Diagnostics (ACD)) in a steamer for 15 min, washed in distilled water followed by a wash with 100% EtOH, and air dried for 10 min. The sections were then incubated with pre-warmed ISH target probe pairs at 40°C in the hybridization oven for 2 h. After incubation, sections were washed with RNAScope washing buffer. The signal was amplified using the pre-amplifier and amplifier conjugated to alkaline phosphatase and incubated with a Fast-Red substrate solution for 10 min RT, according to the instructions of the manufacturer. Excess of dye was removed by washing the sections in ultrapure water. Before microscopy visualization, brain

sections were either counterstained with hematoxylin for nuclei visualization or dually stained with immunofluorescence for GFAP, as described in section 3.6.3.

3.6.3 Immunofluorescence combined with RNAScope

Brain sections submitted to the RNAScope ISH protocol (section 3.6.2) or 5 µm rehydrated brain sections (section 3.6.1) were incubated in PBS for 1 hour at room temperature. Antigens and epitopes were unmasked by boiling the sections in sodium citrate buffer (Table 42). Sections were washed twice with PBS for 5 min and then blocked by incubation with 10% normal donkey serum diluted in PBS for 1 hour at RT. Brain sections were incubated overnight at 4°C in a wet chamber with a primary antibody (anti GFAP) diluted in PBS (Table 4). On the next day, sections were washed 3x for 5 min each with PBS, incubated with a suitable secondary antibody diluted in PBS for 2 hours at room temperature in a dark room. Finally, sections were washed 3x for 5 min each with PBS, and were mounted with Vectashield mounting medium containing nuclei staining 4, 6-diamidino-2-phenylindole (DAPI) and covered with a cover slip.

Table 42 - Buffer used for immunofluorescence.

Buffer	Components
sodium citrate buffer, pH 6.0	10 mM Sodium citrate 0.05% (v/v) Tween-20
Phosphate-buffered saline (PBS), pH 7.4	See Table 15

3.6.4 Immunofluorescence in cryosections

Sample preparation: Mice were sacrificed and the whole brains were carefully removed and fixed in buffered 4% paraformaldehyde solution (Otto Fischar) for 24 hours at 4 °C. Then, brains were transferred to 30% (w/v) sucrose solution and incubated at 4°C until the brain sunk to the bottom of the tube (~ 3 days). Brains were then frozen in isopentane on dry ice and stored at -20 °C until cryosectioning. 50 µm brain coronal cryosections were prepared using a cryostat (Thermo Scientific) fixing brain samples at the platform with Tissue-Tek (Sakura). The sections were washed at room temperature twice with 1x PBS to remove excess of Tissue-Tek.

Immunostaining: Free-floating sections were permeabilized by incubation in PBS containing 0.1% (v/v) Triton-X 100 for 1 hour and blocked by incubation in 10% (v/v) normal donkey diluted in PBS for 1 hour at room temperature. Brain sections were then incubated for at least 20 hours at 4°C with a primary antibody (anti AVP) diluted in PBS (Table 4). Subsequently,

sections were washed 3x with PBS to remove excess of primary antibody and incubated with a secondary antibody conjugated to a fluorophore (anti-rabbit-Cy3, Table 4) for 2 hours at room temperature. Sections were then washed 3x with PBS and mounted on SuperFrost® Plus slides, air dried for 30 minutes and coverslipped with Vectashield mounting medium containing nuclei staining DAPI. Images were taken next day using Keyence light/fluoresecence Microscope (BZ 9000, Germany).

3.6.5 Haematoxylin-Eosin staining

Kidney Haematoxylin-Eosin (HE) staining was performed to have a general morphological overview of the organ in the different mouse strains. Deparaffinized and rehydrated sections were initially incubated 10 min in tap water. To stain the cellular nuclei, the slides were incubated in haematoxylin for 5 min and washed 3x with tap water, 10 min each. To remove haematoxylin excess and nuclear differentiation, the slides were incubated in hydrochloric acid solution (0.11% HCl, 67.2% ethanol) for 3 sec, and rinsed in tap water. Cellular cytoplasm was stained incubating the slides in an eosin solution (eosin Y, 0.5 % (w/v) in acidified 90% ethanol) for 3 min. Sections were dehydrated in increasing alcohol concentration (80%, 90%, 100% ethanol,) 1 min each, and xylene for 3 min twice. Finally, the slides were mounted with Eukitt mounting medium and covered with a cover slip. Slides were allowed to air-dry for at least 24 hours before the observation and pictures were obtained with an inverted microscope BZ-9000 (Keyence).

3.6.6 Picro sirius red staining

Renal fibrosis was visualized using the picro sirius red staining technique. Deparaffinized and rehydrated sections were washed with tap water for 10 min. After, the sections were incubated in Picro Sirius Red solution (0.1% Sirius red F3B in saturated aqueous solution of picric acid) for 1 hour at room temperature. Finishing the incubation, the slides were washed twice with acidified tap water (0.5% glacial acetic acid), dehydrated (3x 100% ethanol), cleared with xylene, and coverslipped using Eukitt mounting medium (ORSAtec GmbH, Bobingen, Germany). Slides were allowed to air-dry for at least 24 hours before the observation and pictures were obtained with an inverted microscope BZ-9000 (Keyence, Osaka, Japan).

3.7 Biochemistry methods

3.7.1 Plasma and urine clinical chemistry

Several plasmatic and urinary biomarkers were measured using an automated chemistry analyzer AU480 (Beckman Coulter, Brea, USA) by trained personnel at the animal phenotyping facility of the Max Delbrück Center for Molecular Medicine. Electrolyte measurements were performed with ion selective electrodes and other parameters with colorimetric reactions that are photometrically measured. The following parameters were measured in urine (sodium, potassium, albumin and creatinine) and plasma (sodium, potassium, chloride, albumin, total proteins, urea, creatinine, glucose). Blood urea nitrogen (BUN) was calculated using the formula BUN = (Urea*0.467). Plasma osmolality was calculated with the formula Osmolality = {[2(Na)+(GLC)]/[18+(BUN)/2.8]}. Note: Plasma electrolytes were measured from blood collected in a tube containing lithium-heparin MiniCollect®.

3.7.2 NE quantification

Urine samples were readily used in the ELISA, while kidneys were homogenized with a benchtop homogenizer (MP Biomedicals, Germany) and FastPrep™ lysing matrix tubes containing 4-5 ceramic matrix beads (diameter 2.8 mm) (MP Biomedicals). Kidneys and mesenteric arteries were homogenized 1:40 and 1:100 (w/v), respectively in tissue NE homogenization buffer (Table 43). The homogenization in acid solution prevents NE oxidation during homogenization. Homogenates were then centrifuged at 10.000 × g for 10 min at 4 °C and the supernatant collected into a new tube and used for NE measurements. NE levels were measured using an enzyme-linked immunosorbent assays (ELISA) kit (Labor Diagnostika Nord, Nordhorn, Germany) following manufacturer's instructions. Briefly, first, NE is extracted using a 48-well plate containing a cis-diol-specific affinity gel, acylated, and enzymatically metabolized. Second, a competitive immune assay is performed transferring the extracted NE to a 96-well plate containing antigen bound to its solid phase. Third, an antiserum is added to the plate and washed out. Finally, the amount of remaining antisera bound to the plate is quantified at 450 nm using an antibody anti-rabbit IgG-peroxidase conjugate. Sample NE concentrations were deduced from a 6 points (0 - 1000 pg/mL) standard curve prepared with supplied standards. Urinary NE concentration was normalized to the urinary creatinine levels, while tissue NE to the tissue

weight obtained before the homogenization with a precision balance. To avoid any inter-assay variance, all samples contained in a graphic were run on a single 96 well ELISA plate.

Table 43 - Buffer used to homogenize tissues for NE quantification.

Buffer	Components
Tissue NE homogenization buffer	1 mM EDTA 4 mM Sodium disulfite 0.01 N Hydrochloric acid (HCl)

3.7.3 Urinary Nitrate and Nitrites (NOx)

To estimate overall nitric oxide (NO) production, the byproducts of NO metabolism (nitrate and nitrites) were quantified in timed urine samples using a commercial nitrate/nitrite colorimetric assay kit (Cayman). First, urine samples were diluted 1:40 (v/v) in ultrapure water. Second, nitrate was enzymatically converted to nitrite using nitrate reductase. Third, NOx (nitrite) levels were calorimetrically measured adding the Griess reagent that leads to the formation of a purple azo compound that was measured at 540 nm. Urinary sample NOx concentration was calculated using a nitrite standard curve supplied with the kit.

3.7.4 Protein extraction

Frozen organs were weighed using a precision scale and homogenized in RIPA buffer (100 mg/mL, cell signaling) supplemented with protease and phosphatase cocktail inhibitors. Samples were homogenized 2-4 times (depending on the organ) in FastPrep™ tubes containing 4-5 ceramic matrix beads (diameter 2.8 mm, MP Biomedical) for 40 s at speed level 4 using a Benchtop homogenizer, FastPrep-24 (MP Biomedical). After homogenization samples were frozen and thawed 3 times to break intracellular membranes, and incubated on a wheel shaker for 30 min at 4 °C. Next, cellular debris were separated by centrifugation at 13.000 *g* for 10 min at 4 °C. The supernatant was transferred into a clean 1.5 mL tube and stored at -20 °C until usage. Plasma protein extracts were prepared diluting EDTA-plasma in ultrapure water (1:10, v/v).

3.7.5 Protein concentration determination

Sample total protein concentration was determined using the bicinchoninic acid assay with a commercial kit (Sigma). In this method, proteins reduce Cu^{2++} to Cu^{+}, which reacts with

bicinchoninic acid, forming a purple-colored complex with shade intensity proportional to the protein amount. For the protein quantification assay, protein extracts were diluted either 1:10 or 1:20 in ultrapure water. The assay was prepared mixing 5 µL of sample and 100 µL of working solution (4% copper sulfate and bicinchoninic acid, 1:50) freshly prepared in a 96-well plate. After mixing the protein extract with the reagent, the plate was incubated for 30 min at 37 °C and the absorbance read with a microplate reader at 562 nm. All samples were pipetted in duplicates, and each measurement (plate) contained a 5 points standard curve prepared with BSA (0.1 - 1.0 µg/µL). In addition, a zero (blank) measurement was performed mixing the sample preparation buffer with the working solution as above, the resulting absorbance measurement was subtracted from standard all curve points and samples. Protein levels were calculated using the line equation generated by plotting the linear standard curve values.

3.7.6 SDS-polyacrylamide gel electrophoresis (SDS-PAGE)

Sodium dodecyl sulphate (SDS) polyacrylamide gel electrophoresis was used to separate tissue extracted proteins by their molecular weight. Proteins extracts from section 3.7.4 were mixed with 4x concentrated reducing buffer based on the Laemmli formulation (Carl Roth). Proteins were denatured by boiling the mixture at 95 °C for 5 min. This buffer contains SDS and β-mercaptoethanol which denature the proteins resulting in linear polypeptides with the same charge to molecular mass ratio. SDS is a negatively charged detergent that uniformly binds to proteins resulting in linear sequence meaning that secondary, tertiary and quaternary structures are lost, and β-mercaptoethanol irreversible destroys disulfide bridges.

Gels were casted using a 1 mm mini-PROTEAN® Tetra Handcast Systems (Bio-Rad), casting 4,5 cm of 10 or 15 % acrylamide/bisacrylamide gel (Table 44). Immediately after pouring the gel, 1 mL of water was added on top to develop a straighten line. After polymerization water was carefully removed with a Whatman paper stripe, and 2.5 cm of 5% acrylamide/bisacrylamide stacking gel was added (Table 44). A comb containing either 10 or 15 wells was added to the gel, and after gel polymerization gels were wrapped in wet (tap water) towel paper and stored at 4 °C until use but not longer than a month. 20-50 µg of denatured proteins were loaded on a gel and the gels run using the electrophoresis buffer (Table 45) in a gel electrophoresis chamber (Bio-Rad). Electrophoresis was performed first at fixed voltage 60 mV until the proteins migrated from the stacking into the separating gel, and 120 mV until the dye front migrated out of the gel.

One of the wells was loaded with 5 µL molecular weight marker Precision plus protein™ standards all blue (Bio-Rad).

Table 44 - Composition of the SDS polyacrylamide gels.

Component	10% Separation gel	15% Separation gel	5% stacking gel
Ultrapure water	7.9 mL	6.54 mL	5.5mL
1.5 M Tris-HCl pH 8.8	5.0 mL	5.0 mL	-
1 M Tris pH 6.8	-	-	1.0mL
SDS 10%	200 µL	200 µL	80 µL
30% Acrylamide/bisacrylamide (37.5:1, Carl Roth)	6.8 mL	8.16 mL	1.3 mL
10% (w/v) APS	100 µL	100 µL	50 µL
TEMED	20 µL	20 µL	20 µL

The volume shown is used to cast four 1mm gels.

Table 45 - Composition of the electrophoresis buffer.

Buffer	Component
10x Electrophoresis buffer, pH 8.3	192 mM Glycine 25 mM Tris 0.1% (w/v) SDS

3.7.7 Western blotting

Proteins separated by electrophoresis were transferred from the SDS-PAGE gel onto a nitrocellulose membrane. The stacking gel was removed, and the separating gel was placed in a "sandwich". For this, Whatman paper and the membrane were shortly rinsed in transfer buffer (Table 46), and mounted as 3x Whatman paper, membrane, gel and 3x Whatman paper. Protein transfer was performed using a semi-dry transblot turbo (Bio-Rad) at 25V, 1.0A for 30 min. Membranes were stained reversibly with Ponceau solution for 3-5 min (Table 46), the membrane was rinsed in tap water to remove Ponceau excess. Transfer quality and equal protein loading control were visually controlled observing the Ponceau staining pattern. To remove the Ponceau staining, the membrane was incubated in PBS-T for 20 min (Table 46) under constant rolling.

Subsequently, membranes were blocked with a PBS based blocking solution (LI-COR) for 1 hour at room temperature. After blocking, membranes were incubated with the primary antibody which was diluted as shown in Table 4. 5 mL of primary antibody was incubated with the membrane overnight at 4 °C under constant rolling. On the next day, the primary antibody

was removed and the membrane was washed twice with 10 mL of PBS-T for 10 min. After washing, membranes were incubated with an appropriate fluorescent conjugated secondary antibody (Table 5) for 2 hours at room temperature. Membranes were washed twice with 10 mL of PBS for 10 min. Finally, the membrane was scanned using an Odyssey infrared imaging system (LI-COR). The signals were visualized and/or analyzed using the Image Studio Lite Software (LI-COR). For protein quantification, brain and kidney protein levels were normalized to glyceraldehyde-3-phosphate dehydrogenase (GAPDH) following the protocol above using the same membrane. Plasma Agt levels were normalized to a total protein stain of the membrane with a commercial kit (LI-COR) after protein transfer and before membrane blocking.

Table 46 - Composition of the transfer buffer.

Buffer	Component
10x Transfer buffer, pH 8.3	192 mM Glycine 25 mM Tris 20% (v/v) Methanol
Ponceau staining solution	0.5 % (w/v) Ponceau-S 1 % (v/v) Acetic acid
PBS-T	0.05 % (v/v) Tween-20 in 1x PBS from Table 15

3.7.8 Angiotensin peptides quantification

Tissue angiotensin peptides levels were measured in plasma and brain using liquid chromatography–tandem mass spectrometry (LC-MS/MS) by the company Attoquant Diagnostics (Vienna, Austria), except for one experiment in section 4.3.1.3 where plasma Ang II levels were measured using a radioimmunoassay as described by Schelling *et al.* (131). This experiment was performed before the start of this PhD thesis.

Sample collection: A cardiac puncture was used to collect ~800 µL of blood with a 23 G needle coupled to a 1 mL syringe containing 40 µL of a blood collection cocktail (specific inhibitors for Ren and aminopeptidases, EDTA, pepstatin A, p-hydroxymercuribenzoic acid and phenanthroline) provided by the company. Blood was centrifuged at 3000 *g* for 10 min at 4 °C , and plasma was transferred to a new tube, and snap frozen in dry-ice. Whole brains were rapidly removed from the skull, briefly washed in ice-cold PBS to remove blood excess and snap frozen in liquid nitrogen. Finally, the samples (brains and plasma) were shipped in dry-ice to Attoquant diagnostics (Vienna, Austria) for the LC-MS/MS Ang peptides quantification.

Sample processing and quantifications: These steps were performed at Attoquant Diagnostics (Vienna, Austria) as previously described (78, 132). Briefly, whole brains were pulverized in liquid nitrogen, and immediately dissolved in solution (ice-cold 6M guanidine hydrochloride supplemented with 1 % (v/v) trifluoroacetic acid). Brain homogenates and plasma were spiked with known concentrations of stable isotope-labeled internal standards peptides for Ang I, Ang II, Ang III, Ang 1-7 and Ang 1-12 previous to C18-based solid-phase extraction and LC-MS/MS.

3.8 Computer biology methods

3.8.1 Genome-wide association study (GWAS)

Experimental measurements: The acute baseline MAP of 67 F2 Agt-KO (males and females) was established as described in section 3.3.3. In addition, the MAP phenotype was correlated to the wet heart weight measured to confirm the phenotype (see section 3.3.8). In case the heart weight was not in the expected range for the animal measured MAP, the sample in question was excluded from the analyses.

Genome-wide association study (GWAS). The resulting SNP mapping sequences of 67 samples generated by Neogen (Scotland, UK) as described in section 3.4.13 were analyzed in collaboration with Dr. Zouhair Aherrahrou and Syed M. I. Haider from the Institute for Cardiogenetics at the university of Lübeck. Briefly, out of 143.259 markers from the GIGA-MUGA, 33.069 autosomal polymorphic markers "SNPs" among C57BL/6 and FVB/N were identified and used for the analyses. The data analysis was performed with PLINK 1.9 or 2.0 using two logistic regression models a general additive model and a dominant model. In the dominant model hypotensive mice were treated as controls (as C57BL/6) and normotensives as cases (as FVB/N).

3.9 Statistical analyses

Statistical analysis and graphs were performed using the GraphPad Prism software. Data are displayed as mean ± SD or mean ± SEM. Data Gaussian distribution was tested using D'Agostino & Pearson omnibus normality test as well as Shapiro-Wilk, and Kolmogorov-Smirnov-test (depending on the sample size). Data was analyzed by two-sided unpaired or paired Student's *t*

tests to compare means differences among two groups. For comparison of more than 2 groups one-way analysis of variance (ANOVA) with post-hoc test of Tukey was applied. To calculate the effect of two variables of interest 2-way ANOVA followed by Tukey's post hoc test was used. To access treatment effect overtime among different experimental groups, 2-way repeated-measures ANOVA followed by Tukey´s or Dunnett´s multiple comparison post hoc test was applied. Differences between two groups with a P value < 0.05 were considered statistically significant; the symbols representing the degree of significance are included in each figure legend.

4 Results

4.1 Basic characterization of Agt-Tg "FVB/N-*Tg*(hGFAP-*rAgt*)24*Bdr*"

Agt-Tg was already generated before the start of my PhD project. The major goal was to increase brain RAS activity by increasing the expression of the RAS precursor protein Agt. To achieve high levels of brain Agt, this transgenic mouse line overexpresses the rAgt gene under the control of the hGFAP promoter. Thus, Agt is overexpressed in astrocytes which is the main cell type naturally producing Agt in the brain (61, 71, 133). The model was thoroughly validated to assure that any cardiovascular phenotype developed is due to central RAS activity instead of off-target Agt expression. The most relevant tests for transgenic model validation typically include cellular specificity and quantification of transgene expression, especially for secreted proteins such as Agt with receptors binding to Agt-derived peptides located virtually in all cardiovascular organs with potential to modulate cardiovascular homeostasis.

4.1.1 Generation and establishment of Agt-Tg

Following the pronuclear microinjection procedure, all putative line founders were genotyped. The genotyping PCR indicated the presence of one positive founder; this transgenic mouse was bred with wildtype FVB/N. The genotyping of the F1 generation confirmed transgene germline transmission and the Agt-Tg line was established. In addition, the males and females from the F1 offspring were crossed with FVB/N wildtypes, and both generated litters containing transgenic and wildtype mice. In subsequent breeding rounds, heterozygous transgenics were intercrossed to induce transgene homozygosity in the F2. The expected mendelian ratio for the offspring´s genotype is ~75% transgene (25% Tg/Tg, and 50% Tg/wt) and ~25% wildtype (wt/wt), however, the genotype of 103 offspring yielded ~50% transgenic and ~50% wildtype (Table 47). In addition, a PCR mix with 3 primers at the transgene integration site was used to search for mice with biallelic copies of the transgene. However, the PCR indicated that all transgenic mice (59) contained monoallelic transgene copies. In addition, stillborn and post-natal mortality was apparently not different among the heterozygous Agt-Tg and wildtype genotypes. Collectively the genotyping of Agt-Tg in the breeding schemes mentioned above revealed 3 main features of

this line: First, males and females are fertile; second, the transgene is not integrated in one of the allosomes; third: a failure to induce homozygosity. One possible explanation is that the construct integration may have disrupted a key genomic region which is essential during development and therefore homozygous transgenic mice are not viable. However, heterozygous Agt-Tg mice developed normally (see Table 48 in section 4.2), and do not display any gross morphological alteration. Therefore, we decided to further validate the model and perform the cardiovascular phenotyping in this transgenic line.

Table 47 - Stratified genotyping of 103 offspring from confirmed heterozygous Agt-Tg parents.

Sex	Agt-Tg genotype	Observed	Expected
All	Positive, Tg/wt or Tg/Tg	59	77.25
	Negative, wt/wt	44	25.75
	χ^2	$P = 0.0001$	
Males	Positive, Tg/wt or Tg/Tg	28	34.5
	Negative, wt/wt	18	11.5
	χ^2	$P = 0.0269$	
Females	Positive, Tg/wt or Tg/Tg	31	42.75
	Negative, wt/wt	26	14.25
	χ^2	$P = 0.0001$	

4.1.2 Transgene integration site mapping and copy number

Random foreign DNA integration in the genome may reveal unprecedent gene functions (134). Since homozygosity of the transgene in Agt-Tg mice was not compatible with life, mapping the exact transgene integration site became an attractive experiment to be performed. For this, a vectorette PCR strategy was used, and complemented with nanopore sequencing. After digesting Agt-Tg genomic DNA with Bfa I and ligating with a corresponding adaptor, we could point out that the transgene integrated at the mouse chromosome 5 in the region shown in Figure 14A. Because the sequencing analyses showed chromosome 5 sequence in forward orientation and SV40-PolyA in reverse, we assumed the transgene integrated in reverse orientation as represented in Figure 14A. This was confirmed using conventional PCR used to amplify the transgene 3´ SV40-PolyA junction with the fragment sequenced from the transgenic animal (PCR 1, Figure 14A,C). In parallel, a long read from the nanopore sequencing confirmed the integration site at chromosome 5, and additionally revealed that a part (~350 bp) of the 5´ end of the original hGFAP promoter was lost and there was a fragment of SV40-PolyA integrated upstream in reverse orientation (Figure 14B). To confirm that a part of the hGFAP promoter sequence was lost, we attempted to amplify with conventional PCR the putative deleted region in Agt-Tg but

failed, confirming the nanopore sequencing finding (PCR 2, Figure 14A,C). The transgene orientation suggested by the nanopore sequencing was validated (PCR 1.1, Figure 14A,C) and (PCR 3, Figure 14B,C). Agt-Tg showed positive amplification only in PCR 3 (Figure 14C) suggesting that the transgene integrated in sense orientation regarding the reference sequence (Figure 14B). We attempted to map the transgene 3´end integration site using primers in reverse orientation, 74bp, ~1Kb and 2.5Kb downstream of the integrations site at its 5´end (Figure 14B, PCR 4, 4.1 and 4.2). However, none of the PCRs yielded visual amplicons, suggesting a deletion larger than 2.5Kb during transgene integration. The final mapping of the transgene including its location and orientation is shown in Figure 14B. Figure 14D shows that the transgene integrated in an intergenic region where regulatory elements of downstream genes or genes marked in green might be deleted. However, the precise 3´ integration site remains to be determined.

Often transgenic rodents contain multiple copies of the transgene because it usually integrates in tandem (135). This could potentially lead to chromosomal recombination events explaining the SV40 polyA sequence at the 5´ junctions of the integrated construct. However, downstream copies of the insert would likely still have the full promoter sequence and because PCR 2 at Figure 14B did not show amplification most likely a single copy of the transgene integrated. To confirm this hypothesis, genomic DNA was used to quantify the transgene copy number by qPCR. The most convenient design to perform this experiment would be comparing the Ct values between confirmed homozygous and heterozygous Agt-Tg. Because homozygous animals were not possible to generate, a similar strategy was designed including the endogenous mAgt allele. For this, mice carrying two endogenous wildtype alleles (2 mAgt copies) or with one targeted deleted copy (1 mAgt) were used as controls, and in addition mice harboring the transgene with either 1 or 2 mAgt copies were included (Figure 15A). Genomic DNA loading was verified with by *Adra2a* Ct values (Figure 15B). The comparison of ΔCts among the different mouse genotypes strongly indicates that Agt-Tg harbors a single copy of the transgene (Figure 15A).

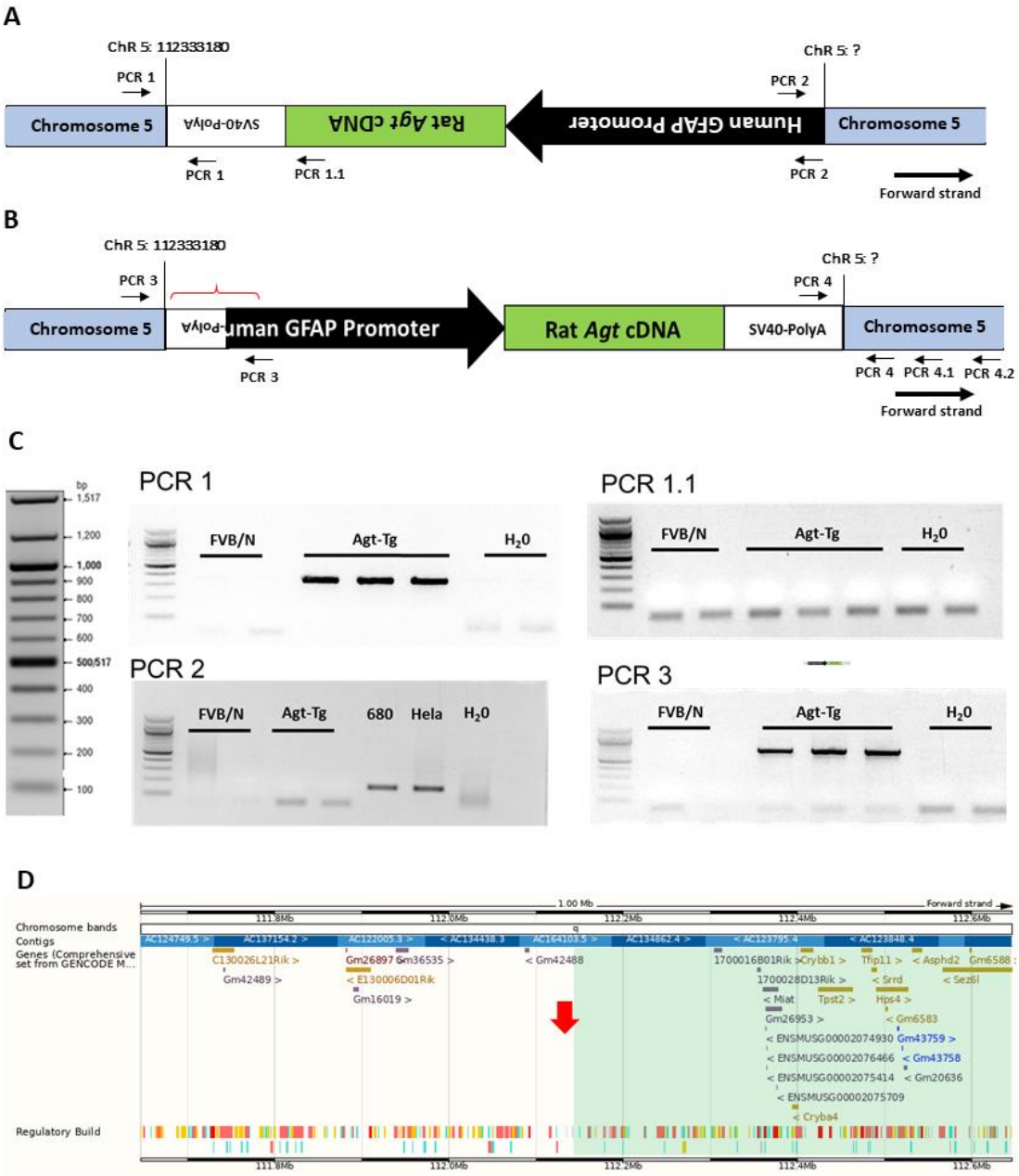

Figure 14 - Schematic representation of the mapped transgene integration.
Using vectorette PCR, a transgene SV-40 poly A junction was found at the chromosome 5, and PCR 1 was used for confirmation. Because the SV-40 was found in reverse orientation and chromosome 5 sequence in forward the transgene was assumed to be integrated in reverse orientation (**A**). Using nanopore sequencing, it turned out that part of the hGFAP promoter was lost and a piece of SV-40 polyA integrated upstream of the promoter in reverse orientation but hGFAP in forward orientation (see red bracket). This unexpected phenomenon was validated by PCRs 1.1 and 3 (**B**). Agarose gel electrophoresis products of the PCRs 1, 1.1, 2 and 3 (**C**). Intergenic transgene integration at chromosome 5 with neighboring genes. The red arrow represents the integration site of the transgene, and marked in green the possibly deleted chromosomal segment during transgene integration (**D**). PCR 4, 4.1 and 4.2 were performed to verify the 3´end integration of the transgenic with a reverse primer at the positions ~100, 1000 and 2500bp downstream of the 5´-transgene integration site at Chr 5, respectively. However, none of these PCRs yielded visual amplifications. Chromosomal coordinates are based on GRCm39 for the mouse reference strain (C57BL/6). The arrow lines indicate the forward and reverse primers. Chr 5 = chromosome 5. **D** was generated online[9].

[9] https://www.ensembl.org/

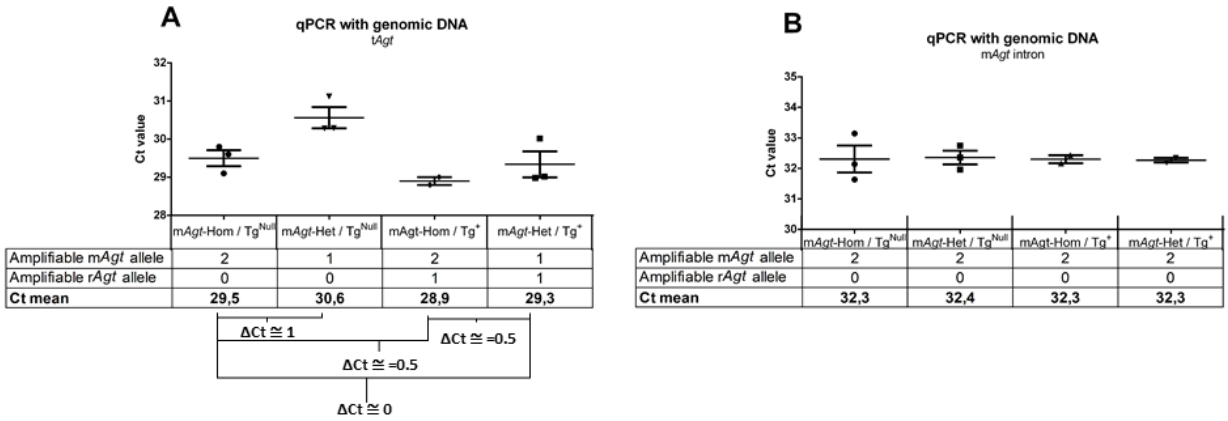

Figure 15 - Quantification of the transgene copy number in Agt-Tg.
Ct values obtained by qPCR using genomic DNA of mice positive or not for the transgene and containing 1 or 2 copies of the wildtype mAgt allele (**A**). Control qPCR for genomic DNA loading (**B**). Note in **A** the ΔCt difference between mAgt-Hom / Tg^{null} x mAgt-Het / Tg^{null} of 1 Ct is expected (≅ 1 Ct per copy) validating the strategy. ΔCt difference between mAgt-Hom / Tg^{null} x mAgt-Hom / Tg^{+} of 0.5 Ct indicate a single transgene copy (mAgt-Hom / Tg^{+}, 2 mAgt + *1* rAgt). In addition, the fact there is no ΔCt difference between mAgt-Hom / Tg^{null} and mAgt-Het / Tg^{+} confirms the finding (mAgt-Het / Tg^{+}, 1mAgt + *1* r*Agt*). Finally, the ΔCt difference of 0.5 between mAgt-Hom / Tg^{+} x mAgt-Het / Tg^{+} confirms the transgene single copy integration in Agt-Tg. mAgt-Hom = 2 wildtype copies of the mAgt allele, mAgt-Het = 1 wildtype and 1 gene targeted copy of the mAgt allele, Tg^{null} = 0 allele for the transgene, 1 Tg^{+} = 1 allele positive for the transgene (rAgt).

4.1.3 Validation of the brain specificity of transgene expression

To validate the brain specificity of the transgene expression in Agt-Tg, qualitative RT-PCR with the same primer pair used for the transgene copy number identification[10] was used in organs of Agt-KO-Tg and wildtype. In the wildtype mice, *Agt* expression was observed in expected tissues as liver and brain. However, in Agt-KO-Tg line, only brain expression was observed confirming brain-specificity of transgene expression not only in Agt-KO-Tg but also in Agt-Tg (Figure 16A). Additionally, PCR products from wildtype and Agt-KO-Tg brains samples were sequenced, and the resulting DNA alignment of the sequences matched the mouse and rat *Agt* cDNAs in wildtype and Agt-KO-Tg, respectively. Because Agt is a secreted protein, the presence of Agt protein in plasma was investigated in Agt-KO-Tg and Agt-Tg using western blot. Figure 16B shows a lack of the expected ~53 kDa Agt band in Agt-KO validating the specificity of the antibody. Wildtype, Agt-Tg and rat plasma displayed the characteristic Agt band as expected but Agt-KO-

[10] The primer pair recognizes both mAgt and rAgt cDNA, but it is designed at the deleted region of Agt-KO. Therefore any PCR product in Agt-KO-Tg must be transgene-derived "rAgt"`

Tg lacks plasma Agt immunoreactivity indicating a lack of peripheral Agt production as wells as a lack of brain Agt spillover into the circulation.

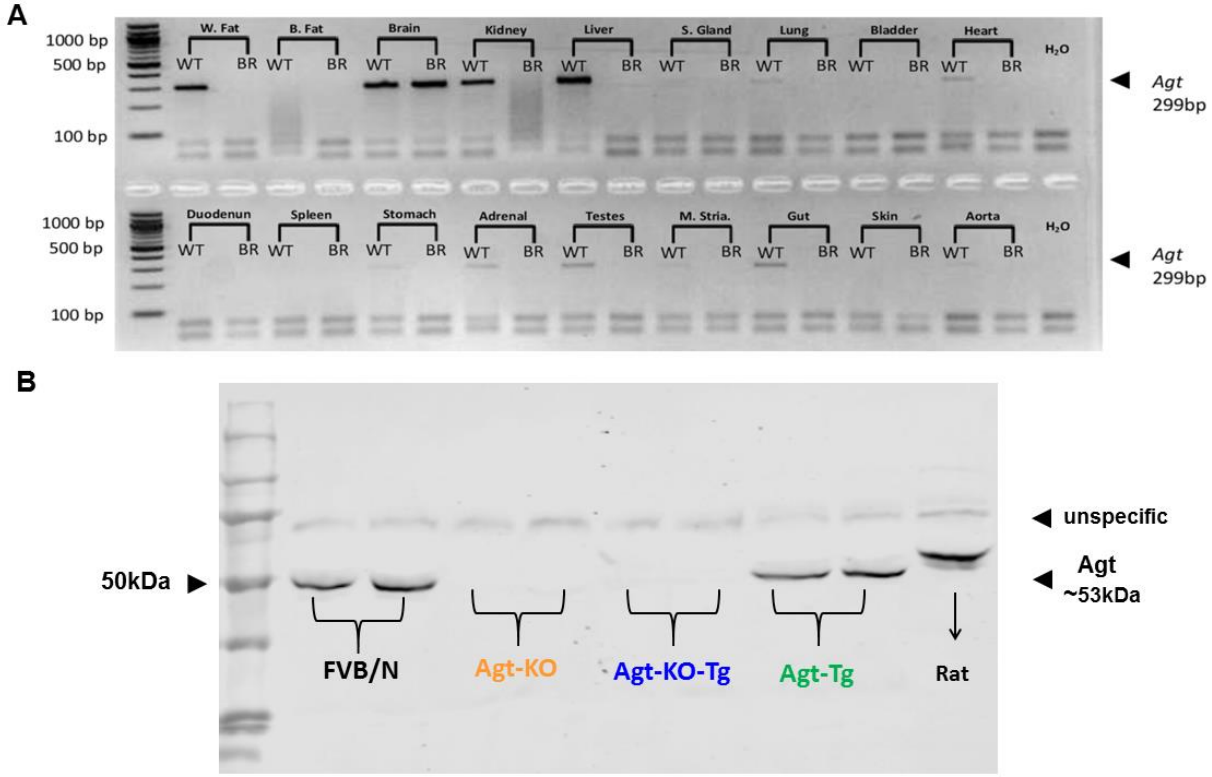

Figure 16 - Brain specific Agt expression in transgenic animals.
Brain-specific transgenic rAgt expression in BR = brain-rescue = Agt-KO-Tg, and organ specific expression of the endogenous mAgt in WT = wildtype (**A**). Agt protein was detected by western blot in FVB/N (wildtype), Agt-Tg and rat plasma. Agt was not detected in Agt-KO and Agt-KO-Tg. An unspecific band was detected in all samples therefore used as loading control. Each lane was loaded with 40 µg of plasma extract (**B**). W=white; B=Brown; S= salivary and M= muscle, H_20 = negative control.

4.1.4 Brain transgene distribution

To localize transgene expression in the brain, ISH with the RNAScope method was used. The transgene was found to be wide-spread expressed in the brain of Agt-Tg mice (Figure 17), including, the hypothalamic and brainstem regions where cardiovascular homeostasis controlling nuclei are located as the paraventricular nucleus of the hypothalamus (PVN) (Figure 17). Because of the highly conserved mouse and rat Agt mRNA sequences, the probe designed to target the transgene (rAgt) also binds to mAgt (Figure 17). Therefore, quantification of total Agt (tAgt, endogenous + transgene [mAgt + rAgt]) and mAgt were performed using RT-qPCR with specific primers to quantify brain *Agt* mRNA see section 4.1.5.

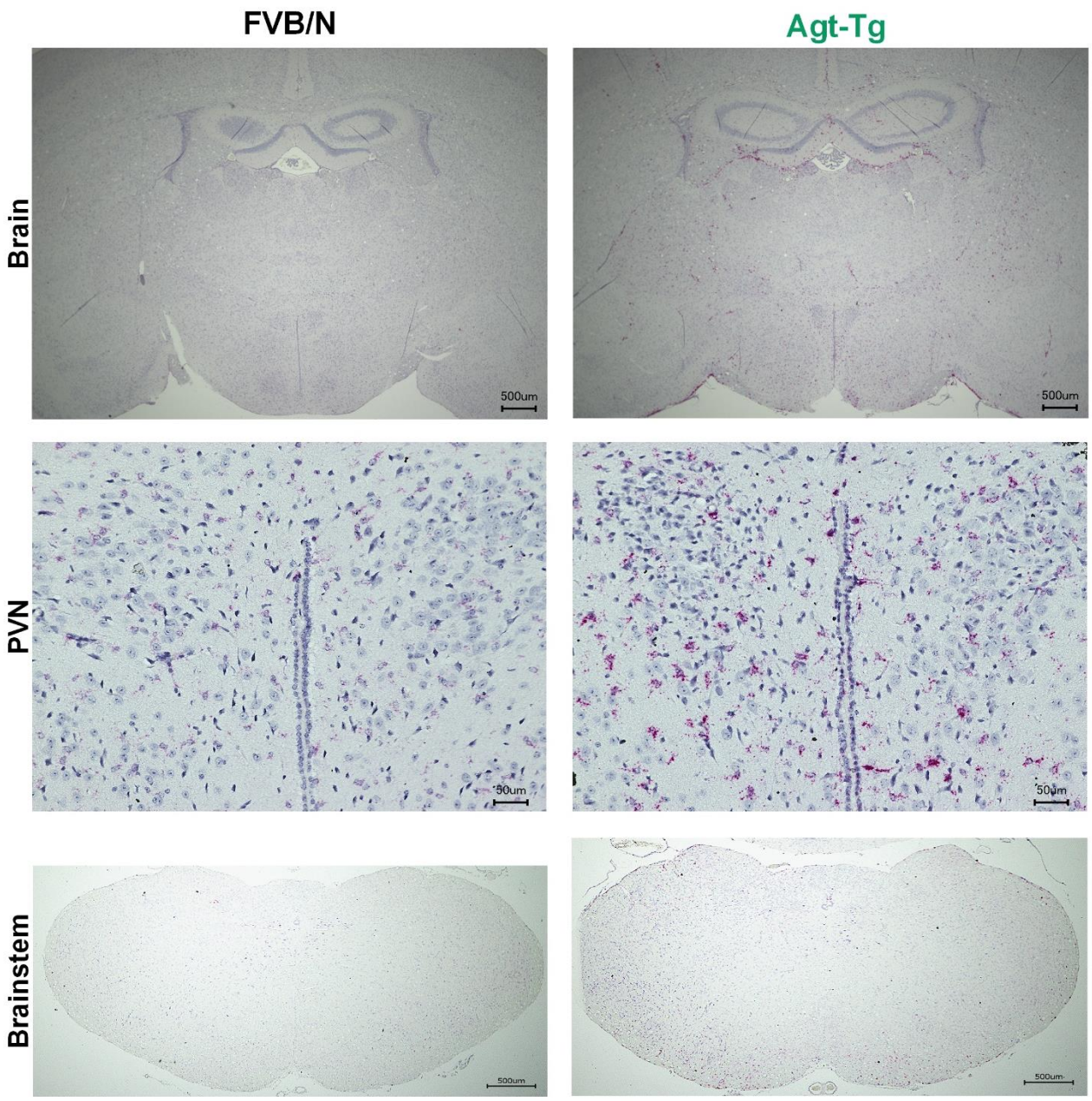

Figure 17 - Brain transgene expression visualization.
Chromogenic visualization of transgene expression using RNAScope (red dots) in wildtype and Agt-Tg brain sections, nuclei were counterstained with hematoxylin (blue dots). Scale bar = 500 μm (magnification ×2); scale bar = 50 μm (magnification ×20). paraventricular nucleus of the hypothalamus (PVN).

In order to validate if the transgene is expressed by astrocytes, we combined RNAScope for rAgt with immunofluorescence staining with an antibody against mouse GFAP. Figure 18 shows abundant transgene expression in GFAP positive cells, demonstrating successful astrocyte-specific transgene expression.

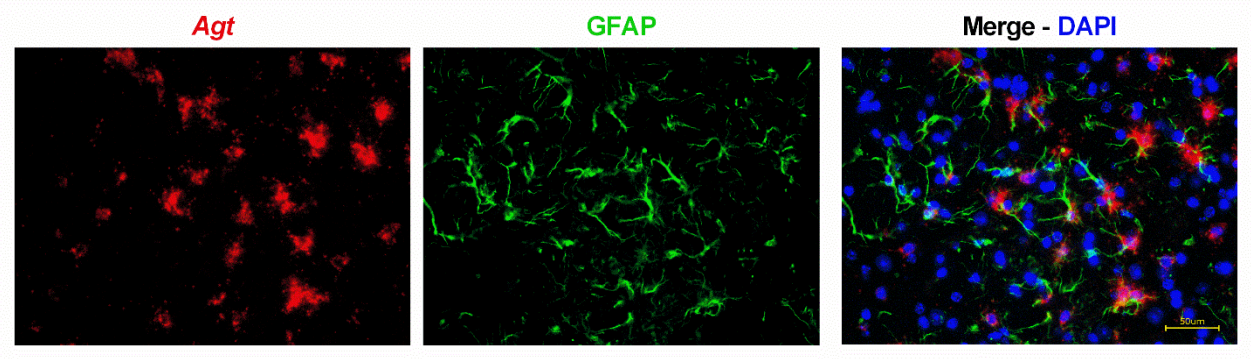

Figure 18 - Brain transgene mRNA localization in GFAP positive cells.
ISH using RNAScope against rAgt (red) combined with immunostaining against GFAP protein (green) in Agt-Tg brain, nuclei were counterstained with DAPI (blue). Scale bar = 50 μm.

4.1.5 Quantification of transgene expression in the brain

To quantify the brain transgene expression in transgenic mice, RT-qPCR was used to measure tAgt mRNA levels. Initially, tAgt mRNA was quantified in whole brains of Agt-KO-Tg and Agt-Tg. Figure 19A shows increased levels of tAgt in Agt-KO-Tg and Agt-Tg. Next, tAgt expression levels were quantified by RT-qPCR in key brain regions for cardiovascular control. tAgt mRNA was found increased in Agt-Tg hypothalamus (Figure 19B), and Agt-KO-Tg and Agt-Tg brainstem (Figure 19C). mAgt expression was analyzed in the same samples with the same method. Figure 19D-F shows that wildtype and Agt-Tg have comparable levels of mAgt mRNA in the whole brain as well as in the cardiovascular areas, indicating a non-suppressive effect of the transgene overexpression on the endogenous mAgt gene. Interestingly, AT1a-KO mice presented a small increase in mAgt only in the brainstem (Figure 19F). Additionally, Agt protein levels were found increased in Agt-Tg whole brains by western blot quantification confirming an overall increased brain RAS precursor protein Agt in Agt-Tg central nervous system (Figure 19G).

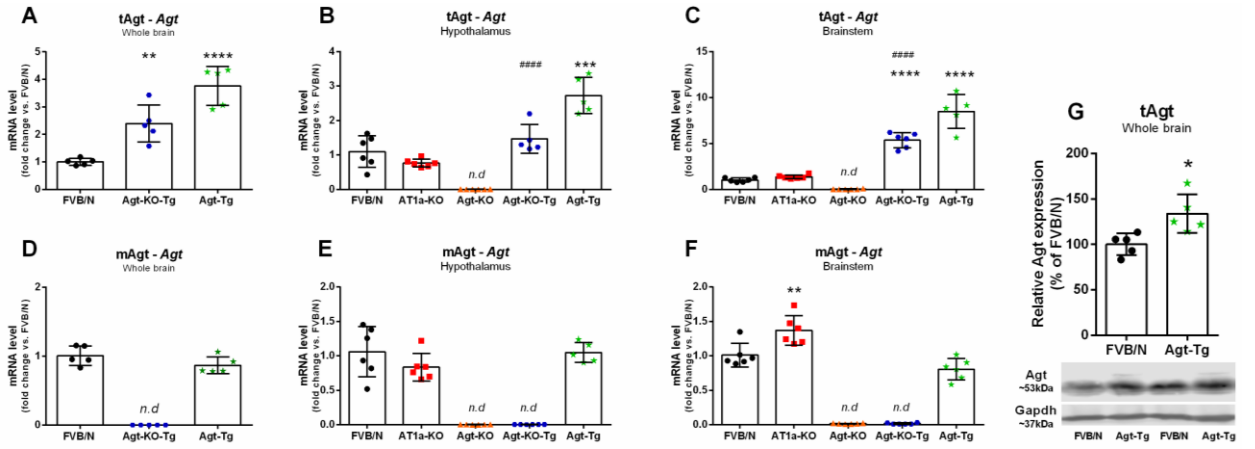

Figure 19 - Brain Agt expression.
Total (rat and mouse) Agt (tAgt) mRNA expression in whole brain (**A**), hypothalamus (**B**) and brainstem (**C**). Mouse Agt (mAgt) mRNA expression in whole brain (**D**), hypothalamus (**E**) and brainstem (**F**). Increased tAgt protein levels in brains of Agt-Tg (**G**). For (**A**-**F**) values are mean ± SD; $^{**}P<0.01$, $^{***}P<0.001$; $^{****}P<0.0001$ vs FVB/N; $^{\#\#\#\#}P<0.0001$ vs Agt-KO; (ANOVA followed Tukey multiple comparison post hoc test). For (**G**) values are mean ± SD $^{*}P<0.05$, vs FVB/N (Student's *t* test).

In addition to Agt mRNA GFAP mRNA levels were quantified in brain relevant areas for cardiovascular control mainly for two reasons. First, Agt-KO was previously described to produce lower GFAP protein in experimental cold induced astrogliosis (136). Second, to test if increased Agt expression could induce astrogliosis itself therefore further increasing its expression because transgene expression is controlled by the hGFAP promoter. Agt-KO presented reduced GFAP expression in the hypothalamus (Figure 20A) and brainstem (Figure 20B) but the rAgt astrocyte-specific expression did not recover the phenotype in Agt-KO-Tg, and Agt-Tg presented unaltered brain levels of GFAP mRNA. Finally, the levels of rAgt mRNA were measured to compare the transgene expression among Agt-KO-Tg and Agt-Tg. Despite of displaying slightly reduced GFAP mRNA, Agt-KO-Tg presented similar levels of brain rAgt mRNA in comparison to Agt-Tg (Figure 20C,D).

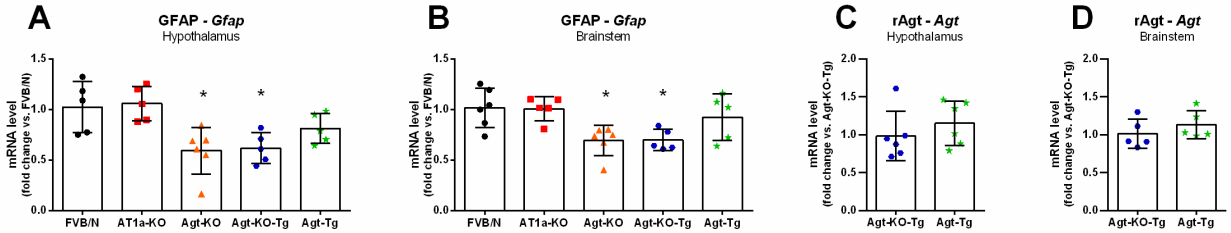

Figure 20 - Brain expression of GFAP and transgene "rAgt".
Decreased GFAP mRNA levels in hypothalamus (**A**) and brainstem (**B**) of Agt-KO and Agt-KO-Tg. Comparable rAgt gene expression among Agt-KO-Tg and Agt-Tg in the hypothalamus (**C**) and brainstem (**D**). Values are mean ± SD $^{*}P<0.05$ vs FVB/N; (ANOVA followed by Tukey multiple comparison post hoc test).

4.2 Morphometry

Baseline body weight was obtained from the most used mouse strains at the age of 13-14 weeks which comprises the age used for the cardiovascular phenotyping. Interestingly, AT1a-KO presented elevated body weight (Table 48). In addition, tibia length measurements revealed that AT1a-KO has longer tibia, indicating this line likely presents increased body size. When the body weight was normalized to the tibia length, no difference in body weight was observed except for a trend in AT1a-KO (Table 48). The wet weight of the adrenal grands, kidneys, lungs, and spleen were indistinguishable among all lines, except for the spleen in Agt-Tg that was heavier in comparison to controls (Table 48). The heart weight / tibia length ratio was also measured, since this parameter strongly correlated with the BP, the data is found in section 4.3.2, Figure 27.

Table 48 - Body and wet organ weight at age of 13-14 weeks.

Parameter (unit)	FVB/N, *n*=7	AT1a-KO, *n*=7	Agt-KO, *n*=7	Agt-KO-Tg, *n=6*	Agt-Tg, *n=8*
Body weight (g)	29.6 ± 1.7	32.8 ± 2.1*	29. 4 ± 0.9	28.9 ± 1.7	31.6 ± 2.0
Tibia length (mm)	17.4 ± 0.3	18.0 ± 0.1*	17.6 ± 0.3	17.6 ± 0.2	17.7 ± 0.3
Body weight/tibia length (g/mm)	1.69 ± 0.10	1.82 ± 0.12	1.67 ± 0.04	1.64 ± 0.08	1.78 ± 0.10
Kidney weight/tibia length (mg/mm)	12.7 ± 0.51	13.6 ± 1.75	12.09 ± 1.00	11.09 ± 0.75	12.93 ± 1.12
Adrenal weight/tibia length (mg/mm)	0.34 ± 0.12	0.18 ± 0.06	0.32 ± 0.13	0.36 ± 0.15	0.37 ± 0.10
Spleen weight/tibia length (mg/mm)	7.28 ± 0.48	7.00 ± 0.94	7.90 ± 0.77	7.59 ± 0.78	8.48 ± 0.65*
Lung weight/tibia length (mg/mm)	9.19 ± 1.02	10.05 ± 0.58	8.42 ± 0.66	8.86 ± 0.85	9.62 ± 0.96

Kidney weight = left kidney. Adrenal gland weight = both adrenals polled. Values are mean ± SD. *P<0.05vs FVB/N; (ANOVA followed by Tukey multiple comparison test).

4.3 Brain Ang II and cardiovascular modulation

4.3.1 Evidence of local brain Ang II formation

Modulatory effects of brain Ang II on cardiovascular control are largely acknowledged, however, local brain Ang II formation lacks robust evidence. A major caveat in the field is the very low levels of central Ren and the truncated Ren protein expressed in the brain accumulates in the cytosol with no access to secreted Agt (77, 137). Furthermore, attempts to measure Ang II in rodent brain often yield very low or undetectable Ang II levels. Another confounding factor is the peripheral Ang II that can bind to its receptors at the brain vasculature and circumventricular organs, which could possibly account for the detected brain Ang II (76). Because a synthesis pathway for brain Ang II formation is not yet defined, we sought to use our newly generated transgenic model with brain-specific increased Agt production to verify if the brain Ang II formation increases. In addition, we took advantage of the transgene expression to be restricted to

the brain and used the brain rescued line (Agt-KO-Tg) lacking peripheral Agt (see Figure 16B) to avoid contamination by the circulating Ang II.

Plasma LC-MS/MS Ang peptide measurements detected Ang I, Ang II and Ang III in wildtype, and as expected none of these peptides were detected in Agt-KO (negative control). Also Agt-KO-Tg had no detectable levels of all peptides measured in plasma (Table 49). The brain ability to produce Ang II *in vivo* was tested by measuring Ang peptides in whole brain samples. Table 49 shows detectable levels of Ang II in whole brains of Agt-KO-Tg and Agt-Tg while none of the peptides were detected in wildtype brains. Interestingly, both Agt-KO-Tg and Agt-Tg despite abundant Ang II levels lacked the canonical Ang II precursor peptide Ang I. Therefore, we attempted to quantify Ang 1-12, a RAS peptide detected in tissues as the heart, which is believed to be an alternative intermediate for local Ang II synthesis (138, 139). However, Ang 1-12 was not detected in whole brains of Agt-KO-Tg and Agt-Tg. Altogether 3 important features of brain Ang II formation became evident: First, the brain locally produces Ang II; second, brain Ang II does not spillover into the circulation; third, the absence of brain Ang I indicates a possible Ren independent Ang II production in the brain.

Table 49 - Plasma and whole brain RAS peptides measurement by LC-MS/MS.

Plasma				
RAS peptide (concentration)	**FVB/N,** *n*=1	**Agt-KO,** *n*=1	**Agt-KO-Tg,** *n*=4	**Agt-Tg**
Ang I (pmol/L)	49.7 ± 0.0	< 4	< 4	NM
Ang II (pmol/L)	29.0 ± 0.0	< 2	< 2	NM
Ang III (pmol/L)	14.6 ± 0.0	< 2	< 2	NM
Ang 1-7 (pmol/L)	< 2	< 2	< 2	NM
Whole brain				
RAS peptide (concentration)	**FVB/N,** *n*=3	**Agt-KO,** *n*=1	**Agt-KO-Tg,** *n*=4	**Agt-Tg,** *n*=3
Ang I (fmol/g)	< 10	< 10	< 10	< 10
Ang II (fmol/g)	< 10	< 10	134.3 ± 54.5	84.3 ± 5.7
Ang III (fmol/g)	< 10	< 10	< 10	< 10
Ang 1-7 (fmol/g)	< 15	< 15	< 15	< 15
Ang 1-12 (fmol/g)	NM	NM	< 15	< 15

Values are mean ± SD. Red numbers represent the lower limit of quantification. NM = not measured.

4.3.1.1 Brain Ang II formation in cardiovascular relevant nuclei

As demonstrated in section 4.1.4 the transgene rAgt expression is distributed across the brain similar to the endogenous mAgt. However, the major site(s) of brain Ang II production are

unknown. Immunofluorescence was used to find brain regions with enriched Ang II production in Agt-Tg which could be potentially explored in further studies to identify brain enzyme(s) producing Ang II. However, the staining patterns of Agt-Tg and Agt-KO were not different indicating an unspecific binding of the antibody (*data not shown*). Therefore, indirect markers namely MAP response to Ang II receptor blockade, vasopressin release, and c-Fos expression were used to validate if Agt-Tg and Agt-KO-Tg produce Ang II at cardiovascular brain centers and/or brain Ang II reaches these neuronal populations.

The MAP response to AT1 receptor blockade was investigated in acute and subchronic conditions. For this purpose, candesartan (CV-11974) was chosen due to its ability to cross the BBB therefore blocking brain AT1 receptors in addition to the peripheral ones (140). The acute treatment elicited a MAP reduction in wildtype, Agt-Tg and Agt-KO-Tg but not in Agt-KO as expected (Figure 21A), collectively indicating that Ang II produced in the brain in transgenic lines reaches cardiovascular nuclei and modulates BP, because Agt-KO-Tg without peripheral Ang II (see Table 49) responded to candesartan treatment (Figure 21A). Administering candesartan subchronically for 3 days induced a similar pattern of MAP response (Figure 21B).

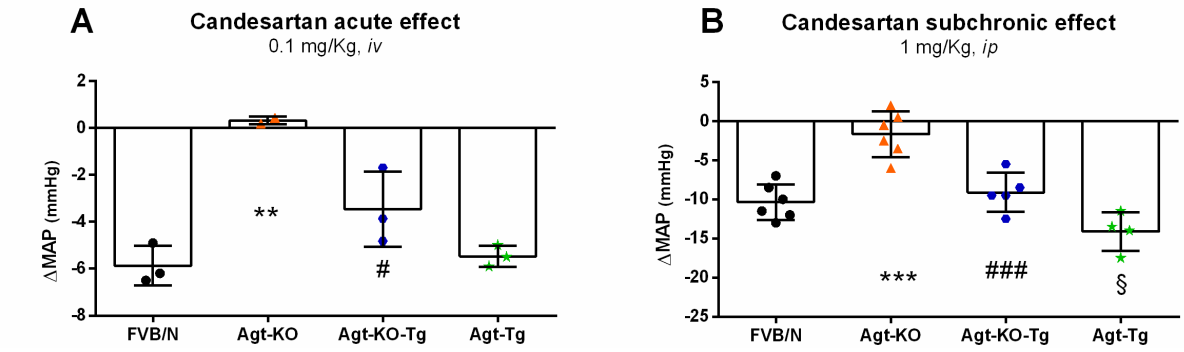

Figure 21 - Effect of AT1 receptor blockade with candesartan on BP.
30 min averaged MAP response to candesartan (**A**). Delta MAP after 3 intraperitoneal (once a day) injections of candesartan (**B**) In **B** MAP was measured 24 hours after the last injection of candesartan to avoid acute effect. Values are mean ± SD. $^{**}P<0.01$, $^{***}P<0.001$ vs FVB/N; $^{\#\#\#}P<0.001$vs Agt-KO (ANOVA followed by Tukey multiple comparison test). $^{\S}P<0.05$ vs FVB/N (Student's *t* test).

Plasma levels of copeptin, a surrogate marker of AVP (141), was quantified as another functional read-out for increased brain Ang II. Figure 22A shows increased circulating copeptin levels in Agt-KO-Tg and Agt-Tg. The quantification of AVP mRNA in the whole hypothalamus did not show a significant difference among the groups besides a tendency in Agt-KO (Figure 22B). Finally, brain sections containing the two major centers in the brain producing AVP (PVN

and SON) were immonostained against AVP. The representative images in Figure 22C indicate a stronger AVP staining in the PVN of Agt-KO-Tg.

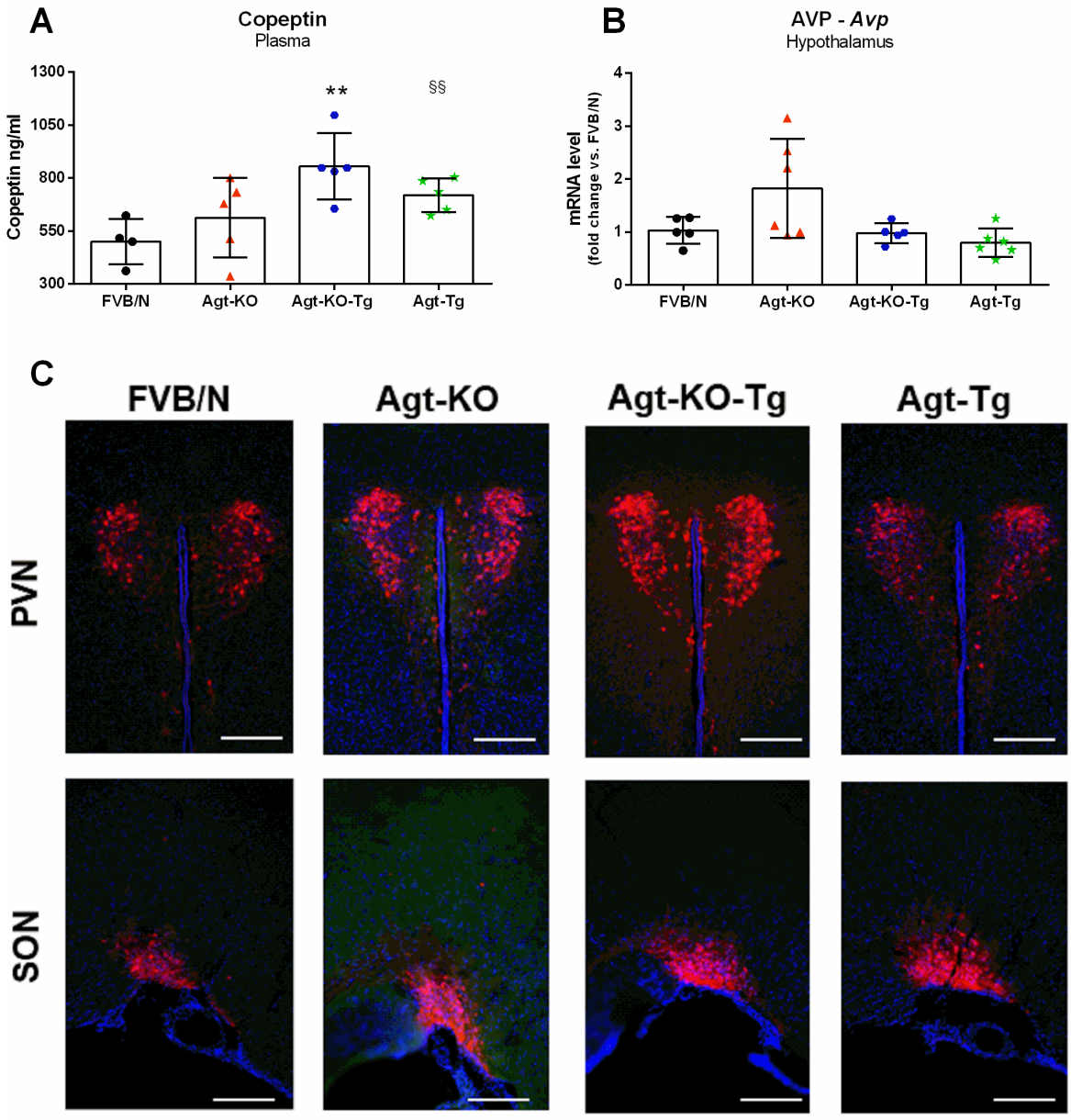

Figure 22 - AVP (Copeptin) release.
Increased circulating plasma levels of copeptin in Agt-KO-Tg and Agt-Tg (**A**). Hypothalamic mRNA levels of AVP (**B**). Brain sections immunostained for vasopressin (Red) containing the paraventricular nucleus of the hypothalamus (PVN) and the supraoptic nucleus (SON) (**C**). Values are mean ± SD **p<0.01 vs FVB/N; (ANOVA followed by Tukey's test). §§p<0.01 vs FVB/N (Student's *t* test). Scale bars are 200 µm.

AT1 receptors are expressed by specific neuronal populations that are in most of the cases glutamatergic and control BP via SNA (3, 33). Indeed, intracerebroventricular Ang II

administration triggers an increase in MAP and vasopressin release among different other physiological responses due to neuronal activation (142, 143). To test if Ang II activated cardiovascular nuclei in mice with altered brain RAS, the mRNA expression of the neuronal activation marker c-Fos was quantified in whole brain as well as in areas with cardiovascular centers (hypothalamus and brainstem). Interestingly, c-Fos was increased in whole brains of Agt-Tg but not in Agt-KO-Tg even though both lines presented elevated brain Ang II (Figure 23A). Hypothalamic c-Fos mRNA was increased in both Agt-KO-Tg and Agt-Tg, however, higher in Agt-Tg (Figure 23B). Finally, Agt-KO presented slightly decreased c-Fos expression in hypothalamus and brainstem (Figure 23B,C).

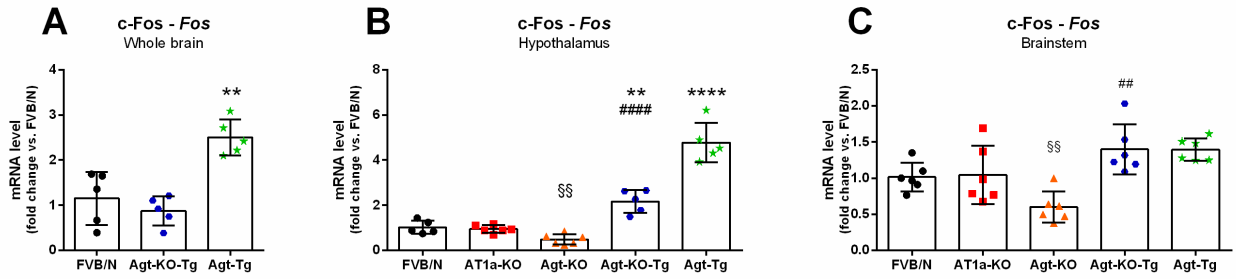

Figure 23 - Brain expression of c-Fos mRNA.
c-Fos mRNA expression in whole brain (**A**), hypothalamus (**B**) and brainstem (**C**). Values are mean ± SD $^{**}P<0.01$, $^{****}P<0.0001$ vs FVB/N; $^{\#\#}P<0.01$, $^{\#\#\#}P<0.001$ vs Agt-KO (ANOVA followed by Tukey multiple comparison post hoc test). $^{\S\S}P<0.01$vs FVB/N (Student's *t* test). *n.d* = not detected.

4.3.1.2 Ang II receptor expression in brain cardiovascular areas

Ligand abundancy may influence the receptor expression. Thus, the expression of the Ang II receptors was quantified in hypothalamus and brainstem. Figure 24 shows that in general there were few changes at the receptor mRNA expression level. Hypothalamic expression of the AT1b receptor was found decreased in Agt-KO, and AT2 receptor expression was reduced in Agt-KO-Tg (Figure 24B,C). In the brainstem, only the AT1a mRNA levels were found increased in Agt-KO-Tg (Figure 24D). Altogether there is no clear Ang II receptor expression pattern induced by increased brain Ang II, because Agt-KO-Tg and Agt-Tg lack a common trend.

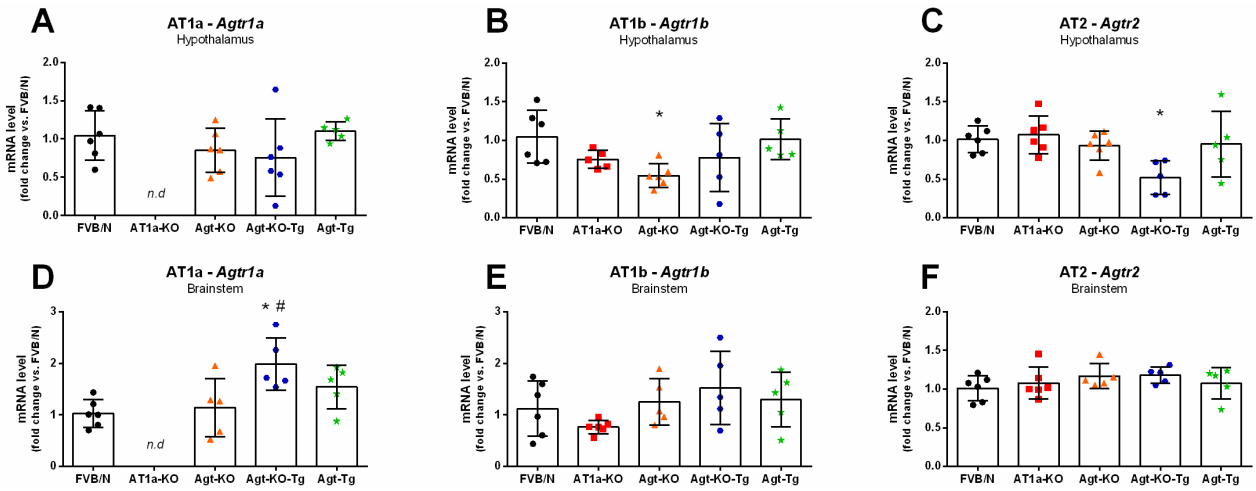

Figure 24 - Ang II receptor expression in hypothalamus and brainstem.
Hypothalamic mRNA levels of the Ang II receptors: AT1a (**A**) AT1b (**B**) and AT2 (**C**). Brainstem mRNA levels of the Ang II receptors: AT1a (**D**) AT1b (**E**) and AT2 (**F**). Values are mean ± SD $^{*}P<0.05$ vs FVB/N; $^{\#}P<0.05$ vs Agt-KO (ANOVA followed by Tukey multiple comparison post hoc test). *n.d* = not detected.

4.3.1.3 Peripheral RAS homeostasis in Agt-Tg

Our data indicates that peripheral and central Ang II formation likely do not share a common pathway, however, there is evidence that both systems may modulate each other's activity (144). Therefore, we evaluated the impact of increased brain RAS activity on the peripheral RAS homeostasis in Agt-Tg. Agt-Tg has normal plasma levels of the RAS precursor protein Agt measured by western blot (Figure 25A). However, Agt-Tg presented reduced renal Ren gene expression (Figure 25B) and reduced plasma levels of Ang II, measured by RT-qPCR and radioimmunoassay, respectively (Figure 25C). The data underscores an inhibition of the peripheral RAS induced by increased brain Ang II levels.

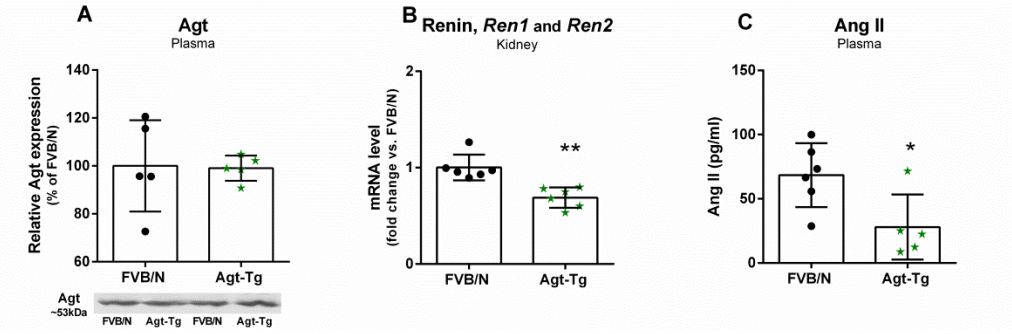

Figure 25 - Peripheral RAS homeostasis in Agt-Tg.
Unaltered plasma Agt protein levels in Agt-Tg (**A**). Decreased renal expression of Ren (**B**), and plasma levels of Ang II (**C**) in Agt-Tg. Values are mean ± SD $^{*}P<0.05$, $^{**}P<0.01$ vs FVB/N (Student's *t* test).

4.3.2 Establishment of baseline cardiovascular parameters

To measure the impact of life-long gain and loss of function of RAS components on basal cardiovascular parameters (MAP and HR), two distinct invasive methodologies in freely moving mice were used. Acute recordings were performed using saline-heparin filled catheters (~1 hour), and chronic recordings with radiotelemetry (24 hours for 5 days). Acute recordings revealed reduced MAP in AT1a-KO. Surprisingly, Agt-KO were normotensive (Figure 26A). In former studies, global knockout mice of *Agt* in mixed, C57BL/6 and ICR strains display ~25 mmHg MAP reduction (112, 145, 146). Even more surprisingly was the fact that restoring Agt production specifically in the brain of the Agt-KO line induced hypotension in Agt-KO-Tg (Figure 26A). The hypotensive effect is unlikely attributed to a primary effect of the transgene integration, because Agt-Tg presented elevated MAP as consequence of increased brain Ang II (Figure 26A). The baseline MAP of these lines was confirmed in chronic BP recordings using radiotelemetry, the only exception was Agt-Tg that displayed normotensive baseline MAP levels instead of raised ones (Figure 26B). All lines presented similar HR levels in both recording methodologies (Figure 26C,D). In addition, the baseline locomotor activity was estimated by tracking the mice movement during radiotelemetry recordings. Figure 26E shows no significant difference in baseline locomotion, discarding a possible effect on the BP caused by physical activity level.

Our FVB/N Agt-KO line is undoubtedly knockout because it lacks Agt protein (Figure 16), Ang peptides production (Table 49), presents the characteristic renal development impairment (Figure 38) and does not respond to candesartan (Figure 21), moreover as described in section 3.2.2.2, we backcrossed the mixed strain background hypotensive Agt-KO to the FVB/N background. Collectively analyzing the baseline MAP data, it suggests an atypical differential role on BP regulation exerted by increased brain Ang II production in FVB/N wildtype and Agt-KO mice, which may be unique to the FVB/N strain but also could be present in human subjects. Therefore, these mouse lines were phenotyped in depth further.

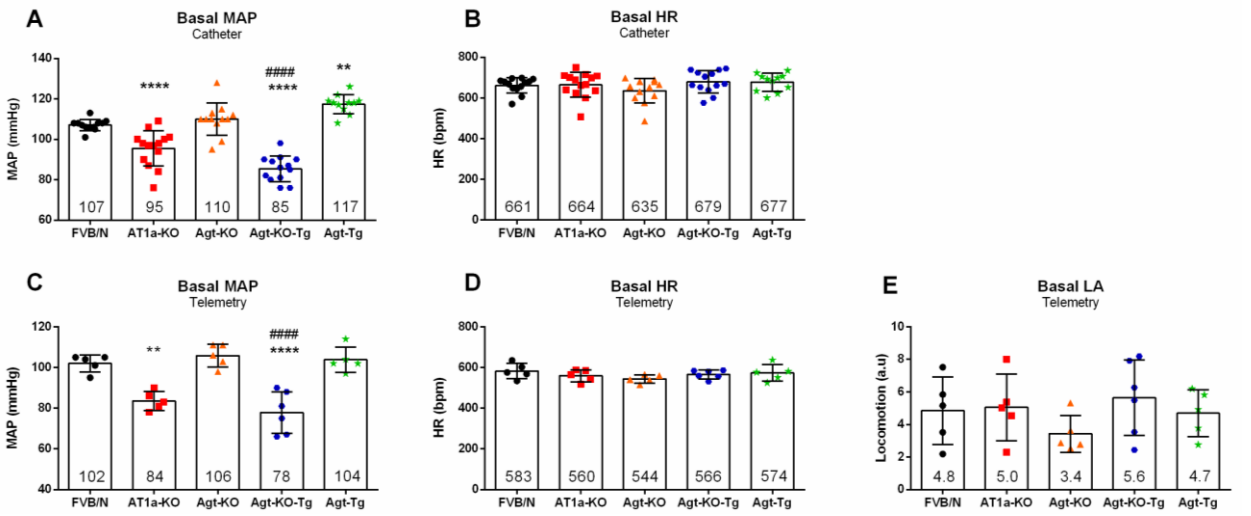

Figure 26 - Cardiovascular homeostasis.
Baseline MAP in freely-moving mice acutely recorded with saline-heparin filled catheter (**A**), and by radiotelemetry (5 days 24 hours averaged) (**B**). Baseline HR measured with saline-heparin filled catheter (**C**) and telemetry (**D**). LA estimation by telemetry (**E**). Values are mean ± SD $^{**}P<0.01$, $^{****}P<0.0001$ vs FVB/N; $^{\#\#\#\#}P<0.0001$ *vs* Agt-KO (ANOVA followed by Tukey multiple comparison post hoc test). MAP = mean arterial pressure, HR = heart rate, LA = locomotor activity.

Additional components and aspects of the telemetric BP recordings were quantified to deepen understand the BP phenotypic alterations. The hypotensive lines AT1a-KO and Agt-KO-Tg presented decreased systolic and diastolic pressures (Figure 27A,B). Interestingly, the normotensive Agt-KO presented increased systolic pressure (Figure 27A) and consequently Agt-KO displayed elevated pulse pressure (systolic - diastolic) (Figure 27C). The hypotensive lines AT1a-KO and Agt-KO-Tg presented decreased pulse pressure (Figure 27C). The MAP, HR, pulse pressure and systolic pressure findings in Agt-KO when analyzed collectively indicate a possible increase in total peripheral resistance and/or vascular stiffness, factors that are modulated by vascular sympathetic outflow (18, 147). In other words, Agt-KO likely presents increased vasoconstriction forcing the heart to constrict stronger (systolic pressure increases) to push the blood throughout the body. To test if the hearts of Agt-KO are indeed strongly contracting, the cardiac mass was measured. Strikingly, Agt-KO presented heavier hearts in comparison to wildtypes while the hypotensive lines, AT1a-KO and Agt-KO-Tg, presented reduced cardiac mass as predicted (Figure 27D,E).

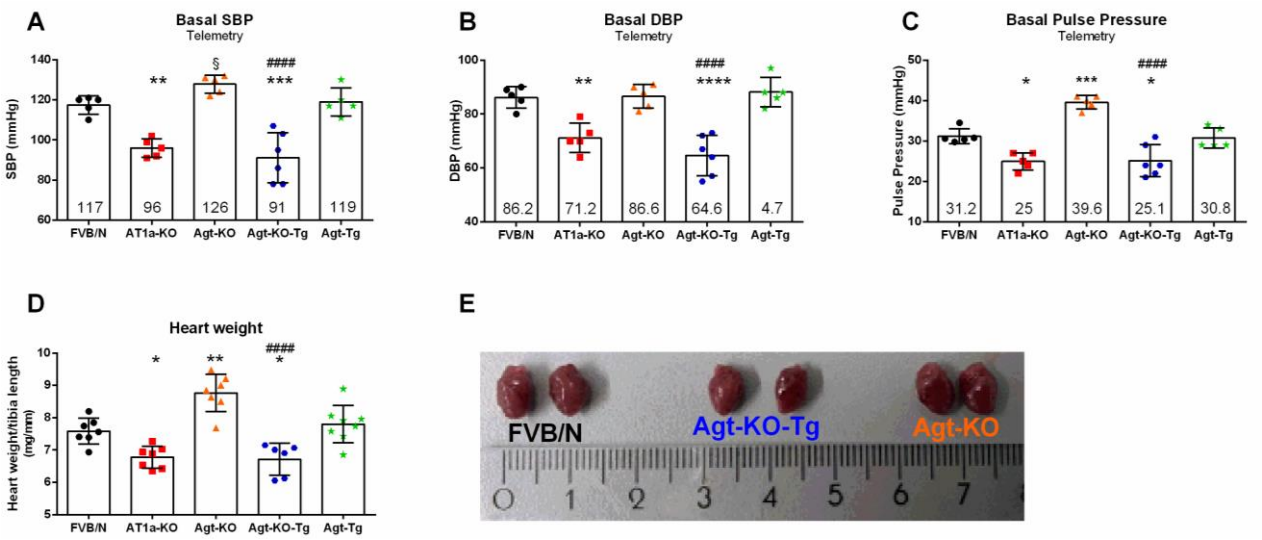

Figure 27 - Further BP and cardiac phenotyping.
Telemetric measurements (5 days 24 hours averaged) of the basal systolic pressure (**A**), diastolic pressure (**B**) and pulse pressure (**C**). Heart weight (**D**). Representative pictures of wildtype, Agt-KO and Agt-KO-Tg hearts (**E**). Values are mean ± SD $^{*}P<0.05$, $^{**}P<0.01$, $^{***}P<0.001$, $^{****}P<0.0001$ vs FVB/N; $^{\#\#\#\#}P<0.0001$ vs Agt-KO (ANOVA followed by Tukey multiple comparison post hoc test). $^{\S}P<0.001$ vs FVB/N (Student's *t* test). SBP = systolic blood pressure, DBP = diastolic blood pressure.

Furthermore, the circadian rhythmicities of the MAP, HR and locomotor activity were calculated from the 24-hour telemetry data obtained. All lines presented a circadian rhythm or a strong statistical tendency for these parameters, as expected all markers were increased during the active phase of mice, night (Figure 28A-C). Interestingly, the circadian MAP amplitude (night - day) was higher in Agt-KO and Agt-KO-Tg in comparison to controls (Figure 28D) while there were no circadian differences in the HR and LA (Figure 28E,F) indicating that the high MAP during the active phase is likely driven by some intrinsic factor independent of the HR and physical activity. To better visualize the increased circadian MAP amplitude in Agt-KO, the 5 days hourly averaged MAP as well as the HR and locomotion of Agt-KO and controls were plotted hourly (Figure 28G). As can be observed in Figure 28A and G MAP values are higher in Agt-KO than in FVB/N during the dark phase, demonstrating that their increased circadian MAP difference is driven by higher MAP during the active phase.

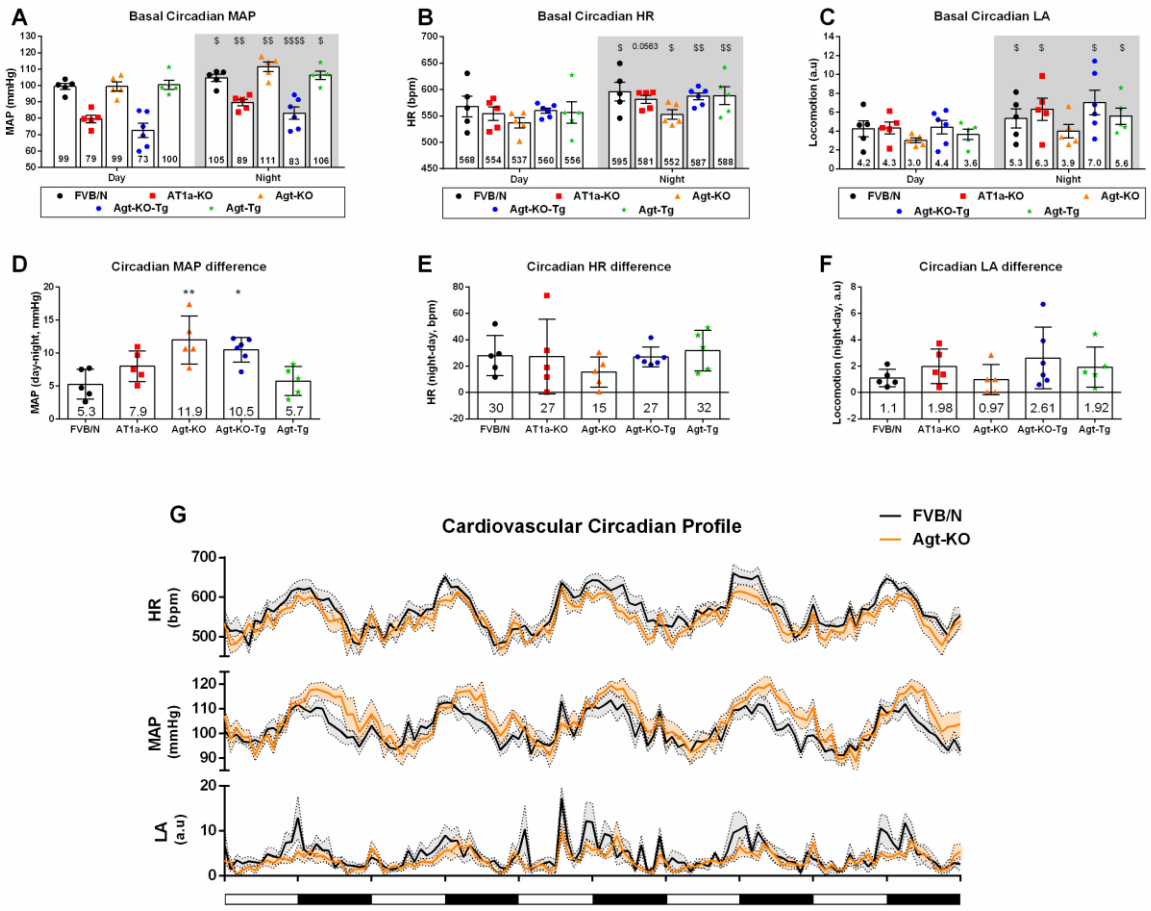

Figure 28 - Circadian profile of the cardiovascular parameters.
Telemetric measurements (5 days 24 hours averaged) of the diurnal and nocturnal MAP (**A**), HR (**B**) and LA (**C**), the grey background represents the dark period. Difference (night-day) mean of MAP (**D**), HR (**E**) and LA (**F**). Circadian profile of the HR, MAP and LA in wild-type and Agt-KO obtained by continuous telemetry recording for 5 days, filled and white intervals below the x axis represent dark and light periods, respectively (**G**). For (**A-F**) values are mean ± SD $^{*}P<0.05$, $^{**}P<0.01$ vs FVB/N (ANOVA followed by Tukey multiple comparison post hoc test). $^{\$}P<0.05$, $^{\$\$}P<0.01$, $^{\$\$\$\$}P<0.0001$ vs FVB/N (Student's paired *t* test). For **G,** values are the hour average for each parameter ± SEM for five animals in each group. MAP = mean arterial pressure, HR = heart rate, LA = locomotor activity.

4.3.3 SNA and baseline cardiovascular control

We suspected the normotension in adult Agt-KO to be a product of increased SNA, as a compensation for the RAS loss. To test this hypothesis, we submitted the same mice used for cardiovascular baseline characterization (section 4.3.1) to a peripheral SNS ablation protocol using 6-OHDA. Immediately, after baseline data acquisition, mice received 6-OHDA for five days while recording cardiovascular parameters by telemetry. Cardiovascular parameters were recorded for five additional days after the 6-OHDA treatment (Figure 29A). Agt-KO presented a stronger maximum MAP response to 6-OHDA (Figure 29B). This effect was rescued in the

hypotensive Agt-KO-Tg (Figure 29B) indicating a higher BP dependency on SNA in Agt-KO mice. Agt-Tg presented a potentiated increase in HR during 6-OHDA despite the MAP response to be similar to the control group, this could be a compensatory effect of the HR to maintain BP levels (Figure 29C).

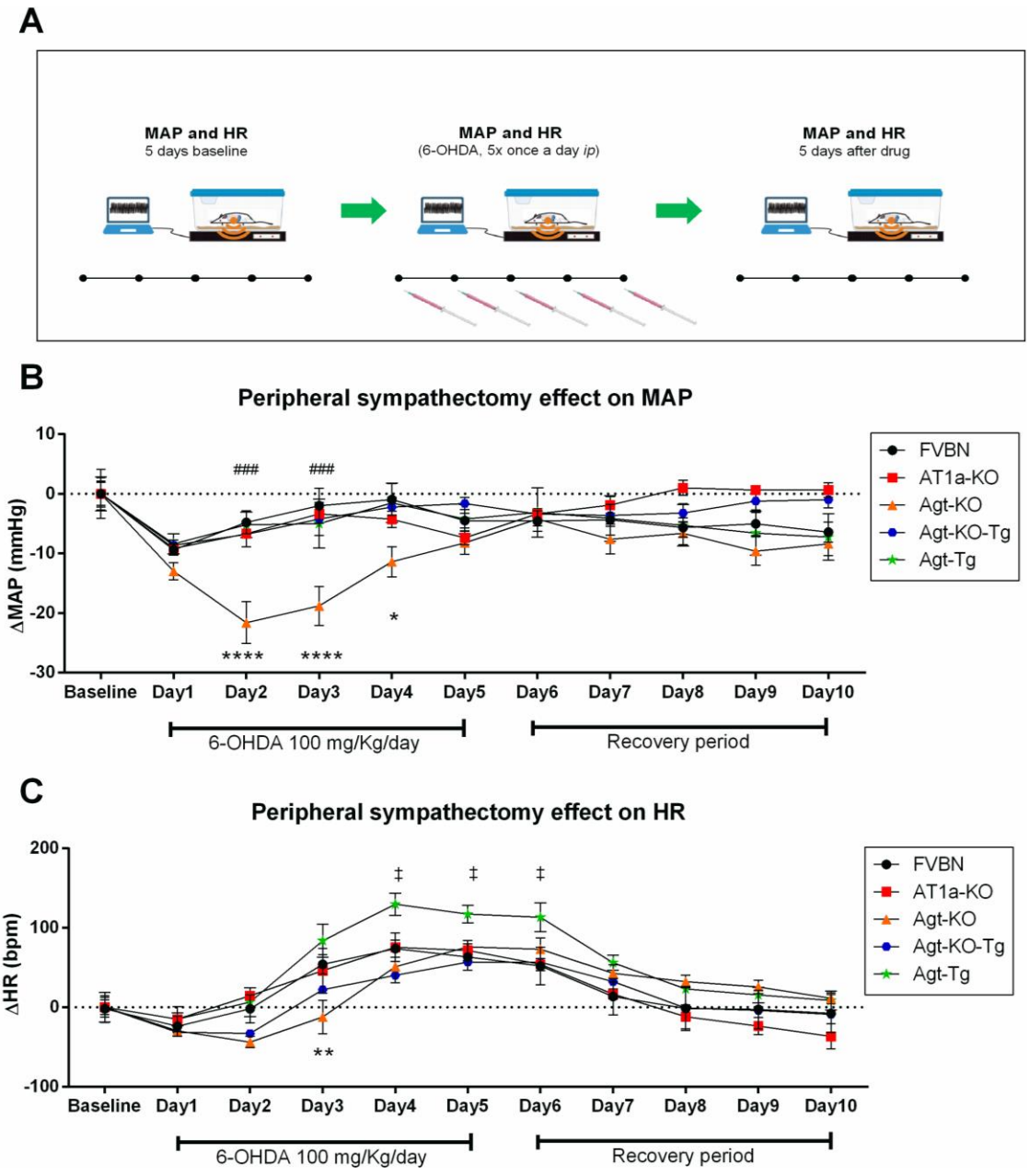

Figure 29 - Cardiovascular response to peripheral sympathectomy.
Schematic representation of the cardiovascular phenotyping during peripheral sympathectomy with 6-hydroxydopamine (6-OHDA) (**A**). Change from baseline in MAP (ΔMAP) (**B**) and HR (ΔHR) (**C**) upon peripheral sympathectomy by treating the mice for 5 days with 6-OHDA. Values are mean ± SEM for 4-6 animals in each group. $^{*}P<0.05$, $^{**}P<0.01$, $^{****}P0.0001$ Agt-KO post sympathectomy vs FVB/N post sympathectomy; $^{\#\#\#}P<0.0001$ Agt-KO-Tg post sympathectomy vs Agt-KO post sympathectomy; $^{‡}P<0.05$ Agt-Tg post sympathectomy vs FVB/N post sympathectomy (2-way ANOVA with repeated measurements followed by Tukey multiple comparison post hoc test). MAP = mean arterial pressure, HR = heart rate, *ip* = intraperitoneal. The illustration in **A** was partially created in BioRender.com.

4.3.3.1 Vascular sympathetic tone

The 6-OHDA treatment impairs SNA across the whole periphery, therefore any cardiovascular organ or organ system modulated by SNA could potentially be involved in the BP response found in Agt-KO. In order to assess the specific contribution of the vascular sympathetic tone (vasoconstriction induced by vascular sympathetic innervation firing), the maximal MAP drops to a ganglionic blocker, and adrenergic receptor blockers (α1 and α2) were measured and used as indirect markers. Similarly to the 6-OHDA response, Agt-KO presented stronger maximum MAP responses to the ganglionic blocker hexamethonium (Figure 30A), as well as to the α1 and α2 antagonists, prazosin (Figure 30B) and yohimbine (Figure 30C), respectively. This increased response to the sympatholytic drugs was not observed in the hypotensive line Agt-KO-Tg, but the other hypotensive line AT1a-KO presented a stronger MAP response to prazosin (Figure 30B) and yohimbine (Figure 30C). Finally, Agt-Tg also displayed enhanced vascular SNA, characterized by increased response to hexamethonium and yohimbine (Figure 30A,C). NE levels were measured in the urine and resistance vessels, namely mesenteric arteries, to indirectly quantify SNA *ex vivo.* However, NE was unaltered in both urine (Figure 30D) and mesenteric vessels (Figure 30E) with exception of NE levels in the mesenteric arteries of Agt-KO-Tg that was reduced (Figure 30E).

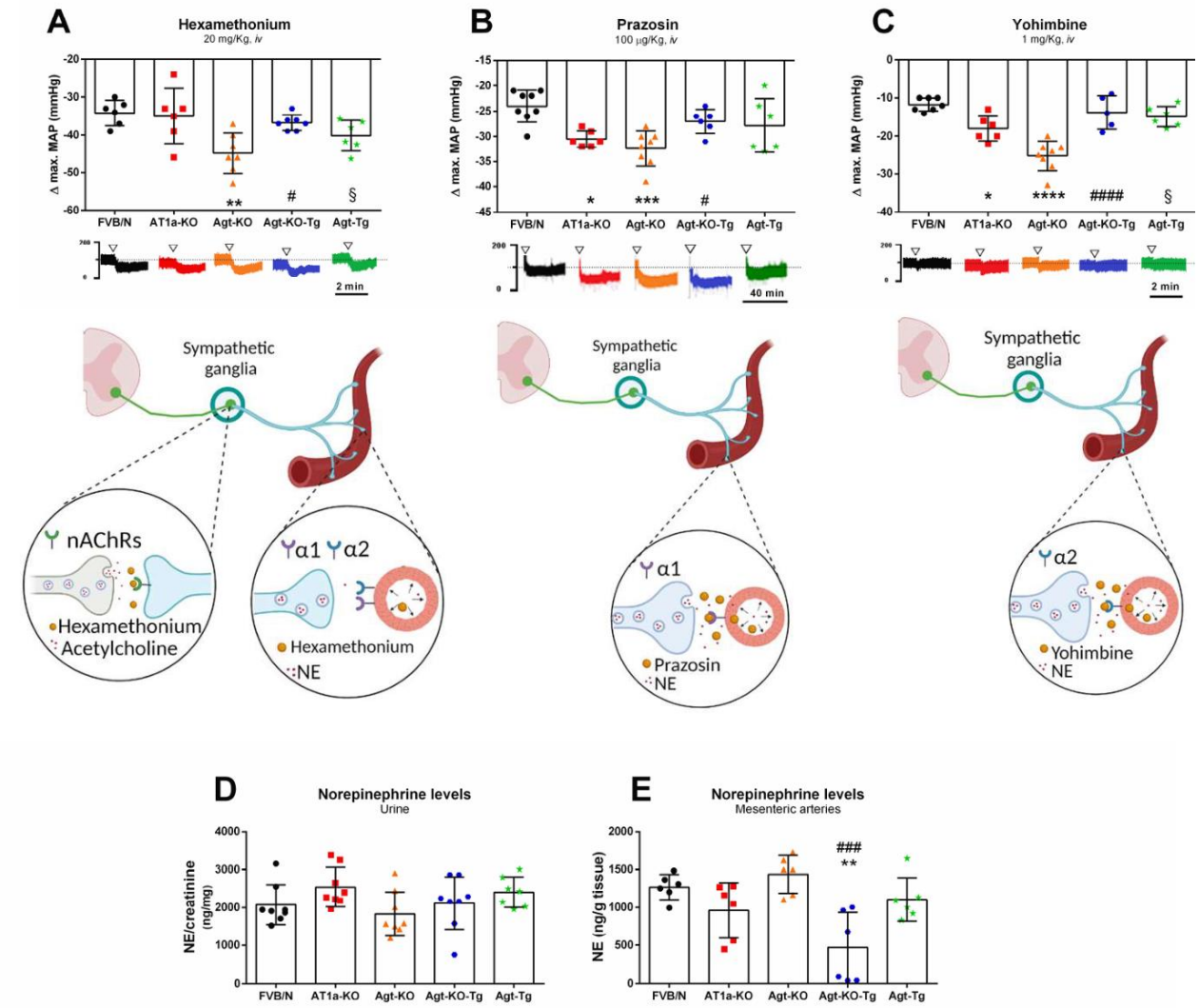

Figure 30 - Acute MAP response to sympatholytic drugs and NE levels.
Maximal MAP response induced by the ganglionic blocker hexamethonium (**A**), and to the α1 and α2 antagonists prazosin (**B**) and yohimbine (**C**), respectively. Norepinephrine quantification in the urine (**D**) and mesenteric arteries (**E**). Values are mean ± SD $^{*}P<0.05$, $^{**}P<0.01$, $^{***}P<0.001$, $^{****}P<0.0001$ vs FVB/N; $^{\#}P<0.05$, $^{\#\#\#}P<0.001$, $^{\#\#\#\#}P<0.0001$ vs Agt-KO (ANOVA followed by Tukey multiple comparison post hoc test). $^{\S}P<0.001$ vs FVB/N (Student's *t* test). MAP = mean arterial pressure, NE = norepinephrine, *iv* = intravenous. The ▽ over the pulsatile arterial pressure trace represents the approximate time of the bolus injection of a given substance in a representative mouse. Illustrations were created in BioRender.com.

After finding increased vascular sympathetic tone in Agt-KO despite normal vascular NE release, we tested if the phenotype is mediated by an increased vascular reactivity to NE. For this purpose, tyramine a natural compound found in animals and plants which is derived from the aminoacidic tyrosine was chosen. Tyramine has a peripheral sympathomimetic effect mainly by entering synaptic vesicles of presynaptic neurons containing NE resulting in neurotransmitter release in vascular tissue which triggers an immediate pressor response (148, 149). The intravenous tyramine administration triggered a pressor response in all lines, but AT1a-KO, Agt-KO and Agt-KO-Tg presented reduced maximal pressor responses to tyramine (Figure 31A). An

impaired vascular adrenergic receptor signaling is unlikely because the adrenergic blockers elicited equal or stronger pressure responses in these lines in comparison to control mice (Figure 30A-C). However, an overactive vascular SNA could potently exhaust presynaptic vesicular NE content, thereby reducing the tyramine pressor response. To test this hypothesis, the MAP responses to controlled concentrations of intravenously infused α1 and α2 adrenergic receptor agonists (phenylephrine and dexmedetomidine, respectively) were measured. Interestingly, similar to tyramine AT1a-KO, Agt-KO and Agt-KO-Tg presented reduced MAP responses to phenylephrine (Figure 31B) and dexmedetomidine (Figure 31C) pointing to an unlikely reduced vesicular NE content.

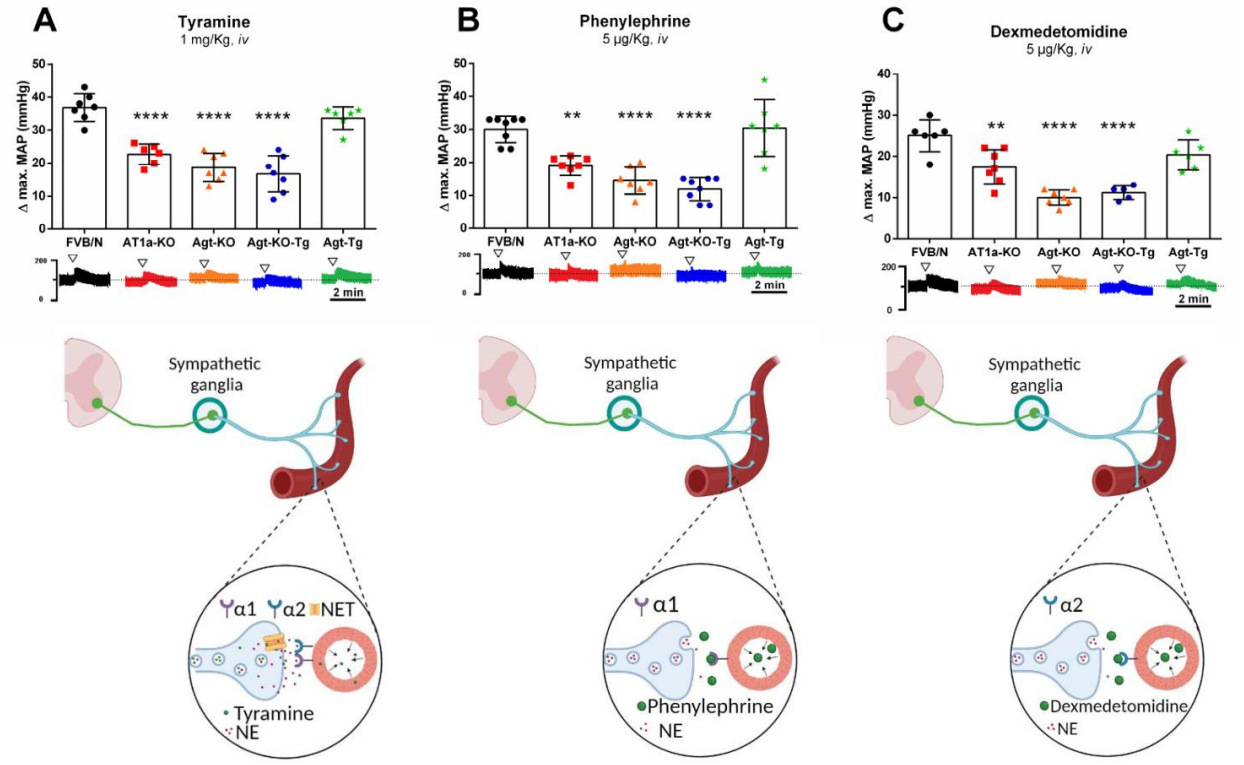

Figure 31 - Acute MAP response to sympathomimetic drugs.
Maximal MAP response induced by tyramine (**A**), and to the α1 and α2 agonists phenylephrine (**B**) and dexmedetomidine (**C**), respectively. Values are mean ± SD $^{**}P<0.01$, $^{****}P<0.0001$ vs FVB/N (ANOVA Tukey multiple comparison post hoc test). MAP = mean arterial pressure, *iv* = intravenous. NET = NE transporter. The ▽ over the pulsatile arterial pressure trace represents the approximate time of the bolus injection of a given substance in a representative mouse. Illustrations were created in BioRender.com..

4.3.3.2 Vascular adrenergic receptor expression

To further study the nature of the reduced MAP response induced by sympathomimetic drugs in mice with depleted peripheral RAS, the mRNA expression of the α and β adrenergic receptors

was quantified in conducting and resistance arteries, aorta and mesenteries, respectively. The mRNA expression of the adrenergic receptors is displayed in Table 50. α1 receptors are the most relevant receptor class controlling vasoconstriction induced by NE, and resistance vessels are controlling peripheral resistance and thereby BP levels. Moreover, the major α1 receptor subtype expressed in resistance vessels is the $\alpha1_A$ while in large conduit vessels it is the $\alpha1_D$ (150). Interestingly, $\alpha1_A$ expression was downregulated in Agt-KO mesenteric arteries (Figure 32A and Table 50) as was $\alpha1_D$ expression in the aorta, $\alpha1_D$ mRNA levels in aorta were also downregulated in the AT1a-KO, Agt-KO-Tg and Agt-Tg lines (Figure 32B and Table 50). Another interesting observation is the fact that the mRNA levels of the β2 adrenergic receptor, the most widely expressed β receptor in the vasculature that controls vasorelaxation, were found upregulated in AT1a-KO and Agt-Tg mesenteric arteries (Figure 32C and Table 50). The β2 adrenergic receptor expression was found increased in the aorta of the lines Agt-KO, Agt-KO-Tg and Agt-Tg (Figure 32D and Table 50).

Table 50 - Vascular α and β adrenergic receptors mRNA expression.

Tissue	Protein - *Gene*	FVB	AT1a-KO	Agt-KO	Agt-KO-Tg	Agt-Tg
Mesenteric arteries	$\alpha1_A$ - *Adra1a*	1.1 ± 0.4	0.6 ± 0.3	0.4 ± 0.2**	0.8 ± 0.3	0.7 ± 0.2
	$\alpha1_B$ - *Adra1b*	1.0 ± 0.1	0.8 ± 0.2	0.6 ± 0.2*	0.7 ± 0.1*	0.9 ± 0.2
	$\alpha1_D$ - *Adra1d*	1.0 ± 0.2	0.9 ± 0.3	0.5 ± 0.1**	0.6 ± 0.1	1.0 ± 0.2
	$\alpha2_A$ - *Adra2a*	1.0 ± 0.2	0.4 ± 0.1*	0.4 ± 0.1*	0.7 ± 0.2	1.4 ± 0.5
	$\alpha2_B$ - *Adra2b*	1.2 ± 0.7	3.9 ± 1.3***	0.6 ± 0.3	0.5 ± 0.2	0.7 ± 0.2
	α2c - *Adra2c*	1.1 ± 0.4	0.4 ± 0.3*	0.5 ± 0.2*	0.3 ± 0.1**	1.0 ± 0.4
	β1 - *Adrb1*	1.1 ± 0.5	0.7 ± 0.1	0.9 ± 0.3	1.2 ± 0.4	2.4 ± 1.1*
	β2 - *Adrb2*	1.1 ± 0.5	2.4 ± 0.8*	1.3 ± 0.5	1.0 ± 0.2	2.6 ± 1.0*
Aorta	$\alpha1_A$ - *Adra1a*	1.1 ± 0.6	3.2 ± 1.2	2.9 ± 1.0	6.2 ± 2.3**	6.6 ± 3.2**
	$\alpha1_B$ - *Adra1b*	1.0 ± 0.2	1.2 ± 0.5	0.6 ± 0.2	0.6 ± 0.2	0.7 ± 0.2
	$\alpha1_D$ - *Adra1d*	1.0 ± 0.3	0.6 ± 0.2*	0.4 ± 0.1***	0.4 ± 0.1***	0.5 ± 0.2**
	$\alpha2_A$ - *Adra2a*	1.2 ± 0.9	0.7 ± 0.2	0.9 ± 0.4	1.2 ± 1.0	2.1 ± 1.3
	$\alpha2_B$ - *Adra2b*	*n.d*	*n.d*	*n.d*	*n.d*	*n.d*
	α2c - *Adra2c*	1.0 ± 0.2	2.9 ± 1.2	2.2 ± 0.9	2.8 ± 1.5	2.7 ± 1.8
	β1 - *Adrb1*	1.4 ± 0.7	2.7 ± 0.8	5.0 ± 1.3*	6.9 ± 2.7***	5.3 ± 2.1*
	β2 - *Adrb2*	1.1 ± 0.4	2.1 ± 0.7	4.3 ± 1.2**	4.0 ± 0.6**	4.2 ± 1.7**

Values are mean ± SD for 4–6 animals in each group. $^{*}P<0.05$, $^{**}P<0.01$, $^{***}P<0.001$ vs FVB/N (ANOVA followed by Tukey multiple comparison test). *n.d* = not detected.

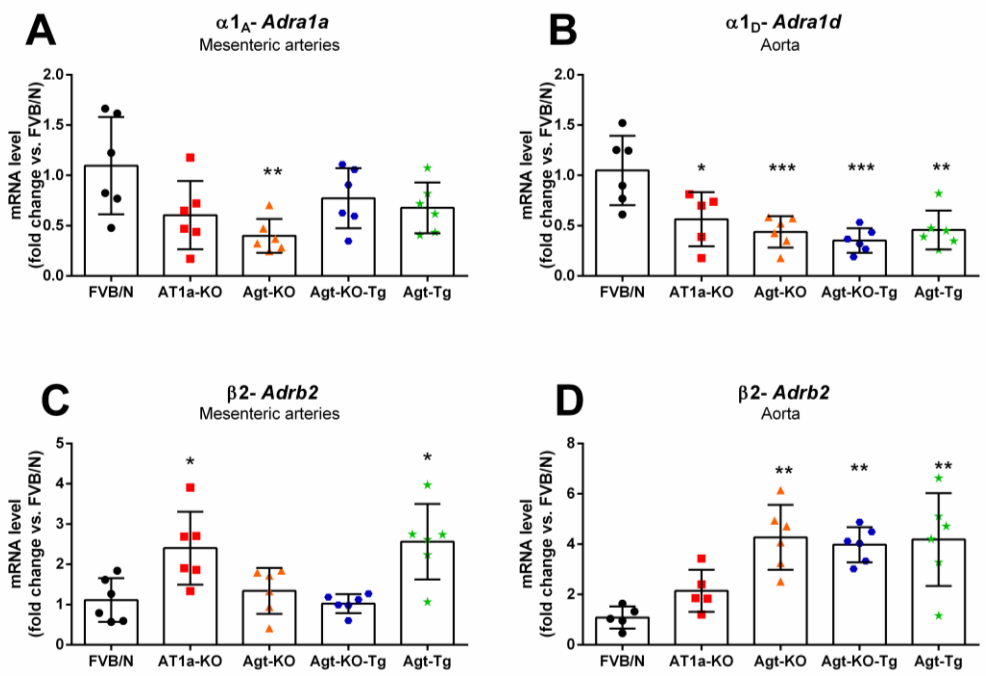

Figure 32 - Most expressed α and β adrenergic receptors in aorta and mesenteric arteries.
$\alpha 1_A$ adrenergic receptor mRNA expression in mesenteric arteries (**A**). $\alpha 1_A$ adrenergic receptor mRNA expression in aorta (**B**). β2 adrenergic receptor expression in mesenteric arteries (**C**) and aorta (**D**). Values are mean ± SD. $^{*}P<0.05$, $^{**}P<0.01$, $^{***}P<0.001$, vs FVB/N (ANOVA followed by Tukey multiple comparison post hoc test).

4.3.4 Pressor response to Endothelin-1

To discard that the blunted MAP response to sympathomimetic drugs is a product of an impaired vascular constrictor machinery induced by absent or blunted peripheral RAS reactivity in AT1a-KO, Agt-KO and Agt-KO-Tg lines, the pressure response to endothelin-1 a peptide hormone independent of that RAS and SNS was assessed *in vivo*. All lines presented a similar maximal pressor response to endothelin-1 demonstrating a normal vascular constrictor capacity in these lines (Figure 33A). In addition, the gene expression of the endothelin type A receptor which is the most relevant receptor mediating the vasoconstrictor effect of endothelin-1 at vascular smooth muscle cells was measured in blood vessels using RT-qPCR. The receptor expression was similarly increased in Agt-KO and Agt-KO-Tg aorta (Figure 33B), however, the receptor expression in the mesenteric arteries was not altered in any of the lines (Figure 33C).

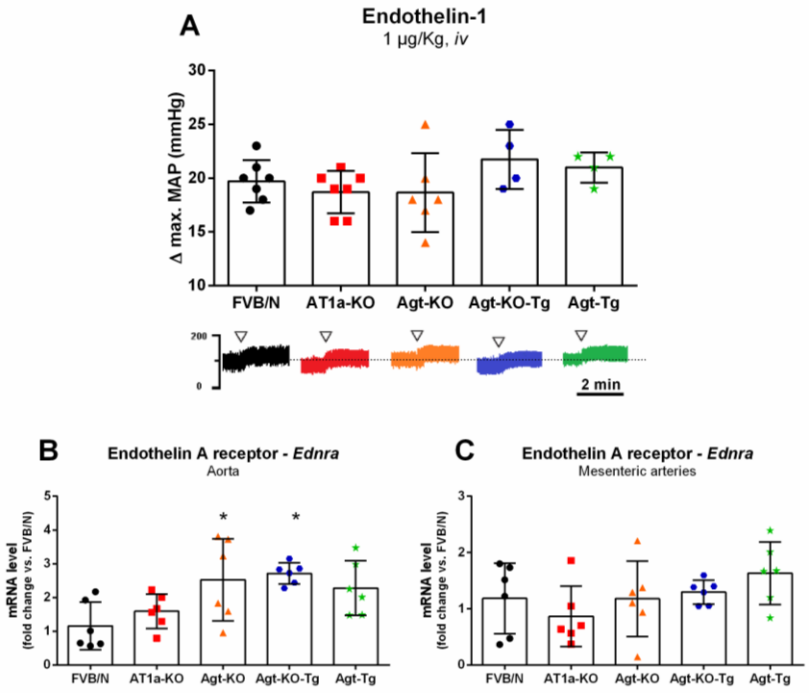

Figure 33 - Acute MAP response to Endothelin-1.
Maximal MAP response to endothelin-1 (**A**). mRNA levels of endothelin receptor type A in aorta (**B**) and mesenteric arteries (**C**). $^{*}P<0.05$ vs FVB/N; (ANOVA followed by Tukey multiple comparison test). MAP = mean arterial pressure, *iv* = intravenous.

4.3.5 Vascular NO homeostasis

Endothelial-released substances play a key role in regulating smooth muscle tone, among these substances NO is a major factor dumping vasoconstriction and thereby BP. NO easily diffuses across cell membranes reaching smooth muscle cells where the molecule promotes vasodilation by locally increasing cGMP levels. NO homeostasis was assessed *in vivo* using the delta MAP increase upon NO synthase blockade with the inhibitor L-NAME as well as the MAP drop to the exogenous NO donor sodium nitroprusside. The parameters revealed an impaired NO homeostasis in Agt-KO, these mice displayed a weaker response to L-NAME (Figure 34A), and a stronger response to SNP (Figure 34B) while Agt-KO-Tg only presented a tendency to have reduced response to L-NAME. Overall body NO generation was estimated by measuring the levels of nitrate and nitrite (NOx) in the urine. Agt-KO presented reduced urinary NOx while this parameter was slightly improved in Agt-KO-Tg (Figure 34C). Finally, the endothelial NO synthase (eNOS) expression level was quantified at the mRNA level in vessels. In agreement with the *in vivo* findings and the NOx quantification, Agt-KO presented lower levels of eNOS mRNA in the aorta and mesenteric arteries, and Agt-KO-Tg had reduce eNOS mRNA in the mesenteric arteries (Figure 34D,E). Collectively, the data points out that Agt-KO presents

impaired NO homeostasis characterized by reduced endothelial NO production due to impaired vascular eNOS expression.

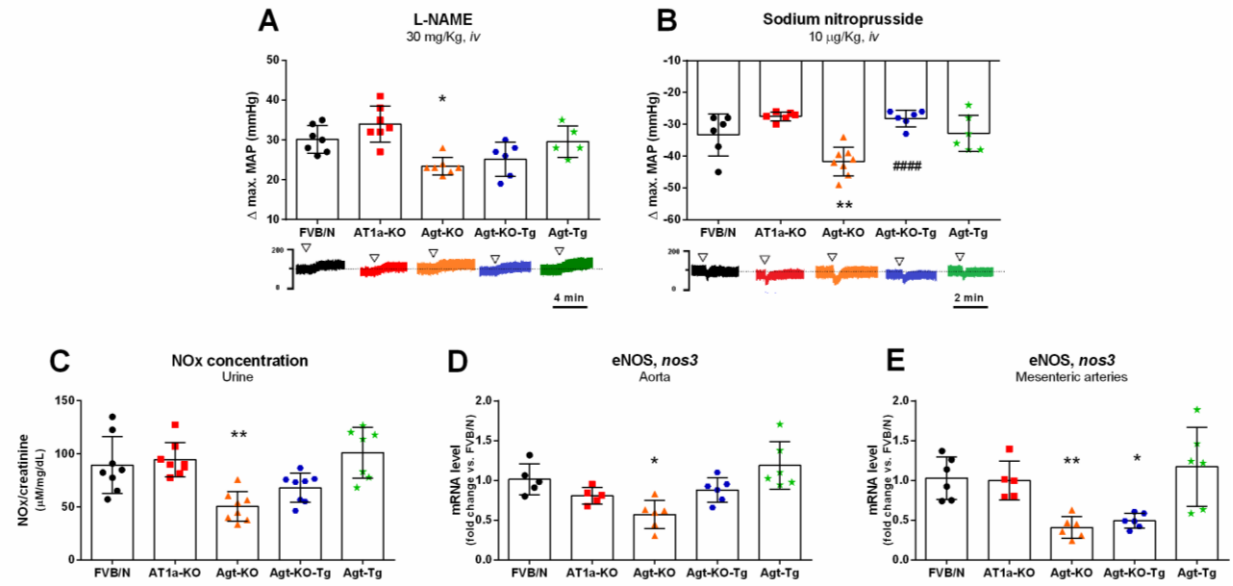

Figure 34 - Vascular NO balance.
Maximal MAP response induced by the NO synthase inhibitor N5-[imino(nitroamino)methyl]-L-ornithine, methyl ester (L-NAME) (**A**), and to the NO donor sodium nitroprusside (**B**). Urinary total nitrate and nitrite (NOx) levels (**C**). mRNA expression of endothelial NO synthase (eNOS) in aorta (**D**) and mesenteric arteries (**E**). Values are mean ± SD $^{*}P<0.05$, $^{**}P<0.01$, $^{***}P<0.001$ vs FVB/N; $^{\#\#\#}P<0.001$ vs Agt-KO (ANOVA followed by Tukey multiple comparison post hoc test). MAP = mean arterial pressure, *iv* = intravenous. The ▽ over the pulsatile arterial pressure trace represents the approximate time of the bolus injection of a given substance in a representative mouse.

4.3.6 Overall vasoconstrictor tone

The vascular tone is controlled by a myriad of intrinsic and extrinsic factors with vasoconstrictor and/or vasorelaxant stimuli that not only modulate the vascular tone but potentially baseline BP. However, the vasoconstrictor machinery at smooth muscle cells is controlled by calcium dependent and calcium independent pathways that ultimately impact the myosin light chain interaction with actin (85). Our findings strongly indicate that the vascular sympathetic tone is increased in Agt-KO, and on top this line presents reduced NO production. Both phenotypes enhance vascular constriction and ultimate BP levels. However, the overall vasoconstrictor tone might not be increased because compensatory regulation by other unpredicted factor(s) may balance the SNA and NO effects. To assess the overall vasoconstrictor tone, the depressor responses triggered upon blocking calcium dependent and independent pathways were quantified. For this, nifedipine, a L-type calcium blocker that controls extracellular calcium entry, and Y-

27632, a ROCK kinases inhibitor that blocks ROCK2 activity that is a central hub in calcium independent vasoconstriction, were injected intravenously and the maximal MAP response was quantified. As expected, both drugs reduced BP but the hypotensive lines AT1a-KO and Agt-KO-Tg displayed a reduced maximal MAP response while Agt-KO and Agt-Tg presented an increased response to nifedipine (Figure 35A). Y-27632 caused an increased MAP response in Agt-KO and, interestingly, also AT1a-KO responded stronger to Y-27632 in comparison to control mice (Figure 35B). Collectively, the data shows that FVB/N Agt-KO has a higher overall vascular tone contributing to the unexpected normotension in this line.

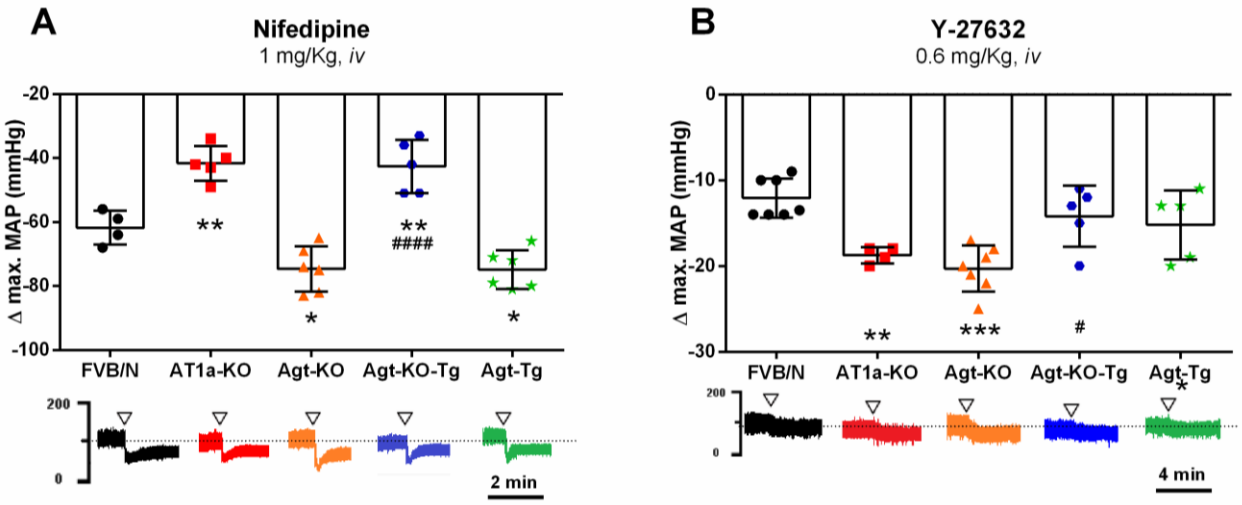

Figure 35 - Unspecific vascular constriction blockade.
Maximal MAP response to the L-type calcium channel blocker nifedipine (**A**) and the ROCK kinases inhibitor Y-27632 (**B**). Values are mean ± SD $^{*}P<0.05$, $^{**}P<0.01$, $^{***}P<0.001$ vs FVB/N; $^{\#}P<0.05$ vs Agt-KO (ANOVA followed by Tukey multiple comparison post hoc test). MAP = mean arterial pressure, *iv* = intravenous. The ▽ over the pulsatile arterial pressure trace represents the approximate time of the bolus injection of a given substance in a representative mouse.

4.3.7 Baroreflex control of the HR

Vascular SNA is regulated moment-to-moment by peripheral reflexes in a negative feedback loop manner (3). An important autonomic reflex is the baroreflex control of the HR which goes in opposite direction of the BP upon acute changes in BP (26). The heart is innervated by sympathetic and parasympathetic nerves whose firing frequency directly controls the HR. However, the baroreflex response might be altered by different factors such as large vessel compliance which directly impacts the baroreceptor signal or factors such as Ang II that modulate the activity of central circuits coordinating the downstream response (151). The baroreflex sensitivity of the HR control was calculated using drug-induced bradycardia and tachycardia with phenylephrine and sodium nitroprusside, respectively. Figure 36A,B shows an

impaired baroreflex control of the HR to induced bradycardia and tachycardia in Agt-Tg and Agt-KO-Tg indicating that Ang II likely acts on brain circuits and dysregulates the cardiac response to BP changes. The pressure responses as the bradycardia and tachycardia are depicted in detail in Table 51.

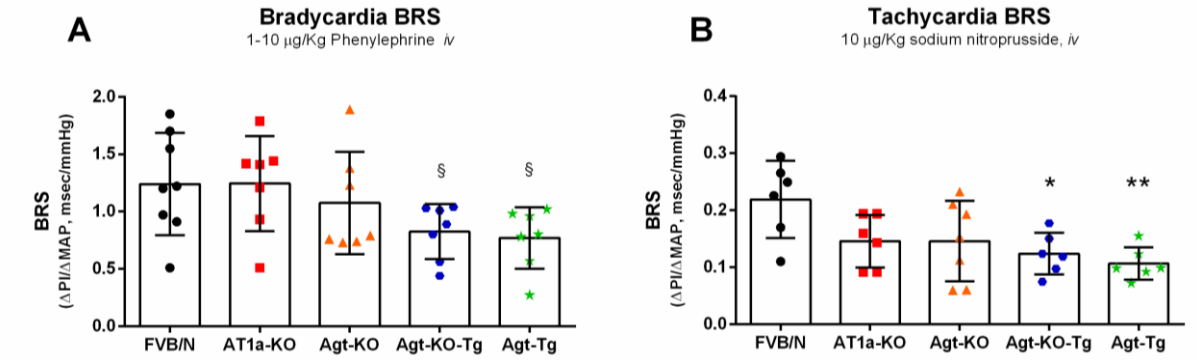

Figure 36 - Baroreflex control of the HR.
Quantification of the cardiac baroreflex sensitivity using drug induced bradycardia (**A**) tachycardia (**B**). Values are mean ± SD $^{*}P<0.05$, $^{**}P<0.01$ vs FVB/N (ANOVA followed by Tukey multiple comparison post hoc test). $^{\S}P<0.05$ vs FVB/N (Student's *t* test). BRS = baroreflex sensitivity, *iv* = intravenous.

Table 51 - Calculation of the cardiac baroreflex sensitivity index.

Baroreflex Control of the HR							
Reflex Bradycardia (1-10 µg/kg phenylephrine, *iv*)							
Line	**MAP basal** (mmHg)	**MAP peak** (mmHg)	**ΔMAP** (mmHg)	**HR basal** (bpm)	**HR peak** (bpm)	**ΔHR** (bpm)	**BRS ΔPI/ΔMAP** (ms/mmHg)
FVB/N	107.4 ± 7.3	128.4 ± 8.7	20.6 ± 3.1	704.5 ± 51.5	546.6 ± 64.3	-157.9 ± 41.5	1.24 ± 0.42
AT1a-KO	91.0 ± 7.8*	111.1 ± 9.6*	21.0 ± 4.1	675. 7 ± 61.6	527.3 ± 65.6	-148.4 ± 48.7	1.24 ± 0.36
Agt-KO	108.6 ± 13.5	129.4 ± 13.0	20.9 ± 3.7	666.3 ± 65.9	542.4 ± 71.7	-123.9 ± 19.1	1.07 ± 0.41
Agt-KO-Tg	85.7 ± 5.6$^{***\#\#\#}$	104.9 ± 6.9$^{***\#\#\#}$	19.1 ± 3.7	731.0 ± 25.4	612. 7 ± 35.2	-118.3 ± 39.8	0.82 ± 0.22§
Agt-Tg	116.1 ± 4.5§	138.0 ± 4.8§	21.9 ± 4.1	702.7 ± 17.6	583.9 ± 37.0	-118.9± 33.7	0.80 ± 0.19§
Reflex Tachycardia (10 µg/kg sodium nitroprusside, *iv*)							
Line	**MAP basal** (mmHg)	**MAP peak** (mmHg)	**ΔMAP** (mmHg)	**HR basal** (bpm)	**HR peak** (bpm)	**ΔHR** (bpm)	**BRS ΔPI/ΔMAP** (ms/mmHg)
FVB/N	104.2 ± 4.5	70.8 ± 7.7	-33.3 ± 6.0	704.2 ± 39.2	767.3 ± 44.3	63.2 ± 14.2	0.22 ± 0.06
AT1a-KO	87.1 ± 5.0***	59.6 ± 5.0*	-27.5 ± 1.3	701.4 ± 34.5	742.3 ± 33.0	40.9 ± 16.6	0.15 ± 0.04
Agt-KO	101.7 ± 5.4	59.9 ± 7.8*	-41.8 ± 4.6**	690.3 ± 28.0	748.6 ± 26.8	58.3 ± 19.0	0.17 ± 0.06
Agt-KO-Tg	85.5 ± 4.1$^{****\#\#\#\#}$	57.3 ± 4.4*	-28.2 ± 2.4$^{\#\#\#}$	716.2 ± 32.4	747.5 ± 29.6	31.3 ± 9.5*	0.12 ± 0.03*
Agt-Tg	116.5 ± 4.2**	83.7 ± 3.6*	-32.8 ± 5.2	717.8 ± 29.2	749.3 ± 36.4	31.5 ± 9.8*	0.11 ± 0.03**

Values are mean ± SD for 6-7 animals in each group. $^{*}P<0.05$, $^{**}P<0.01$, $^{***}P<0.001$, $^{****}P<0.0001$ vs FVB/N; $^{\#\#\#}P<0.001$, $^{\#\#\#\#}P<0.0001$ vs Agt-KO (ANOVA followed by Tukey multi comparison post hoc test). $^{\S}P<0.05$ vs FVB/N (Student's *t* test). BRS = baroreflex sensitivity

4.3.8 Brain Ang II modulation of GABAergic gene expression in brainstem

The brain expression of AT2 receptor is restricted to few areas, one of these areas is the NTS where AT2 receptors are expressed mostly by GABAergic neurons (74, 152). Recently, it was demonstrated that chronic administration of an AT2 specific agonist attenuated experimental hypertension due to reduction of GABA receptors and GABA producing enzymes (glutamate decarboxylases) in the NTS (153). Agt-KO-Tg and Agt-Tg likely has Ang II action in the NTS because the baroreflex response of the HR is integrated at this nucleus and Ang II is known to blunt this process (154). Because brain Ang II reduced BP in Agt-KO-Tg, we sought this could be a possible mechanism of BP reduction. To test this, the mRNA levels of glutamate decarboxylases 1 and 2 were quantified in the brainstem. However, increased brain Ang II formation did not change the expression of these enzymes in Agt-KO-Tg or Agt-Tg (Figure 37A,B). In addition, the mRNA levels of the vesicular GABA transporter and the GABA B receptors 1 and 2 were also not altered in brainstem (Figure 37C-E).

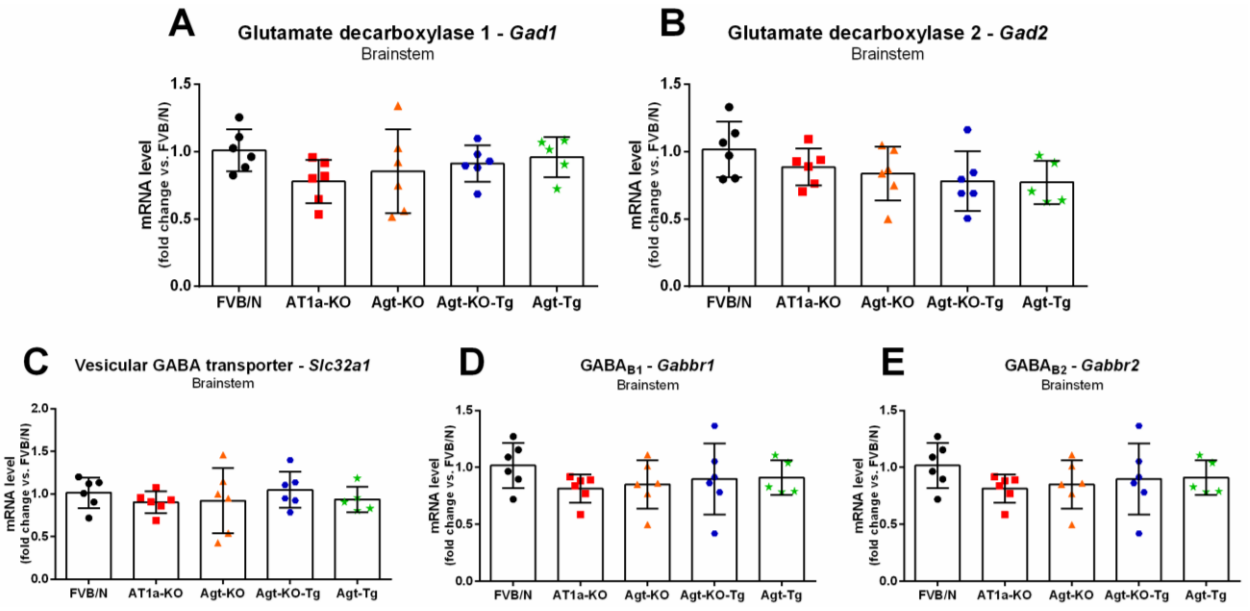

Figure 37 - Brainstem expression of GABAergic genes.
mRNA levels of glutamate decarboxylases 1 (**A**) and 2 (**B**), vesicular GABA transporter (**C**), and the GABA B receptors 1 ($GABA_{B1}$, **D**) and 2 ($GABA_{B2}$, **E**).

4.3.9 Brain Ang II and renal physiology

4.3.9.1 Renal morphology

Circulating Ang II acting on renal AT1 receptors are important for priming renal development, in the absence of AT1 postnatal injuries are found in rodents (146, 155). Histological examination of kidneys from AT1a-KO mice showed mild damage, while Agt-KO and Agt-KO-Tg displayed similarly damaged kidneys. In these lines, marked reduced medullary area was found due to hydronephrosis and atrophy of the renal papilla. In addition, mononuclear cell infiltration seems to be increased in Agt-KO and Agt-KO-Tg. Finally, the wall thickness of small arteries was found exaggeratedly increased in Agt-KO and Agt-KO-Tg, this effect was only mild in AT1a-KO (Figure 38). These results point to a dispensable involvement of brain Ang II in renal development, and suggest the peptide does not reach the circulation, at least not at enough concentration, during embryonic development when BBB is permeable.

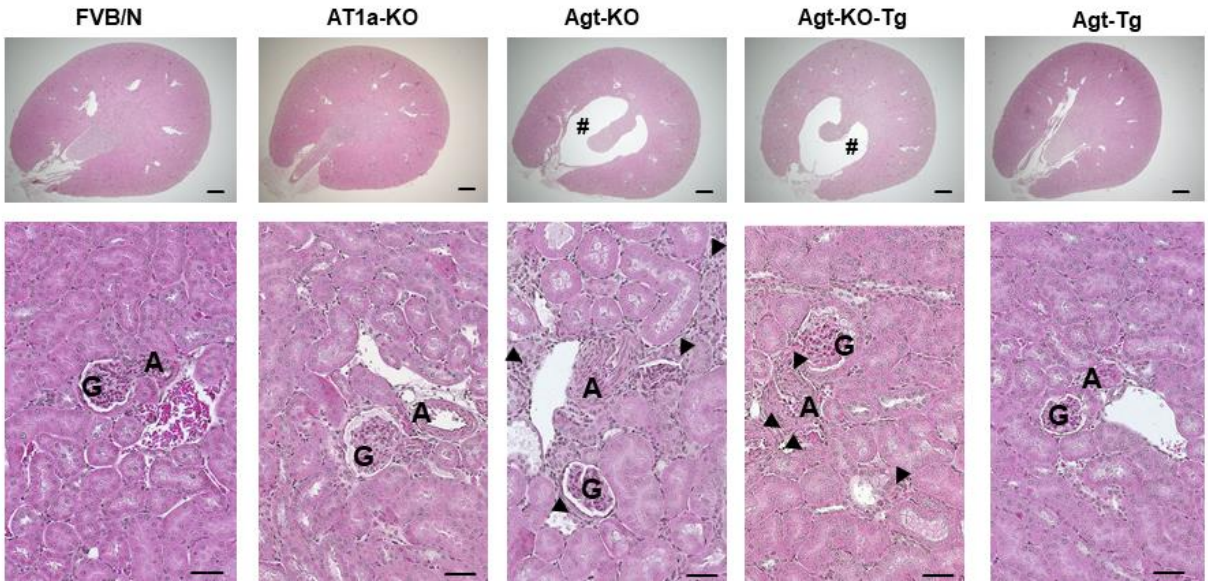

Figure 38 - Renal morphology.
Representative images of coronal kidney sections stained with hematoxylin eosin. Agt-KO and Agt-KO-Tg present hydronephrosis (**#**), small artery hypercellularity leading to wall thickening (**A**), and increased mononuclear cell infiltration (**arrowheads**). AT1a-KO presents only mild arterial wall thickening. G = glomerulus. Top panels scale bars are 500 µm, lower panels bars are 200 µm.

4.3.9.2 Renal Fibrosis

To visualize renal fibrosis, kidney renal coronal sections were stained with Picro sirius red. AT1a-KO displayed slightly increased staining however Agt-KO and Agt-KO-Tg presented

diffuse fibrosis including peritubular, perivascular, periglomerular, and intra-arterial collagen accumulation (Figure 39).

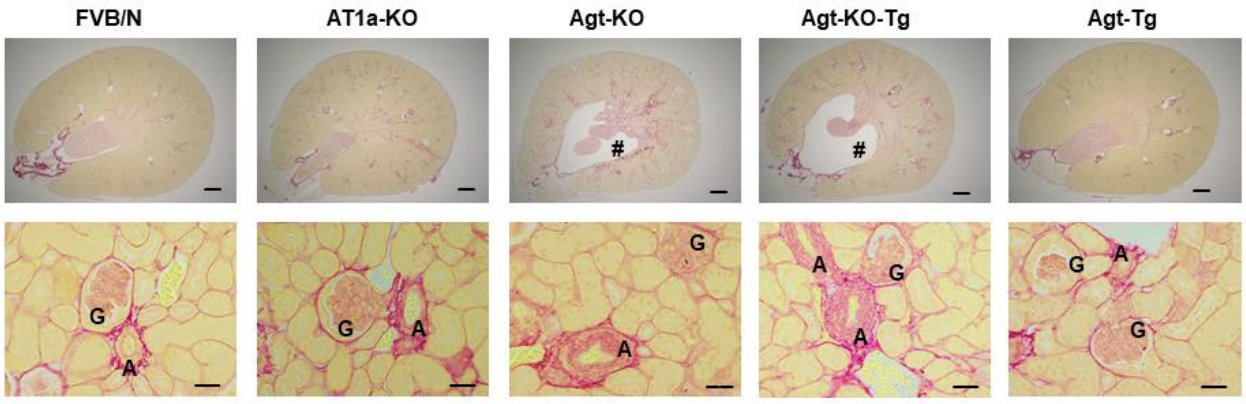

Figure 39 - Renal collagen staining.
Histochemical collagen staining in representative kidney sections. Top panels are showing diffuse collagen accumulation (pink) in AT1a-KO, Agt-KO and Agt-KO coronal kidney sections. Lower panels are showing increased perivascular fibrosis in all lines, and intravascular fibrosis exclusive to AT1a-KO, Agt-KO and Agt-KO-Tg. # = hydronephrosis, G = glomerulus, A = artery. Top panels scale bars are 500 µm, lower panels bars are 40 µm.

To quantify the renal fibrosis, the expression of the collagens I, III, and IV were quantified by RT-qPCR in kidneys. Collagen I and III expression was likewise increased in Agt-KO and Agt-KO-Tg, while Collagen IV expression was not altered (Figure 40A-C). Accordingly, the mRNA levels of fibronectin, an essential protein for fibrillogenesis, were found increased in Agt-KO and Agt-KO-Tg (Figure 40D). Interestingly, the expression of transforming growth factor beta (TGF-β), a master regulator of collagen secretion and fibroblast differentiation, was only slightly upregulated in Agt-KO (Figure 40E). Accordingly, the protein expression of alpha smooth muscle actin (α-SMA), a marker of myofibroblasts, which are pathogenic differentiated fibroblasts, was not altered as measured by Western blots (Figure 40F).

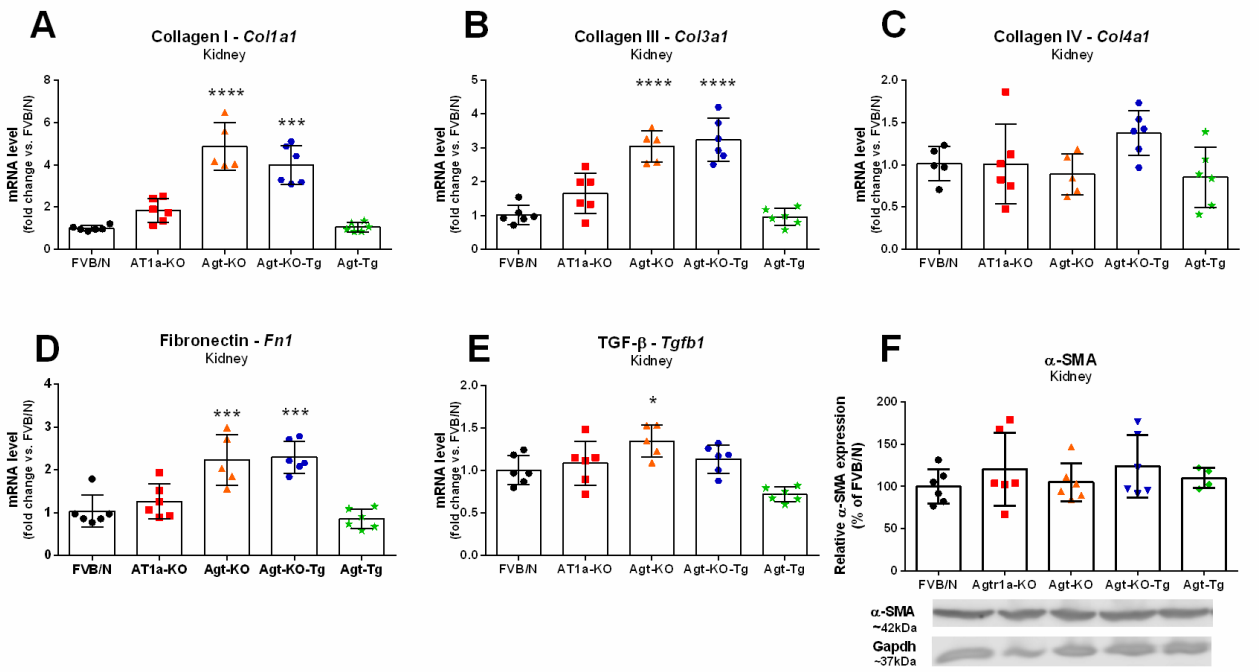

Figure 40 - Renal fibrosis.
Renal mRNA levels of collagen I (**A**), collagen III (**B**), collagen IV (**C**), fibronectin (**D**) and transforming growth factor beta (TGF-β) (**E**). Alpha smooth muscle actin (α-SMA) protein expression in kidneys (**F**). Values are mean ± SD $^{*}P<0.05$, $^{***}P<0.001$, $^{****}P<0.0001$ vs FVB/N (ANOVA followed by Tukey multiple comparison post hoc test).

4.3.9.3 Renal inflammation

The histological findings indicated increased infiltration of immune cells in the kidneys of Agt-KO and Agt-KO-Tg (see section 4.3.9.1). Therefore, RT-qPCR was used to estimate renal immune cell infiltration by quantifying gene expression of CD68 and CD3, which are macrophage- and T-cell-specific markers, respectively. As suggested by the histological findings Agt-KO and Agt-KO-Tg presented increased expression of T-cell and macrophage markers however in Agt-KO-Tg the levels of CD68 were slightly decreased in comparison to Agt-KO (Figure 41A,B). Additionally, the macrophage infiltration was confirmed at the protein level using an antibody against another macrophage marker, Iba-1 in Western blots (Figure 41C). In agreement both lines displayed increased levels of vascular cell adhesion molecule-1 (VCAM-1) and intercellular adhesion molecule-1 (ICAM-1) (Figure 41D,E) that are essential scaffolds for circulating leucocytes migration into tissues. Finally, the gene expression of the leucocyte chemoattractant cytokines TNFα and RANTES as well as the T-cell activator CD86 were found increased in Agt-KO and partially rescued in Agt-KO-Tg (Figure 41F-H). Altogether, the data

suggests that Agt-KO likely presents a more proinflammatory kidney environment that could gradually contribute to renal function deterioration.

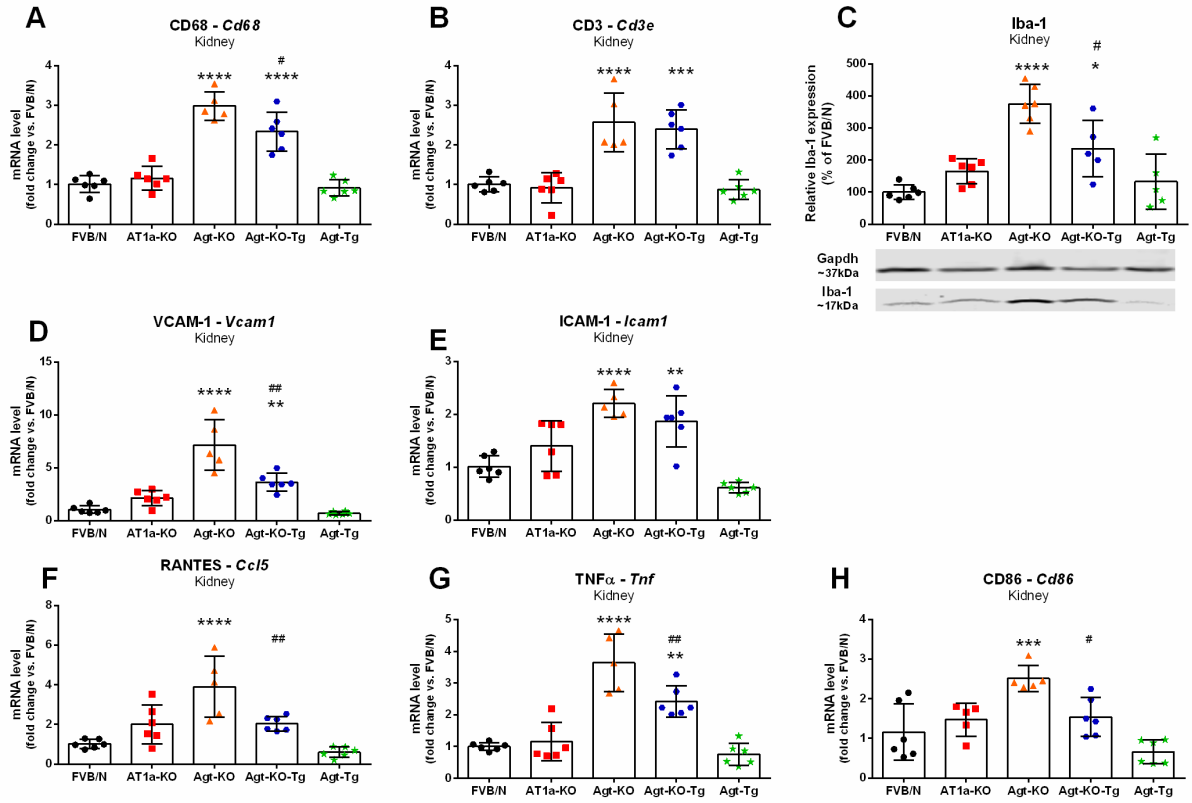

Figure 41 - Renal immune cell infiltration.
Macrophage marker, CD68 (**A**), and T-cell marker, CD3 (**B**) mRNA expression in kidney. Iba-1 protein levels in the kidney (**C**). Renal mRNA levels of the adhesion molecules VCAM-1 (**D**) and ICAM-1 (**E**). Renal mRNA levels of the cytokines RANTES (**F**) and TNFα (**G**), and the T-cell activator CD86 (**H**). Values are mean ± SD $^{**}P<0.01$, $^{***}P<0.001$, $^{****}P<0.0001$ vs FVB/N; $^{\#}P<0.05$. $^{\#\#}P<0.01$ vs Agt-KO (ANOVA followed by Tukey multiple comparison post hoc test).

4.3.9.4 Renal function

In order to evaluate the impact of the morphological renal damage on renal function, urinary and plasmatic markers were measured. Previously, Agt-KO mice have been described having an impaired urine concentration ability (146, 156). This phenotype was confirmed in the FVB/N Agt-KO, by urinary creatinine measurement. Creatinine is a metabolite constantly excreted and the reduced creatinine concentration in Agt-KO and Agt-KO-Tg urine indicates increased urinary output (Table 52). Using the creatinine concentration in spot urine, the urinary volume was estimated, as observed in Table 52, Agt-KO produces ~3 times more urine than wildtype while Agt-KO-Tg ~2 times more, demonstrating a partial rescue of the phenotype in Agt-KO-Tg. As consequence of a high urinary output, sodium and potassium concentrations were also decreased

in Agt-KO and Agt-KO-Tg urine (Table 52). However, these values were not different from controls when the concentration was corrected by the creatinine concentration, except in AT1a-KO that presented increased sodium and potassium excretion (Table 52). Interestingly despite presenting several morphological alterations and immune cell infiltration, the renal damage marker albumin was only marginally increased in AT1a-KO (Table 52).

Table 52 - Urine parameters and urinary volume estimation.

Parameter (unit)	FVB/N, *n*=8	AT1a-KO, *n*=8	Agt-KO, *n*=8	Agt-KO-Tg, *n*=8	Agt-Tg, *n*=7
Na^+ (mmol/L)	93.4 ± 39.8	131.7 ± 51.0	28.6 ± 7.7**	50.0 ± 11.4	74.7 ± 41.0
K^+ (mmol/L)	242.7 ± 45.9	264.3 ± 33.8	102.8 ± 14.9****	158.9 ± 46.4$^{***\#}$	285.5 ± 19.8
ALB (µg/dL)	608.8 ± 68.0	890.0 ± 385.5	327.5 ± 174.2	392.5 ± 67.1	558.6 ± 109.3
CRE (mg/dL)	30.9 ± 5.6	25.1 ± 5.5	9.9 ± 0.9****	15.2 ± 3.0**** §§§	32.1 ± 4.3
$[Na^+]/[K^+]$	0.39 ± 0.20	0.50 ± 0.18	0.28 ± 0.08	0.33 ± 0.10	0.27 ± 0.17
$[Na^+]$/[CRE]	2.99 ± 1.17	5.18 ± 1.14**	2.92 ± 0.83	3.34 ± 0.70	2.41 ± 1.35
$[K^+]$/[CRE]	8.11 ± 2.28	10.92 ± 2.26*	10.40 ± 1.09	10.35 ± 2.12	9.01 ± 1.36
[ALB]/[CRE]	20.2 ± 3.9	34.5 ± 11.6*	32.3 ± 15.2	26.3 ± 4.4	17.7 ± 4.7
eUvol. (% of FVB/N)	102.6 ± 17.5	130.2 ± 33.7	314.8 ± 28.0****	211.3 ± 46.6**** #####	97.6 ± 13.0

Values are mean ± SD. $^{*}P<0.05$, $^{***}P<0.001$, $^{****}P<0.0001$ vs FVB/N; $^{\#}P<0.05$, $^{\#\#\#\#}P<0.0001$ vs Agt-KO (ANOVA followed by Tukey multi comparison post hoc test). §§§$P<0.001$ vs FVB/N (Student's *t* test). K^+ = potassium, Na^+ = sodium, ALB = albumin, CRE = creatinine, [ALB] = albumin concentration, [CRE] = creatinine concentration, $[K^+]$ = potassium concentration, $[Na^+]$ = sodium concentration, eUvol. = estimated urinary volume.

Plasma markers of renal function, urea and creatinine, were increased in Agt-KO and Agt-KO-Tg, however, Agt-KO-Tg partially rescued the phenotype in comparison to Agt-KO (Table 53). Agt-KO and Agt-KO-Tg presented increased plasma sodium concentration (Table 53), and potassium was decreased in Agt-KO-Tg (Table 53). After observing increased sodium levels in Agt-KO and Agt-KO-Tg, total proteins and albumin levels were measured in the same samples as markers of dehydration. Both parameters were found increased in Agt-KO and Agt-KO-Tg (Table 53). Finally, the plasma osmolality was calculated and Agt-KO and Agt-KO-Tg presented increased plasma osmolality, but Agt-KO-Tg presented lower levels in comparison to Agt-KO. Comparing the plasma osmolality and urea levels, clearly, plasma osmolality levels paralleled the plasma urea, pointing to urea as the most relevant osmolyte influencing plasma osmolality in Agt-KO and Agt-KO-Tg (Table 53).

Table 53 - Plasma parameters for renal function and hydromineral balance.

Parameter (unit)	FVB/N, *n*=6	AT1a-KO, *n*=6	Agt-KO, *n*=6	Agt-KO-Tg, *n*=5	Agt-Tg, *n*=5
CRE (mg/dL)	0.12 ± 0.01	0.14 ± 0.01**	0.17 ± 0.01****	0.15 ± 0.01**	0.12 ± 0.01
BUN (mg/dl)	26.8 ± 2.3	26.9 ± 1.8	81.4 ± 8.0****	45.8 ± 4.4$^{****\#\#\#\#}$	26.8 ± 1.4
Na^+ (mmol/L)	147.6 ± 0.6	146.6 ± 0.7	150.6 ± 2.2*	150.8 ± 2.3*	148.5 ± 0.8
K^+ (mmol/L)	7.01 ± 0.66	7.29 ± 0.87	7.40 ± 0.50	6.00 ± 0.16$^{\#\#}$	6.51 ± 0.43
Cl^- (µg/dL)	107.1 ± 0.77	108.3 ± 2.98	110.6 ± 2.77	110.7 ± 2.46	108.2 ± 0.50
$[Na^+]/[K^+]$	21.2 ± 2.1	19.9 ± 2.3	20.3 ± 1.6	25.1 ± 0.8$^{**\#\#}$	22.9 ± 1.3
TP (g/l)	50.0 ± 1.2	50.1 ± 0.8	53.1 ± 2.3**	55.1 ± 1.3****	50.0 ± 0.9
ALB (g/l)	25.5 ± 1.4	26.5 ± 0.9	27.8 ± 1.1**	27.6 ± 0.6*	26.0 ± 0.6
GLC (mg/dl)	271.3 ± 37.1	283.1 ± 17.1	262.2 ± 53.7	262. 5 ± 39.6	259.6 ± 29.3
Osmolality (mosmol/kg H_2O)	319.9 ± 2.5	318.5 ± 3.5	345.5 ± 3.4****	331.1 ± 5.6$^{***\#\#\#\#}$	320.9 ± 2.8

Values are mean ± SD for 5–6 animals in each group. $^{*}P<0.05$, $^{**}P<0.01$, $^{***}P<0.001$, $^{****}P<0.0001$ vs FVB/N; $^{\#\#}P<0.01$, $^{\#\#\#\#}P<0.0001$ vs Agt-KO (ANOVA followed by Tukey multi comparison post hoc test). K^+ = potassium, Na^+ = sodium, ALB = albumin, BUN = blood urea nitrogen, CRE = creatinine, eUvol. = estimated urinary volume, GLC = glucose, TP = total proteins, $[K^+]$ = potassium concentration, $[Na^+]$ = sodium concentration.

4.3.9.5 Renal sodium transporters

Finding altered urinary output and plasma sodium levels led us to measure the gene expression of the most relevant renal tubular sodium channels involved in sodium reabsorption from the primary urine. The gene expression of the sodium-hydrogen exchanger 3 (NHE3) expressed at the proximal tubule was modestly increased in Agt-KO-Tg and Agt-Tg (Figure 42A). The mRNA levels of the genes encoding the sodium-potassium-chloride (NKCC2) and sodium-chloride transporter (NCC) cotransporters were downregulated in AT1a-KO and Agt-KO, and AT1a-KO and Agt-KO and Agt-KO-Tg, respectively (Figure 42B,C). In addition, the mRNA levels of *Scnn1a* encoding the α-subunit of epithelial sodium transporter (ENaC) were downregulated in Agt-KO (Figure 42D). The gene expression of the sodium transporters clearly demonstrated that Agt-KO was the most affected line. To discard that the phenotype is due to decreased tubular cells, the mRNA expression of Pax8 was quantified but no differences were observed (Figure 42E). Pax8 is a transcription factor essential for renal development but also expressed in adult kidney specifically on epithelial cells along all tubular segments (157). Finally, the mRNA levels of aquaporin-2, a major protein responsible for renal water reabsorption, were quantified by RT-qPCR. Figure 42F shows that only Agt-KO-Tg presented a small increase in aquaporin-2 gene expression.

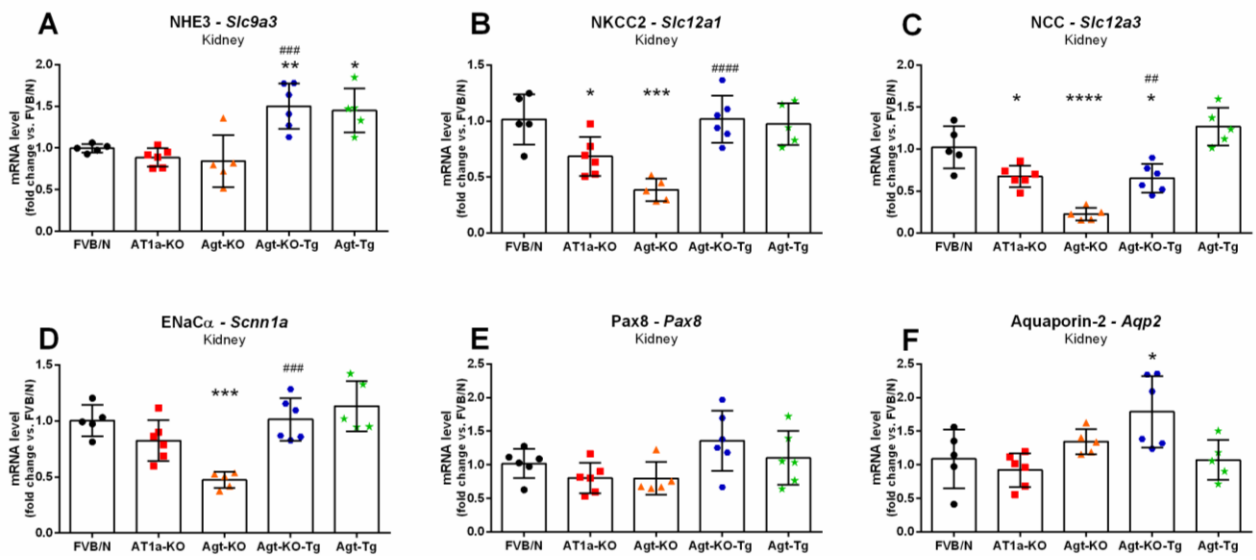

Figure 42 - Tubular sodium transporters expression.
mRNA levels of genes encoding key sodium renal transporters: NHE3 (hydrogen exchanger) (**A**), NKCC2 (sodium-potassium-chloride cotransporters) (**B**), sodium-chloride cotransporter (NCC) (**C**), and the α-subunit of the epithelial sodium channel (ENaC-α) (**D**). Renal mRNA levels of the tubular transcription factor Pax8 (**E**) and aquaporin-2 (**F**). Values are mean ± SD $^{*}P<0.05$, $^{***}P<0.001$, $^{****}P<0.0001$ vs FVB/N; $^{\#\#}P<0.01$, $^{\#\#\#}P<0.001$ vs Agt-KO (ANOVA followed by Tukey multi comparison post hoc test).

4.3.9.6 Renal SNA, Ren, and NO producing enzymes

Renal SNA modulates water and sodium reabsorption but also Ren release, and SNA is suggested to influence the renal immune cell traffic. Therefore, renal SNA was estimated quantifying renal NE. AT1a-KO and Agt-KO presented similar elevated renal SNA, and brain Ang II potentiates renal SNA in Agt-KO-Tg only, because Agt-Tg presented normal renal SNA (Figure 43A). In addition to NE quantification, the expression of the adrenergic receptors was evaluated using RT-qPCR in kidneys of these mice (Table 54). Renal total Ren expression (*Ren1* plus *Ren2*) was increased AT1a-KO and Agt-KO-Tg, while in Agt-KO Ren gene expression was curiously not altered (Figure 43B). In addition, Agt-Tg presented reduced renal Ren expression as shown in section 4.3.1.3. Altogether Ren mRNA expression is most likely influenced by baseline BP rather than reduced Ang II signaling or lack of Agt. To confirm the Ren finding, aldo-keto reductase family 1 member B7 (Akr1b7) gene expression was verified, because this protein was recently described to be a marker for renal Ren cells (158). Surprisingly, Akr1b7 mRNA levels did not parallel the Ren mRNA levels as expected, since all lines presented unaltered Akr1b7 expression except Agt-KO that presented reduced levels of the Akr1b7 (Figure 43C). In addition to NE, NO controls the renal blood flow and therefore the glomerular filtration rate. For which reason renal

NO synthetizing enzymes were measured by RT-qPCR. Interestingly, neuronal NO synthase expression was slightly increased in Agt-KO but around 4-fold in Agt-KO-Tg (Figure 43D). The levels of endothelial NO synthase were not altered (Figure 43E).

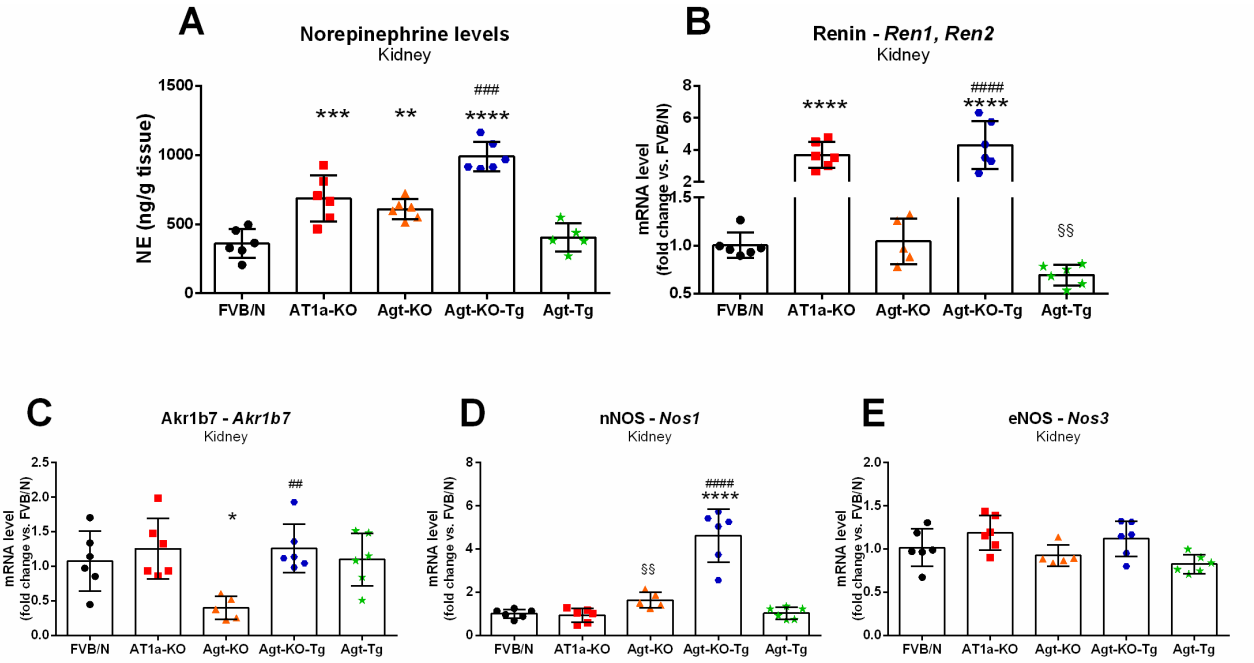

Figure 43 - Renal SNA, and mRNA levels of Ren and NO producing enzymes.
Renal SNA estimated by renal norepinephrine quantification (**A**). mRNA levels of Ren encoding genes (**B**) and the Ren expression marker Akr1b7 in kidneys (**C**). Renal mRNA levels of neuronal NO synthase (nNOS) (**D**) and endothelial NO synthase (eNOS) (**E**). Values are mean ± SD $^{*}P<0.05$, $^{**}P<0.01$, $^{***}P<0.001$, $^{****}P<0.0001$ vs FVB/N; $^{\#\#}P<0.01$, $^{\#\#\#}P<0.001$, $^{\#\#\#\#}P<0.0001$ vs Agt-KO (ANOVA followed by Tukey multi comparison post hoc test); $^{\S\S}P<0.01$ vs FVB/N (Student's *t* test).

Table 54 - Renal α and β adrenergic receptors mRNA expression.

Protein - *Gene*	FVB/N	AT1a-KO	Agt-KO	Agt-KO-Tg	Agt-Tg
$\alpha1_A$ - *Adra1a*	1.0 ± 0.11	0.9 ± 0.27	0.6 ± 0.05**	0.9 ± 0.17	0.9 ± 0.12
$\alpha1_B$ - *Adra1b*	1.0 ± 0.16	1.2 ± 0.25	2.0 ± 0.48****	1.6 ± 0.18**	1.17 ± 0.27
$\alpha1_D$ - *Adra1d*	1.0 ± 0.33	1.2 ± 0.42	1.5 ± 0.27	1.16 ± 0.35	1.2 ± 0.22
$\alpha2_A$ - *Adra2a*	1.0 ± 0.10	1.0 ± 0.35	1.2 ± 0.34	1.4 ± 0.17*	0.7 ± 0.14
$\alpha2_B$ - *Adra2b*	1.0 ± 0.34	1.8 ± 0.33**	1.5 ± 0.26	1.2 ± 0.13	1.5 ± 0.41
α2c - *Adra2c*	1.0 ± 0.24	0.6 ± 0.18**	0.4 ± 0.09****	0.5 ± 0.08**	0.7 ± 0.13**
β1 - *Adrb1*	1.0 ± 0.25	1.7 ± 0.51*	0.8 ± 0.29	1.1 ± 0.18	1.4 ± 0.27
β2 - *Adrb2*	1.0 ± 0.23	1.8 ± 0.50***	1.9 ± 0.20***	1.4 ± 0.26$^{\#}$	1.0 ± 0.16

Values are mean ± SD for 5–6 animals in each group. $^{*}P<0.05$, $^{**}P<0.01$, $^{***}P<0.001$, $^{****}P<0.0001$ vs FVB/N; $^{\#}P<0.05$ vs Agt-KO (ANOVA followed by Tukey multi comparison post hoc test).

4.3.9.7 Renal denervation effect on baseline BP

We suspected that brain Ang II switched the vasculature and renal SNA balance in Agt-KO-Tg. In other words, the damaged kidney of Agt-KO may either require higher SNA or BP to control its function. Owing to the fact that the kidney is innervated by the SNS and afferents that relay

information to the brain that may influence downstream SNA, renal denervation was chosen to test if altered renal nerves activity modulates BP. Baseline BP was quantified before renal denervation, and the BP response to a bilateral renal denervation procedure was recorded constantly over a week (Figure 44A). One week after surgery and cardiovascular data acquisition the animals were sacrificed, and renal NE was measured to validate the procedure. Figure 44B indicates that renal denervation was successful because NE was reduced by over 90% in comparison to intact kidneys, except for the right kidney of one Agt-KO mouse for which the cardiovascular data was excluded.

Before surgery baseline MAP was indistinguishable between Agt-KO and wildtype but reduced in Agt-KO-Tg as in previous measurements, but interestingly baseline HR in Agt-KO and Agt-KO-Tg was found slightly reduced (Figure 44C,E). As previously reported, wildtype mice displayed reduced MAP immediately after denervation and this effect was sustained over a week (Figure 44D). Surprisingly, Agt-KO and Agt-KO-Tg only presented a slight MAP reduction in comparison to controls however contrary to controls the effect developed gradually after denervation reaching the peak around four to five days after surgery (Figure 44D). In all lines the HR increased the day after surgery (20-40 bpm) and gradually returned to baseline levels except in Agt-KO in which HR remained elevated during the whole recording period (Figure 44F).

Altogether it can be concluded from this data set that normal BP in Agt-KO is unlikely driven by altered renal efferent or afferent nerve firing. However very interestingly, denervating these mouse lines suggested that the main BP lowering effect of renal denervation is most likely mediated by reducing the peripheral RAS activity. In other words, only wildtype mice have circulating Agt, thus, reducing renal Ren release in Agt-KO and Agt-KO-Tg would not impact Ang II production once the substrate of Ren, Agt, is absent.

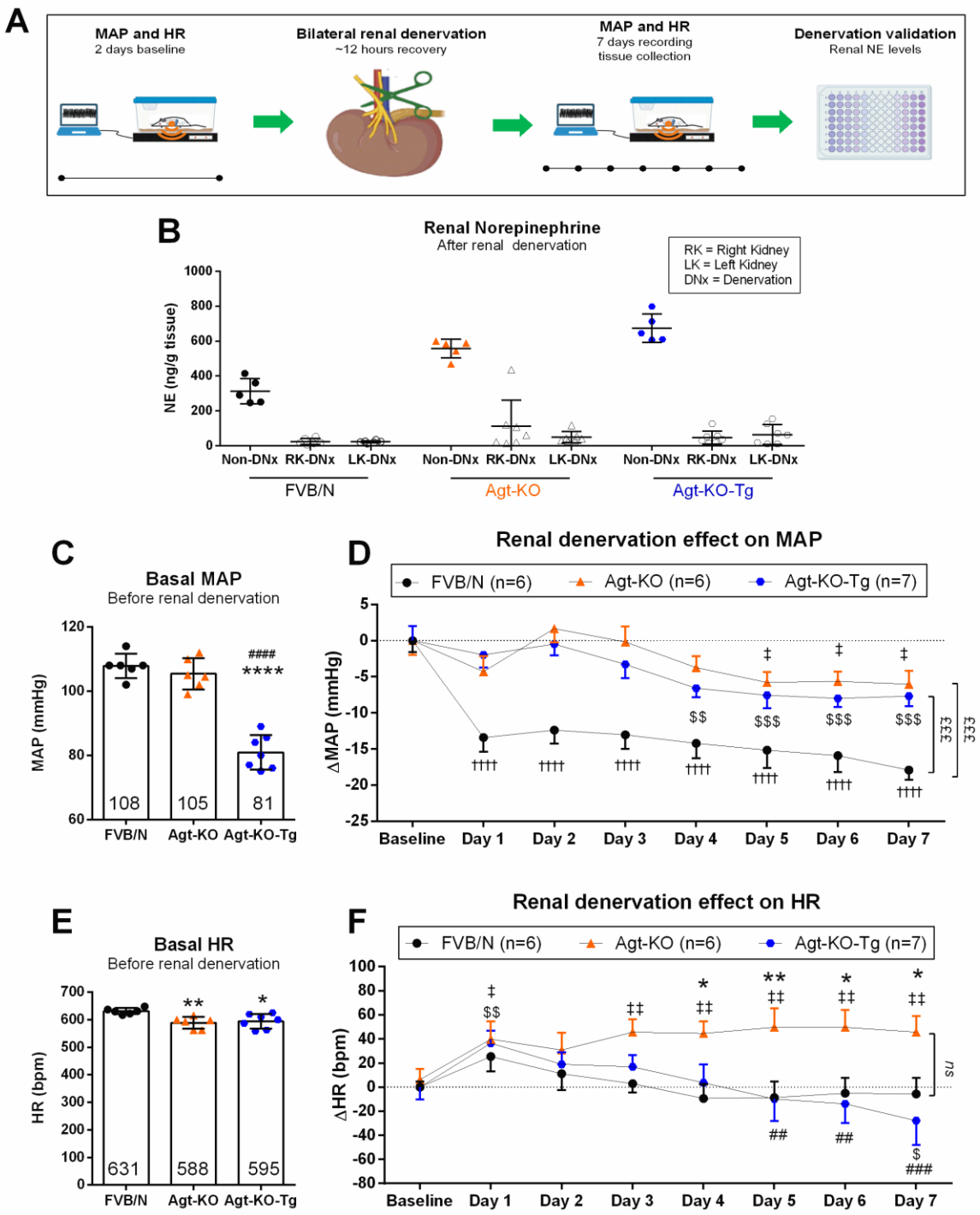

Figure 44 - Effect of renal denervation on cardiovascular homeostasis.
Schematic representation of the renal denervation protocol to quantify cardiovascular effects using telemetry (**A**). Quantification of renal norepinephrine (NE) to validate the renal denervation procedure in each kidney of each mouse (**B**). 48-hour baseline MAP before renal denervation (**C**). MAP response to bilateral renal denervation (**D**). 48-hour baseline HR before renal denervation (**E**). HR response to bilateral renal denervation (**F**). For **B**, **C** and **E** values are mean ± SD $^{*}P<0.05$, $^{**}P<0.01$, $^{****}P<0.0001$ vs FVB/N; $^{\#\#\#\#}P<0.0001$ vs Agt-KO; (ANOVA followed by Tukey multiple comparison post hoc test). For **D**, **F** values are mean ± SE $^{\dagger\dagger\dagger\dagger}P<0.0001$ FVB/N post-denervation vs FVB/N baseline. $^{\ddagger}P<0.05$, $^{\ddagger\ddagger}P<0.01$ Agt-KO post-denervation vs Agt-KO baseline; $^{\$}P<0.05$, $^{\$\$}P<0.01$, $^{\$\$\$}P<0.001$ Agt-KO-Tg post-denervation vs Agt-KO-Tg baseline; $^{*}P<0.05$, $^{**}P<0.01$ Agt-KO post-denervation vs FVB/N post-denervation, $^{\#\#\#}P<0.001$, $^{\#\#}P<0.01$ Agt-KO-Tg post-denervation vs Agt-KO post-denervation; $^{£££}P<0.001$ vs FVB/N post-denervation; *ns* = not significant (2-way ANOVA with repeated measurements followed by Tukey or Dunnett multiple comparison post hoc test). MAP = mean arterial pressure, HR = heart rate. The illustration in **A** was partially created in BioRender.com.

4.4 Genetic basis of the BP resilience in FVB/N Agt-KO

4.4.1 Baseline BP phenotype of F2 Agt-KO

Previous studies using Agt-KO either on mixed, outbred ICR, or inbred C57BL/6 background reported hypotension with around 25 mmHg MAP reduction, contrary to the FVB/N Agt-KO reported in this study (112, 159, 160). Genome sequences of inbred mouse strains only subtly differ among each other (161), therefore, we suspected that the BP phenotype in FVB/N Agt-KO is likely driven by a single gene. A GWAS was developed to test this hypothesis by crossing FVB/N Agt-KO with C57BL/6N wildtype (Figure 45A). The resulting heterozygous F1 littermates were intercrossed, and the MAP of males and females of the F2 Agt-KO offspring was measured (Figure 45A). Strikingly, the phenotyping of 67 F2 Agt-KO FVB/N (males and females aging between 20-40 weeks) presented a mendelian bimodal distribution of MAP where most of the mice were hypotensive and a smaller fraction normotensive. This phenotypic distribution suggests a single locus associated with the trait (Figure 45B,D). Interestingly, among the normotensive group part of the mice presented baseline MAP that could be categorized as hypertensive however these animals were treated as normotensive for posterior GWAS analyses (Figure 45B). Plotting the HR of hypotensive and normotensive mice no differential distribution was observed but rather a continuum (Figure 45C), discarding an involvement of the cardiac frequency on the basal MAP phenotype. Note: 7 wildtype mice (4 males and 3 females), F2-Agt-KO littermates, were included in the cardiovascular phenotyping to estimate basal MAP and HR in mixed background mice (C57BL/6 x FVB/N) (Figure 45BC) but these mice were not included in the association analyses.

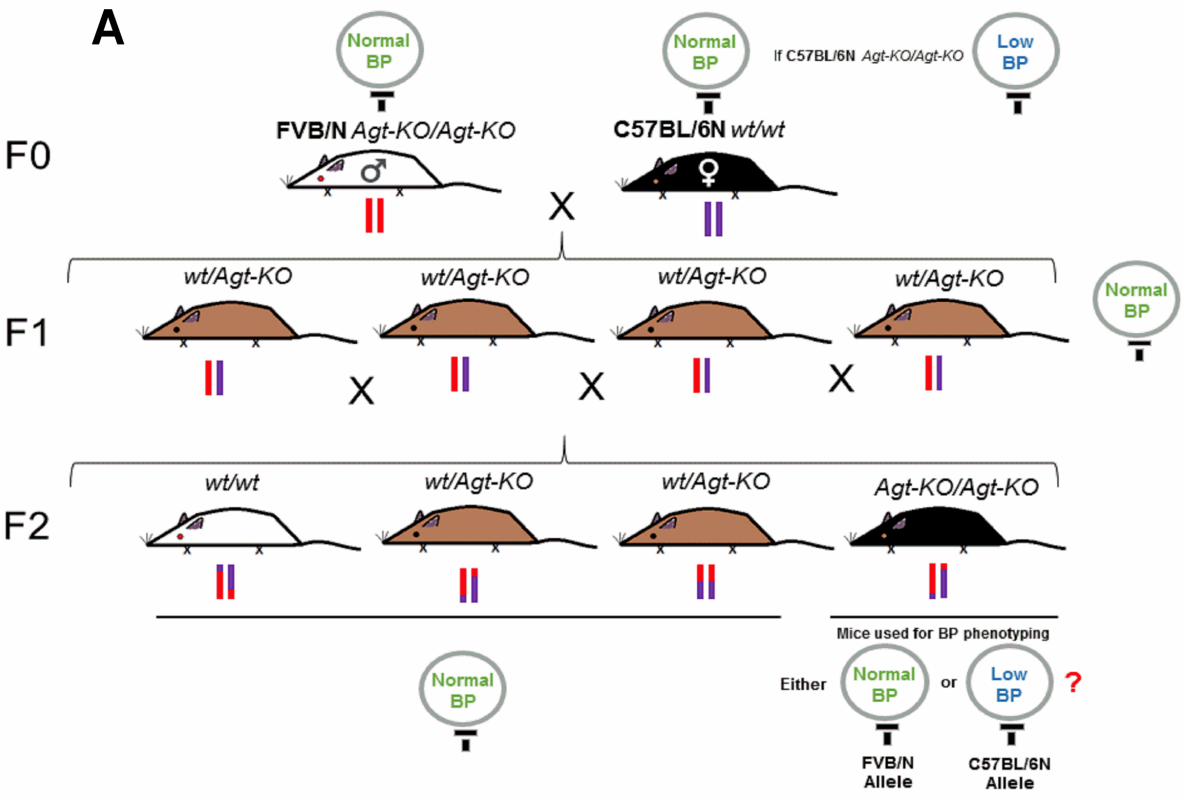

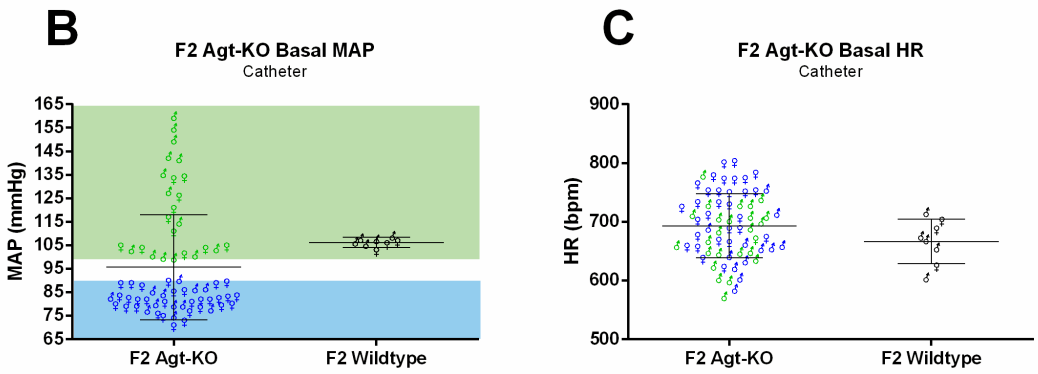

D

	Frequency	Percentage
Hypotensive	42	63%
Normotensive	25	37%
Total	67	100%

Figure 45 - Generation and phenotyping of F2 Agt-KO to find the locus responsible for normotension in FVB/N Agt-KO. Schematic representation of the mouse breeding strategy used to produce F2 Agt-KO (**A**), red and purple stripes represent FVB/N and C57BL/6N chromosomes, respectively. Mixed striped colors are representing random chromosomal crossing over events during meiosis. Note, the fur color does not associate to the *knockout* allele neither to the locus responsible for the BP phenotype. MAP phenotype in 25-40 weeks old males and females F2 Agt-KO and wildtype littermates (**B**). Mice with basal MAP ≤ 90 mmHg were considered hypotensive (blue background) and mice with basal MAP ≥ 100 normotensive (green background). MAP was acquired using the catheter method. HR in F2 Agt-KO and wildtype littermates (**C**). Proportion of F2 Agt-KO hypotensive and normotensive mice (**D**). ♂ = data points from male mice, ♀ = data points from female mice. Green data points = data points from mice classified as hypotensive; blue data points = data points from mice classified as normotensives. BP = blood pressure, MAP = mean arterial pressure, HR = heart rate, *wt* = wildtype allele.

To confirm the baseline BP phenotype in F2 Agt-KO, the heart weight tibia length ratio was used as an unbiased read out of the phenotype because the surgical burden unlikely alters these parameters as it may influence the BP during acute quantification. Initially a Pearson correlation coefficient was calculated plotting the heart weight tibia length ration against the baseline MAP. Both females (Figure 46A) and males (Figure 46B) presented a positive correlation indicating that the cardiac mass strongly depends on baseline BP levels. As predicted, hypotensive F2 Agt-KO mice presented lighter hearts in comparison to age matched normotensives (Figure 46C,D).

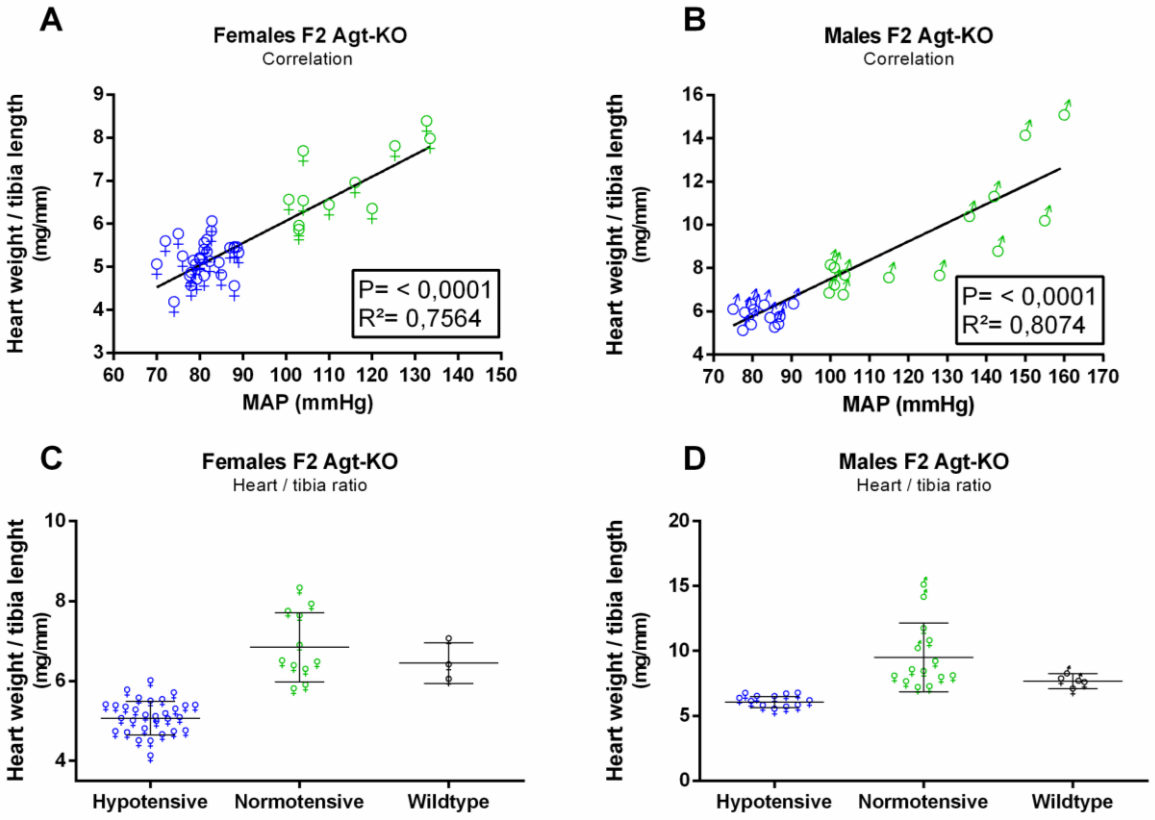

Figure 46 - Cardiac mass and BP relationship in F2 Agt-KO mice.
Correlation between heart weight/tibia length and MAP in F2 Agt-KO females (**A**) and males (**B**), blue and green data points are hypotensive and normotensive mice, respectively. Heart weight tibia length ratios in F2 Agt-KO females (**C**) and males (**D**). R^2 = correlation coefficient, MAP = mean arterial pressure.

4.4.2 Genome-wide association study with the F2 Agt-KO

The GWAS was performed using the 67 F2 Agt-KO (FVB/N x C57BL/6N) mice. Manhattan plots were generated by two distinct logistic regression analyses modeling the MAP phenotype against the whole genome SNP-mapping data obtained with the GigaMUGA markers. For both analysis models, additive (Figure 47A) and dominant (Figure 47B), several loci were found

significantly associated with the normotensive phenotype contrary to our expectations. However, the locus found in chromosome 1 was the most significant in both models (Figure 47A,B) and the SNP rs32049164 was the top hit.

Based on the bimodal BP phenotype observed in the F2 Agt-KO, we expected all mice or at least a high percentage of the normotensive population would present biallelic FVB/N sequence at the linked region on chromosome 1. Thus, a single SNP to control the phenotype discrepancies among our F2 Agt-KO and ultimately among FVB/N and C57BL/6N strains was expected. To test this, we selected the SNP rs31768697 which is ~122Kb upstream of the top hit. Only in the FVB/N allele a restriction site for HincII is present in this SNP which makes it easy to distinguish which SNP (FVB/N and/or C57BL6/N) is present in any sample, after restriction digestion of the PCR product that flanks the SNP sequence. Out of 25 mice classified as normotensives only 13 contained biallelic FVB/N sequence, demonstrating that this locus might not necessarily be alone involved in the BP controlling phenotype. In addition, this locus on chromosome 1 was analyzed *in silico* but none of the genes comprising this region have known BP modulatory function. Therefore, there is not only one gene responsible for the normotension in Agt-KO and the amount of analyzed animals needs to be increased and to fine map candidate gene(s) responsible for the BP phenotype.

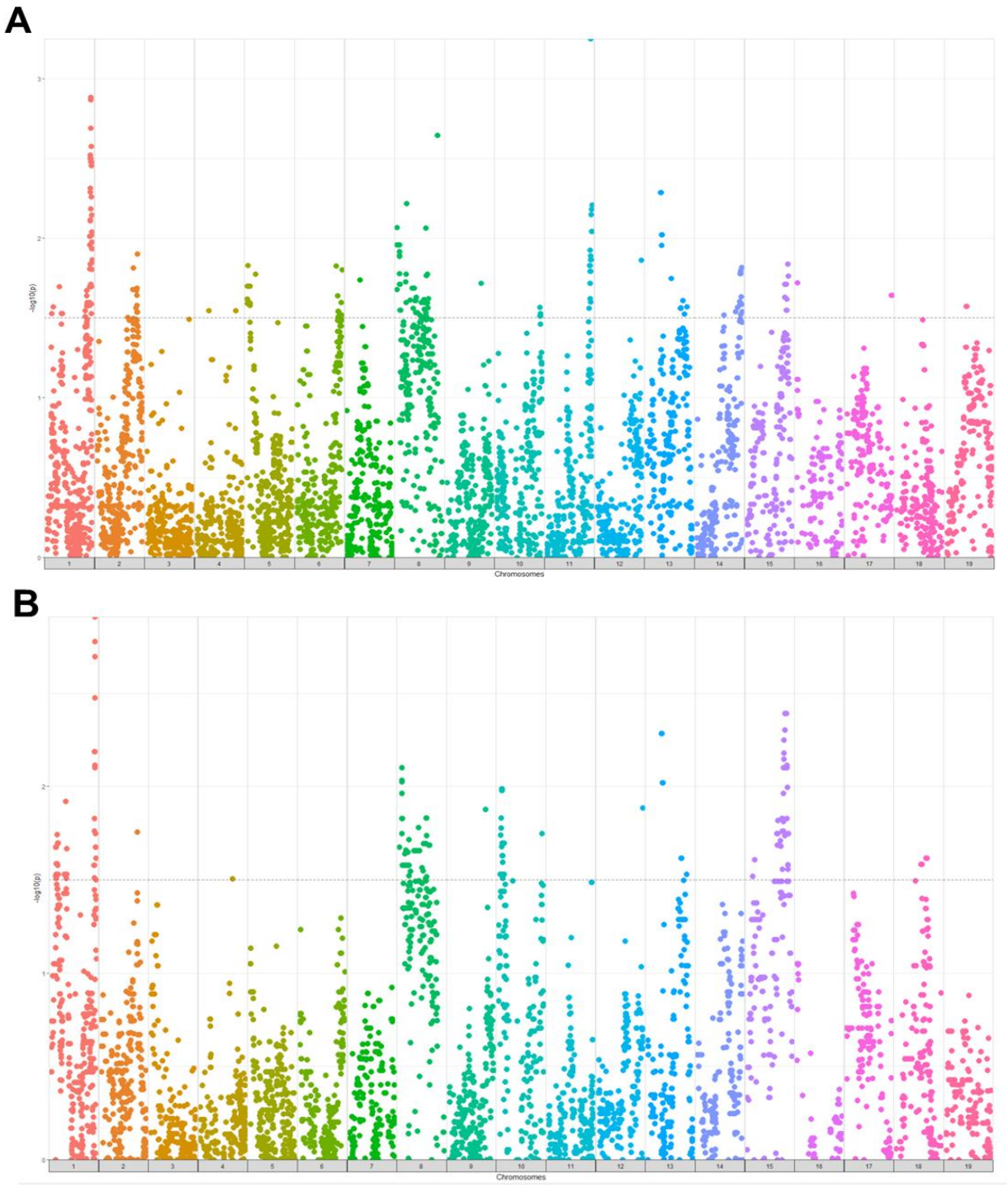

Figure 47 - Manhattan plots of the GWAS.
Manhattan plot for the additive (**A**) and the dominant (**B**) models of the GWAS on baseline MAP in F2 Agt-KO mice in a total of 67 animals, 42 hypotensive and 25 normotensives. The horizontal dotted line represents the threshold for genome-wide significance. For the dominant model in **B,** hypotensive mice were treated as controls and normotensive mice as cases.

4.5 RAS and erythropoiesis control

4.5.1 Baseline erythropoiesis

Since mice with gene targeted deletion of Agt, or one of the enzymes required for Ang II formation (Ren or ACE) as well as mice lacking the expression of both Ang II AT1 receptors had been shown to be anemic (162, 163), a capillary-based method was used to screen the baseline red blood cell (RBC) proportion in blood of our mouse lines. Figure 48A shows that FVB/N Agt-KO is also anemic. Interestingly, brain Ang II rescued the phenotype in Agt-KO-Tg and, accordingly, Agt-Tg displayed an increased hematocrit in comparison to wildtype (Figure 48A). The hematocrit alterations found seem to be independent of the major erythropoiesis controlling factor erythropoietin, because renal erythropoietin mRNA levels were not altered (Figure 48B).

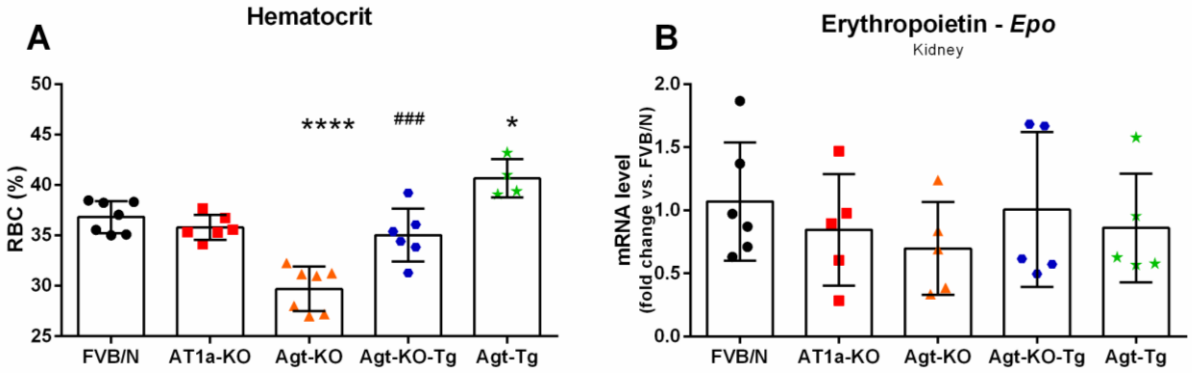

Figure 48 - Baseline hematocrit and erythropoietin expression.
Baseline hematocrit. Values are mean ± SD $^{*}P<0.05$, $^{****}P<0.0001$ vs FVB/N; $^{\#\#\#}P<0.001$ vs Agt-KO (ANOVA followed by Tukey multiple comparison post hoc test). RBC = red blood cell.

4.5.1.1 Hematology of anemic Agt-KO and rescued Agt-KO-Tg

To better understand the anemic phenotype and the rescue of erythropoiesis in Agt-KO and Agt-KO-Tg respectively, EDTA-blood was collected for quantification of hematology parameters. The parameters are displayed in Table 55. Interestingly, Agt-KO presented unaltered RBC counts but hemoglobin (HGB) and RBC hemoglobin content (MCH) was decreased in this line. In addition, RBC size measured by the mean corpuscular volume (MCV) was reduced, contributing to the reduced hematocrit, and indicating microcytic anemia. Interestingly, in comparison to Agt-KO, the erythropoiesis rescue in Agt-KO-Tg involved increased RBC and hemoglobin production. However, RBC size (MCV) and hemoglobin content (MCH) were not rescued,

indicating that the hematocrit was rescued increasing RBC production, but not RBC hemoglobin content and/or size.

Table 55 - Baseline hematology in Agt-KO and Agt-KO-Tg.

Parameter (unit)	FVB/N (*n* =7)	Agt-KO (*n* =7)	Agt-KO-Tg (*n* =6)
RBC (M/µL)	9.4 ± 0.5	8.9 ± 0.6	9.9 ± 0.7$^{\#\#}$
HGB (g/dL)	13.3 ± 0.8	12.0 ± 0.8*	13.72 ± 0.7$^{\#\#}$
MCH (pg)	14.3 ± 0.3	13.5 ± 0.3***	13.7 ± 0.2**
MCHC (g/dL)	29.7 ± 0.7	29.4 ± 0.4	29.8 ± 0.8
MCV (fL)	48.3 ± 1.2	45.7 ± 0.8***	46.2 ± 1.3**
RET (K/µL)	463 ± 99	446 ± 65	465 ± 59
PLT (K/µL)	1194 ± 131	1019 ± 59	1088 ± 207
WBC (K/µL)	5.43 ± 1.90	3.69 ± 2.07	5.26 ± 1.85

Values are mean ± SD $^{*}P<0.05$, $^{**}P<0.01$, $^{***}P<0.001$, vs FVB/N; $^{\#\#}P<0.01$ vs Agt-KO (ANOVA followed by Tukey multiple comparison post hoc test). $^{\S}P<0.001$ vs FVB/N (Student's *t* test). HGB = hemoglobin, RBC = red blood cell, MCH = mean corpuscular hemoglobin, MCHC = mean corpuscular hemoglobin concentration, MCV = mean corpuscular volume, RET = reticulocytes, PLT= platelets, WBC = white blood cell.

4.5.1.2 Brain Ang II controls erythropoiesis via SNA

The hematology of Agt-KO-Tg indicated the brain-borne Ang II increases RBC production. However, these mice present altered urinary volume and dehydration markers (see section 4.3.9.4). Even though Agt-KO and Agt-KO-Tg presented similarly altered plasma dehydration markers one may argue that RBC counts might be influenced by the extracellular volume. Because in Agt-Tg all markers were not altered, we explored in depth the influence of brain Ang II on erythropoiesis in Agt-Tg only using an automated blood cell counter. The results showed that Agt-Tg displays increased RBC counts (Figure 49B). Accordingly, hemoglobin concentration was found increased in Agt-Tg (Figure 49C) but the amount of hemoglobin per RBC remained at normal levels (Figure 49D). In addition, reticulocytes which are the circulating RBC precursors were found increased in Agt-Tg (Figure 49E) demonstrating that central Ang II potentiates erythropoiesis in the transgenic line similarly to the findings in Agt-KO-Tg. Because erythropoietin expression was not altered (Figure 48B), we sought to chemically ablate SNA in the periphery to verify if brain-borne Ang II increases erythropoiesis via SNA to hematopoietic organs (Figure 49A). Remarkably, 6-OHDA made the RBC and hemoglobin values to become indistinguishable between sympathectomized wildtype and Agt-Tg (Figure 49B,C). Accordingly, blood reticulocyte production became even in Agt-Tg mice after sympathectomy (Figure 49E). Collectively, the data strongly supports an unprecedented mechanism in which brain Ang II via

the SNA controls erythropoiesis. In addition, no changes in white blood cells and platelets were detected at baseline between wildtype and Agt-Tg groups (Figure 49F,G). However, the sympathectomy protocol depleted the circulating white blood cell to a similar extent in both wildtype and Agt-Tg (Figure 49G). Table 56 shows the differential leucocyte count demonstrating that all major classes of leucocytes were similarly depleted in wildtype and Agt-Tg.

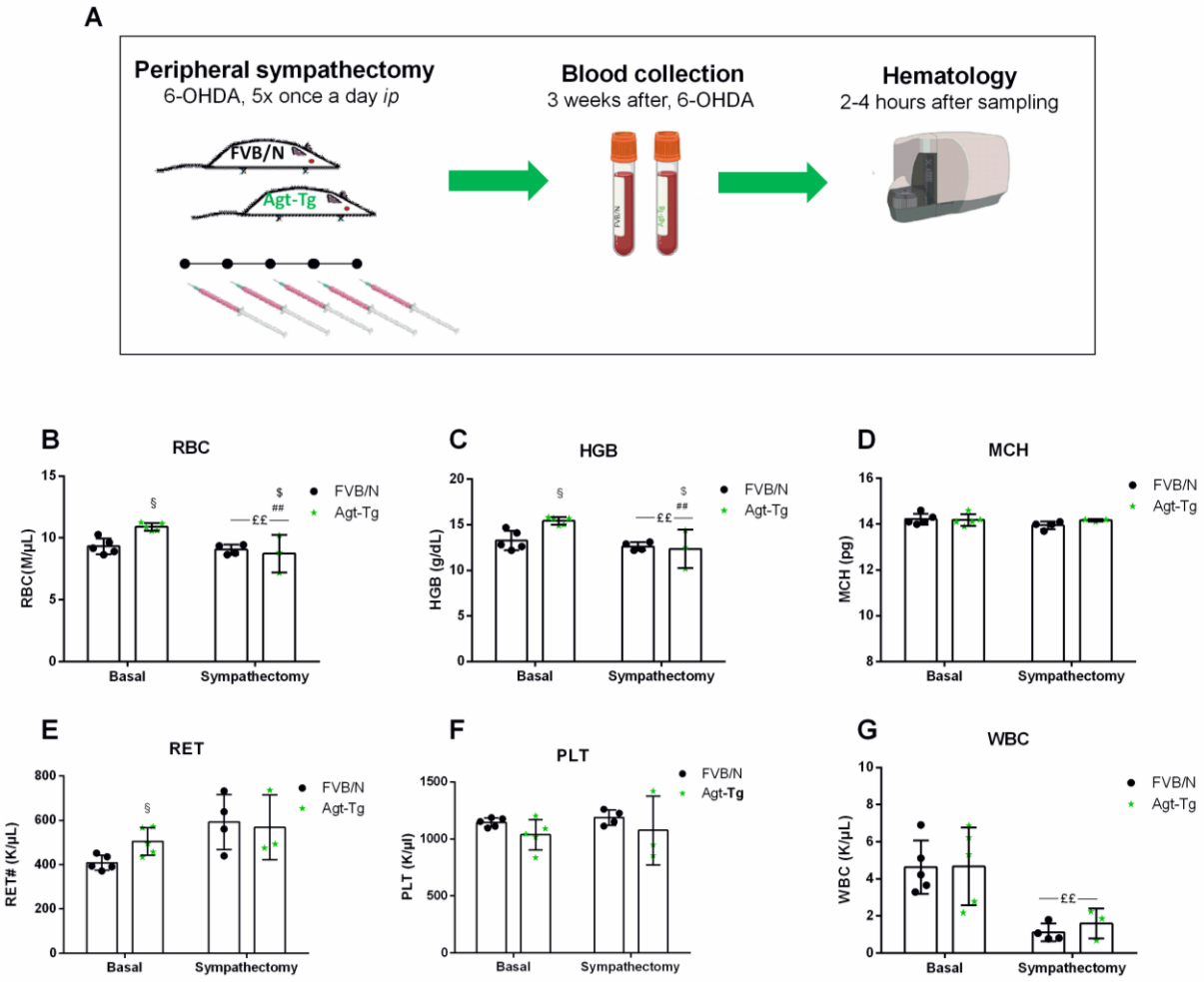

Figure 49 - Effect of peripheral sympathectomy on baseline erythropoiesis in Agt-Tg.
Schematic representation of the peripheral sympathectomy with 6-hydroxydopamine (6-OHDA) to study the impact of SNA on erythropoiesis in Agt-Tg, baseline parameters were obtained including age-matched controls and Agt-Tg that were not treated with 6-OHDA (**A**). Upregulated basal RBC (**B**), HGB (**C**) and RET (**E**) but unaltered MCH (**D**) in Agt-Tg EDTA-whole blood. Peripheral sympathectomy with 6-OHDA normalizes RBC (**B**), HGB (**C**) and RET (**E**) values in Agt-Tg. Baseline and sympathectomy effect on circulating platelets = PLT (**F**) and white blood cell = WBC (**G**). Values are mean ± SD; $^{\S}P<0.05$ vs basal FVB/N; $^{\#\#}P<0.01$ vs basal Agt-Tg; $^{\pounds\pounds}P<0.01$ sympathectomy effect; $^{\$}P<0.05$ interaction between genotype and sympathectomy (two-way ANOVA followed by Tukey multiple comparison post hoc test). HGB = hemoglobin, MCH = mean corpuscular hemoglobin, RBC = red blood cell, RET = reticulocytes, PLT = platelets, WBC = white blood cell. The illustration in **A** was partially created in BioRender.com.

Table 56 - Differential leukocyte counts before and after sympathectomy.

Parameter (unit)	Treatment	FVB/N	Agt-Tg
WBC (K/µL)	Baseline	4.6 ± 1.3	4.7 ± 1.9
	Sympathectomy	1.1 ± 0.4$^{*,£££}$	1.6 ± 0.7$^{£££}$
Lymphocytes (K/µL)	Baseline	3.74 ± 0.95	4.00 ± 1.89
	Sympathectomy	0.78 ± 0.29$^{*,£££}$	1.17 ± 0.55$^{£££}$
Neutrophils (K/µL)	Baseline	0.62 ± 0.29	0.66 ± 0.26
	Sympathectomy	0.25 ± 0.08£	0.31 ± 0.09$^{£}$
Monocytes (K/µL)	Baseline	0.23 ± 0.07	0.17 ± 0.10
	Sympathectomy	0.07 ± 0.04$^{*,££}$	0.07 ± 0.02$^{££}$
Eosinophils (K/µL)	Baseline	0.04 ± 0.02	0.04 ± 0.02
	Sympathectomy	0.02 ± 0.01	0.01 ± 0.00
Basophils (K/µL)	Baseline	0.006 ± 0.005	0.008 ± 0.007
	Sympathectomy	0.003 ± 0.004	*n.d*

Values are mean ± SD for 3-5 animals in each group. The results were analyzed by two-way ANOVA followed by Tukey's post hoc test. $^{*}P < 0.05$ *vs* basal FVB/N. $^{£}P < 0.05$, $^{££}P < 0.01$, $^{£££}P < 0.001$ sympathectomy effect. No significant interaction among sympathectomy and genotype was observed. *n.d.* = not detected.

Because Agt-Tg presents brain Ang II levels that may exceed normal physiological concentrations, the model may not satisfactorily answer whether endogenous brain Ang II influences baseline erythropoiesis. To answer this question, we used a transgenic rat model carrying an antisense RNA against *Agt* in astrocytes leading to 90% Agt protein depletion exclusively in the brain thus brain-specifically decreasing the RAS activity including Ang II. Strikingly, the transgenic rat (TGR-680) displayed reduced hematocrit in comparison to age-matched controls (10 weeks old) suggesting indeed an involvement of brain Ang II in baseline erythropoiesis (Figure 50A). In agrement TGR-680 presented reduced RBC (Figure 50B) and hemoglobin (Figure 50C) while the mean corpouscular hemoglobin was not changed by decreased central Ang II (Figure 50D). Additionaly reduced brain RAS activity had no effect on platelets and white blood cell counts (Figure 50E,F). Collectively, the hematological phenotyping of TGR-680 strongly supports a modulatory role of Ang II in baseline erythropoiesis homeostasis that is mediated via SNA as shown using the Agt-Tg transgenic mouse line.

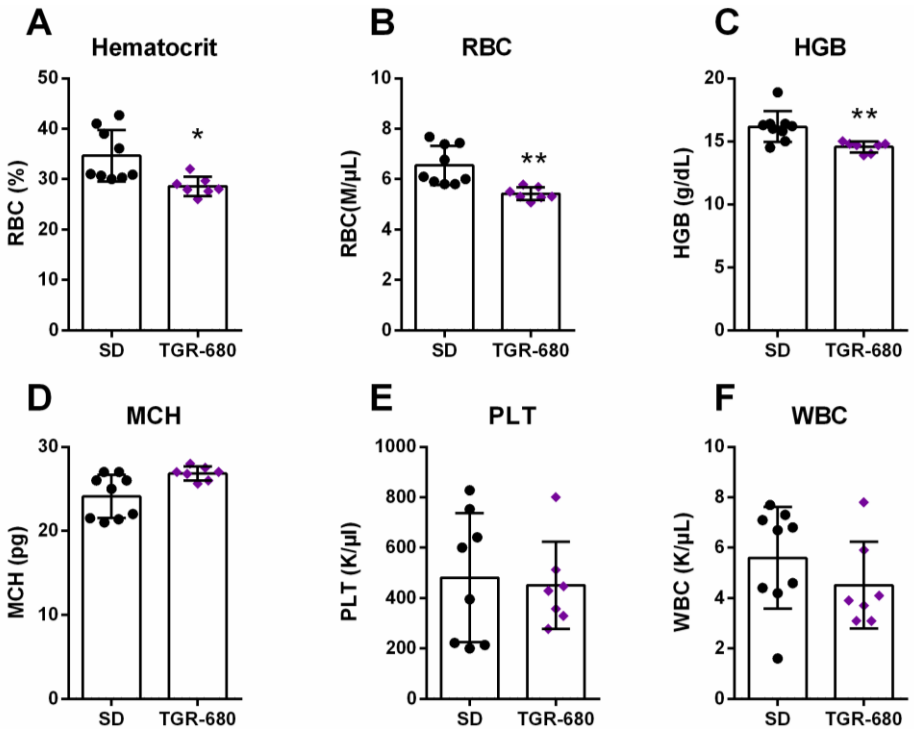

Figure 50 - Hematology in rats with depleted brain RAS.
Decreased hematocrit (**A**), RBC (**B**) and HGB (**C**) in 10 weeks old rats with depleted brain RAS, TGR-680 compared to their controls Sprague-Dawley (SD). Unaltered MCH (**D**), PLT (**E**) and WBC (**F**) in rats with depleted brain RAS. $^{*}P < 0.05$, $^{**}P < 0.01$ vs SD (Student's *t* test). RBC = red blood cell, HGB = hemoglobin, MCH = mean corpuscular hemoglobin, PLT = platelets, WBC = white blood cell.

4.5.2 RAS and iron homeostasis

Because microcytic anemia was identified in mice lacking circulating RAS, plasma iron and ferritin were quantified because this phenotype is indicative of body iron deficiency (100). In agreement with the microcytic anemia, the anemic line Agt-KO presented reduced iron levels in the plasma (Figure 51A) but also the Agt-KO-Tg line with partially rescued hematocrit. In this line, iron levels were even further reduced in comparison to Agt-KO (Figure 51A). In agreement with the iron measurements ferritin levels were decreased in plasma of Agt-KO and Agt-KO-Tg indicating that iron storage within organs is also depleted in these lines (Figure 51B). Hepcidin is a major factor controlling gut iron uptake. Upon liver release, hepcidin internalizes the gut epithelial iron transporter ferroportin by direct binding and thereby reduces iron uptake (100). The hepatic mRNA levels of the two genes encoding hepcidin (*Hamp1/Hamp2*) in the mouse were quantified. Interestingly, *Hamp1* liver expression was downregulated in Agt-KO only (Figure 51C), while *Hamp2* was unaltered in all lines (Figure 51D). In addition, interleukin 6 gene expression was measured because of its fundamental role in regulating hepcidin expression.

Hepatic interleukin 6 mRNA levels showed no alteration among the lines (Figure 51E). The data indicates that hepcidin is not causative of the iron phenotype in Agt-KO and Agt-KO-Tg, on the contrary, this factor is downregulated in Agt-KO likely because of the low plasma iron levels. In addition, a pilot measurement of urinary iron levels was performed with 3 FVB/N and 3 Agt-KO to verify if the renal damage led to higher iron excretion. The measurements were possible but below the limit of quantification of the AU480 analyzer in Agt-KO. Nevertheless, the calculated [iron]/[CRE] was apparently reduced in Agt-KO 0.3 ± 0.05 vs FVB/N 1.2 ± 0.71. Collectively, our data suggests that Ang II has peripheral and central mechanisms modulating erythropoiesis which are completely independent. In the brain, Ang II increases SNA to hematopoietic tissues, and in the periphery, Ang II seems to modulate iron absorption. Interestingly, the central mechanism increases RBC production even during iron deficiency caused by the lack of peripheral RAS peptides.

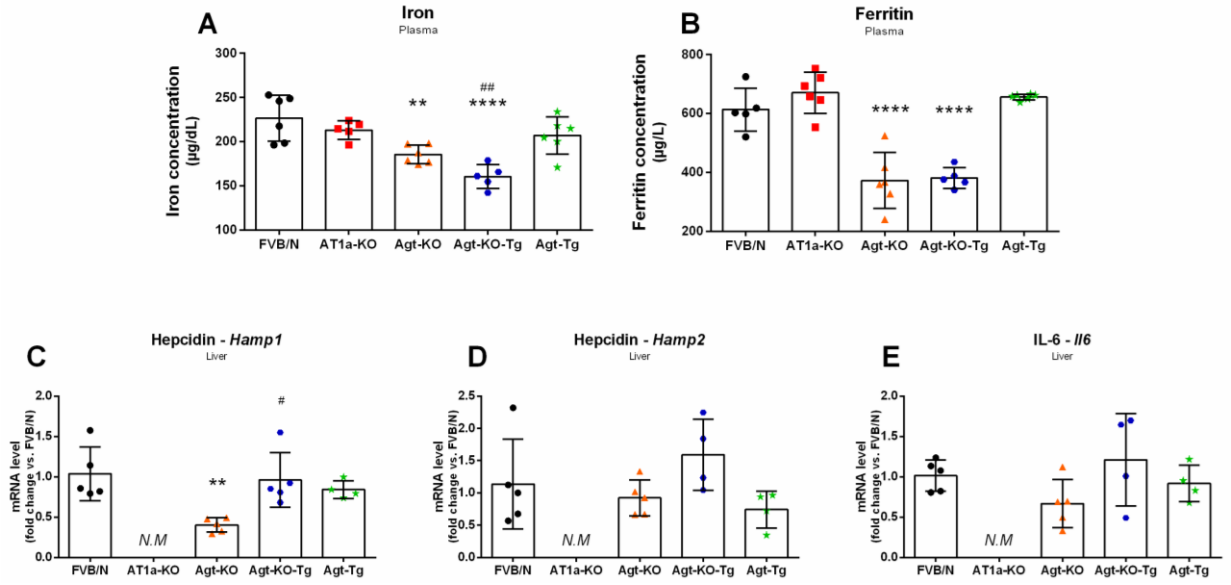

Figure 51 - Erythropoietin production, and iron balance.
Renal erythropoietin mRNA levels (**A**). Plasma levels of iron (**B**) and ferritin (**C**). mRNA levels of the hepcidin encoding genes *Hamp1*(**D**) and *Hamp2* (**E**) and *Il6* (**F**). Values are mean ± SD $^{**}P<0.01$, $^{****}P<0.0001$ vs FVB/N; $^{\#\#}P<0.01$ vs Agt-KO (ANOVA followed by Tukey multiple comparison post hoc test). IL-6 = interleukin 6, N.M = not measured.

Agt is expressed in the gut (Figure 16A) and circulating Agt protein infiltrates peripheral tissues and accounts for the majority tissue Agt (59). To discard a direct involvement of Agt itself on iron uptake as a possible interaction with gut iron transporters such as ferroportin (100), we investigated body iron homeostasis in Ren-KO. Using glass capillary hematocrit, we confirmed that Ren-KO are anemic (Figure 52A). Strikingly, these mice also displayed reduced circulating

levels of iron (Figure 52B), indicating an unlikely direct effect of Agt protein on iron absorption. However, ferritin levels were not significantly reduced in Ren-KO as in Agt-KO and Agt-KO-Tg (Figure 52C). The iron homeostasis in the mouse lines studied suggests that the iron deficiency may be associated with peripheral Ang II modulation of the iron uptake. Of note, spontaneous bleeding was never observed in these lines.

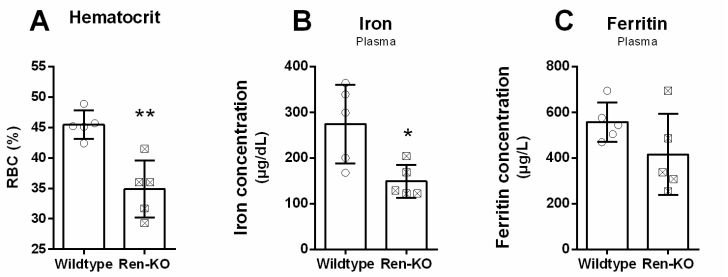

Figure 52 - Hematocrit, and iron balance in Ren-KO mice.
Baseline hematocrit (**A**). Plasma levels of iron (**B**) and ferritin (**C**). Values are mean ± SD $^{*}P<0.05$, $^{**}P<0.01$ vs FVB/N (Student's *t* test). RBC = red blood cell.

4.6 Generation of knockout and knockin rats

We primarily focused on the generation of a knockin rat in which the sequence coding ChR2 was planned to be introduced in the locus coding the *Agtr1a*, AT1a. This model was designed to combine optogenetics with cardiovascular phenotyping in order to understand brain circuits subjected to Ang II modulation. AT1a-KO knockout animals were generating in parallel in experiments used to optimize the CRISPR/Cas9 gene editing efficiency in SD rat embryos.

4.6.1 AT1a knockout rats

Initially, the *in vitro* generated sgRNA was microinjected together with recombinant Cas9 protein into SD rat zygotes to assess the efficiency of the sgRNA in targeting the rat *Agtr1a* allele in the zygote. Although 13 putative founders were born, none of these rats carried mutations at the *Agtr1a* locus (Table 1). Therefore, we changed to a novel method in which 2-cell stage embryos were used to electroporate *in vitro* transcribed sgRNA plus Cas9 protein, this methodology yielded 2 rats containing NHEJ mutations (Table 1). Because the NHEJ events happened at a rate too low to generate knockin rats, the methodology was changed again using purchased sgRNA. This time an efficiency of ~33% was observed, because 5 out of 15 born offspring from electroporated embryos carried mutations at the targeted region of the *Agtr1a* locus (Table 1). To establish an AT1a-KO line, one of the 5 mutant rats that carried a monoallelic insertion of 2

adenosines was selected (Figure 53). This mutant rat was mated with SD rats and heterozygous littermates intercrossed to obtain AT1a-KO rats used to establish a line and validate the model.

Table 57 - Summary of CRISPR/Cas9 mediated NHEJ.

Target cell	sgRNA	Cas9	Offspring	NHEJ (%)	Germeline transmition
Zygote	*In vitro* transcribed	Recombinant protein	13	0 (0.0%)	NT
2-cell embryo	*In vitro* transcribed	Recombinant protein	23	2 (8.7%)	NT
2-cell embryo	Commercial (crRNA/tracrRNA)	Recombinant protein	15	5 (33%)	Yes

NHEJ = non-homologous-end-joining, crRNA = CRISPR RNA, tracRNA = trans-activating CRISPR RNA, NT = not tested.

Figure 53 - Generation of AT1a-KO rats using CRISPR/Cas9.
Chromatogram displaying sequences from amplified PCR products flanking the sgRNA binding sequence. Wildtype (top panel), heterozygous (middle panel) and homozygous (lower panel). The red rectangle shows a mutation induced by NHEJ (2 adenosines insertion "AA", lower panel) in the rat *Agtr1a* locus upon CRISPR/Cas9 mediated DNA double strand break. The sequencing was performed using the forward primer used in the PCR. PAM = protospacer adjacent motif, sgRNA = single-guided RNA.

4.6.1.1 Functional validation of AT1a-KO knockout rats

AT1a-KO mice were generated over 25 years ago. Two well described major phenotypes are hypotension and blunted pressor response to acute Ang II administration, demonstrating that AT1a is the major Ang receptor expressed in resistance vessels (111, 164). Therefore, AT1a-KO rats were functionally validated *in vivo* comparing with wildtype littermates the Ang II pressure response as well as the baseline cardiovascular parameters (Figure 53). Acute cardiovascular

phenotyping demonstrated that AT1a-KO presented reduced baseline MAP (Figure 54A) with no alterations in the HR (Figure 54B). Moreover AT1a-KO presented a drastically reduced maximal MAP response to intravenous bolus injection of Ang II (Figure 54C). The low baseline BP together with the blunted pressure response to Ang II indicates that a functional AT1a-KO rat line was created by inducing a mutation in the *Agtr1a* locus with the CRISPR/Cas9 technology. The same animals were used in an additional experiment to quantify the maximal pressor response to the adrenergic α1 agonist prazosin. Similar to FVB/N AT1a-KO mice (data in Figure 31B), SD AT1a-KO rats presented reduced maximal MAP response to phenylephrine (Figure 54D).

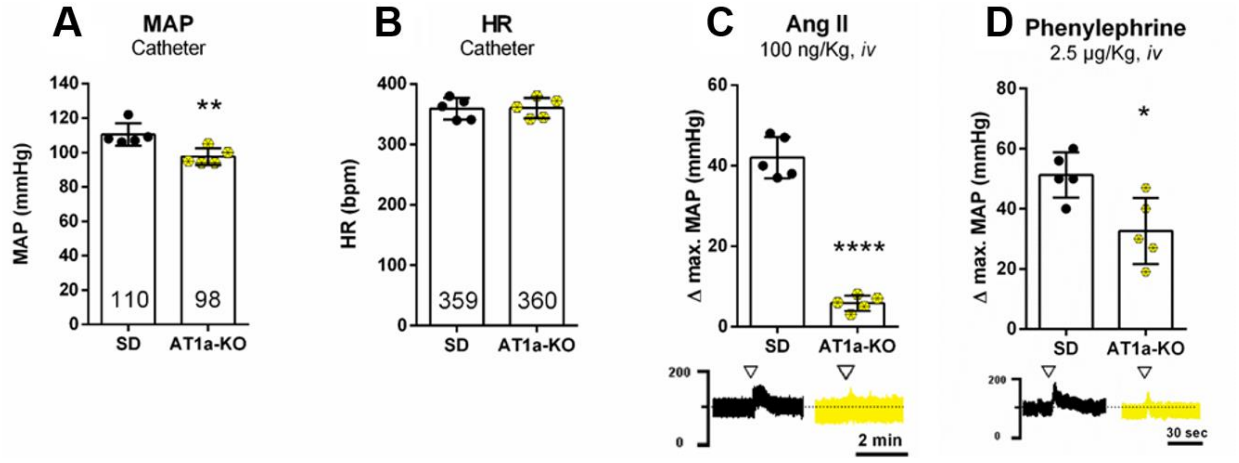

Figure 54 - Baseline cardiovascular parameters and pressor responses to Ang II and phenylephrine in AT1a-KO rats. Decreased baseline MAP (**A**) and unaltered HR (**B**) in awake 10-weeks-old SD rats globally lacking the AT1a receptor. Blunted maximal pressor response to acute Ang II infusion (**C**) and reduced maximal pressure response to phenylephrine (**D**) in awake 10-weeks-old SD rats globally lacking the AT1a receptor. $^{*}P < 0.05$, $^{**}P < 0.01$, $^{****}P < 0.0001$ vs SD (Student's *t* test). SD = Sprague-Dawley, MAP = mean arterial pressure, HR = heart rate. The ▽ over the pulsatile arterial pressure trace represents the approximate time of the bolus injection of Ang II in a representative rat.

After the *in vivo* functional validation protocol, the animals were sacrificed, and some morphometric parameters were taken. The body weight was not different among wildtype and AT1a-KO rats (Figure 55A). However, AT1a-KO presented lower cardiac mass which is an effect that most likely parallels the lower baseline BP in the line (Figure 55B). The wet weight of the left kidney and adrenal glands were indistinguishable (Figure 55C,D). In addition, a gross anatomy inspection did not reveal any evident phenotype, and males and females AT1a-KO were fertile.

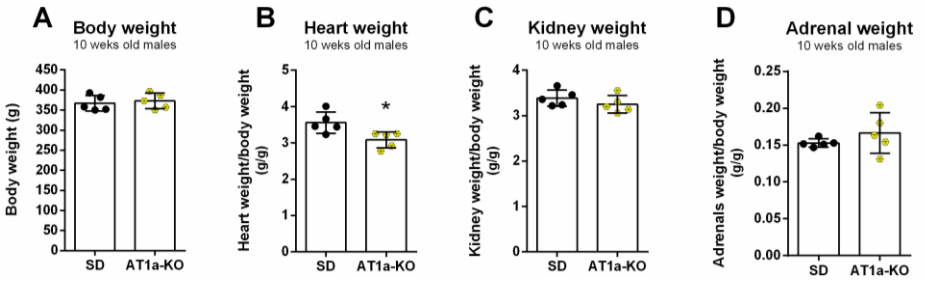

Figure 55 - Morphometry in AT1a-deficient rats.
Body (**A**), heart (**B**), left kidney (**C**) and adrenal glands (**D**) weight in 10 weeks old AT1a-KO SD rats. $^{*}P < 0.05$ *vs* SD (Student's *t* test). SD = Sprague-Dawley, MAP = mean arterial pressure.

4.6.2 AT1a knockin rats

We endeavored to knockin the ChR2 within the rat *Agtr1a* locus to explore the role of neuronal populations expressing the AT1a receptor on BP control mediated by SNA. Several trials were performed either microinjecting or electroporating zygotes or two-cell stage with commercial sgRNA (crRNA/tracrRNA), Cas9 and a HDR templates (dsDNA, ssDNA or circular vector). Despite a high rate of chromosomal cutting by CRISPR/Cas9 observed by mutations introduced by NHEJ (Table 58), 63 founders were born but none were knockin (Table 58). One animal which the HDR template was microinjected was positively genotyped however the construct did not integrate in the desired place. Therefore, this animal was considered as a transgenic with random construct integration. The transgene was transmitted to the germ line thus a transgenic line was established, and animals from this line were mated for the isolation of transgene-containing embryos. These embryos were electroporated with sgRNA and Cas9 to evaluate if endogenous HDR could possibly knockin the transgene in the *Agtr1a* locus. 20 founders carrying the transgene were born but none was positively genotyped for the knockin (Table 58).

Table 58 - Summary of CRISPR/Cas9 mediated HDR.

Target cell	Cas9 crRNA/tracr RNA	Construct	Born Offspring	NHEJ (% of offspring)	Transgene (% of offspring)	HDR "knockin"	Transgene germline transmission
Zygote	MI	MI	7	6 (85.7)	1 (14.2)	0 (0)	Yes
2-cell	MI	MI	3	3 (0)	0 (0)	0 (0)	-
Zygote	E	E	25	18 (72)	0 (0)	0 (0)	-
2-cell	E	E	11	8 (72.7)	0 (0)	0 (0)	-
Zygote/2-cell*	E	MI	17	17 (100)	0 (0)	0 (0)	-
Zygote	E	Endogenous+	9	8 (88.8)	9 (100)	0 (0)	-
2-cell	E	Endogenous+	11	10 (90.9)	11 (100)	0 (0)	-

+These embryos contained the transgene randomly integrated in the genome. *In these experiments the HDR template was microinjected into zygotes and the crRNA/tracrRNA with Cas9 electroporated in 2-cell embryos. MI = microinjection, E = electroporation, cr/tracRNA = commercial sgRNA.

5 Discussion

5.1 Generation and validation of rodent models

Agt-Tg was previously generated. In the frame of this PhD thesis this transgenic line was extensively validated, phenotyped and used to rescue brain Agt expression in Agt deficient mice (Agt-KO-Tg). The gain of function of brain Agt in Agt-Tg allowed to investigate the local brain formation of angiotensin peptides and to study its impact on cardiovascular and erythropoiesis homeostasis in animals containing or not the peripheral RAS (discussed in sections below). Experiments demonstrated the presence of transgene mRNA only in the brain. The hGFAP promoter has been extensively used to deliver astrocyte expression in rodents (61, 113, 114, 165). Some studies demonstrated transgene expression in unwanted tissues even though in low amounts in most of the cases (114, 166, 167). Experimental mice, Agt-Tg and Agt-KO-Tg, were always heterozygous for the transgene because homozygous were not viable. Curiously, a single copy of the transgene integrated at the chromosome 5. Normally transgenic animals contain more copies of the transgene integrated in tandem which probably drives in many cases high transgene expression in the targeted cell type (135, 168) and potentially off-target. Interestingly, ~350 bp of the 5´ end of the hGFAP promoter was lost, most likely, during integration. The remaining promoter size is about 1.85 Kb from the original ~2.2 Kb. In the hGFAP promoter, key regulatory regions were identified at the basal promoter and ~1.5 Kb upstream (169). The functionality of a shorter variation of the hGFAP promoter with ~1.8 Kb has been previously assessed *in vivo*. Adult mice expressing lacZ under the control of the hGFAP promoter containing either 1.8 Kb or 2.2 Kb expressed β-galactosidase similarly in astrocytes (113, 170). Brain Agt expression in Agt-Tg support the previous findings considering that the transgene mRNA was only found in the brain, and ISH analyses of the transgene mRNA showed a strong co-localization with astrocytes. Further analyses demonstrated that the construct used to generated Agt-Tg integrated at the chromosome 5 in an intergenic region (Figure 14C). Attempts to induce homozygosity in Agt-Tg failed indicating that the transgene deleted some genomic element(s) which are essential during embryonic development.

Potential AT1a-KO rat lines in the SD background strain were successfully generated introducing mutations with CRISPR/Cas9-mediated NHEJ. By breeding one of the founders with SD rats, the mutation in the *Agtr1a* locus of 2 adenosines insertion was transmitted in the germ line, and a mutant homozygous line could be established. As functional validation read out of the gene knockout, the immediate pressure response to intravenous Ang II administration was used, because this physiological response was previously found to be largely suppressed in AT1a-KO mice (111, 171). SD AT1a-KO rats presented a strong reduction in the pressure response triggered by acute Ang II injection. In addition, AT1a-KO rats presented decreased baseline BP and as consequence decreased heart weight. The data indicates that in rats the AT1a receptor but not the AT1b is mostly responsible for the vascular constrictor effect of Ang II as previously found in mice. There is a single report in which an AT1a-KO rat was generated using Zinc Finger nuclease. This AT1a-KO line was generated in the Dahl salt-sensitive line (172), contrary to the model developed in this study in a non-salt sensitive line, but like us the authors demonstrated drastically reduced pressure response to acute Ang II injection (172). The AT1a-KO generated in this study was not extensively phenotyped because of our strong interest in the FVB/N mouse lines. Nevertheless, this rat model is a suitable tool to experimentally address questions regarding the importance of the Ang II/AT1a axis in cardiovascular physiology and beyond that might not be easily addressed in mice as chronic recording of sympathetic nerves.

The first RAS knockout rat reported in the literature was a Ren-KO in the Dahl salt-resistant line (controls), this model was generated with Zinc Finger nuclease. These rats presented low baseline BP and the expected altered renal morphology and function (173). Interestingly, heterozygous animals presented altered renal morphology contrary to what reported in Ren-KO mice (115). The divergent findings among the different species highlights the importance to investigate consequences of targeted gene deletions in different species. In humans, loss of function mutations in genes encoding elements essential for Ang II formation (Agt, ACE or Ren) as well as AT1 mutations, lead to recessive tubular dysgenesis. Contrary to knockout rodents for these genes, affected patients are in most of the cases stillborn or die within the first hours after birth due to the lack of renal proximal tubes as well as lung aplasia among other complications (174–176).

Recently a double transgenic mouse strain expressing fluorescent proteins under the endogenous control of the AT1a and the AT2 receptors consolidated the knowledge from classical ISH studies, demonstrating that these receptors are expressed exclusively by neurons. In addition, neurons do not express both receptor types indicating a functional role (73, 74). Therefore, we attempted to knockin the sequence coding the ChR2 in the rat endogenous *Agtr1a* locus to study the cardiovascular modulatory effects of specific subsets of neurons expressing the AT1a receptors within brain cardiovascular nuclei. Because the minimum AT1a promoter necessary for cell-type specific gene expression has not yet been defined, we chose to introduce the ChR2 directly in the coding region of the endogenous *Agtr1a* gene using enhanced HDR with CRISPR/Cas9. After several trials with methodological modifications, we could not obtain any knockin rat. Recently knockin mouse models with large size inserts (> 2Kb) were generated at low efficiency rate <10% in most cases. These models were generated using CRISPR/Cas9 and long DNA templates which were either ssDNA or dsDNA. sgRNA and Cas9 were in most of cases delivered by electroporation, while large inserts were either microinjected or delivered with an adeno-associated-virus (129, 177). Knockin rats with insertions about the size of the construct designed in this study had been recently generated using sgRNA and Cas9 electroporation in zygotes and HDR template delivery by adeno-associated-virus, proving that enhanced HDR using CRISPR/Cas9 for large inserts is possible in rat embryos (178, 179). The rodent knockin generation field still requires further refinement in order to achieve high success rate and reproducibility across different laboratories. Currently, several strategies are being optimized to improve HDR success these include to carry the template close to the cutting side with Cas9 or gRNA, and activating the HDR pathway with small molecules (180). These methodologies are potentially suitable to be applied in the rat embryology field to increase large insert knockin efficiency and eventually create a ChR2 knockin rat in the *Agtr1a* locus.

5.2 Brain Ang II generation

The brain's ability to locally form Ang II is controversial. Contrary to other peripheral organs, the brain contains the BBB which limits the access of the circulating components of the peripheral RAS such as Agt and Ren. It could be demonstrated that even the octapeptide Ang II does not reach brain areas within the BBB in homeostatic conditions by using peripheral administration of suppressor doses of labeled Ang II (181). In this respect, the modulatory role of Ang II on

physiological processes in the brain has to be triggered by brain-borne Ang II (33, 76). Agt is mostly produced by brain astrocytes with a broad brain distribution however enriched at cardiovascular centers. ACE is expressed by certain neuronal populations and vascular endothelium (73). The limiting factor seems to be brain Ren expression which is reported to be very low and most of it (~98%) remains in the cytosol of neurons, thus, Ren interaction with the astrocyte and secretory vesicle-specific RAS precursor protein Agt is unlikely (71, 76). Previous studies demonstrated brain Ren like activity in brain homogenates (182). However, such methodological approach is subjected to bias by the fact that compartmentalized enzymes as lysosomal cathepsins are released and metabolize Agt in angiotensin peptides *in vitro* (183). Interestingly, Ang I and Ang II were detected in cerebrospinal fluid of dogs but not Ren enzymatic activity supporting brain formation of Ang II (131) but probably independent of Ren.

Some authors posit the existence of a neuronal intracellular Ang II generation, because several neurons express Agt and Ren. Interestingly, these neurons are located at cardiovascular centers including the RVLM (69, 184, 185). The interaction between Ren and Agt is, however, unlikely because as mentioned the dominantly expressed truncated Ren isoform has enzymatic activity, however cytoplasmic Ren is not expected to interact with Agt in secretory vesicles (76). Nevertheless, mouse lines with selective deletion of secreted Ren either in neurons or in astrocytes were generated but both lacked a cardiovascular phenotype (186). The data suggested that intracellular Ren is responsible for Ang II synthesis or at least Ang I, because ACE activity is necessary after Ang I production to form Ang II. ACE is a membrane bound enzyme with the catalytic site to the extracellular space and there is no evidence of cytoplasmic ACE production. The global deletion of secreted Ren led to phenotypic alterations like in global Ren-KO mice including hypotension and renal damage indicating that in secreted Ren in the periphery is crucial for Ang II production. Interestingly, the deficiency of secreted Ren increased brain intracellular Ren expression, unfortunately brain Ang II levels were not measured in these mice (187). Recently, the intracellular Ren isoform was knockout in mice, and curiously these mice developed active phase hypertension. The BP effect was accompanied by increased expression of the secreted Ren isoform in the brain of mice lacking intracellular Ren, supporting that secreted Ren contributes to brain Ang II formation (188). However more recently it has been reported that these animals are normotensive, and currently it is disputed that intracellular Ren downregulation

disinhibits secreted Ren which contributes to brain Ang II formation (69, 189). Based on the studies mentioned no definitive conclusion can be drawn regarding brain Ang II formation and the role of locally produced Ren in the brain.

Classically angiotensin peptides including Ang II were quantified in biological fluids and tissues using radioimmune assays with antibodies validated to be specific for the different peptides (131). Lately, ELISA kits were developed though they seem to lack specificity (190). In addition, LC-MS/MS has been growingly employed to measure concentrations of angiotensin peptides in biological samples, the main advantages are that the measurement does not depend on antibody binding, and known concentration of labeled analog peptides may be added to the samples before measurements (76, 190). LC-MS/MS based Ang II quantification often failed to detect Ang II in rodent brain samples or it was found at low concentrations (59, 78). These low levels of Ang II detected in brain samples are speculated to originate from the circulation (76). Supporting this notion, a study induced DOCA-salt[11] hypertension in rats and Ang II in brainstem did not increase but was even reduced for which one explanation is the fact that the model develops reduced peripheral Ang II formation (59).

Our group made contributions supporting the brain Ang II generation, one important example was the generation of a transgenic rat expressing an antisense RNA against Agt in astrocytes. This rat presented a brain specific reduction of 90% Agt protein which was accompanied by a reduction in BP, stress induced pressure response, renal Ren secretion and AVP secretion (61, 191). Other transgenic models provided further evidence of brain Ang II production and functionality, including a mouse model overexpressing rat AT1a receptors in neurons and a mouse model with increased brain angiotensin converting enzyme 2. In both models, basal BP was not altered, but the baseline BP dependence on brain Ang II was increased, and autonomic dysfunction was improved during induced hypertension, respectively (192, 193). Besides that, many studies that blocked the brain RAS or increased it either using transgenic rodents or directly infusing Ang II into the brain showed several effects triggered by brain Ang II. Nowadays, brain Ang II is known to modulate AVP release, and salt appetite and drinking

[11] DOCA-salt = deoxycorticosterone acetate-salt is a synthetic mineralocorticoid derivative. Thus, the model of DOCA-salt induced hypertension usually constitutes of the chronic administration of DOCA in association with a high salt diet and in some studies one kidney is removed (291).

behavior. In addition brain Ang II modulates several peripheral functions via SNA including BP, metabolism, and immune cell activation alterations modulated by SNA in physiology and pathology (75, 114, 142, 194–196). Several rodent models successfully increased brain Ang II levels mostly using direct brain injections of Ang II in acute or chronic setups. In addition, transgenic models were generated including mice secreting Ang II directly by astrocytes, mouse expressing rat tonin in brain astrocytes and the sRA model. The sRA model is a double transgenic mouse expressing the human Ren in neurons, and human Agt controlled by its endogenous promoter (114, 144, 197). Since human Agt can only be cleaved by human Ren and not by mouse Ren the sRA model is brain-specific. All mentioned gain of function models were essential to generate the current state of the knowledge about Ang II actions in the brain. However, none of the models was suitable to confirm endogenous Ang II formation in the brain.

Agt-Tg and Agt-KO-Tg were key models to support *in vivo* brain Ang II formation. Because Agt transgene expression was delivered by astrocytes that is the normal cellular type producing Agt (61, 71). The most convincing aspect of the models presented here in comparison to other models is the fact that the sole overexpression of the RAS precursor protein Agt led to detectable brain Ang II. These findings suggest that the transgene Agt is most likely metabolized to Ang II by the endogenous pathway normally recruited for brain Ang II formation. Interestingly, the brain rescued line Agt-KO-Tg, which is devoid of endogenous mouse Agt expression showed a similar pattern of Ang II production. In addition, Ang II was not detected in the circulation of Agt-KO-Tg as discussed above due to the inability of Ang II in crossing the BBB. Further experiments revealed increased c-Fos expression in brain structures containing cardiovascular centers of Agt-KO-Tg and Agt-Tg. In agreement with c-Fos expression data, Agt-KO-Tg presented a cardiovascular response to peripherally administered candesartan, an AT1 blocker that crosses the BBB (198). Finally, the mouse lines with increased Ang II formation presented increased levels of circulating AVP estimated by measurements of plasma copeptin concentration. Altogether, our data indicates that Ang II is generated in the brain of the transgenic lines and acts on cardiovascular centers.

Interestingly, Ang I was not detected in the brain of Agt-Tg and Agt-KO-Tg. Usually Ang I is found at higher concentrations in comparison to Ang II in blood, in tissues similar relative

concentrations of both peptides are typically detected (59, 78, 199). Ang II tissue concentration correlates to AT1 receptor expression abundance in peripheral organs. The reason behind this phenomenon is that Ang I is an inactive peptide and does not bind to a receptor while Ang II, at least part of it, is bound to its receptors at the cell surface or intracellularly in vesicular compartments after receptor mediated endocytosis. Bound Ang II has increased half-life and tissue concentration and is also protected from degradation during sample preparation (200). The findings in Agt-KO-Tg and Agt-Tg led us to speculate that a Ren-independent pathway may be responsible for central production of Ang II in these lines, and likely in physiological conditions. Some reports have detected Ang 1-12 in tissues like the heart, but the enzyme(s) responsible for its production are still unknown (138, 139), therefore, we quantified Ang 1-12 in an attempt to identify the mechanisms of central Ang II formation. Similar to Ang I, Ang 1-12 is an inactive peptide, if injected in the brain Ang 1-12 is converted to Ang II by ACE (73, 201). However, Ang 1-12 was not detected in Agt-KO-Tg brains.

Altogether, the findings of this thesis support local Ang II production in the brain, and that neither brain Agt nor Ang II spills over into the circulation. Further experiments are required to validate the relevance of brain Ren activity for local Ang II production in Agt-Tg. One example is crossing Agt-Tg with Ren deficient mice to produce animals with high brain Agt in a Ren-KO background to verify Ren-independent Ang II generation. In addition, the brain site(s) of Ang II production should be further investigated. An important missing piece in the field is the production site of the peptide. Because Agt is secreted, Ang II formation might occur within secretory vesicles or in the extracellular environment.

5.3 RAS and cardiovascular regulation

RAS blockers in particular AT1 receptor antagonists are among the first line choice to lower BP in human hypertension (8, 80). Rodents differ from humans in the number of genes encoding for the Ang II type 1 receptors, humans have a single gene coding for the AT1 receptor while rodents have two genes, *Agtr1a* and *Agtr1b*, encoding AT1a and AT1b, respectively. The AT1a receptor is usually more expressed in comparison to the AT1b across the body (33, 152). Mouse models with targeted deletion of these receptors confirmed the dominant role of the AT1a in cardiovascular control, because AT1a but not AT1b knockout mice are hypotensive and have increased circulating levels of Ren and Ang II as compensatory effects (163, 164, 202, 203).

Gene targeted deletions of Ren and ACE decreases BP due to absence of Ang II production in mice (115, 162). Hypotension is also observed in mice with gene targeted deletion of the RAS precursor protein Agt in different background strains: mixed, ICR, and C57BL/6 (112, 145, 146). Our BP measurements showed hypotension in FVB/N AT1a-KO but unexpected normotension in FVB/N Agt-KO. There is a single report by Lochard *et al.* (197) using FVB/N Agt-KO. In this study, Agt-KO were slightly hypotensive (BP was reduced by 14 mmHg in contrast to about 30 mmHg in other strains). However, BP was measured using tail-cuff plethysmography, a method which is accompanied by stress. Moreover, inbred FVB/N breeding stocks may slightly differ among laboratories that could account for phenotype discrepancies.

Vascular SNA dilate or constrict blood vessels, altering lumen size directly impacting the vascular tone and, therefore, affecting short-term and long-term BP depending on the stimulus duration (3, 16, 18, 26, 35). Life-long exaggerated vascular SNA outflow leads to profound vascular remodeling. These alterations are not yet fully understood, but it is becoming clearer that SNA levels alone not always directly correlate with BP after years of hypertension at least in humans. However, the vascular remodeling induced by increased vascular SNA during hypertension development and establishment plays an important role in the hypertension pathology (18, 147, 204, 205). Because the SNS is seen as one of the most relevant systems for long-term BP control, the autonomic control of the BP was extensively phenotyped in the mouse lines that presented paradoxical BP phenotypes. Very interestingly, FVB/N Agt-KO presented increased sympathetic outflow. This line was the only one that displayed a stronger response to generalized peripheral sympathetic ablation with 6-OHDA. Previous studies with spontaneously hypertensive rats, a model well-known to have increased SNA, demonstrated a similar response to 6-OHDA (10, 32, 206). A curious observation is that all lines recovered baseline BP levels even before the end of the 6-OHDA treatment (5 days). To our knowledge no other study has used telemetry to track the effect of 6-OHDA on baseline cardiovascular parameters in mice. There is a single report in which C56BL/6 mice received 3 doses of 200 mg/Kg 6-OHDA 6, 4, and 2 days before BP recording by telemetry but no difference in baseline BP was observed, most likely the BP effect was already gone as our results indicate (207). The recovery of baseline BP levels was previously observed in rats, normally ~2 weeks after denervation, and curiously the vascular sympathetic reinnervation seems to happen even before BP restoration after ~1 week. In

addition, compensatory mechanisms were observed including increased adrenal catecholamine release, increased vascular adrenergic receptor reactivity and peripheral Ang II production (208–211). Our data shows that Ang II is not necessarily essential in this feedback response, because AT1a-KO, Agt-KO and Agt-KO-Tg with reduced or absent peripheral Ang II reactivity recovered BP similarly to wildtype controls.

The 6-OHDA experiment suggested that SNA is increased in Agt-KO contributing to sustain normotensive BP levels. To determine the contribution of vascular SNA, the BP response to sympatholytic drugs was investigated, and Agt-KO in agreement with 6-OHDA presented increased depressor response to α1, α2 and ganglionic blockade indicating an increased vascular SNA in this line in the absence of Ang II. When general vasorelaxant substances interfering with calcium dependent and independent pathways that control the vascular contractile machinery were administered, the normotensive Agt-KO presented even stronger response to these drugs. The data suggested that baseline vasoconstriction is stronger in Agt-KO to sustain normotensive levels when comparing this line to controls. One explanation for having increased vascular constriction to sustain BP levels is that the lack of Ang II signal via AT1a reduces the extracellular volume (202). Interestingly, Agt-KO as well as the hypotensive Agt-KO-Tg presented increased levels of dehydration markers (osmolality, albumin, total proteins and sodium) supporting that this might be indeed the case. Interestingly, these markers were found increased, supposing that the dehydration is chronic. In contrast, other studies suggest that dehydration acutely increases these parameters in mice but not chronically (212). Agt-KO and Agt-KO-Tg both presented increased dehydration suggesting that the phenotype is not a consequence of BP levels but likely attributed to the impaired urine concentrating ability found in RAS deficient animals that is a key feature of the RAS to control blood volume (115, 146). Finally, the normotension in Agt-KO was accompanied by increased systolic pressure and heart weight without changes in the HR, these phenomena might be the result of a complex response involving increased constriction and/or reduced compliance of the vascular tree. These vascular alterations are found in association with increased vascular sympathetic tone and may induce volume and/or pressure overload in the heart leading to hypertrophy (147, 213). In addition, increased SNA to the heart also induces hypertrophy (214).

Contrary to gain of function models of Ang II, the functional autonomic control of the BP is not deeply known in mice deficient of RAS components. The lack of interest is probably due to the fact that these lines are all hypotensive. Nevertheless, NE levels were measured in C57BL/6J Agt-KO in plasma and turned out to be comparable to controls, also submitting these mice to cold induced hypertension elevated plasma NE similarly in controls and Agt-KO (145). Plasma and urinary NE were found increased in AT1a-KO (215). Interestingly two independent studies found evidence of increased vascular SNA in AT1a-KO because these mice presented increased response to α1 and ganglionic blockade with prazosin and hexamethonium, respectively (216, 217). In the FVB/N AT1a-KO here presented, similarly increased response to prazosin was found. In addition, the α2 adrenergic blocker yohimbine induced a stronger response in AT1a-KO. Contrary we could not detect alterations in urine NE levels in any of the FVB/N lines. Importantly, the studies mentioned above used intraperitoneal injections of sympatholytic drugs contrary to the present study where substances were delivered by intravenous route. The increased vascular SNA in Agt-KO is not related to increased vascular adrenergic receptor reactivity in fact the opposite was observed when stimulating endogenous NE release or using specific α1 and α2 agonists. All lines with reduced or absent Ang II signaling presented a blunted pressor response to these substances. In parallel these animals presented reduced expression of relevant adrenergic receptor subtypes mediating the vasoconstriction response. Concordantly there have been studies showing that smooth muscle adrenergic receptor expression is stimulated by Ang II in culture (218, 219).

Agt-KO-Tg presented lower baseline BP, which was paralleled by reduced vascular SNA. All drugs used *in vivo* to block SNA showed that Agt-KO-Tg presented a reduced vascular sympathetic tone in comparison to Agt-KO. In addition, this line presented reduced NE levels in mesenteric arteries. The findings are puzzling because high levels of brain Ang II has been previously demonstrated to cause hypertension in rodents either by intracerebroventricular Ang II infusions or in transgenic models (69, 114, 142, 144, 220), except if Ang II is injected at certain specific sites as the CVLM. At the CVLM, the Ang II/AT1 axis causes hypotension because the nucleus consists of inhibitory neurons that project to the RVLM, the central hub for SNA control (221, 222). In addition, brain specific AT2 agonist administration causes hypotension mediated by peripheral SNA suppression (153, 223). Interestingly, mice lacking AT2 receptors in the NTS

lack the BP lowering effect of the AT2 agonist compound 21 administered in the third ventricle. The mechanism proposed is that Ang II/AT2 axis reduces GABA producing enzymes of inhibitory circuits (153). Curiously, Agt-KO-Tg presented reduced expression of AT2 in the hypothalamus and increased AT1a expression in the brainstem. The measurements of GABA producing enzymes showed no differences among the groups. Finally, neither acute nor sub-chronic AT1 receptor blockade with candesartan increased BP in Agt-KO-Tg indicating that Ang II exerts a pressor response rather than a depressor as strongly suggested by the baseline BP. This finding is not easily interpreted because Ang II receptors are expressed in several interconnected nuclei and therefore the response is rather complex. Moreover, receptor blockade probably does not homogeneously and completely inhibit the binding of Ang II. In addition, AT2 receptor activation mostly mediates BP reduction (74, 153), thus, AT1 blockade could potentially enhance the Ang II/AT2 axis and/or the production of other downstream peptides as Ang 1-7 via ACE2. Another explanation is that Ang II not only affects neuronal activity directly but in addition it modulates some unknown factors at gene expression level that may not be satisfactorily blocked with the pharmacological approach used.

Agt-Tg presented increased BP only in acute BP recordings, radiotelemetry recording of baseline cardiovascular parameters showed no BP alteration. The BP response in Agt-Tg is somehow a predicted finding because during the acute BP recordings the animal is likely exposed to higher levels of stress in comparison to radiotelemetry sampling. Acute stressor conditions are known to increase BP, and a positive association with brain Ang II exists. The peptide hormone contributes to this physiological response potentiating SNA and renal Ren release (75, 191). An interesting question raised by this BP finding is whether preexisting elevated Ang II levels potentiate the stress response or if the stress stimuli itself further raise brain Ang II formation to a level exceeding the normotension. As mentioned above such mechanism may be potentially mediated by disinhibition of secreted brain Ren. The cardiovascular regulation found in Agt-Tg is consistent with previous reports for brain-specific Ang II gain of function including increased BP and SNA as well as augmented AVP release (33, 41, 152, 224). Recent studies identified that during chronic Ang II-induced hypertension the splanchnic vasculature, containing approximately 20% of the blood volume, is particularly affected by increased SNA. Accordingly the removal of the splanchnic sympathetic neurons by celiac ganglionectomy attenuates Ang II-induced hypertension (41, 225). In these models of peripheral Ang II overload, the SNA increase

is mediated by Ang II actions at brain circumventricular organs or direct access of Ang II to nuclei normally protected by the BBB (19, 181, 226). Interestingly, peripheral Ang II was decreased in Agt-Tg due to reduction in Ren expression which is negatively controlled by BP levels sensed by juxtaglomerular cells of the kidney[12] (36, 107). Recently, a study suggested that a mechanotransducing mechanism (BP dependent) mediated by β1 integrin-laminA/C rearranges the chromatin structure and Ren expression (227). Collectively, the data suggests that brain Ang II induced a new neurohormonal balance controlling baseline BP in Agt-Tg.

Initially, we expected brain Ang II overproduction would further raise BP in Agt-KO-Tg. The study of Lochard *et al.* (197) that rescued Ang II in their hypotensive FVB/N Agt-KO using a construct that secreted Ang II specifically by brain astrocytes showed no BP changes in Agt-KO rescued, but BP was increased in their wildtype FVB/N expressing the same construct similarly to Agt-Tg. To our knowledge except from our study this is the only study that restored brain Ang II in Agt-KO. The transgene is unlikely to be purely responsible for the phenotype, otherwise Agt-Tg and Agt-KO-Tg should present BP changes in the same direction. Comparisons of the BP phenotypes between Agt-Tg and Agt-KO-Tg should consider the fact that the endogenous Agt is not present in the second therefore the endogenous pool of Ang II is lacking. Nevertheless, based on the fact Ang II is generated in the brain of Agt-KO-Tg and Agt-Tg, the findings suggests that Ang II has a completely opposite regulatory functions on SNA and BP in these lines. One missing piece in our findings is the source of increased SNA in Agt-KO, whether the origin is from a peripheral reflex or brain intrinsic. Even the hypotension observed in Agt-KO-Tg might be attributed to a modulatory effect of Ang II on altered peripheral reflexes or brain intrinsic pathways. These hypotheses were partially addressed with renal denervation and a GWAS discussed below.

Besides increased SNA Agt-KO presented evidence of endothelial dysfunction characterized by reduced NO production. NO released by endothelial cell diffuses into smooth

[12] In adult animals, renal juxtaglomerular cells supply the blood with Ren. These cells themselves sense BP via the indicated mechanism and adjust Ren expression accordingly to maintain BP levels constant. This pressure-dependent increase in Ren expression does not only operate in existing Ren producing cells but also on smooth-muscle cells of the renal vasculature that may be retransformed in Ren producing cells and vice versa.

muscle cells with a potent vasorelaxant effect dependent on cGMP production (88). Moreover, studies demonstrated that NO acts on sympathetic terminal and lowers vascular SNA (32, 88, 204). Hence, the lower NO production likely contributes to the BP phenotype in Agt-KO. External Ang II overload and or mice lacking ACE2 enzyme (with Ang II accumulation) present endothelial dysfunction involving superoxide production (228, 229). In agreement with the fact that Ang II blunts NO production, "hypotensive" C57BL/6J Agt-KO presented increased levels of plasma and urine NOx indicating improved endothelial function (145). Interestingly, the hypotensive Agt-KO-Tg presented an improved endothelial dysfunction and partially recovered urinary NOx but these levels may also be influenced by the high expression of renal neuronal NO synthase found in this line. One hypothesis is that increased vascular sympathetic tone deteriorates NO production but interestingly both Agt-KO and Agt-KO-Tg presented reduced endothelial NO synthase expression in mesenteric arteries.

Collectively, we identified unexpected mechanisms of BP regulation involving exaggerated SNA using FVB/N mice with gain and loss of function of RAS components. Dissecting the altered molecular pathway(s) behind the phenotype found in the FVB/N Agt-KO mice may not only add new knowledge for BP and SNA regulation but also open new avenues for treating human hypertension. However, as previously mentioned SNA and BP are products of multi-organ and hormonal systems interactions, therefore, the causes and consequences of these alterations are not always easily distinguishable. Future studies including double knockout for AT1a/AT1b on the FVB/N background would be interesting to better understand the BP phenotype. We have preliminary evidence (not presented) that the unexpected normotension in FVB/N Agt-KO is also present in FVB/N Ren-KO meaning that the absence of the RAS drives the phenotype and not Agt exclusively.

5.3.1 Renal Physiology

The kidneys play a key role in maintaining and adjusting fluid homeostasis that may impact long-term BP levels mostly via pressure natriuresis mechanisms (16, 230, 231). During renal development AngII/AT1 receptor signaling is necessary to avoid post-natal renal developmental damage. This lesion can be induced by AT1 blocker administration during active nephrogenesis in rodents or genetically induced in a double knockout mouse model (AT1a and AT1b) as well as by deleting Ren, Agt, or ACE (164, 232). FVB/N Agt-KO presented similar renal morphology to

previous studies with Agt-KO, including leucocyte infiltration, fibrosis, and concentric vascular hypertrophy demonstrating that the phenotype develops independent of the BP levels (136, 156, 159). Agt is expressed by kidney proximal tubule cells and there is evidence of intrarenal Ang II generation from locally produced Agt specially during hypertension (233). However, the rescue of tubular Agt expression in Agt-KO does not rescues the developmental problems, in agreement renal specific Agt deletion has no effect on the renal morphology, but hepatic-specific Agt deletion induced the phenotype. Altogether, these studies demonstrated that circulating Agt and/or Ang II is required for correct renal development (60, 155). A previous study mentioned above that restored brain Ang II production in Agt-KO demonstrated improved renal morphology (197). The brain rescued line Agt-KO-Tg presented a similar renal morphology comparing to Agt-KO, indicating that local Ang II acting on renal cells is most likely relevant to prevent the phenotype in Agt-KO. In their model even though Ang II was not detected in plasma of adult animals it may had well been present during development either by off-target expression or spill over in situations of open BBB during development (68).

An interesting observation in our study was the fact that the normotensive Agt-KO presented normal renal Ren expression. The control of Ren expression and production has been suggested to be under the control of several mechanisms including a feedback loop involving Ang II, because the AT1a receptor is found on Ren cells. However, two independent studies deleted AT1a receptors on Ren cells and observed no influence on Ren production (234, 235) and this is now supported by our findings with mice lacking peripheral Ang II with different levels of baseline BP which is obviously more relevant for the long-term Ren cell identity acquisition as well as Ren secretion as previously reported (227, 236). In our hypotensive lines Agt-KO-Tg and AT1a-KO high renal Ren expression was found while Agt-KO had normal Ren expression and importantly none of these lines confirmed the Ang II/AT1a feedback on Ren cells due to AT1a deletion or absent Ang II production.

Excessive Ren cell recruitment has been suggested to cause concentric vascular hypertrophy which is an intriguing phenotype. It seems to be dependent on an interplay between Ren cells and AT1 signaling, because mice lacking either Ren cells or AT1a-KO with increased Ren cell recruitment develop an attenuated version of the phenotype, while Ren-KO, Agt-KO,

ACE-KO are all strongly affected (36, 115, 159, 237, 238). Importantly during concentric vascular hypertrophy Ren positive cells usually localized at the outer layer of the hypertrophied arteries indicating that not all smooth muscle cells turn into Ren producing cells like during a low-salt diet (238, 239). Pentz et al. (237) deleted renal Ren producing cells using diphtheria toxin and thereby prevented renal artery morphological alterations. However, the mouse model used expresses *Ren2* by the salivary glands therefore small amounts of Ang II might still be generated in the circulation besides diphtheria toxin is under the control of *Ren1d* gene meaning that the cells only die when Ren is expressed. Moreover, Ren cells give origin to renal smooth muscle cells that are likely killed in this model preventing the phenotype. Interestingly in RAS deficient mice, the vascular phenotype appears already in the first there weeks of age, and the Ren cell excess during intrauterine renal cortex formation (239, 240). Therefore, the mentioned model has to be further explored to know if Ren cells are not accumulated in excess or Ang II is produced early during development, one option is crossing this line with Agt-KO mice.

The findings in the present study of AT1a-KO (with high Ren cell recruitment) and Agt-KO (with low Ren cell recruitment) support the idea that the lack of AT1 signaling plays a major role in renal vascular hypertrophy development. Also rats treated with AT1 blockers during renal development develop arteriolar hypertrophy (232, 241). However, the specific deletion of AT1a from FoxD1 positive cells in a AT1b global knockout background had no effect at all on the renal morphology and function, also baseline BP and Ren release were unchanged at least in adult mice. Renal FoxD1 positive descendent lineage includes kidney vascular smooth muscle cells, pericytes, and Ren cells (242, 243). Finally, studies using mice lacking aldosterone production with high Ren cell recruitment and Ang II production showed vascular hypertrophy arguing against the involvement of the AT1 but in favor or an exacerbated Ren cell recruitment early in development (244). In contrast we found arteriolar hypertrophy in the absence of Ren cell recruitment. One major caveat is that we have not evaluated the Ren cell recruitment during active nephrogenesis in FVB/N Agt-KO which might not reflect the renal Ren expression in the adult animal, because BP is possibly altered during early life.

Agt-KO presented increased urinary output and renal function markers such as urea and creatinine. Interestingly, these phenotypes were partially rescued in Agt-KO-Tg, whether this effect is cause or consequence is not easy to affirm. Agt-KO-Tg presented more renal SNA and

AVP secretion, normally water reabsorption is improved by both stimuli (16, 20). Previously Agt-KO mice were reported not to respond to AVP, and to have lost their urine concentrating ability during water deprivation challenge (146, 156). The lack of AVP response is not yet studied in detail, but one explanation is the altered extracellular sodium concentration in hydronephrosis. AVP probably translocates aquaporin-2 to the cell membrane however a hypertonic extracellular environment is essential for water reabsorption via passive transport (245). The fact that Agt-KO presented increased blood osmolality could itself have a dipsogenic effect ultimately leading to polydipsia. However, the osmolality was heavily influenced by urea a metabolite that crosses cell membranes and previously shown not to induce dipsogenic effects in comparison to other osmolytes as sodium (246). The high urea levels in Agt-KO might be explained by aestivation, a mechanism usually observed in amphibians during adverse environmental conditions to conserve water. A recent study observed this phenomena of urea accumulation using the 5/6 nephrectomy model that is accompanied by polyuria (247). Our data supports this hypothesis because AT1a-KO presented elevated creatinine like Agt-KO-Tg suggesting a similar glomerular filtration rate, but AT1a-KO had normal urinary volume and normal urea levels. Finally, Agt-KO presented the highest plasma accumulation of urea which curiously correlates with the highest urinary output.

Glomerular filtration rate is influenced by several factors including nephron number, blood pressure and renal blood flow which all are subjected to modulatory effects of Ang II and local SNA (248). From one side long term-high renal SNA is associated with structural changes in the kidney leading to renal function decline, from the other side increased renal perfusion deteriorates renal function (20, 249). Previous reports showed decreased glomerular filtration rate and decreased tubular sodium transporters similar to our findings during experimental-induced hydronephrosis in rodents (250, 251). Another factor influencing renal glomerular filtration rate might be the high levels of immune cell infiltration found in Agt-KO. However, we have not determined whether infiltrating cells are cytotoxic or not. Altogether, the reason why Agt-KO-Tg present a better GFR suggested by the plasma creatinine levels might involve a complex differential adjustment of renal function modulated by mechanical, immune and neurohumoral factors in Agt-KO and Agt-KO-Tg involving systemic BP, renal blood flow and net glomerular filtration pressure.

It has been shown that Agt-KO mice exhibit increased renal SNA (160), and the same effect was observed in the FVB/N Agt-KO line, and similarly in AT1a-KO. Interestingly, Agt-KO-Tg displayed higher SNA in comparison to Agt-KO while Agt-Tg presented levels similar to controls, confirming that long-term elevated brain Ang II has no effect on resting renal SNA in normal conditions (16, 252). Renal pathologies are growingly recognized to invert the reno-renal-reflex exerted by the renal afferent that when activated in physiological conditions reduces renal SNA (16, 253). All the factors contributing to this misbalance are not yet fully comprehended, but renal immune cell infiltration and brain Ang II are indicated as modulators of renal afferent and renal efferent activities, respectively (254–256). Interestingly, immune cells often co-localize with renal afferent and efferent nerves, and renal SNA was suggested to increase renal immune cell infiltration in experimental models of hypertension because renal denervation prevented this effect (255, 257, 258). We observed the opposite because Agt-KO-Tg with a higher renal SNA activity in comparison to Agt-KO presented less immune cell infiltration. However, besides sympathetic activation renal perfusion pressure levels was positively correlated to renal leucocyte infiltration, and this might explain the lower levels found in the hypotensive Agt-KO-Tg (249).

Brain Ang II led to an apparent shift in SNA from the vasculature to the kidney in Agt-KO-Tg when compared to Agt-KO, and as consequence BP levels were altered. Originally we hypothesized that the damaged kidneys of Agt-KO and Agt-KO-Tg could impair the reno-renal-reflex by activating renal afferents as previously shown in preclinical models of hypertension (257, 259–261) and that the differential SNA to the vasculature and kidneys would be dictated by the presence or not of brain Ang II. To test this hypothesis, a bilateral renal denervation was performed, and the BP fall monitored. Interestingly, MAP decreased in Agt-KO and Agt-KO-Tg much less than in wildtype mice, and the hypotensive response in Agt-KO and Agt-KO-Tg started only four days after denervation contrary to the immediate response in wildtype. The BP fall after renal denervation has been previously observed in control rats and mice, but there is not yet a consensus on the mechanisms. Reduced renal Ren release, vascular resistance, and renal sodium and water reabsorption are suggested (16). The late BP response observed in Agt-KO and Agt-KO-Tg might be driven by an increase in natriuresis in which the effects on BP are late and gradual in contrast to Ren release with immediate BP effects (16). This data invalidated our original hypothesis, but it demonstrated that the main pressure lowering effect in normal conditions of renal denervation is a reduction on Ren release, and because only wildtype mice

have circulating Agt, BP was found immediately and strongly lowered in these animals. However, the impact of renal denervation in rodents on kidney Ren expression and release has generated controversial results, either decreases or no effects were described (108, 262, 263). Importantly, the time after denervation should be considered because reinnervation has been described to be fast in rodents (within few weeks) (264). The chronic suppression of the NE signal in mice by the genetic deletion of β1 and β2 adrenergic receptors lead to reduced Ren expression and release (265). Moreover three months after renal denervation hypertensive patients presented low level of circulating Ren and those patients with higher levels of circulating Ren before surgery had a stronger pressure lowering effect after surgery (266). One should consider that acute and chronic effects on BP elicited by renal SNA manipulation may not necessarily be the same including Ren release, and Agt-KO mice with renal damage and lack of Ang II may misrepresent physiological conditions.

5.4 GWAS in FVB/N Agt-KO

One of the most surprising and at the same time puzzling findings of the present study is that FVB/N Agt-KO is normotensive. So far all knockout mouse models affecting the Ang II/AT1a axis displayed low blood pressure (111, 112, 115, 164, 267). In addition, recent studies of targeted gene knockout rats demonstrated similarly reduced baseline BP including the SD AT1a-KO rat from this study (Figure 54A) (172, 173). By phenotyping the FVB/N lines in this study, AT1a-KO and Agt-KO-Tg, it became evident that the SNA contributes to the unexpected BP phenotype in Agt-KO. However, the molecular mechanism driving this physiological response is not easy to dissect. Nevertheless, this mechanism is very interesting since an equivalent mechanism could account for BP control in humans and be a potential source of increased BP in some manifestations of hypertension.

Importantly, inbred mouse strains are genetically very similar, and the full genome sequences are available. Consequently, genetic markers as microsatellites and SNPs have been identified across the genome and may be used as landmarks to identify locus and/or loci associated to traits (161, 268). The fact the normotension in Agt-KO is completely unexpected based on the knowledge acquired in the last three decades with Agt-KO model in mixed or other inbred strains (112, 145, 146) led us to postulate that the phenotype is monogenic. To test this

hypothesis, a F2 Agt-KO (FVB/N x C57BL/6) was generated. Strikingly, the BP data in the F2 mice seems to be dictated by a single gene because the individual MAP data points cluster in two distinct populations, one with low and another with normal BP. In addition, the F2 Agt-KO BP phenotype suggested that the normotension in FVB/N Agt-KO is of recessive nature, because most of the F2 Agt-KO mice were hypotensive resembling the previously reported BP phenotype of C57BL/6 Agt-KO.

However surprisingly, the association analyses performed in our study pointed to several significant loci associated with the BP trait in the F2 Agt-KO, indicating that more than a single locus likely prevents BP to fall in FVB/N Agt-KO. The fact that some animals develop BP levels even in the hypertensive range confirm that more genes might be required in parallel to develop the phenotype. One limitation in our experimental design is that we had no C57BL/6 Agt-KO available. Otherwise, a F1 Agt-KO (C57BL/6 Agt-KO x FVB/N Agt-KO) could have been generated, in addition, to study the BP phenotype in these mice. This experiment is particularly important to confirm the dominancy findings identified in the F2 generation, because if a single locus indeed predicts the phenotype and the C57BL/6 allele is dominant all F1 mice generated by the breeding scheme mentioned must be hypotensive as pure C57BL/6 Agt-KO.

Currently, we assume that the BP phenotype in FVB/N Agt-KO is unique and genetically driven by the FVB/N genome because we could experimentally demonstrate this phenomenon in the F2 Agt-KO. Direct comparison of baseline MAP among wildtypes FVB/N and C57BL/6 from our breeding stock showed minimal differences (maximal 5 mmHg), thus, this would not account for the large difference of baseline BP observed in the F2 Agt-KO (229, 269). Interestingly, this unknown factor(s) increases SNA and BP probably only in total absence of brain Ang II, because brain Ang II completely suppresses this compensatory response in Agt-KO-Tg that has BP at expected low levels for Agt-KO, and FVB/N AT1a-KO is also hypotensive. As mentioned above, the combination of double or triple Ang II receptor knockout in the FVB/N background would be interesting to narrow down the phenotype discarding the involvement of other RAS peptides as Ang 1-7. Altogether, the uncommon BP regulation in FVB/N Agt-KO renders it a promising tool to identify genes controlling SNA and BP. First the F2 number should be increased to gain statistical power. Second, one could study the effect of each significant chromosomal region separately by transferring these FVB/N chromosomal regions to the C57BL/6 background by

breeding. Once these lines are established one may use CRISPR/Cas9 to knockout Agt and study the BP phenotype to narrow down candidate genes.

5.5 Erythropoiesis

Erythropoiesis is orchestrated by several factors inducing proliferation and survival of erythroid progenitors. Well known key elements essential during RBC production are the hormone erythropoietin and the metal iron responsible for erythroid progenitor survival and hemoglobin synthesis, respectively (97, 100). In adult rodents during homeostatic conditions, erythropoiesis mostly takes place in the bone marrow and perhaps a very small fraction of RBCs are produced by the spleen (94, 270, 271). Ang II has been acknowledged for a long time to modulate erythropoiesis because RAS inhibition leads to anemia development in rodents and humans (110, 272). Later this effect was observed in mice with genetic deletion of both AT1 receptors (AT1a and AT1b). Here, contrary to BP regulation the AT1b expression satisfactorily sustains erythropoiesis (163). Accordingly, mice lacking Ang II production via gene targeted deletion of Agt, ACE, or Ren present anemia (162, 163, 187, 273). Our findings with FVB/N AT1a-KO and Agt-KO fully agree that Ang II controls RBC production via its both receptors in rodent erythropoiesis because only Agt-KO was anemic. Patients suffering from chronic kidney disease develop anemia (274). However, the anemic phenotype in mice lacking RAS seems to be independent of the renal developmental damage, because mice expressing soluble instead of membrane bound ACE present reduced Ang II levels in plasma consequently develop anemia but have no renal damage (162).

It has been demonstrated that the AT1a receptor controls renal erythropoietin release in the kidney, because increased Ang II in transgenic animals enhances erythropoietin release and RBC production but not in double transgenic model with increased circulating Ang II and deficient in AT1a receptor (275). On the contrary the deletion of AT1a and AT1b receptors from erythropoietin producing cells had no effect on the hematocrit and circulating levels of erythropoietin (242). *In vivo* studies using anemic mice due to genetic deletion of RAS components showed either increased erythropoietin or unaltered levels in plasma (162, 163) demonstrating that the phenotype is not developed due to erythropoietin deficiency, similarly to the findings of this study. Perhaps the effects observed in mouse models with increased Ang II on

erythropoietin release *in vivo* is secondary due to pathological mechanisms related to hypertension as renal hypoxia (276). Interestingly, chronic Ang II delivery in RAS knockout lines rescues the RBC production and co-administration of Ang II with the AT1 receptor blocker losartan preventing the rescue (108, 163). The data collectively suggests that the AT1/Ang II axis is responsible for erythropoiesis control however the mechanisms are not yet fully described.

Our studies on Ang II and erythropoiesis led us to identify the presence of an unrecognized mechanism by which Ang II controls erythropoiesis at the level of the central nervous system involving SNA. Increased central Ang II production led to increased erythropoiesis in Agt-KO-Tg and Agt-Tg most likely via the same mechanisms. Therefore, we decided to further study this phenotype in Agt-Tg only. Using a long-term peripheral sympathectomy protocol, we could uncover that elevated brain Ang II led to a SNA-dependent increase in erythropoiesis in Agt-Tg. Reducing the SNA influence on erythropoiesis lowered Agt-Tg RBC to levels comparable to controls. A study using the sRA double transgenic model with increased brain Ang II supports our findings because this double transgenic mouse has an increased hematocrit. However, the double-transgenic animals have an altered fluid intake and urinary volume. Thus the phenotype was originally seen as an effect of dehydration (144). However, Agt-Tg mice likely have an unaltered fluid balance hence we conclude that the increased hematocrit observed in excess of brain Ang II production results in an increase in RBC production stimulated by SNA.

The hematopoietic organs, bone marrow and spleen, are innervated by the SNS as other peripheral organs (25, 277, 278). There has been previous studies describing increased SNA to these organs induced by brain Ang II infusion (25, 196, 252). NE has been recognized to stimulate erythropoiesis by increasing erythroid precursor cell growth via β2 adrenergic signaling by a mechanism apparently operating synergistic to erythropoietin (104, 279). This finding is supported by sympathectomized rats treated with 6-OHDA that develop anemia (211). Importantly, it seems that NE has a dose dependent effect on erythropoiesis because too high NE concentration inhibits growth (280, 281). Interestingly, Agt-Tg presented increased spleen size. In rodents, spleen erythropoiesis usually helps to recovery from acute anemia insults, but the spleen is also known to degrade aged erythrocytes and animals with increased RBC production develop a larger spleen. Hence, the splenomegaly in Agt-Tg might be cause or consequence of

increased erythropoiesis (94, 282). Recently it was demonstrated that social stress induces an increase in SNA to bone marrow and spleen and shifts the bone marrow hematopoietic stem and progenitor cell migration into the circulation and the spleen increasing spleen erythropoiesis and decreasing myeloid erythropoiesis. The same effect was observed systemically applying the β-adrenergic agonist isoprenaline (283). In the present study, the local site of increased erythropoiesis was not determined but further potential studies should be performed to verify if increased brain Ang II reallocates erythropoiesis.

Agt-Tg as other gain of function models may not well represent physiological conditions *e.g* Ang II formation site and Ang II levels. To test the role of brain-borne Ang II in baseline erythropoiesis, the hematology of a loss of function model was evaluated. The transgenic rat used has normal circulating RAS and around 90% depletion of brain Agt leading to diabetes insipidus due to reduced AVP release. Despite a higher water intake and urinary output this transgenic rat presents normal plasma electrolytes and natriuresis (61). If the water balance influences the RBC counts in this line it should increase due to plasma volume decrease. However, these rats with reduced brain RAS presented a lower hematocrit, RBC counts and hemoglobin strongly supporting a central effect mediated by Ang II on baseline erythropoiesis. Because peripheral RAS is not affected in the model, the effect observed on erythropoiesis is apparently mediated by Ang II locally generated in the brain independently of circulating Ang II acting on circumventricular organs.

All previous reports indicated an apparent normal iron homeostasis in mice lacking RAS peptides and also the RBC morphology was not altered therefore normocytic anemia was characterized (162, 163, 273). Contradicting previous reports iron deficiency was found in Agt-KO and Ren-KO in this study (162). The low iron levels led to microcytic anemia, without altering the RBC production but rather reduced volume characterizing microcytic anemia similarly to what described in mouse with iron deficiency (284). Most of the iron content is absorbed by a subset of gut enterocytes localized in the duodenum and part of the jejunum involving the transporters DMT1 and ferroportin. Hepcidin is recognized as the major body iron homeostasis regulator because it regulates iron uptake by controlling the internalization of ferroportin (100, 102). The measurements of hepcidin showed reduced levels in Agt-KO and

normal levels in Agt-KO-Tg as consequence the second had lower plasma iron in comparison to the first. The data discards that hepcidin overproduction leads to iron deficiency in Agt-KO, but shows that hepcidin is secondarily regulated according to the iron levels in the animals.

Despite that previous studies failed to identify reduced iron levels in plasma of RAS knockout models, chronic overload of Ang II in mice upregulated the expression of both proteins, DMT1 and ferroportin, mediating duodenal iron uptake. As consequence Ang II treated mice presented increased tissue iron accumulation and reduced hepcidin expression. These alterations were prevented by the co-administration of an AT1 blocker indicating a role of Ang II/AT1 axis in iron uptake in agreement with the findings of this study (285). Moreover there is evidence that DMT1 and ferroportin in rat kidney is upregulated during Ang II infusion (286, 287). Our data agrees with previous studies investigating iron metabolism in Ang II excess by demonstrating the reverse phenotype, the complete absence of Ang II leading to iron absorption impairment. Further studies are still pending to add robust evidence to the phenotype which include investigating the expression of DMT1 and ferroportin in gut samples and the iron uptake in Agt-KO.

Collectively, our data indicates that Ang II influences erythropoiesis by two distinct mechanisms. In the periphery, Ang II modulates body iron homeostasis and most likely iron uptake that ultimately is necessary for proper hemoglobin and RBC production. Within the brain brain-borne Ang II increases SNA and potentiates erythropoiesis resulting in increased RBC counts.

6 Conclusions and outlook

Attempts to quantify brain angiotensin peptides in preclinical models using LC-MS/MS often failed to detect RAS peptides in brain samples. Several lines of evidence, mostly pharmacological interventions, support local Ang II formation in the brain. Locally expressed Agt and ACE are abundant in the brain, but Ren is the limiting factor. Collectively, these points are the reason of a general discordance within field of brain RAS. To test if the brain has the ability to form RAS peptides, we have used a novel strategy that increased the precursor protein Agt expression exclusively in the brain. The fact that Ang I was not detected supports the idea of a Ren-independent pathway in the brain. Therefore, validating the dispensability of Ren for brain Ang II formation is still a fundamental question. Furthermore, brain Ang II formation location, extracellular or intracellular, must be determined. With new technologies to measure Agt, it would be interesting to go back to larger animals and measure intact and cleaved Agt in the cerebrospinal fluid[13].

There are two major aspects that need further understanding regarding the nature of SNA regulation of long-term BP. First, how branch-specific activation of the SNA is regulated (26). Several experimental evidence placed the RVLM as the major hub for SNA branch specific modulation (32, 288). Slowly the regulation is being uncovered as exemplified by the pathologically increased cardiac and renal SNA during heart failure, and the increased splanchnic SNA during Ang II induced hypertension (35, 41, 289). However, such questions have ultimately to be addressed in complicated *in vivo* preparations that in many cases use acute manipulations to infer long-term SNS regulation *e.g* inhibition of specific neuronal circuits (32, 290). Second, if the SNS controls long-term BP, a set point likely exists. The big open question is whether the brain itself senses BP and responds accordingly via SNA, or peripheral sensors control SNA via brain projections (3).

[13] Cleaved Agt is des(Ang I)Agt, the Agt protein products of after Ren cleavage. If this metabolite is measurable in the cerebrospinal fluid this would support brain Ang II formation as well as the dispensability of Ren or not.

To our knowledge this is the first time that a model lacking Ang II production is normotensive, and that unspecific brain Ang II production induced hypotension. The findings of this study demonstrated that FVB/N Agt-KO has an overactivated SNA that compensates the loss of the RAS and that brain rescue of Ang II production reduced BP by mediating a decrease in the vascular sympathetic tone in this animal. Importantly, SNA is locally regulated by factors such as Ang II but also tuned by peripheral inputs (afferents) such as the renal. We took advantage of the BP phenotype discrepancy in comparison to the C57BL/6 strain to dissect the molecular basis of the alterations found, and potentially point out new molecular players in SNA and BP control. Even though the BP phenotype indicated a single gene associated with the trait it seems that several loci contribute to the unexpected BP phenotype in FVB/N Agt-KO. Such complex interactions are not easy to genetically fine map, thus, future studies are necessary to complement the current one. If this mechanism(s) could be identified one could better speculate how brain Ang II reverts or prevents this puzzling phenotype in FVB/N animals lacking RAS.

Finally, the data set of this thesis suggested mechanisms whereby anemia develops in mice with gene targeted deletion of RAS components. The role(s) of Ang II in erythropoiesis control is not yet precisely defined. Ang II is known to increase SNA to hematopoietic organs, and we identified that increased central Ang II increases erythropoiesis via SNA. Further, studies should be designed to find the erythropoiesis source in these conditions, especially because the SNS is known to stimulate hematopoietic progenitor cell migration. If brain Ang II indeed has a modulatory role also in human erythropoiesis by SNA, the use of RAS blockers in conditions of altered erythropoiesis should be considered. Interestingly, another mechanism whereby Ang II controls erythropoiesis was identified, namely body iron homeostasis. This point was poorly addressed in this study, but the strong phenotype found in association with the RAS absence indicates that the iron balance is inappropriate. Gut iron transporter expression, iron uptake studies and rescue of the phenotype in Agt-KO by exogenous Ang II are among the next experiments to be performed in upcoming studies.

7 References

1. Oparil S, Acelajado MC, Bakris GL, Berlowitz DR, Cífková R, et al. 2018. Hypertension. *Nat. Rev. Dis. Prim.* 4(1):18014
2. Mancia G. 2012. Short- and Long-Term Blood Pressure Variability. *Hypertension*. 60(2):512–17
3. Guyenet PG. 2006. The sympathetic control of blood pressure. *Nat. Rev. Neurosci.* 7(5):335–46
4. Page IH. 1949. Pathogenesis of arterial hypertension. *J. Am. Med. Assoc.* 140(5):451–58
5. Lohmeier TE. 2012. Angiotensin II Infusion Model of Hypertension. *Hypertension*. 59(3):539–41
6. Harrison DG, Coffman TM, Wilcox CS. 2021. Pathophysiology of Hypertension. *Circ. Res.* 128(7):847–63
7. Johnson AK, Xue B. 2018. Central nervous system neuroplasticity and the sensitization of hypertension. *Nat. Rev. Nephrol.* 14(12):750–66
8. Carey RM, Whelton PK. 2018. Prevention, Detection, Evaluation, and Management of High Blood Pressure in Adults: Synopsis of the 2017 American College of Cardiology/American Heart Association Hypertension Guideline. *Ann. Intern. Med.* 168(5):351
9. Muntner P, Carey RM, Gidding S, Jones DW, Taler SJ, et al. 2018. Potential US population impact of the 2017 ACC/AHA high blood pressure guideline. *Circulation*. 137(2):109–18
10. Pijacka W, Moraes DJA, Ratcliffe LEK, Nightingale AK, Hart EC, et al. 2016. Purinergic receptors in the carotid body as a new drug target for controlling hypertension. *Nat. Med.* 22(10):1151–59
11. Zhou B, Perel P, Mensah GA, Ezzati M. 2021. Global epidemiology, health burden and effective interventions for elevated blood pressure and hypertension. *Nat. Rev. Cardiol.* 18(11):785–802
12. Chobanian A V. 2009. The Hypertension Paradox — More Uncontrolled Disease despite Improved Therapy. *N. Engl. J. Med.* 361(9):878–87
13. Roth, Gregory A.Johnson C, Abajobir A, Abd-Allah F, Abera SF, Abyu G, et al. 2017. Global, Regional, and National Burden of Cardiovascular Diseases for 10 Causes, 1990 to 2015. *J. Am. Coll. Cardiol.* 70(1):1–25
14. Go AS, Mozaffarian D, Roger VL, Benjamin EJ, Berry JD, et al. 2014. Executive summary: Heart Disease and Stroke Statistics - 2014 Update: A report from the American Heart Association. *Circulation*. 129(3):399–410
15. Brands MW. 2012. Chronic Blood Pressure Control. In *Comprehensive Physiology*. 2(4):2481–94. Wiley
16. Osborn JW, Foss JD. 2017. Renal Nerves and Long-Term Control of Arterial Pressure. In *Comprehensive Physiology*, pp. 263–320. Hoboken, NJ, USA: Wiley
17. Stocker SD, Kinsman BJ, Sved AF. 2017. Recent Advances in Neurogenic Hypertension. *Hypertension*. 70(3):474–78
18. Asirvatham-Jeyaraj N, Gauthier MM, Banek CT, Ramesh A, Garver H, et al. 2021. Renal Denervation and Celiac Ganglionectomy Decrease Mean Arterial Pressure Similarly in Genetically Hypertensive Schlager (BPH/2J) Mice. *Hypertension*. 77(2):519–28
19. Johnson AK, Xue B. 2018. Central nervous system neuroplasticity and the sensitization of hypertension. *Nat. Rev. Nephrol.* 14(12):750–66
20. Sata Y, Head GA, Denton K, May CN, Schlaich MP. 2018. Role of the Sympathetic Nervous System and Its Modulation in Renal Hypertension. *Front. Med.* 5(MAR):82
21. Mancia G, Grassi G. 2014. The Autonomic Nervous System and Hypertension. *Circ. Res.* 114(11):1804–14
22. Masuo K, Kawaguchi H, Mikami H, Ogihara T, Tuck ML. 2003. Serum Uric Acid and Plasma

Norepinephrine Concentrations Predict Subsequent Weight Gain and Blood Pressure Elevation. *Hypertension*. 42(4):474–80

23. Grassi G, Pisano A, Bolignano D, Seravalle G, D'Arrigo G, et al. 2018. Sympathetic Nerve Traffic Activation in Essential Hypertension and Its Correlates. *Hypertension*. 72(2):483–91
24. Montani J-P, Van Vliet BN. 2009. Understanding the contribution of Guyton's large circulatory model to long-term control of arterial pressure. *Exp. Physiol.* 94(4):382–88
25. Carnevale D. 2020. Neural Control of Immunity in Hypertension: Council on Hypertension Mid Career Award for Research Excellence, 2019. *Hypertension*. 76(3):622–28
26. Kaufmann H, Norcliffe-Kaufmann L, Palma J-A. 2020. Baroreflex Dysfunction. *N. Engl. J. Med.* 382(2):163–78
27. Macarthur H, Wilken GH, Westfall TC, Kolo LL. 2011. Neuronal and non-neuronal modulation of sympathetic neurovascular transmission. *Acta Physiol.* 203(1):37–45
28. Kobilka BK, Hein L, Altman JD. 1999. Two functionally distinct alpha2-adrenergic receptors regulate sympathetic neurotransmission. *Nature*. 402(6758):181–84
29. Link RE, Desai K, Hein L, Stevens ME, Chruscinski A, et al. 1996. Cardiovascular regulation in mice lacking α2-adrenergic receptor subtypes b and c. *Science (80-.).* 273(5276):803–5
30. Shoemaker JK, Badrov MB, Al-Khazraji BK, Jackson DN. 2016. Neural control of vascular function in skeletal muscle. *Compr. Physiol.* 6(1):303–29
31. Stornetta RL. 2009. Neurochemistry of bulbospinal presympathetic neurons of the medulla oblongata. *J. Chem. Neuroanat.* 38(3):222–30
32. Guyenet PG, Stornetta RL, Souza GMPR, Abbott SBG, Brooks VL. 2020. Neuronal Networks in Hypertension. *Hypertension*. 76(2):300–311
33. Bader M. 2010. Tissue Renin-Angiotensin-Aldosterone Systems: Targets for Pharmacological Therapy. *Annu. Rev. Pharmacol. Toxicol.* 50(1):439–65
34. Colombari E, Sato MA, Cravo SL, Bergamaschi CT, Campos RR, Lopes OU. 2001. Role of the Medulla Oblongata in Hypertension. *Hypertension*. 38(3):549–54
35. Victor RG. 2015. Carotid baroreflex activation therapy for resistant hypertension. *Nat. Rev. Cardiol.* 12(8):451–63
36. Sequeira-Lopez MLS, Gomez RA. 2021. Renin Cells, the Kidney, and Hypertension. *Circ. Res.* 128:887–907
37. Thomas GD. 2011. Neural control of the circulation. *Adv. Physiol. Educ.* 35(1):28–32
38. Thomas GD, Segal SS. 2004. Neural control of muscle blood flow during exercise. *J. Appl. Physiol.* 97(2):731–38
39. DeLalio LJ, Sved AF, Stocker SD. 2020. Sympathetic Nervous System Contributions to Hypertension: Updates and Therapeutic Relevance. *Can. J. Cardiol.* 36(5):712–20
40. Nishida Y, Tandai-Hiruma M, Kemuriyama T, Hagisawa K. 2012. Long-term blood pressure control: is there a set-point in the brain? *J. Physiol. Sci.* 62(3):147–61
41. Osborn JW, Fink GD, Kuroki MT. 2011. Neural Mechanisms of Angiotensin II–Salt Hypertension: Implications for Therapies Targeting Neural Control of the Splanchnic Circulation. *Curr. Hypertens. Rep.* 13(3):221–28
42. Ng FL, Saxena M, Mahfoud F, Pathak A, Lobo MD. 2016. Device-based Therapy for Hypertension. *Curr. Hypertens. Rep.* 18(8):61
43. Mahfoud F, Schlaich MP, Lobo MD. 2021. Device Therapy of Hypertension. *Circ. Res.* 128(7):1080–99
44. Basso N, Terragno NA. 2001. History About the Discovery of the Renin-Angiotensin System. *Hypertension*. 38(6):1246–49

45. Van Epps HL. 2005. Harry Goldblatt and the discovery of renin. *J. Exp. Med.* 201(9):1351–1351

46. Braun-Menendez E, Page IH. 1958. Suggested Revision of Nomenclature--Angiotensin. *Science*. 127(3292):242

47. Helmer OM. 1957. Differentiation Between Two Forms of Angiotonin by Means of Spirally Cut Strips of Rabbit Aorta. *Am. J. Physiol. Content*. 188(3):571–77

48. Forrester SJ, Booz GW, Sigmund CD, Coffman TM, Kawai T, et al. 2018. Angiotensin II Signal Transduction: An Update on Mechanisms of Physiology and Pathophysiology. *Physiol. Rev.* 98(3):1627–1738

49. Santos RAS, Sampaio WO, Alzamora AC, Motta-Santos D, Alenina N, et al. 2018. The ACE2/Angiotensin-(1–7)/MAS Axis of the Renin-Angiotensin System: Focus on Angiotensin-(1–7). *Physiol. Rev.* 98(1):505–53

50. Bader M, Turner AJ, Alenina N. 2020. ACE2, a multifunctional protein – from cardiovascular regulation to COVID-19. *Clin. Sci.* 134(23):3229–32

51. Kurtz A. 2012. Control of Renin Synthesis and Secretion. *Am. J. Hypertens.* 25(8):839–47

52. Sparks MA, Crowley SD, Gurley SB, Mirotsou M, Coffman TM. 2014. Classical Renin-Angiotensin System in Kidney Physiology. In *Comprehensive Physiology*, pp. 1201–28. Wiley

53. Wu C, Lu H, Cassis LA, Daugherty A. 2011. Molecular and Pathophysiological Features of Angiotensinogen: A Mini Review. *N. Am. J. Med. Sci. (Boston).* 4(4):183–90

54. Matsusaka T, Miyazaki Y, Ichikawa I. 2002. The Renin Angiotensin System and Kidney Development. *Annu. Rev. Physiol.* 64(1):551–61

55. Bekassy Z, Lopatko Fagerström I, Bader M, Karpman D. 2021. Crosstalk between the renin–angiotensin, complement and kallikrein–kinin systems in inflammation. *Nat. Rev. Immunol.*, pp. 1–18

56. Baltatu OC, Campos LA, Bader M. 2011. Local renin–angiotensin system and the brain—A continuous quest for knowledge. *Peptides*. 32(5):1083–86

57. Allen AM, O'Callaghan EL, Mendelsohn FAO, Chai S-Y. 2009. Neuronal Angiotensin. In *Encyclopedia of Neuroscience*, pp. 697–702. Elsevier

58. Ganten D, Hayduk K, Brecht HM, Boucher R, Genest J. 1970. Evidence of renin release or production in splanchnic territory. *Nature*. 226(5245):551–52

59. Uijl E, Ren L, Mirabito Colafella KM, van Veghel R, Garrelds IM, et al. 2021. No evidence for brain renin–angiotensin system activation during DOCA-salt hypertension. *Clin. Sci.* 135(2):259–74

60. Matsusaka T, Niimura F, Shimizu A, Pastan I, Saito A, et al. 2012. Liver Angiotensinogen Is the Primary Source of Renal Angiotensin II. *J. Am. Soc. Nephrol.* 23(7):1181–89

61. Schinke M, Baltatu O, Bohm M, Peters J, Rascher W, et al. 1999. Blood pressure reduction and diabetes insipidus in transgenic rats deficient in brain angiotensinogen. *Proc. Natl. Acad. Sci.* 96(7):3975–80

62. Ying J, Stuart D, Hillas E, Gociman BR, Ramkumar N, et al. 2012. Overexpression of mouse angiotensinogen in renal proximal tubule causes salt-sensitive hypertension in mice. *Am. J. Hypertens.* 25(6):684–89

63. Chang L, Xiong W, Zhao X, Fan Y, Guo Y, et al. 2018. Bmal1 in Perivascular Adipose Tissue Regulates Resting-Phase Blood Pressure Through Transcriptional Regulation of Angiotensinogen. *Circulation*. 138(1):67–79

64. Mullins JJ, Peters J, Ganten D. 1990. Fulminant hypertension in transgenic rats harbouring the mouse Ren-2 gene. *Nature*. 344(6266):541–44

65. Gonzalez-Villalobos RA, Janjoulia T, Fletcher NK, Giani JF, Nguyen MTX, et al. 2013. The absence of intrarenal ACE protects against hypertension. *J. Clin. Invest.* 123(5):2011–23

66. Campbell DJ. 2014. Clinical relevance of local renin angiotensin systems. *Front. Endocrinol. (Lausanne).*

5(JUL):113

67. Uijl E, Mirabito Colafella KM, Sun Y, Ren L, van Veghel R, et al. 2019. Strong and Sustained Antihypertensive Effect of Small Interfering RNA Targeting Liver Angiotensinogen. *Hypertension*. 73(6):1249–57

68. Haddad-Tóvolli R, Dragano NRV, Ramalho AFS, Velloso LA. 2017. Development and function of the blood-brain barrier in the context of metabolic control. *Front. Neurosci.* 11(APR):224

69. Nakagawa P, Gomez J, Grobe JL, Sigmund CD. 2020. The Renin-Angiotensin System in the Central Nervous System and Its Role in Blood Pressure Regulation. *Curr. Hypertens. Rep.* 22(1):7

70. Szczepanska-Sadowska E, Czarzasta K, Cudnoch-Jedrzejewska A. 2018. Dysregulation of the Renin-Angiotensin System and the Vasopressinergic System Interactions in Cardiovascular Disorders. *Curr. Hypertens. Rep.* 20(3):19

71. Stornetta RL, Hawelu-Johnson CL, Guyenet PG, Lynch KR. 1988. Astrocytes synthesize angiotensinogen in brain. *Science (80-.).* 242(4884):1444–46

72. Bader M. 2010. Rat Models of Cardiovascular Diseases. In *Rat Genomics: Methods and Protocols, Methods in Molecular Biology*, pp. 403–14. Humana Press

73. de Kloet AD, Liu M, Rodríguez V, Krause EG, Sumners C. 2015. Role of neurons and glia in the CNS actions of the renin-angiotensin system in cardiovascular control. *Am. J. Physiol. - Regul. Integr. Comp. Physiol.* 309(5):R444–58

74. Sumners C, Alleyne A, Rodríguez V, Pioquinto DJ, Ludin JA, et al. 2020. Brain angiotensin type-1 and type-2 receptors: cellular locations under normal and hypertensive conditions. *Hypertens. Res.* 43(4):281–95

75. de Kloet AD, Wang L, Pitra S, Hiller H, Smith JA, et al. 2017. A Unique "Angiotensin-Sensitive" Neuronal Population Coordinates Neuroendocrine, Cardiovascular, and Behavioral Responses to Stress. *J. Neurosci.* 37(13):3478–90

76. Uijl E, Ren L, Danser AHJ. 2018. Angiotensin generation in the brain: a re-evaluation. *Clin. Sci.* 132(8):839–50

77. Mirabito Colafella KM, Danser AHJ. 2017. Recent Advances in Angiotensin Research. *Hypertension*. 69(6):994–99

78. Van Thiel BS, Góes Martini A, Te Riet L, Severs D, Uijl E, et al. 2017. Brain Renin-Angiotensin System Does It Exist? *Hypertension*. 69(6):1136–44

79. Danser AHJ. 2015. The Role of the (Pro)renin Receptor in Hypertensive Disease. *Am. J. Hypertens.* 28(10):1187–96

80. Shah SJ, Stafford RS. 2017. Current Trends of Hypertension Treatment in the United States. *Am. J. Hypertens.* 30(10):1008–14

81. Ho JK, Moriarty F, Manly JJ, Larson EB, Evans DA, et al. 2021. Blood-Brain Barrier Crossing Renin-Angiotensin Drugs and Cognition in the Elderly: A Meta-Analysis. *Hypertension*. 78(3):629–43

82. Laurent S. 2017. Antihypertensive drugs. *Pharmacol. Res.* 124:116–25

83. Dendorfer A, Thornagel A, Raasch W, Grisk O, Tempel K, Dominiak P. 2002. Angiotensin II induces catecholamine release by direct ganglionic excitation. *Hypertension*. 40(3):348–54

84. Milanez MIO, Nishi EE, Bergamaschi CT, Campos RR. 2020. Role of spinal neurons in the maintenance of elevated sympathetic activity: a novel therapeutic target? *Am. J. Physiol. Integr. Comp. Physiol.* 319(3):R282–87

85. Touyz RM, Alves-Lopes R, Rios FJ, Camargo LL, Anagnostopoulou A, et al. 2018. Vascular smooth muscle contraction in hypertension. *Cardiovasc. Res.* 114(4):529–39

86. Brozovich FV, Nicholson CJ, Degen CV, Gao YZ, Aggarwal M, Morgan KG. 2016. Mechanisms of Vascular Smooth Muscle Contraction and the Basis for Pharmacologic Treatment of Smooth Muscle Disorders. *Pharmacol. Rev.* 68(2):476–532

87. Konukoglu D, Uzun H. 2016. Endothelial Dysfunction and Hypertension. In *Advances in Experimental Medicine and Biology*. 956:511–40. Springer, Cham

88. Farah C, Michel LYM, Balligand J-L. 2018. Nitric oxide signalling in cardiovascular health and disease. *Nat. Rev. Cardiol.* 15(5):292–316

89. Mathew J, Sankar P, Varacallo M. 2021. *Physiology, Blood Plasma*. StatPearls Publishing

90. Feher J. 2012. Overview of the Cardiovascular System and the Blood. In *Quantitative Human Physiology*, pp. 489–97. Elsevier

91. Maestroni GJM. 2020. Adrenergic Modulation of Hematopoiesis. *J. Neuroimmune Pharmacol.* 15(1):82–92

92. Pinho S, Frenette PS. 2019. Haematopoietic stem cell activity and interactions with the niche. *Nat. Rev. Mol. Cell Biol.* 20(5):303–20

93. Van Putten LM. 1958. The life span of red cells in the rat and the mouse as determined by labeling with DFP32 in vivo. *Blood*. 13(8):789–94

94. Chen L, Wang J, Liu J, Wang H, Hillyer CD, et al. 2021. Dynamic changes in murine erythropoiesis from birth to adulthood: implications for the study of murine models of anemia. *Blood Adv.* 5(1):16–25

95. Valent P, Büsche G, Theurl I, Uras IZ, Germing U, et al. 2018. Normal and pathological erythropoiesis in adults: from gene regulation to targeted treatment concepts. *Haematologica*. 103(10):1593–1603

96. Palis J. 2014. Primitive and definitive erythropoiesis in mammals. *Front. Physiol.* 5:3

97. Jelkmann W. 2011. Regulation of erythropoietin production. *J. Physiol.* 589(6):1251–58

98. Jelkmann W. 2016. Erythropoietin. In *Frontiers of Hormone Research*. 47:115–27

99. Hentze MW, Muckenthaler MU, Galy B, Camaschella C. 2010. Two to Tango: Regulation of Mammalian Iron Metabolism. *Cell*. 142(1):24–38

100. Camaschella C, Nai A, Silvestri L. 2020. Iron metabolism and iron disorders revisited in the hepcidin era. *Haematologica*. 105(2):260–72

101. Gulec S, Anderson GJ, Collins JF. 2014. Mechanistic and regulatory aspects of intestinal iron absorption. *Am. J. Physiol. Liver Physiol.* 307(4):G397–409

102. Nemeth E, Ganz T. 2009. The Role of Hepcidin in Iron Metabolism. *Acta Haematol.* 122(2–3):78–86

103. Fielding C, Méndez-Ferrer S. 2020. Neuronal regulation of bone marrow stem cell niches. *F1000Research*. 9([version 1; peer review: 3 approved]):614

104. Saba F, Saki N, Khodadi E, Soleimani M. 2017. Crosstalk between catecholamines and erythropoiesis. *Front. Biol. (Beijing).* 12(2):103–15

105. Biaggioni I. 1994. The Anemia of Primary Autonomic Failure and its Reversal with Recombinant Erythropoietin. *Ann. Intern. Med.* 121(3):181

106. Haznedaroglu IC, Malkan UY. 2016. Local bone marrow renin-angiotensin system in the genesis of leukemia and other malignancies. *Eur. Rev. Med. Pharmacol. Sci.* 20(19):4089–4111

107. Gomez RA, Sequeira-Lopez MLS. 2018. Renin cells in homeostasis, regeneration and immune defence mechanisms. *Nat. Rev. Nephrol.* 14(4):231–45

108. Doan TN, Gletsu N, Cole J, Bernstein KE. 2001. Genetic manipulation of the renin-angiotensin system. *Curr. Opin. Nephrol. Hypertens.* 10(4):483–91

109. Vlahakos D V, Marathias KP, Madias NE. 2010. The Role of the Renin-Angiotensin System in the Regulation of Erythropoiesis. *YAJKD*. 56:558–65

110. Kim Y-C, Mungunsukh O, Day RM. 2017. Erythropoietin Regulation by Angiotensin II. In *Vitamins and Hormones*. 105:57–77. Elsevier Inc. 1st ed.

111. Ito M, Oliverio MI, Mannon PJ, Best CF, Maeda N, et al. 1995. Regulation of blood pressure by the type 1A angiotensin II receptor gene. *Proc. Natl. Acad. Sci.* 92(8):3521–25

112. Tanimoto K, Sugiyama F, Goto Y, Ishida J, Takimoto E, et al. 1994. Angiotensinogen-deficient mice with hypotension. *J. Biol. Chem.* 269(50):31334–37

113. Brenner M, Kisseberth W, Su Y, Besnard F, Messing A. 1994. GFAP promoter directs astrocyte-specific expression in transgenic mice. *J. Neurosci.* 14(3):1030–37

114. Cardoso CC, Alenina N, Ferreira AJ, Qadri F, Lima MP, et al. 2010. Increased blood pressure and water intake in transgenic mice expressing rat tonin in the brain. *Biol. Chem.* 391(4):435–41

115. Takahashi N, Lopez MLSS, Cowhig JE, Taylor MA, Hatada T, et al. 2005. Ren1c Homozygous Null Mice Are Hypotensive and Polyuric, but Heterozygotes Are Indistinguishable from Wild-Type. *J. Am. Soc. Nephrol.* 16(1):125–32

116. Homberg JR, Wöhr M, Alenina N. 2017. Comeback of the Rat in Biomedical Research. *ACS Chem. Neurosci.* 8(5):900–903

117. Cardin JA, Carlén M, Meletis K, Knoblich U, Zhang F, et al. 2010. Targeted optogenetic stimulation and recording of neurons in vivo using cell-type-specific expression of Channelrhodopsin-2. *Nat. Protoc.* 5(2):247–54

118. Carnevale L, Carnevale R, Mastroiacovo F, Cifelli G, Carnevale D, Lembo G. 2021. Ultrasound-guided catheter implantation improves conscious radiotelemetric blood pressure measurement in mice. *Cardiovasc. Res.* 117(3):661–62

119. Kurtz TW, Griffin KA, Bidani AK, Davisson RL, Hall JE. 2005. Recommendations for Blood Pressure Measurement in Humans and Experimental Animals. *Hypertension*. 45(2):299–310

120. Todiras M, Alenina N, Bader M. 2017. Evaluation of Endothelial Dysfunction In Vivo. In *Methods in Molecular Biology*. 1527:355–67. Springer New York

121. Caligiorne SM, Silva AQG, Fontes MAP, Silva JR, Baltatu O, et al. 2008. Baroreflex control of heart rate and renal sympathetic nerve activity in rats with low brain angiotensinogen. *Neuropeptides*. 42(2):159–68

122. Clark DW, Laverty R, Phelan EL. 1972. Long-lasting peripheral and central effects of 6-hydroxydopamine in rats. *Br. J. Pharmacol.* 44(2):233–43

123. Ben-Shaanan TL, Schiller M, Azulay-Debby H, Korin B, Boshnak N, et al. 2018. Modulation of anti-tumor immunity by the brain's reward system. *Nat. Commun.* 9(1):2723

124. Horvathova L, Tillinger A, Padova A, Mravec B. 2016. Sympathectomized tumor-bearing mice survive longer but develop bigger melanomas. *Endocr. Regul.* 50(4):207–14

125. Popova E, Krivokharchenko A, Ganten D, Bader M. 2004. Efficiency of transgenic rat production is independent of transgene-construct and overnight embryo culture. *Theriogenology*. 61(7–8):1441–53

126. Livak KJ, Schmittgen TD. 2001. Analysis of Relative Gene Expression Data Using Real-Time Quantitative PCR and the $2^{-\Delta\Delta CT}$ Method. *Methods*. 25(4):402–8

127. Ohtsuka M, Sato M, Miura H, Takabayashi S, Matsuyama M, et al. 2018. i-GONAD: a robust method for in situ germline genome engineering using CRISPR nucleases. *Genome Biol.* 19(1):25

128. Bai H, Liu L, An K, Lu X, Harrison M, et al. 2020. CRISPR/Cas9-mediated precise genome modification by a long ssDNA template in zebrafish. *BMC Genomics*. 21(1):67

129. Miura H, Quadros RM, Gurumurthy CB, Ohtsuka M. 2018. Easi-CRISPR for creating knock-in and conditional knockout mouse models using long ssDNA donors. *Nat. Protoc.* 13(1):195–215

130. Sanger F, Coulson AR. 1975. A rapid method for determining sequences in DNA by primed synthesis with DNA polymerase. *J. Mol. Biol.* 94(3):441–48

131. Schelling P, Ganten U, Sponer G, Unger T, Ganten D. 1980. Components of the Renin-Angiotensin System in the Cerebrospinal Fluid of Rats and Dogs with Special Consideration of the Origin and the Fate of Angiotensin II. *Neuroendocrinology*. 31(5):297–308

132. Alves-Lopes R, Montezano AC, Neves KB, Harvey A, Rios FJ, et al. 2021. Selective Inhibition of the C-Domain of ACE (Angiotensin-Converting Enzyme) Combined With Inhibition of NEP (Neprilysin): A Potential New Therapy for Hypertension. *Hypertension*. 78(3):604–16

133. Thomas WG, Greenland KJ, Shinkel TA, Sernia C. 1992. Angiotensinogen is secreted by pure rat neuronal cell cultures. *Brain Res.* 588(2):191–200

134. Jacobsen JC, Erdin S, Chiang C, Hanscom C, Handley RR, et al. 2017. Potential molecular consequences of transgene integration: The R6/2 mouse example. *Sci. Rep.* 7(1):41120

135. Kong Q, Wu M, Huan Y, Zhang L, Liu H, et al. 2009. Transgene Expression Is Associated with Copy Number and Cytomegalovirus Promoter Methylation in Transgenic Pigs. *PLoS One*. 4(8):e6679

136. Kakinuma Y, Hama H, Sugiyama F, Yagami K-I, Goto K, et al. 1998. Impaired blood–brain barrier function in angiotensinogen-deficient mice. *Nat. Med.* 4(9):1078–80

137. Ren L, Lu X, Danser AHJ. 2019. Revisiting the Brain Renin-Angiotensin System—Focus on Novel Therapies. *Curr. Hypertens. Rep.* 21(4):28

138. Ferrario CM, Groban L, Wang H, Cheng CP, VonCannon JL, et al. 2021. The Angiotensin-(1–12)/Chymase axis as an alternate component of the tissue renin angiotensin system. *Mol. Cell. Endocrinol.* 529:111119

139. Reyes S, Cheng CP, Roberts DJ, Yamashita T, Ahmad S, et al. 2019. Angiotensin-(1–12)/chymase axis modulates cardiomyocyte L-type calcium currents in rats expressing human angiotensinogen. *Int. J. Cardiol.* 297:104–10

140. Unger T. 2003. Inhibiting angiotensin receptors in the brain: possible therapeutic implications. *Curr. Med. Res. Opin.* 19(5):449–51

141. Christ-Crain M, Fenske W. 2016. Copeptin in the diagnosis of vasopressin-dependent disorders of fluid homeostasis. *Nat. Rev. Endocrinol.* 12(3):168–76

142. Leenen FHH. 2014. Actions of Circulating Angiotensin II and Aldosterone in the Brain Contributing to Hypertension. *Am. J. Hypertens.* 27(8):1024–32

143. Qadri F, Culman J, Veltmar A, Maas K, Rascher W, Unger T. 1993. Angiotensin II-induced vasopressin release is mediated through alpha-1 adrenoceptors and angiotensin II AT1 receptors in the supraoptic nucleus. *J. Pharmacol. Exp. Ther.* 267(2):567–74

144. Grobe JL, Grobe CL, Beltz TG, Westphal SG, Morgan DA, et al. 2010. The Brain Renin-Angiotensin System Controls Divergent Efferent Mechanisms to Regulate Fluid and Energy Balance. *Cell Metab.* 12(5):431–42

145. Sun Z, Cade R, Zhang Z, Alouidor J, Van H. 2003. Angiotensinogen Gene Knockout Delays and Attenuates Cold-Induced Hypertension. *Hypertension*. 41(2):322–27

146. Kihara M. 1998. Genetic deficiency of angiotensinogen produces an impaired urine concentrating ability in mice. *Kidney Int.* 53:548–55

147. Nardone M, Floras JS, Millar PJ. 2020. Sympathetic neural modulation of arterial stiffness in humans. *Am. J. Physiol. Circ. Physiol.* 319(6):H1338–46

148. Goldstein DS. 2008. Genotype and Vascular Phenotype Linked by Catecholamine Systems. *Circulation*. 117(4):458–61

149. Burns C, Kidron A. 2021. *Biochemistry, Tyramine*. StatPearls Publishing

150. Philipp M, Hein L. 2004. Adrenergic receptor knockout mice: distinct functions of 9 receptor subtypes. *Pharmacol. Ther.* 101(1):65–74

151. Gu F, Randall EB, Whitesall S, Converso-Baran K, Carlson BE, et al. 2020. Potential role of intermittent functioning of baroreflexes in the etiology of hypertension in spontaneously hypertensive rats. *JCI Insight*. 5(19):

152. Llorens-Cortes C, Touyz RM. 2020. Evolution of a New Class of Antihypertensive Drugs. *Hypertension*. 75(1):6–15

153. Mohammed M, Johnson DN, Wang LA, Harden SW, Sheng W, et al. 2021. Targeting angiotensin type-2 receptors located on pressor neurons in the nucleus of the solitary tract to relieve hypertension in mice. *Cardiovasc. Res.* in press:

154. Polson JW, Dampney RAL, Boscan P, Pickering AE, Paton JFR. 2007. Differential baroreflex control of sympathetic drive by angiotensin II in the nucleus tractus solitarii. *Am. J. Physiol. Integr. Comp. Physiol.* 293(5):R1954–60

155. Ding Y, Stec DE, Sigmund CD. 2001. Genetic Evidence That Lethality in Angiotensinogen-deficient Mice Is Due to Loss of Systemic but Not Renal Angiotensinogen. *J. Biol. Chem.* 276(10):7431–36

156. Okubo S, Niimura F, Matsusaka T, Fogo A, Hogan BLM, Ichikawa I. 1998. Angiotensinogen gene null-mutant mice lack homeostatic regulation of glomerular filtration and tubular reabsorption. *Kidney Int.* 53(3):617–25

157. Tong G-X, Yu WM, Beaubier NT, Weeden EM, Hamele-Bena D, et al. 2009. Expression of PAX8 in normal and neoplastic renal tissues: an immunohistochemical study. *Mod. Pathol.* 22(9):1218–27

158. Lin EE, Pentz ES, Sequeira-Lopez MLS, Gomez RA. 2015. Aldo-keto reductase 1b7, a novel marker for renin cells, is regulated by cyclic AMP signaling. *Am. J. Physiol. Integr. Comp. Physiol.* 309(5):R576–84

159. Ishida J, Sugiyama F, Tanimoto K, Taniguchi K, Syouji M, et al. 1998. Rescue of Angiotensinogen-Knockout Mice. *Biochem. Biophys. Res. Commun.* 252(3):610–16

160. Nakamori H, Yoshida S, Ishiguro H, Suzuki S, Yasuzaki H, et al. 2018. Arterial wall hypertrophy is ameliorated by α2-adrenergic receptor antagonist or aliskiren in kidneys of angiotensinogen-knockout mice. *Clin. Exp. Nephrol.* 22(4):773–81

161. Morgan AP, Fu C-P, Kao C-Y, Welsh CE, Didion JP, et al. 2015. The Mouse Universal Genotyping Array: From Substrains to Subspecies. *G3 Genes|Genomes|Genetics*. 6(2):263–79

162. Cole J, Ertoy D, Lin H, Sutliff RL, Ezan E, et al. 2000. Lack of angiotensin II-facilitated erythropoiesis causes anemia in angiotensin-converting enzyme-deficient mice. *J. Clin. Invest.* 106(11):1391–98

163. Kato H, Ishida J, Matsusaka T, Ishimaru T, Tanimoto K, et al. 2015. Erythropoiesis and Blood Pressure Are Regulated via AT1 Receptor by Distinctive Pathways. *PLoS One*. 10(6):e0129484

164. Gembardt F, Heringer-Walther S, Esch JHM, Sterner-Kock A, Veghel R, et al. 2008. Cardiovascular phenotype of mice lacking all three subtypes of angiotensin II receptors. *FASEB J.* 22(8):3068–77

165. Cho W, Hagemann TL, Johnson DA, Johnson JA, Messing A. 2009. Dual transgenic reporter mice as a tool for monitoring expression of glial fibrillary acidic protein. *J. Neurochem.* 110(1):343–51

166. Sapouckey SA, Morselli LL, Deng G, Patil CN, Balapattabi K, et al. 2020. Exploration of cardiometabolic and developmental significance of angiotensinogen expression by cells expressing the leptin receptor or agouti-related peptide. *Am. J. Physiol. Integr. Comp. Physiol.* 318(5):R855–69

167. Yu X, Nagai J, Khakh BS. 2020. Improved tools to study astrocytes. *Nat. Rev. Neurosci. 2020 213*. 21(3):121–38

168. Jankowsky JL, Slunt HH, Ratovitski T, Jenkins NA, Copeland NG, Borchelt DR. 2001. Co-expression of multiple transgenes in mouse CNS: a comparison of strategies. *Biomol. Eng.* 17(6):157–65

169. Besnard F, Brenner M, Nakatani Y, Chao R, Purohit HJ, Freese E. 1991. Multiple interacting sites regulate astrocyte-specific transcription of the human gene for glial fibrillary acidic protein. *J. Biol. Chem.* 266(28):18877–83

170. Andra J, Bongcam-Rudloff E, Hansson I, Lendahl U, Westermark B, Nistér M. 2001. A 1.8 kb GFAP-promoter fragment is active in specific regions of the embryonic CNS. *Mech. Dev.* 107(1–2):181–85

171. Schleifenbaum J, Kassmann M, Szijártó IA, Hercule HC, Tano J-Y, et al. 2014. Stretch–Activation of Angiotensin II Type 1 a Receptors Contributes to the Myogenic Response of Mouse Mesenteric and Renal Arteries. *Circ. Res.* 115(2):263–72

172. Exner EC, Geurts AM, Hoffmann BR, Casati M, Stodola T, et al. 2020. Interaction between Mas1 and AT1RA contributes to enhancement of skeletal muscle angiogenesis by angiotensin-(1-7) in Dahl salt-sensitive rats. *PLoS One*. 15(4):e0232067

173. Moreno C, Hoffman M, Stodola TJ, Didier DN, Lazar J, et al. 2011. Creation and Characterization of a Renin Knockout Rat. *Hypertension*. 57(3):614–19

174. Gribouval O, Gonzales M, Neuhaus T, Aziza J, Bieth E, et al. 2005. Mutations in genes in the renin-angiotensin system are associated with autosomal recessive renal tubular dysgenesis. *Nat. Genet.* 37(9):964–68

175. Gribouval O, Morinière V, Pawtowski A, Arrondel C, Sallinen S-L, et al. 2012. Spectrum of mutations in the renin-angiotensin system genes in autosomal recessive renal tubular dysgenesis. *Hum. Mutat.* 33(2):316–26

176. Tseng M-H, Huang S-M, Huang J-L, Fan W-L, Konrad M, et al. 2020. Autosomal Recessive Renal Tubular Dysgenesis Caused by a Founder Mutation of Angiotensinogen. *Kidney Int. Reports*. 5(11):2042–51

177. Erwood S, Gu B. 2020. Embryo-Based Large Fragment Knock-in in Mammals: Why, How and What's Next. *Genes (Basel).* 11(2):140

178. Honda A, Tachibana R, Hamada K, Morita K, Mizuno N, et al. 2019. Efficient derivation of knock-out and knock-in rats using embryos obtained by in vitro fertilization. *Sci. Rep.* 9(1):11571

179. Mizuno N, Mizutani E, Sato H, Kasai M, Ogawa A, et al. 2018. Intra-embryo Gene Cassette Knockin by CRISPR/Cas9-Mediated Genome Editing with Adeno-Associated Viral Vector. *iScience*. 9:286–97

180. Chenouard V, Remy S, Tesson L, Ménoret S, Ouisse L-H, et al. 2021. Advances in Genome Editing and Application to the Generation of Genetically Modified Rat Models. *Front. Genet.* 12:334

181. Biancardi VC, Son SJ, Ahmadi S, Filosa JA, Stern JE. 2014. Circulating Angiotensin II Gains Access to the Hypothalamus and Brain Stem During Hypertension via Breakdown of the Blood–Brain Barrier. *Hypertension*. 63(3):572–79

182. Ganten D, Minnich JL, Granger P, Hayduk K, Brecht HM, et al. 1971. Angiotensin-forming enzyme in brain tissue. *Science*. 173(3991):64–65

183. Cruz-López EO, Uijl E, Danser AHJ. 2021. Cardiac Angiotensin II Is Generated Locally by ACE and Not Chymase. *J. Am. Coll. Cardiol.* 78(5):540–41

184. Lavoie JL, Liu X, Bianco RA, Beltz TG, Johnson AK, Sigmund CD. 2006. Evidence Supporting a Functional Role for Intracellular Renin in the Brain. *Hypertension*. 47(3):461–66

185. Grobe JL, Xu D, Sigmund CD. 2008. An Intracellular Renin-Angiotensin System in Neurons: Fact, Hypothesis, or Fantasy. *Physiology*. 23(4):187–93

186. Xu D, Borges GR, Davis DR, Agassandian K, Luisa Sequeira Lopez MS, et al. 2011. Neuron-or glial-specific ablation of secreted renin does not affect renal renin, baseline arterial pressure, or metabolism. *Physiol Genomics*. 43:286–94

187. Xu D, Borges GR, Grobe JL, Pelham CJ, Yang B, Sigmund CD. 2009. Preservation of Intracellular Renin Expression Is Insufficient to Compensate for Genetic Loss of Secreted Renin. *Hypertension*. 54(6):1240–47

188. Shinohara K, Liu X, Morgan DA, Davis DR, Sequeira-Lopez MLS, et al. 2016. Selective Deletion of the Brain-Specific Isoform of Renin Causes Neurogenic Hypertension. *Hypertension*. 68(6):1385–92

189. Nakagawa P, Gomez J, Lu K-T, Grobe JL, Sigmund CD. 2021. Studies of salt and stress sensitivity on arterial pressure in renin-b deficient mice. *PLoS One*. 16(7):e0250807

190. Chappell MC, Pirro NT, South AM, Gwathmey TM. 2021. Concerns on the Specificity of Commercial ELISAs for the Measurement of Angiotensin (1–7) and Angiotensin II in Human Plasma. *Hypertension*. 77(3):E29–31

191. Baltatu O, Campos LA, Bader M. 2004. Genetic targeting of the brain renin-angiotensin system in transgenic rats: Impact on stress-induced renin release. *Acta Physiol. Scand.* 181(4):579–84

192. Feng Y, Xia H, Cai Y, Halabi CM, Becker LK, et al. 2010. Brain-Selective Overexpression of Human Angiotensin-Converting Enzyme Type 2 Attenuates Neurogenic Hypertension. *Circ. Res.* 106(2):373–82

193. Lazartigues E, Dunlay SM, Loihl AK, Sinnayah P, Lang JA, et al. 2002. Brain-selective overexpression of angiotensin (AT1) receptors causes enhanced cardiovascular sensitivity in transgenic mice. *Circ. Res.* 90(5):617–24

194. Ko S-H, Cao W, Liu Z. 2010. Hypertension management and microvascular insulin resistance in diabetes. *Curr. Hypertens. Rep.* 12(4):243–51

195. Kamitani A, Higashimori K, Kohara K, Higaki J, Mikami H, Ogihara T. 1994. The effects of central administration of angiotensin II type-1 receptor antagonist, CV-11974, in nephrectomized spontaneously hypertensive rats. *Clin. Exp. Pharmacol. Physiol.* 21(4):271–76

196. Ahmari N, Santisteban MM, Miller DR, Geis NM, Larkin R, et al. 2019. Elevated bone marrow sympathetic drive precedes systemic inflammation in angiotensin II hypertension. *Am. J. Physiol. Circ. Physiol.* 317(2):H279–89

197. Lochard N, Silversides DW, Van Kats JP, Mercure C, Reudelhuber TL. 2003. Brain-specific restoration of angiotensin II corrects renal defects seen in angiotensinogen-deficient mice. *J. Biol. Chem.* 278(4):2184–89

198. Gohlke P, von Kügelgen S, Jürgensen T, Kox T, Rascher W, et al. 2002. Effects of orally applied candesartan cilexetil on central responses to angiotensin II in conscious rats. *J. Hypertens.* 20(5):909–18

199. Wysocki J, Ye M, Batlle D. 2015. Plasma and Kidney Angiotensin Peptides: Importance of the Aminopeptidase A/Angiotensin III Axis. *Am. J. Hypertens.* 28(12):1418–26

200. Van Kats JP, De Lannoy LM, Danser AHJ, Van Meegen JR, Verdouw PD, Schalekamp MADH. 1997. Angiotensin II type 1 (AT1) receptor-mediated accumulation of angiotensin II in tissues and its intracellular half-life in vivo. *Hypertension*. 30(1):42–49

201. Arnold AC, Isa K, Shaltout HA, Nautiyal M, Ferrario CM, et al. 2010. Angiotensin-(1–12) requires angiotensin converting enzyme and AT 1 receptors for cardiovascular actions within the solitary tract nucleus. *Am. J. Physiol. Circ. Physiol.* 299(3):H763–71

202. Cervenka L, Mitchell KD, Oliverio MI, Coffman TM, Navar LG. 1999. Renal function in the AT1A receptor knockout mouse during normal and volume-expanded conditions. *Kidney Int.* 56(5):1855–62

203. Kihara M, Umemura S, Sugaya T, Toya Y, Yabana M, et al. 1998. Expression of neuronal type nitric oxide synthase and renin in the juxtaglomerular apparatus of angiotensin type-1a receptor gene-knockout mice. *Kidney Int.* 53(6):1585–93

204. Bruno RM, Ghiadoni L, Seravalle G, Dell'Oro R, Taddei S, Grassi G. 2012. Sympathetic regulation of vascular function in health and disease. *Front. Physiol.* 3:1–15

205. Palatini P, Julius S. 2009. The role of cardiac autonomic function in hypertension and cardiovascular disease. *Curr. Hypertens. Rep.* 11(3):199–205

206. Vapaatalo H, Hackman R, Anttila P, Vainionpää V, Neuvonen PJ. 1974. Effects of 6-hydroxydopamine on spontaneously hypertensive rats. *Naunyn. Schmiedebergs. Arch. Pharmacol.* 284(1):1–13

207. Stämpfli SF, Camici GG, Keller S, Rozenberg I, Arras M, et al. 2014. Restraint stress enhances arterial thrombosis in vivo – role of the sympathetic nervous system. *Stress*. 17(1):126–32

208. Porlier GA, Nadeau RA, Champlain J de, Bichet DG. 1977. Increased circulating plasma catecholamines and plasma renin activity in dogs after chemical sympathectomy with 6-hydroxydopamine. *Can. J. Physiol. Pharmacol.* 55(3):724–33

209. Vavřínová A, Behuliak M, Bencze M, Vodička M, Ergang P, et al. 2019. Sympathectomy-induced blood pressure reduction in adult normotensive and hypertensive rats is counteracted by enhanced cardiovascular sensitivity to vasoconstrictors. *Hypertens. Res.* 42(12):1872–82

210. Finch L, Haeusler G, Kuhn H, Thoenen H. 1973. Rapid recovery of vascular adrenergic nerves in the rat after chemical sympathectomy with 6-hydroxydopamine. *Br. J. Pharmacol.* 48(1):59–72

211. Obayashi K, Ando Y, Terazaki H, Yamashita T, Nakamura M, et al. 2000. Mechanism of anemia associated

with autonomic dysfunction in rats. *Auton. Neurosci.* 82(3):123–29

212. Bekkevold CM, Robertson KL, Reinhard MK, Battles AH, Rowland NE. 2013. Dehydration parameters and standards for laboratory mice. *J. Am. Assoc. Lab. Anim. Sci.* 52(3):233–39

213. Schiffrin EL. 2020. How Structure, Mechanics, and Function of the Vasculature Contribute to Blood Pressure Elevation in Hypertension. *Can. J. Cardiol.* 36(5):648–58

214. Schlaich MP, Kaye DM, Lambert E, Sommerville M, Socratous F, Esler MD. 2003. Relation Between Cardiac Sympathetic Activity and Hypertensive Left Ventricular Hypertrophy. *Circulation*. 108(5):560–65

215. Kouyama R, Suganami T, Nishida J, Tanaka M, Toyoda T, et al. 2005. Attenuation of Diet-Induced Weight Gain and Adiposity through Increased Energy Expenditure in Mice Lacking Angiotensin II Type 1a Receptor. *Endocrinology*. 146(8):3481–89

216. Chen Y, Joaquim LF, Farah VM, Wichi RB, Fazan R, et al. 2005. Cardiovascular autonomic control in mice lacking angiotensin AT1a receptors. *Am J Physiol Regul Integr Comp Physiol*. 288:1071–77

217. Chen D, Greca L La, Head GA, Walther T, Mayorov DN. 2010. The Day-Night Difference of Blood Pressure Is Increased in AT1A-Receptor Knockout Mice on a High-Sodium Diet. *Am. J. Hypertens.* 23(5):481–87

218. Hu ZW, Shi XY, Okazaki M, Hoffman BB. 1995. Angiotensin II induces transcription and expression of alpha 1-adrenergic receptors in vascular smooth muscle cells. *Am. J. Physiol. Circ. Physiol.* 268(3):H1006–14

219. Lázaro-Suárez ML, Gómez-Zamudio JH, Delgado-Buenrostro NL, Tanoue A, Tsujimoto G, Villalobos-Molina R. 2011. Angiotensin II modifies the expression of α1-adrenoceptors in aorta smooth muscle cells of α1D-adrenoceptor knockout mice. *Auton. Autacoid Pharmacol.* 31(3–4):57–63

220. Sharma NM, Haibara AS, Katsurada K, Nandi SS, Liu X, et al. 2021. Central Ang II (Angiotensin II)-Mediated Sympathoexcitation. *Hypertension*. 77(1):147–57

221. Cangussu LM, de Castro UGM, Machado R do P, Silva ME, Ferreira PM, et al. 2009. Angiotensin-(1-7) antagonist, A-779, microinjection into the caudal ventrolateral medulla of renovascular hypertensive rats restores baroreflex bradycardia. *Peptides*. 30(10):1921–27

222. Dupont AG, Légat L. 2020. GABA is a mediator of brain AT1 and AT2 receptor-mediated blood pressure responses. *Hypertens. Res.* 43(10):995–1005

223. Brouwers S, Smolders I, Wainford RD, Dupont AG. 2015. Hypotensive and sympathoinhibitory responses to selective central AT2 receptor stimulation in spontaneously hypertensive rats. *Clin. Sci.* 129(1):81–92

224. Littlejohn NK, Siel RB, Ketsawatsomkron P, Pelham CJ, Pearson NA, et al. 2013. Hypertension in mice with transgenic activation of the brain renin-angiotensin system is vasopressin dependent. *Am. J. Physiol. Integr. Comp. Physiol.* 304(10):R818–28

225. King AJ, Osborn JW, Fink GD. 2007. Splanchnic circulation is a critical neural target in angiotensin II salt hypertension in rats. *Hypertension*. 50(3):547–56

226. Nishida Y, Tandai-Hiruma M, Kemuriyama T, Hagisawa K. 2012. Long-term blood pressure control: is there a set-point in the brain? *J. Physiol. Sci.* 62(3):147–61

227. Watanabe H, Belyea BC, Paxton RL, Li M, Dzamba BJ, et al. 2021. Renin Cell Baroreceptor, a Nuclear Mechanotransducer Central for Homeostasis. *Circ. Res.* 129(2):262–76

228. Laursen JB, Rajagopalan S, Galis Z, Tarpey M, Freeman BA, Harrison DG. 1997. Role of superoxide in angiotensin II-induced but not catecholamine- induced hypertension. *Circulation*. 95(3):588–93

229. Rabelo LA, Todiras M, Nunes-Souza V, Qadri F, Szijártó IA, et al. 2016. Genetic Deletion of ACE2 Induces Vascular Dysfunction in C57BL/6 Mice: Role of Nitric Oxide Imbalance and Oxidative Stress. *PLoS One*. 11(4):e0150255

230. Malpas S. 2009. Editorial comment: Montani versus Osborn exchange of views Experimental Physiology –

Exchange of Views. *Exp Physiol J Physiol Regul Integr Comp Physiol Ann Rev Physiol Nat Rev Mol Cell Biol Annu Rev Biomed Eng Korner PI*. 94(4):381–97

231. Johns EJ, Kopp UC, DiBona GF. 2011. Neural control of renal function. *Compr. Physiol.* 1(2):731–67

232. Deluque AL, de Almeida LF, Francescato HDC, da Silva CGA, Costa RS, et al. 2020. Effect of Calcitriol on the Renal Microvasculature Differentiation Disturbances Induced by AT1 Blockade During Nephrogenesis in Rats. *Front. Med.* 7:23

233. Prieto MC, Gonzalez AA, Visniauskas B, Navar LG. 2021. The evolving complexity of the collecting duct renin–angiotensin system in hypertension. *Nat. Rev. Nephrol.* 17(7):481–92

234. Neubauer B, Schrankl J, Steppan D, Neubauer K, Sequeira-Lopez ML, et al. 2018. Angiotensin II Short-Loop Feedback. *Hypertension*. 71(6):1075–82

235. Matsusaka T, Nishimura H, Utsunomiya H, Kakuchi J, Niimura F, et al. 1996. Chimeric mice carrying "regional" targeted deletion of the angiotensin type 1A receptor gene. Evidence against the role for local angiotensin in the in vivo feedback regulation of renin synthesis in juxtaglomerular cells. *J. Clin. Invest.* 98(8):1867–77

236. Finke R, Gross R, Hackenthal E, Huber J, Kirchheim HR. 1983. Threshold pressure for the pressure-dependent renin release in the autoregulating kidney of conscious dogs. *Pflugers Arch.* 399(2):102–10

237. Pentz ES, Moyano MA, Thornhill BA, Sequeira Lopez MLS, Gomez RA. 2004. Ablation of renin-expressing juxtaglomerular cells results in a distinct kidney phenotype. *Am. J. Physiol. Integr. Comp. Physiol.* 286(3):R474–83

238. Hilgers KF, Reddi V, Krege JH, Smithies O, Gomez RA. 1997. Aberrant Renal Vascular Morphology and Renin Expression in Mutant Mice Lacking Angiotensin-Converting Enzyme. *Hypertension*. 29(1 II):216–21

239. Machura K, Steppan D, Neubauer B, Alenina N, Coffman TM, et al. 2009. Developmental renin expression in mice with a defective renin-angiotensin system. *Am. J. Physiol. Physiol.* 297(5):F1371–80

240. Niimura F, Labosky PA, Kakuchi J, Okubo S, Yoshida H, et al. 1995. Gene targeting in mice reveals a requirement for angiotensin in the development and maintenance of kidney morphology and growth factor regulation. *J. Clin. Invest.* 96(6):2947–54

241. Madsen K, Marcussen N, Pedersen M, Kjærsgaard G, Facemire C, et al. 2010. Angiotensin II Promotes Development of the Renal Microcirculation through AT1 Receptors. *J. Am. Soc. Nephrol.* 21(3):448–59

242. Schrankl J, Neubauer B, Fuchs M, Gerl K, Wagner C, Kurtz A. 2019. Apparently normal kidney development in mice with conditional disruption of ANG II-AT 1 receptor genes in FoxD1-positive stroma cell precursors. *Am. J. Physiol. Physiol.* 316(6):F1191–1200

243. Bader M. 2017. Of Mice and Renin. *Hypertension*. 70(1):35–37

244. Makhanova N, Lee G, Takahashi N, Sequeira Lopez ML, Gomez RA, et al. 2006. Kidney function in mice lacking aldosterone. *Am. J. Physiol. Physiol.* 290(1):F61–69

245. Maril N, Margalit R, Mispelter J, Degani H. 2004. Functional sodium magnetic resonance imaging of the intact rat kidney. *Kidney Int.* 65(3):927–35

246. McKinley MJ, Johnson AK. 2004. The Physiological Regulation of Thirst and Fluid Intake. *Physiology*. 19(1):1–6

247. Kovarik JJ, Morisawa N, Wild J, Marton A, Takase-Minegishi K, et al. 2021. Adaptive physiological water conservation explains hypertension and muscle catabolism in experimental chronic renal failure. *Acta Physiol.* 232(1):e13629

248. Cowley AW. 1992. Long-Term Control of Arterial Blood Pressure. *Physiol. Rev.* 72(1):

249. Shimada S, Abais-Battad JM, Alsheikh AJ, Yang C, Stumpf M, et al. 2020. Renal Perfusion Pressure Determines Infiltration of Leukocytes in the Kidney of Rats With Angiotensin II–Induced Hypertension. *Hypertension*. 76(3):849–58

250. Li C, Wang W, Kwon T-H, Knepper MA, Nielsen S, et al. 2003. Altered expression of major renal Na

transporters in rats with bilateral ureteral obstruction and release of obstruction. *J Physiol Ren. Physiol*. 285:889–901

251. Zhang Y, Sun Y, Ding G, Huang S, Zhang A, Jia Z. 2015. Inhibition of Mitochondrial Complex-1 Prevents the Downregulation of NKCC2 and ENaCα in Obstructive Kidney Disease. *Sci. Rep.* 5(1):12480

252. King AJ, Osborn JW, Fink GD. 2007. Splanchnic Circulation Is a Critical Neural Target in Angiotensin II Salt Hypertension in Rats. *Hypertension*. 50(3):547–56

253. Osborn JW, Tyshynsky R, Vulchanova L. 2021. Function of Renal Nerves in Kidney Physiology and Pathophysiology. *Annu. Rev. Physiol.* 83(1):429–50

254. Cao W, Li A, Wang L, Zhou Z, Su Z, et al. 2015. A Salt-Induced Reno-Cerebral Reflex Activates Renin-Angiotensin Systems and Promotes CKD Progression. *J. Am. Soc. Nephrol.* 26(7):1619–33

255. Xiao L, Kirabo A, Wu J, Saleh MA, Zhu L, et al. 2015. Renal Denervation Prevents Immune Cell Activation and Renal Inflammation in Angiotensin II–Induced Hypertension. *Circ. Res.* 117(6):547–57

256. Banek CT, Gauthier MM, Van Helden DA, Fink GD, Osborn JW. 2019. Renal Inflammation in DOCA-Salt Hypertension. *Hypertension*. 73(5):1079–86

257. Banek CT, Knuepfer MM, Foss JD, Fiege JK, Asirvatham-Jeyaraj N, et al. 2016. Resting Afferent Renal Nerve Discharge and Renal Inflammation. *Hypertension*. 68(6):1415–23

258. Ditting T, Tiegs G, Veelken R. 2009. Autonomous innervation in renal inflammatory disease—innocent bystander or active modulator? *J. Mol. Med.* 87(9):865–70

259. Lopes NR, Milanez MIO, Martins BS, Veiga AC, Ferreira GR, et al. 2020. Afferent innervation of the ischemic kidney contributes to renal dysfunction in renovascular hypertensive rats. *Pflügers Arch. - Eur. J. Physiol.* 472(3):325–34

260. Campese VM, Kogosov E. 1995. Renal Afferent Denervation Prevents Hypertension in Rats With Chronic Renal Failure. *Hypertension*. 25(4):878–82

261. Ong J, Kinsman BJ, Sved AF, Rush BM, Tan RJ, et al. 2019. Renal sensory nerves increase sympathetic nerve activity and blood pressure in 2-kidney 1-clip hypertensive mice. *J. Neurophysiol.* 122(1):358–67

262. Jacob F, LaBine BG, Ariza P, Katz SA, Osborn JW. 2005. Renal denervation causes chronic hypotension in rats: role of beta1-adrenoceptor activity. *Clin. Exp. Pharmacol. Physiol.* 32(4):255–62

263. Li S, Hildreth CM, Rahman AA, Barton SA, Wyse BF, et al. 2021. Renal denervation does not affect hypertension or the renin-angiotensin system in a rodent model of juvenile-onset polycystic kidney disease: clinical implications. *Sci. Rep.* 11(1):14286

264. Li S, Hildreth CM, Rahman AA, Barton SA, Wyse BF, et al. 2021. Renal denervation does not affect hypertension or the renin-angiotensin system in a rodent model of juvenile-onset polycystic kidney disease: clinical implications. *Sci. Rep.* 11(1):14286

265. Kim SM, Chen L, Faulhaber-Walter R, Oppermann M, Huang Y, et al. 2007. Regulation of Renin Secretion and Expression in Mice Deficient in β1- and β2-Adrenergic Receptors. *Hypertension*. 50(1):103–9

266. Mahfoud F, Townsend RR, Kandzari DE, Kario K, Schmieder RE, et al. 2021. Changes in Plasma Renin Activity After Renal Artery Sympathetic Denervation. *J. Am. Coll. Cardiol.* 77(23):2909–19

267. Cole J, Quach D Le, Sundaram K, Corvol P, Capecchi MR, Bernstein KE. 2002. Mice Lacking Endothelial Angiotensin-Converting Enzyme Have a Normal Blood Pressure. *Circ. Res.* 90(1):87–92

268. Flint J, Eskin E. 2012. Genome-wide association studies in mice. *Nat. Rev. Genet.* 13(11):807–17

269. Xu P, Costa-Goncalves AC, Todiras M, Rabelo LA, Sampaio WO, et al. 2008. Endothelial Dysfunction and Elevated Blood Pressure in Mas Gene-Deleted Mice. *Hypertension*. 51(2):574–80

270. Bozzini C, Barrio Rendo M, Devoto F, Epper C. 1970. Studies on medullary and extramedullary erythropoiesis in the adult mouse. *Am. J. Physiol. Content*. 219(3):724–28

271. Pantel K, Loeffler M, Bungart B, Wichmann HE. 1990. A mathematical model of erythropoiesis in mice and rats. Part 4: Differences between bone marrow and spleen. *Cell Prolif.* 23(4):283–97

272. Cheungpasitporn W, Thongprayoon C, Chiasakul T, Korpaisarn S, Erickson SB. 2015. Renin-angiotensin system inhibitors linked to anemia: a systematic review and meta-analysis. *QJM*. 108(11):879–84

273. Oka M, Medrano S, Sequeira-López MLS, Gómez RA. 2017. Chronic Stimulation of Renin Cells Leads to Vascular Pathology. *Hypertension*. 70(1):119–28

274. Portolés J, Martín L, Broseta JJ, Cases A. 2021. Anemia in Chronic Kidney Disease: From Pathophysiology and Current Treatments, to Future Agents. *Front. Med.* 8:328

275. Kato H, Ishida J, Imagawa S, Saito T, Suzuki N, et al. 2005. Enhanced erythropoiesis mediated by activation of the renin-angiotensin system via angiotensin II type 1a receptor. *FASEB J.* 19(14):2023–25

276. Nangaku M, Fujita T. 2008. Activation of the renin-angiotensin system and chronic hypoxia of the kidney. *Hypertens. Res.* 31(2):175–84

277. Hanoun M, Maryanovich M, Arnal-Estapé A, Frenette PS. 2015. Neural Regulation of Hematopoiesis, Inflammation, and Cancer. *Neuron*. 86(2):360–73

278. Ahmari N, Hayward LF, Zubcevic J. 2020. The importance of bone marrow and the immune system in driving increases in blood pressure and sympathetic nerve activity in hypertension. *Exp. Physiol.* 105(11):1815–26

279. Mladenovic J, Adamson JW. 1984. Adrenergic modulation of erythropoiesis: in vitro studies of colony-forming cells in normal and polycythaemic man. *Br. J. Haematol.* 56(2):323–32

280. Penn A, Mohr AM, Shah SG, Sifri ZC, Kaiser VL, et al. 2010. Dose-Response Relationship between Norepinephrine and Erythropoiesis: Evidence for a Critical Threshold. *J. Surg. Res.* 163(2):e85–90

281. Fonseca RB, Mohr AM, Wang L, Clinton E, Sifri ZC, et al. 2004. Adrenergic Modulation of Erythropoiesis Following Severe Injury Is Mediated Through Bone Marrow Stroma. *Surg. Infect. (Larchmt).* 5(4):385–93

282. Vogel J, Kiessling I, Heinicke K, Stallmach T, Ossent P, et al. 2003. Transgenic mice overexpressing erythropoietin adapt to excessive erythrocytosis by regulating blood viscosity. *Blood*. 102(6):2278–84

283. McKim DB, Yin W, Wang Y, Cole SW, Godbout JP, Sheridan JF. 2018. Social Stress Mobilizes Hematopoietic Stem Cells to Establish Persistent Splenic Myelopoiesis. *Cell Rep.* 25(9):2552-2562.e3

284. Schwartz AJ, Converso-Baran K, Michele DE, Shah YM. 2019. A genetic mouse model of severe iron deficiency anemia reveals tissue-specific transcriptional stress responses and cardiac remodeling. *J. Biol. Chem.* 294(41):14991–2

285. Tajima S, Ikeda Y, Enomoto H, Imao M, Horinouchi Y, et al. 2015. Angiotensin II alters the expression of duodenal iron transporters, hepatic hepcidin, and body iron distribution in mice. *Eur. J. Nutr.* 54(5):709–19

286. Ishizaka N, Aizawa T, Yamazaki I, Usui S, Mori I, et al. 2002. Abnormal Iron Deposition in Renal Cells in the Rat with Chronic Angiotensin II Administration. *Lab. Investig.* 82(1):87–96

287. Ishizaka N, Saito K, Furuta K, Matsuzaki G, Koike K, et al. 2007. Angiotensin II-induced regulation of the expression and localization of iron metabolism-related genes in the rat kidney. *Hypertens. Res.* 30(2):195–202

288. Guyenet PG, Stornetta RL, Holloway BB, Souza GMPR, Abbott SBG. 2018. Rostral Ventrolateral Medulla and Hypertension. *Hypertension*. 72(3):559–66

289. Booth LC, May CN, Yao ST. 2015. The role of the renal afferent and efferent nerve fibers in heart failure. *Front. Physiol.* 6(OCT):270

290. Lohmeier T. 2001. The sympathetic nervous system and long-term blood pressure regulation. *Am. J. Hypertens.* 14(11):S147–54

291. Iyer A, Chan V, Brown L. 2010. The DOCA-Salt Hypertensive Rat as a Model of Cardiovascular Oxidative and Inflammatory Stress. *Curr. Cardiol. Rev.* 6(4):291

8 Appendix

8.1 List of units

% = percent
°C = degree Celsius
µg = microgram
µL = microliter
µM = micromolar
a.u = arbitrary unit
bp = base pairs
bpm = beats per minute
cm = centimeter
fmol = femtomole
g = centrifugal force
G = gauge
g = gram
Hz = herz
Kb = kilobase
kDa = kilodalton
Kg = kilogram
L = liter
M = molar
mA = milliampere
mg = milligram
min = minute
mL = milliliter
mm = millimeter
mmHg = millimeters of mercury
mV = millivolt
ng = nanogram
nm = nanometer
pg = picogram
pmol = picomole
rpm = rotations per minute
s = second
U = unit
V = volt
v/v = volume/volume
w/v = weight/volume

8.2 List of abbreviations

3′ = three prime end
5′ = five prime end
6-OHDA = 6-hydroxydopamine
ACE = angiotensin converting enzyme
ACE2 = angiotensin converting enzyme 2
AD = aspartate decarboxylase
ADH = antidiuretic hormone
Agt = angiotensinogen
Akr1b7 = aldo-keto reductase family 1 member B7
ALB = albumin
Ang 1-12 = angiotensin 1-12
Ang 1-7 = angiotensin 1-7
Ang I = angiotensin I
Ang II = angiotensin II
Ang III = angiotensin III
ANOVA = analyses of variance
APA = aminopeptidase A
APN = aminopeptidase N
APS = ammonium persulphate
AT1 = angiotensin type 1 receptor
AT1a = angiotensin II type 1a receptor
AT1b = angiotensin II type 1b receptor
AT2 = angiotensin II type 2 receptor
ATP = adenosine triphosphate
AVP = arginine vasopressin
B = Brown
BBB = blood-brain-barrier
BCA = bicinchoninic acid
BFU-E = burst-forming unit erythroid
BP = blood pressure
BR = brain-rescue
BRS = baroreflex sensitivity
BSA = bovine serum albumin
BUN = blood urea nitrogen
Cas9 = CRISPR associated protein 9
CD3 = cluster of differentiation 3
CD68 = cluster of differentiation 68
CD68 = cluster of differentiation 86
cDNA = complementary DNA
CFU-E = colony-forming unit erythroid
cGMP = cyclic guanosine monophosphate
Chr = chromosome
ChR2 = channelrhodopsin 2
CIP = calf intestinal alkaline phosphatase
CRE = creatinine
CRISPR = clustered regularly interspaced short palindromic repeats
crRNA = CRISPR RNA
Ct = cycle threshold
CVLM = caudal ventrolateral medulla
DAPI = 4, 6-diamidino-2-phenylindole

DBP = diastolic blood pressure

ddH2O = double-distilled water
DEPC = Deoxyribonucleic acid
DMSO = dimethyl sulfoxide
DMT1 = divalent metal transporter 1
DNA = Deoxyribonucleic acid
Dnase = deoxyribonuclease
dNTPs = deoxynucleotide triphosphates
DOCA-salt = deoxycorticosterone acetate-salt
dsDNA = double-stranded DNA
E = electroporation
EDTA = ethylenediaminetetraacetic acid

EGFP = enhanced green fluorescent protein
ELISA = enzyme-linked immunosorbent assay
ENaC = epithelial sodium channel ENaC
eNOS = endothelial nitric oxide synthase
eUvol. = estimated urinary volume
F1 = first filial generation
F2 = second filial generation
GABA = gamma-aminobutyric acid
GAPDH = glyceraldehyde 3-phosphate dehydrogenase
GFAP = glial fibrillary acidic protein
GLC = glucose
GPCRs = G protein coupled receptors
gRNA = guide RNA
GWAS = genome-wide association study
HDR = homology-directed repair
het = heterozygous
HGB = hemoglobin
hGFAP = human glial fibrillary acidic protein
HIF-2α = hypoxia-inducible factor 2α
Hom = homozygous
HR = heart rate
HSC = Hematopoietic stem cell
i.p = intraperitoneal
i.v = intravenous
IBA-1 = ionized calcium binding adaptor molecule 1
ICAM-1 = intercellular adhesion molecule-1
IF = immunofluorescence
IgG = Immunoglobulin G
IL-6 = interleukin 6
IML = intermediolateral cell column
ISH = in situ hybridization
KO = knockout
LA = locomotor activity
LaGeSo = Landesamt für Gesundheit und Soziales
LB = lysogeny broth
LC-MS/MS = liquid chromatography–tandem mass spectrometry
L-DOPA = L-3,4-Dihydroxyphenylalanine
L-NAME = Nω-nitro-L-arginine methyl ester hydrochloride
M= muscle
mAgt = mouse angiotensinogen
MAP = mean arterial pressure
MCH = mean corpuscular hemoglobin
MCHC = mean corpuscular hemoglobin concentration
MCV = mean corpuscular volume
MDC = Max Delbrück Center for Molecular Medicine
MI = microinjection
M-MLV = moloney murine leukemia virus reverse transcriptase
mRNA = messenger ribonucleic acid
MUGA = mouse universal genotyping array
n = number of individuals
n.d = not detected
NCC = sodium-chloride cotransporter
NE = norepinephrine
Neo = neomycin
NEP = neprilysin
NHE3 = hydrogen exchanger
NHEJ = non-homologous end joining
NKCC2 = sodium-potassium-chloride cotransporters
NM = not measured
nNOS = neuronal nitric oxide synthase
NO = nitric oxide
Nox = nitrate and nitrites
ns = not significant
NT = not tested
NTS = nucleus tractus solitarii
OVLT = organum vasculosum of the lamina terminalis
P = probability
PAM = protospacer adjacent motif
PAP = pulsatile arterial pressure
PBS = phosphate buffered saline
PBS-T = phosphate buffered saline- Tween20
PCR = polymerase chain reaction
PEP = prolyl endopeptidase
PFA = paraformaldehyde
pH = potential of hydrogen
PI = pulse interval
PLT= platelets
PNK = polynucleotide kinase
PRCP = prolylcarboxypeptidase
PVN = paraventricular nucleus of the hypothalamus

rAgt = rat angiotensinogen
RAS = renin angiotensin system
RBC = red blood cells
Ren = renin
RET = reticulocytes
RIPA = radioimmunoprecipitation assay buffer
RNA = ribonucleic acid
RNase = ribonuclease
RNasin = ribonuclease inhibitor
ROCK = Rho-associated protein kinase
RT = reverse transcription
RT-PCR = reverse transcriptase PCR
RT-qPCR = reverse transcriptase quantitative PCR
RVLM = rostroventrolateral medulla
S = salivary
SBP = systolic blood pressure
SD = Sprague-Dawley
SDS = sodium dodecylphosphate
SDS-PAGE = sodium dodecylsulfate polyacrylamide gel electrophoresis
SFO = subfornical organ
sgRNA = single-guide RNA
siRNA = short interfering RNA
SNA = sympathetic nerve activity
SNPs = single nucleotide polymorphisms
SNS = sympathetic nerve system
SNS = sympathetic nervous system
SON = supraoptic nuclei
ssDNA = single-stranded DNA
Sv-40 = simian virus 40
TAE = tris-Acetate-EDTA
tAgt = total angiotensinogen
TE = Tris-EDTA
TEMED = tetramethylethylendiamine
Tg = transgenic
TGF-β = transforming growth factor beta
THOP = thimet oligopeptidase
TNFα = tumor necrosis factor alpha
TP = total proteins
tracRNA = trans-activating CRISPR RNA
TRIS = tris(hydroxymethyl)aminomethane
UV = ultraviolet
VCAM-1 = vascular cell adhesion molecule-1
vs = versus

W = white
WB = western blot
WBC = white blood cells
wt = wildtype
α-SMA = alpha-smooth muscle actin
Δ = delta
$\chi 2$ = chi-squared

8.3 List of tables

8.4 List of figures

8.5 Scientific output during the doctoral period

8.5.1 Publications

Rodrigues AF, Todiras M, Qadri F, Campagnole-Santos MJ, Alenina N & Bader M. Increased angiotensin II formation in the brain modulates cardiovascular homeostasis and erythropoiesis, *Clinical Science*, 2021 Jun 11;135(11):1353-1367. DOI: 10.1042/CS20210072

Veronez CL, Maghsodi S, Todiras M, Popova E, **Rodrigues AF**, Qadri F, Pesquero JB, Bader M. Endothelial B2-receptor overexpression as an alternative animal model for hereditary angioedema. *Allergy*, 2019 Oct;74(10):1998-2002. DOI: 10.1111/all.13836

8.5.2 Oral presentations

XIII International Symposium on Vasoactive Peptides. e-conference, 2021. Title: Generation and validation of AT1a Receptor deficient Sprague-Dawley Rats.

23rd Meeting of the European Council for Cardiovascular Research (ECCR), 2020 e-conference. Title: Unexpected normal blood pressure in FVB/N mice lacking angiotensinogen. *Award for the best oral presentation in the PhD student category.*

XII International Symposium on Vasoactive Peptides. Belo Horizonte, Brazil, 2019. Title: Brain Angiotensin II and the Vascular Sympathetic control in health and Renal Disease.

8.5.3 Poster presentations

Angiotensin Gordon Research Conference, Barga (Luca), Italy, 2020 Title: Brain Angiotensin synthesis and its Role in Vascular Sympathetic Control.

21st Meeting of the European Council for Cardiovascular Research (ECCR), Garda, Italy, 2017. Title: Central Angiotensin II Modulates Circadian Rhythm of Blood Pressure in Rats.